V. P. Nerubatskyi, O. A. Plakhtii, D. A. Hordiienko

SCIENTIFIC FOUNDATIONS OF HIGHER ENERGY EFFICIENCY AND ELECTROMAGNETIC COMPATIBILITY OF SEMICONDUCTOR ELECTRIC ENERGY CONVERTERS

Monograph

MINISTRY OF SCIENCE AND EDUCATION OF UKRAINE

UKRAINIAN STATE UNIVERSITY OF RAILWAY TRANSPORT

V. P. Nerubatskyi, O. A. Plakhtii, D. A. Hordiienko

SCIENTIFIC FOUNDATIONS OF HIGHER ENERGY EFFICIENCY AND ELECTROMAGNETIC COMPATIBILITY OF SEMICONDUCTOR ELECTRIC ENERGY CONVERTERS

Monograph

Recommended by the Academic Council of Ukrainian State University of Railway Transport

Kharkiv – 2023

UDC 621.314
N547

Reviewers:

Tomashevskyi Roman Serhiiovych, Doctor of Engineering Sciences, Professor, Director of the Educational and Scientific Institute of Energy, Electronics and Electromechanics of the National Technical University "Kharkiv Polytechnic Institute";

Tugai Dmytro Vasyliovych, Doctor of Engineering Sciences, Associate Professor, Head of the Department of Alternative Electric Power and Electrical Engineering of the O. M. Beketov National University of Urban Economy in Kharkiv.

Recommended by the Academic Council of Ukrainian State University of Railway Transport for publishing as monograph of September 30, 2022, report no. 5

N547 Nerubatskyi V. P., Plakhtii O. A., Hordiienko D. A. Scientific foundations of higher energy efficiency and electromagnetic compatibility of semiconductor electric energy converters: Monograph. – Kharkiv: Publisher Machulin L., 2023. – 220 p.
ISBN 978-617-8195-29-8

The monograph describes the methods to ensure the energy efficiency of systems and the electromagnetic compatibility of semiconductor converters of electric energy. The results of the scientific research into the operation of semiconductor converters that provide rational electric power parameters and efficient use of electric power have been systematized and presented. It will be of value to researchers, postgraduate students, students of higher educational institutes of power engineering and specialists in the field of converter equipment.

181 figures, 40 tables, 109 references

UDC 621.314

ISBN 978-617-8195-29-8

CONTENTS

ABBREVIATIONS

AFR	Amplitude Frequency Response
AM	Asynchronous Machine
APF	Active Power Filter
ARS	Automatic Regulating System
AVI	Autonomous Voltage Inverter
AVR	Active Voltage Rectifier
CS	Control System
CVC	Current Voltage Characteristic
DCUS PWM	Double Channel Uniformly Shifted Pulse Width Modulation
EMC	Electromagnetic Compatibility
ERS	Electric Rolling Stock
ETL	Electric Transmission Line
FC	Frequency Converter
IEC	International Electrotechnical Commission
LAFR	Logarithmic Amplitude Frequency Response
PFC	Power Factor Compensation
PWM	Pulse Width Modulation
RMS	Root Mean Square
THD	Total Harmonic Distortion
TS	Traction Substation
VB	Voltage Booster

INTRODUCTION

More stringent requirements for the characteristics of electromagnetic compatibility is conditioned by the fact that the field of application of electronic devices is expanding. The system solutions based on microelectronics and semiconductor electronics are applied in all spheres of production, household and transport. At present the product evaluation in terms of electromagnetic compatibility is more necessary than it was at the early stage of the electronics development. The main concepts of electromagnetic compatibility deal with the effect of both radiated and conductive interferences (guidance) generated by conductors (for example, guidance along power supply circuits), as well as the sensitivity of electrical equipment to interferences (resistance).

The operation of semiconductor power converters at traction substations, frequency-controlled electric drives and other powerful nonlinear loads cause a significant emission of higher current harmonics to electrical networks. Higher current harmonics in electrical networks cause a complex negative effect on the energy efficiency of a network. All these problems are closely connected with a widespread application of advanced technologies.

The material of the monograph is of value to researchers, graduate students, university students majoring in electric power engineering and specialists in the field of converter equipment; it can be used for scientific research and organization of the educational process in higher educational establishments. Moreover, the monograph can be used to systematize the knowledge and understand complex processes running in converter equipment.

The monograph is prepared in the framework of the project “Development of scientific bases for improving energy efficiency and improving the quality of electricity in electricity networks” (State Registration No. 0121U109440) at the Department of Electrical Energetics, Electrical Engineering and Electromechanics of Ukrainian State University of Railway Transport (Kharkiv) according to the results of the contest of scientific projects and technical developments by young researchers under the auspices of the Ministry of Education and Science of Ukraine.

CHAPTER 1

UNIVERSAL METHOD FOR MODELLING POWER LOSSES IN SEMICONDUCTOR CONVERTERS

1.1. Power quality indices

The term “power quality” means the conformity of the main parameters of a power system with the established norms of production, transmission and distribution of electric energy [1, 2].

In accordance with DSTU EN 50160-2014 there are main and additional power quality indices.

The main indices of power quality describing its properties and quality are:

– voltage deviation (δU, %);

– peak-to-peak voltage deviation (δU_t, %);

– voltage oscillation dose (ψ, %);

– coefficient of non-sinusoidality of voltage curve (k_nU, %);

– coefficient of the n-th harmonic voltage component of the odd (even) order ($kU(n)$, %);

– coefficient of the negative voltage sequence (k_2U, %);

– coefficient of the zero voltage sequence (k_0U, %);

– duration of a voltage failure (Δt_f, s);

– pulse voltage (U_{pulse}, V);

– frequency deviation (f, Hz).

The quantitative indicator of electric power quality is expressed by voltage and frequency deviations, peak-to-peak voltage and frequency oscillations, voltage non-sinusoidality ratio, and voltage unbalance ratio of the main frequency.

The frequency deviation is an average difference over 10 min between the actual value of the main frequency and its nominal value. It is assumed that the frequency deviation from the nominal value in the normal operational mode can be in a range of ±0.1 Hz. Short-term deviations can reach ±0.2 Hz.

The frequency oscillation is a difference between the highest and the lowest values of the main frequency in the process of a rapid change in the mode characteristics at which a frequency change rate is over 0.2 Hz per second. The frequency oscillations have not to be 0.2 Hz over the allowable deviations equalling 0.1 Hz. The voltage oscillation is evaluated by the peak-to-peak voltage change δU_t, i.e., a difference between the highest and the lowest actual voltage values in the process

of a rapid change in the mode characteristics, at which a voltage change rate is over 1 % per second.

The non-sinusoidality of the network voltage is characterized by the voltage non-sinusoidality ratio (distortion). The voltage unbalance is an inequality of phase or linear voltages by the amplitude and the phase angles between them.

Normalization of power quality indices is one of the main problems in terms of the power quality. The system of power quality indices consists of quantitative characteristics of slow (deviations) and rapid (oscillations) measurements of the effective voltage, its form and the symmetry in a three-phase system, as well as frequency changes. Among additional power quality indices, which are the formats for main power quality indices used in other technical guidance documents, are:

– coefficient of amplitude voltage modulation;

– coefficient of phase-to-phase voltage unbalance; and

– coefficient of phase voltage unbalance.

Let us note the allowable values of the above-mentioned power quality indices. During 95 % of the day and night period (22.8 hours) the power quality indices have to be in a range of the normal allowable values. According to the standard, during each day and night period more than 95 % of time the phase voltage must be in a range of 209...231 V (5 % deviation), the frequency must be in a range of 49.8...50.2 Hz, and the non-sinusoidality ratio should not exceed 5 %. During the remaining 5 % or less of each day and night period the voltage may vary from 198 to 242 V (10 % deviation), the frequency – from 49.6 to 50.4 Hz, and the non-sinusoidality ratio should not exceed 10 %. Also, more considerable frequency changes (from 49.5 to 51 Hz) are allowed, but the total duration of these changes should not exceed 90 hours per year.

The power supply failure is the situation when the power quality indices deviate from the set parameters for a short time. The frequency can deviate by 5 Hz from the nominal value. The voltage may drop to zero. Then, the quality indices must be restored. The control over the power quality in the referent points of power networks is fulfilled by the staff of the power networks enterprises. And the duration of measuring the power quality index must be at least 24 hours.

1.2. Electromagnetic compatibility of semiconductor converters and electric power networks

The electromagnetic compatibility (EMC) is the ability of electric equipment to operate satisfactorily under electromagnetic impacts from the environment, and not to

negatively affect this environment and other electric devices [3, 4]. The EMC characteristics can be determined in a frequency range of 0...400 GHz.

Electromagnetic interferences are caused by natural phenomena or technical processes. Some examples of natural interferences are atmospheric discharges (electromagnetic pulses emerging during a lightning strike) or electrostatic discharges. The latter ones are of particular importance in semiconductor electronics. For industrial equipment, the main source of interferences is electrical switching associated with a very rapid change in the currents and voltages, which, in turn, results in electromagnetic interferences both cyclic or random. The effect of these disturbances can be conductive (in the form of interferences to currents or voltages in conductors) and radiated (due to the alternating magnetic field).

The type of conductive interference, when the induced current has the sign, i.e., has the same amplitude in both directions, is called the symmetrical or differential interference. If the interference current has ground fault or runs along the conductor in one direction, this interference is called asymmetric or common-mode.

The electromagnetic connection between the source and the interference receiver can be a result of:

– galvanic connection (most frequent), which creates symmetrical interferences;

– capacitive coupling resulting from the effect of an alternating electric field on stray structural capacitances;

– inductive coupling caused by the fact that the conductor with the current is in the alternating magnetic field; and

– electromagnetic coupling can be either of conductive nature (emerges as induction to conductors of cable harnesses or conductive tracks of a printed circuit board) or propagate through emission (if the width of a gap between the source and the interference receiver exceeds 0.1 of the emission wavelength).

There are a lot of standards and requirements for EMC equipment. They include the standards for the characteristics of measurement equipment, parameters of testing systems and measuring techniques for various interferences. They describe testing procedures for electrical EMC devices and establish the criteria that can be used for making the conclusion about meeting the set requirements.

The requirements for EMC are standardized internationally, nationally and on the European level. International bodies in charge are International Organization for Standardization (ISO) and International Electrotechnical Commission (IEC), a subdivision of which is International Special Committee on Radio Interference (CISPR). In Europe this is done by European Committee for Standardization (CEN), European Committee for Electrotechnical Standards (CENELEC), and European

Telecommunications Standardization Institute (ETSI). The semiconductor integrated microcircuit is a relatively new object of the EMC standardization with special requirements for compatibility regarding these devices. The EMC requirements for them are almost the same as for other devices and components, however individual components of integrated microcircuits have only one application area. At this time, IEC has developed two groups of standards for the techniques of measuring radiated interferences (Standard IEC 61967) and the interference immunity of integrated microcircuits (Standard IEC 62132). When solving the problems on distortions, one should take into account that technical means for interference suppression or protection against them can be solved in:

– interference sources (individual devices);

– electrical networks (powerful centralized units); and

– interference-sensitive power consumers (buffer devices increasing the level of protection against distortions).

The EMC standards can be classified into:

– those establishing the allowable level of distortions in the network and

– those establishing the rules for connecting distorting equipment to the network.

Each electric consumer is characterized by the ratio of interference susceptibility level and interference resistance to the level of electric compatibility.

The EMC problems can be solved with consideration of the following:

– determination of the amplitude of harmonics and estimation of the total effect of several harmonics;

– determination of the common level of distortions and the admissible individual consumption of the voltage of the *n*-th harmonic at the point of common coupling;

– determination of frequency characteristics of network elements and load centres; and

– determination of the admissible period of power interruption.

1.3. Methods for compensation of higher harmonics and reactive power in electric networks

For modern electric power industry one of the main problems is the power factor compensation (PFC) [5]. In [6] the authors studied the impact of PFC on the parameters of the mode and the electric system stability, found the admissible PFC levels for the stability of load centres and synchronous generators, researched the self-excitation areas of the synchronous generator at PFC.

As a rule, PFC techniques are selected on the basis of calculations of power flows, voltage levels, static and dynamic stability of electric networks. These calculations are made for normal and maintenance electric network diagrams. The established capacity for PFC equipment and the required adjustment range are determined with consideration of the peak load modes in the electric system within the day-and-night period in summer and winter. When choosing the PFC method one should take into accounts restrictions on the value and duration of reactive capacity consumption for generators. The calculation of modes of system-forming networks involves equivalent loads on medium or low-voltage buses for traction substations (TS). During designing the PFC method is selected by means of the highest operation voltage level for electrical equipment, and the PFC method for increasing the power transmission capacity of the electric transmission line (ETL) is based on the calculation of the static and dynamic stability.

Voltage control and reactive power re-distribution, as well as reduction of capacity losses in the 110...330 kV distribution networks are made by transformers and auto-transformers equipped with units regulating the on-load voltage [7].

Thus, the technical and economic assessment of PFC measures in the 110...750 kV electric networks should provide the support of voltages within the allowable values; reduce the capacity losses in the power networks; increase the transmission capacity of ETL ensuring its static and dynamic stability; increase the stability of the load centres; prevent voltage collapses, and, consequently, maintain the reactive capacity of the generators within the allowable limits.

The reactive power flows significantly affect the modes of electrical systems and networks, as well as power quality indices [8, 9]. Modern computer technologies and applications expand our perception of the reactive power nature. Theoretical research is inextricably linked to the practical issues on PFC, which requires the development of modern measures for PFC [10, 11]. The problem of reactive power and the problem of designing means with PFC are of holistic character, which necessitates further theoretical and practical research in this field.

Generally, the electrical system, apart from the main losses associated with the transfer of active power, suffers additional losses due to the reactivity of its elements, asymmetry of loads, non-stationary and non-linear nature of the processes.

One of the most effective and efficient ways to reduce the main and additional losses is to use PFC equipment based on static capacitor batteries. The use of capacitor units enables:

– to unload power lines, transformers and distributing gears;

– to reduce the cost of electricity;

– to reduce the level of higher harmonics when using a certain type of installation; and

– to reduce phase asymmetry.

The calculation and analysis of the parameters of the established mode of the electrical network according to the load-centre diagram by the Newton method involves the use of equations of nodal voltages in the form of a power balance. In matrix form, they look like:

$$\bar{U}_{diag} \cdot \left(Y_y \cdot \bar{U} + Y_b \cdot \bar{U}_b \right) = \bar{S}, \tag{1.1}$$

where $\bar{U}_{diag}$ – the diagonal matrix, the *k*-diagonal element of which is equal to the conjugated voltage complex of the *k*-node; $\bar{S}$ – the column vector, the *k*-element of which is equal to the conjugated power complex of the *k*-node.

The equivalent circuit for the distribution electrical network according to the load-centre diagram is shown in fig. 1.1.

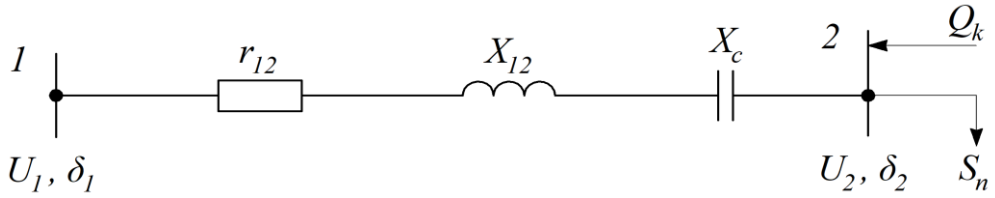

Figure 1.1 – Equivalent circuit for distribution electrical network according to load-centre diagram

Let us investigate the effect of the daily non-uniform electric load on the mode parameters of the electric network, as well as the values of the longitudinal compensation of ETL X_c and the PFC values for the consumer Q_c.

It is known that the electrical load of power supply systems is unbalanced. Experts distinguish daily, weekly and annual imbalances. Changes in the load affect the mode parameters of the electric network.

The daily load for the consumer S_n varies daily from the maximum to the minimum value as follows:

$$S_1 = \left(-60 - j20 \right); \tag{1.2}$$

$$S_2 = \left(-70 - j30 \right); \tag{1.3}$$

$$S_3 = (-80 - j40); \tag{1.4}$$

$$S_4 = (-90 - j50); \tag{1.5}$$

$$S_5 = (-100 - j60). \tag{1.6}$$

The nature of this effect is shown in fig. 1.2. Analysis of the given results shows that with an increase in the load, the losses of active and reactive power in the network increase, moreover, the voltage loss and the angle δ_2 increase, and the voltage for the consumer decreases.

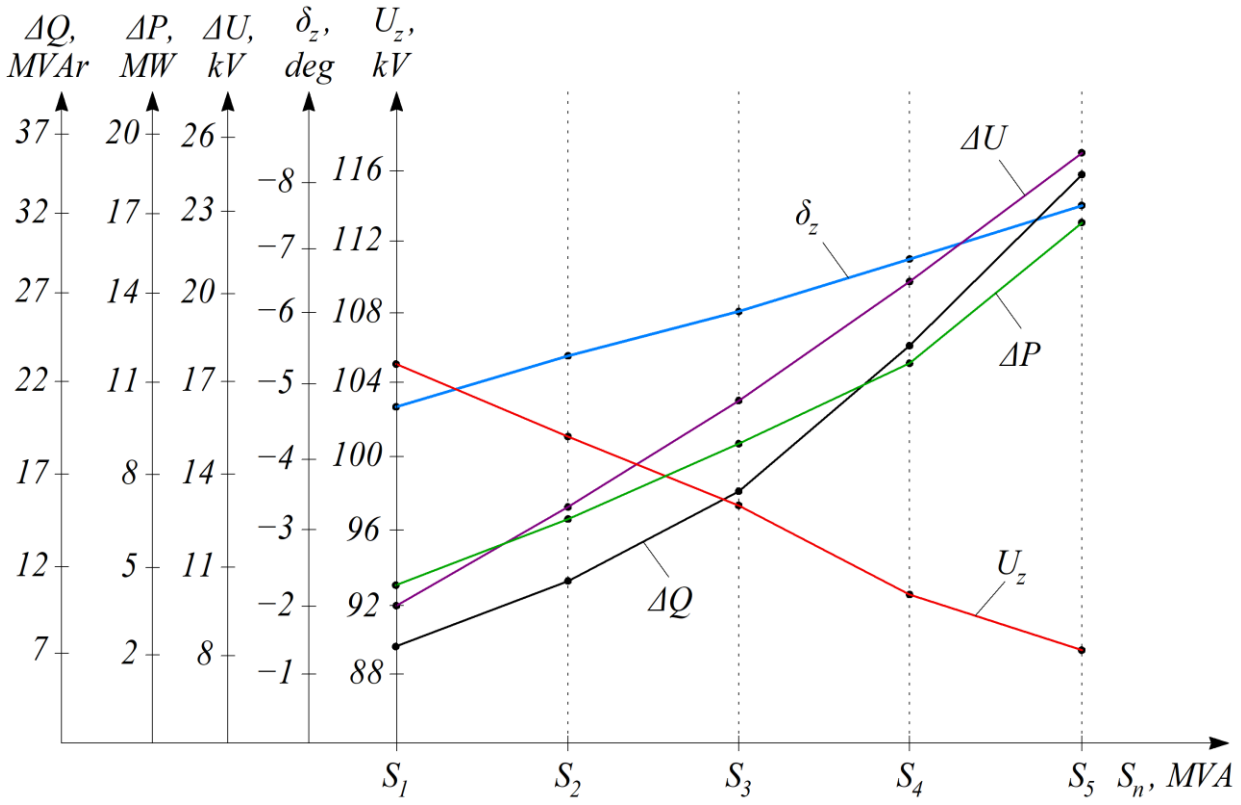

Figure 1.2 – Impact of daily irregular load on mode parameters

Experts believe that one of the most effective ways to improve the mode of the electric network is to compensate for reactive power flows for the consumer. At the same time, the power losses in the network are reduced, and the line transmission capacity is increased. The results of calculations of the influence of PFC on the mode parameters are shown in fig. 1.3. They demonstrate that when the voltage drop is compensated, the losses of active and reactive power decrease, and the voltage and the angle in the consumer increase.

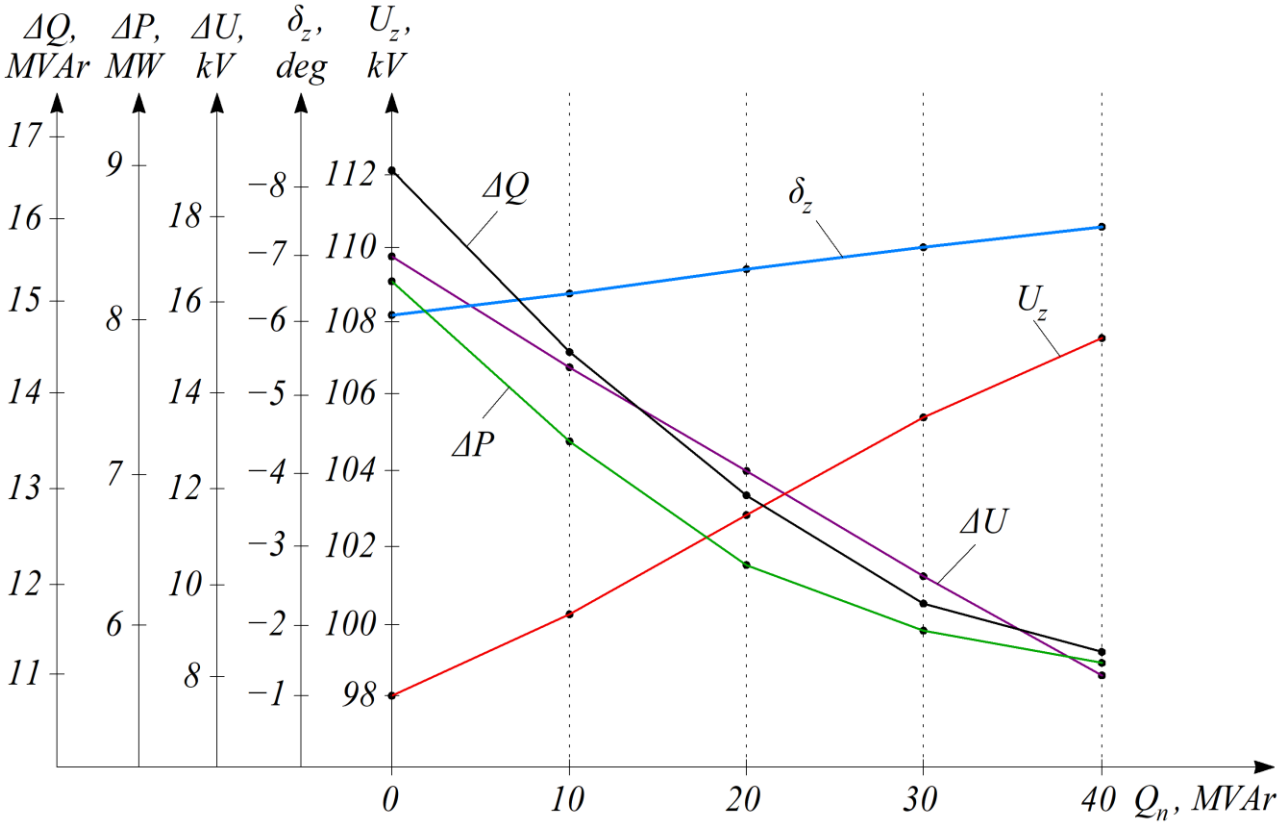

Figure 1.3 – Impact of consumer's PFC on mode parameters

Recently, there has been increased interest in the issues of longitudinal compensation of ETL parameters. By its influence, the increase in the amount of longitudinal compensation is similar to the process of increasing the PFC in the consumer. The difference is the impact on the angle δ_2.

Functional dependencies of the mode parameters on the value of longitudinal compensation are shown in fig. 1.4.

The practical implementation of the research is reduced to determining the location, type and capacity of the PFC equipment. These tasks are solved on the basis of similar feasibility calculations. At present, shunt capacitor banks with an installed capacity of 52 and 108 mV·Ar are usually used to normalize voltage levels and reduce power losses in distribution networks at tie TSs of 110 kV and higher; and when designing new facilities in 110 kV networks, it is recommended to use modular shunt capacitor banks from factory-made units with capacitors with environmentally safe materials. Thus, it is economically feasible for the electricity supplier to have a complete PFC, or close to it. However, in terms of technical feasibility, the consumer and producer of electric energy have questions related to the reduction of stability of load centres and generating stations and the possibility of breaking their stability due to PFC by static capacitor batteries.

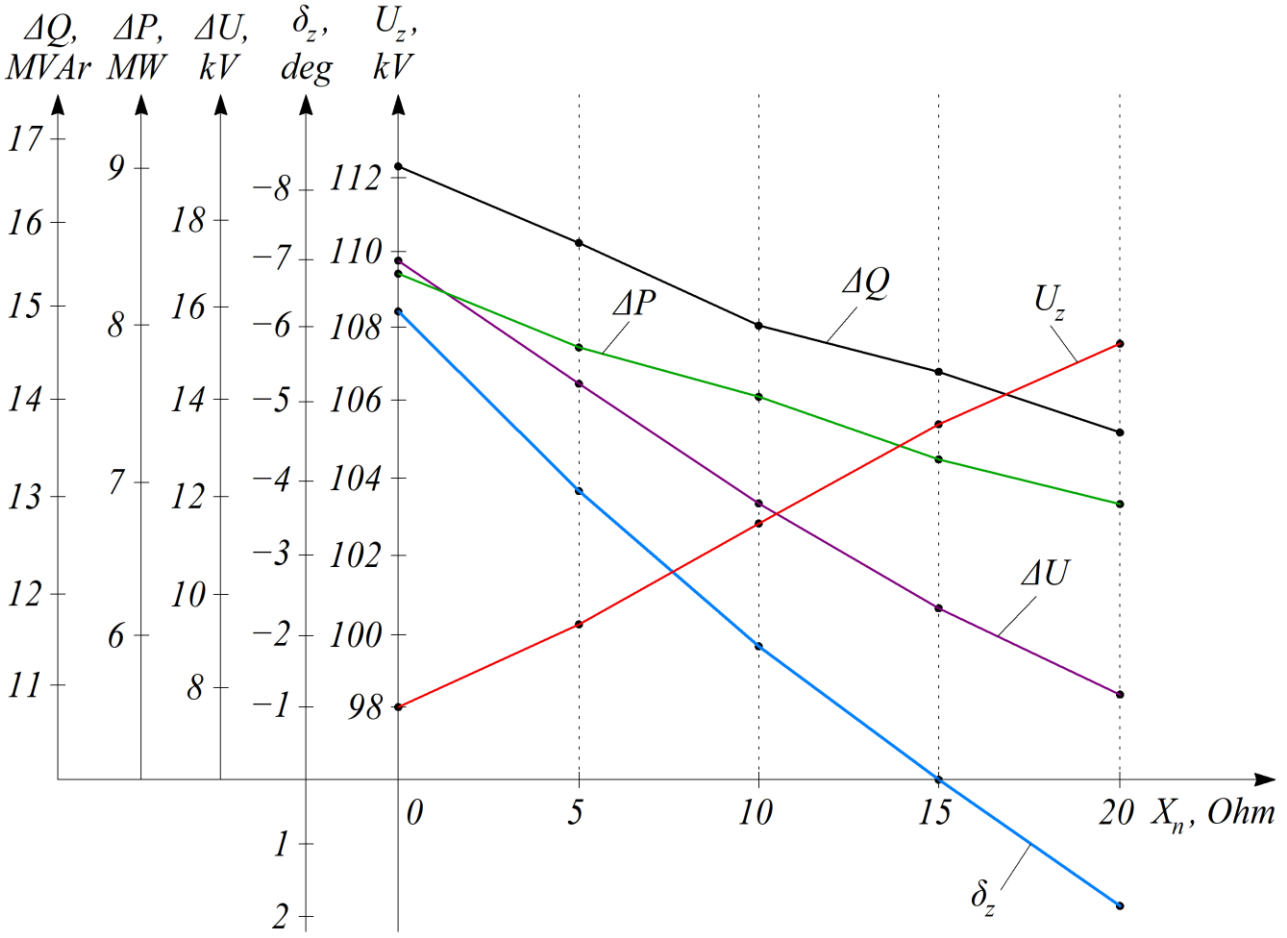

Figure 1.4 – Impact of longitudinal compensation of ETL on mode parameters

It is known that the load of the PFC with static capacitor batteries can sometimes lead to a significant decrease in the stability reserves of asynchronous motors and, with a high degree of compensation, to a voltage collapse. For example, the calculations show that an increase in cosφ from 0.89 to 0.95 reduces the load stability factor by about 1.5 times, and an increase in cosφ to 1 practically leads to the instability of the load centre.

According to the standards for the stability of power systems, the coefficient of static stability reserve by voltage in the normal mode should be over 15 %, and in post-emergency conditions – not less than 10 %.

Thus, taking into account the load centre stability, the reactive power can be compensated to the level at which the value of the static voltage stability factor in the normal mode and the post-emergency conditions will not be less than the minimum standardized value. The impact of the PFC on the synchronous generator stability can be evaluated by considering the simplest electric system in which the generator outputs power through a transformer and a line to the load busbars. The equivalent circuit of such a system is shown in fig. 1.5.

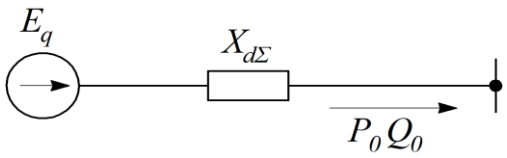

Figure 1.5 – Equivalent circuit of electric system

The following notations are presented on the equivalent circuit: U_0 – the voltage on the load busbars; P_0 and Q_0 – the active and reactive power produced by the generator to the load; $X_{d\Sigma}$ – the resulting inductive resistance of the power transmission.

A simplified vector diagram of a synchronous implicit-pole generator at different degrees of the PFC load is shown in fig. 1.6.

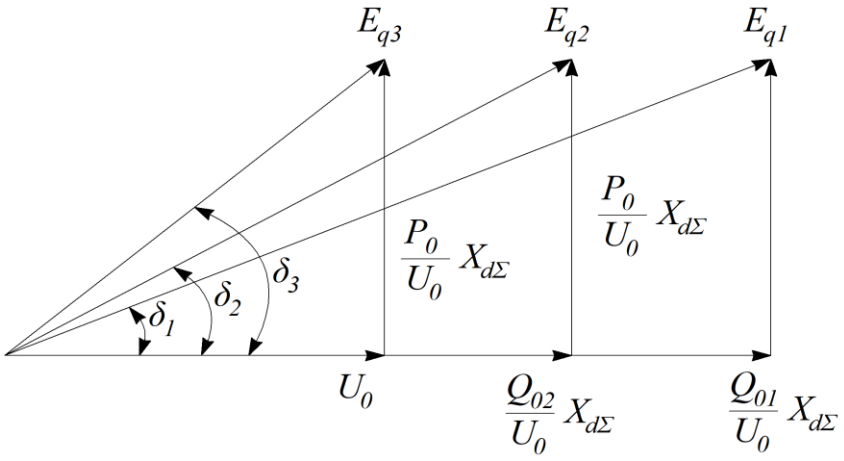

Figure 1.6 – Simplified vector diagram of synchronous generator

The following notations are used on the vector diagram: Q_{01} – the reactive power produced by the generator to the load without PFC; Q_{02} – the reactive power produced by the generator to the load at 50 % of PFC; in the third case, the reactive power of the load is fully compensated, i.e., $Q_{03} = 0$; E_{q1}, E_{q2} and E_{q3} – the generator voltages that provide the same active power at the corresponding reactive power issued by the generator to the load.

As can be seen from the vector diagram, the value of the electric driving force of the generator significantly decreases with an increase in the PFC load. The lower electric driving force of the generator is the result of the current reduction in the generator stator windings with PFC.

This increases the voltage across the generator busbars. As a result, an automatic voltage regulator comes into operation, thus reducing the coil current, which ultimately leads to a decrease in the generator voltage. If we neglect the active resistances of the

power transmission elements, the limit of the transmitted active power of the implicit-pole synchronous generator can be calculated by the expression:

$$P_a = \frac{E_q \cdot U_0}{X_{d\Sigma}}. \quad (1.7)$$

It follows from this expression that the limit of the transmitted active power decreases in proportion to the decrease in the generator voltage and, therefore, the static voltage stability factor is reduced and can be calculated by the expression:

$$K_{s.stab.} = \frac{P_a - P_0}{P_0} \cdot 100\ \%. \quad (1.8)$$

According to the standards for the power system stability, the coefficient of static active capacity stability in normal mode should not be less than 20 %, in post-emergency conditions – not less than 8 %. Thus, the reactive power can be compensated to the level at which the coefficient of the static voltage stability by active capacity in normal mode and post-emergency conditions will not be less than the minimum standardized value.

In networks with capacitive series compensation of the reactance of the stator circle the PFC load using static capacitor batteries can lead to a static stability violation of the self-excitation type. This is due to the fact that when connecting a rather large capacity, an oscillating circuit *R–L–C* is formed, where *L* corresponds to the inductance of generator, transformer and line. At constant values of *R*, *L* and *C* the electrical oscillations fade over time. In this case, the generator inductance varies periodically.

In the case of a salient-pole generator, it varies from L_q to L_d due to the unbalance of the rotor in the longitudinal and transverse axes. Under some conditions it can convert the kinetic energy of the rotor rotation into the electromagnetic energy of the oscillating circuit. If the losses in this circuit are quite small, then the oscillation amplitude can increase and, thus, a parametric resonance occurs.

In an implicit-pole generator, its inductance at rotor oscillations varies from L_d to L_q. With a slip between the stator electromagnetic field and the rotor windings, an asynchronous moment occurs due to the interaction of currents induced in the rotor windings and the stator rotational field. Under the effect of this asynchronous electromagnetic moment, self-excitation develops. This is a nonparametric resonance, based on the periodic variation of the circuit inductance. For its existence, only appropriate capacity and sliding are necessary.

There are two main types of self-excitation: asynchronous and synchronous. Asynchronous self-excitation is possible in all types of machines at the natural frequency of the oscillating circuit, which is less than the generator frequency ω_0. Self-excitation at frequency $\omega_{own} = \omega_0$ (synchronous self-excitation) is possible only in salient-pole generators. The development of both types of self-excitation stops when a high degree of generator saturation occurs, i.e., in a deliberately unacceptable mode.

Approximate estimation of the generator self-excitation capability is performed by constructing self-excitation regions in coordinates R, X_c (fig. 1.7), where R – the total active resistance of the simplest electrical system; X_c – the capacitive resulting resistance of the static capacitor batteries and the series compensation capacitance.

Fig. 1.7 shows: *I* – the synchronous self-excitation zone; *II*, *III* – the asynchronous self-excitation zone. It can be seen that with the total active resistance of the simplest electric system, less than the critical R_{crit}, and the resulting capacity resistance X_c, less than $X_{d\Sigma}$, a violation of the static stability of the self-excitation type is possible.

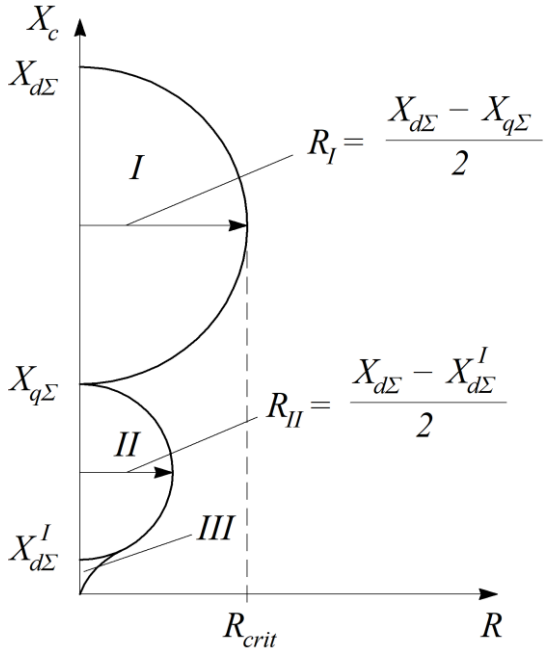

Figure 1.7 – Generator self-excitation areas in coordinates R and X_c

The traditional method for reducing the higher harmonics of the consumed current is the use of network passive filters. Passive filters can be tuned to a particular harmonic, multiple harmonics, or some range. Given that this method is the most commonly used, there is a fairly large number of works devoted to passive filters. So far a fairly large number of topologies of passive filtering devices have been developed.

Variants of circuit solutions for passive filters tuned to one and two harmonics are shown in fig. 1.8.

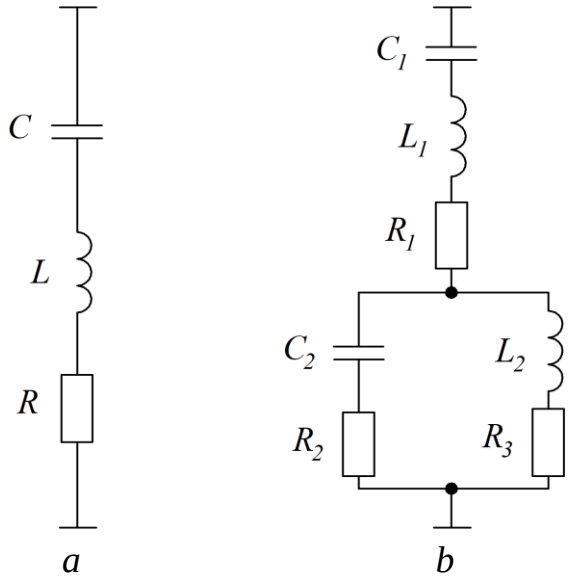

Figure 1.8 – Passive filters:
a – tuned to one harmonic; *b* – tuned to two harmonics

According to the form of the amplitude-frequency response (AFR), low-pass filters, high-pass filters, band-pass filters and rejection filters are distinguished. The number of reactive elements determines the filter order (fig. 1.9).

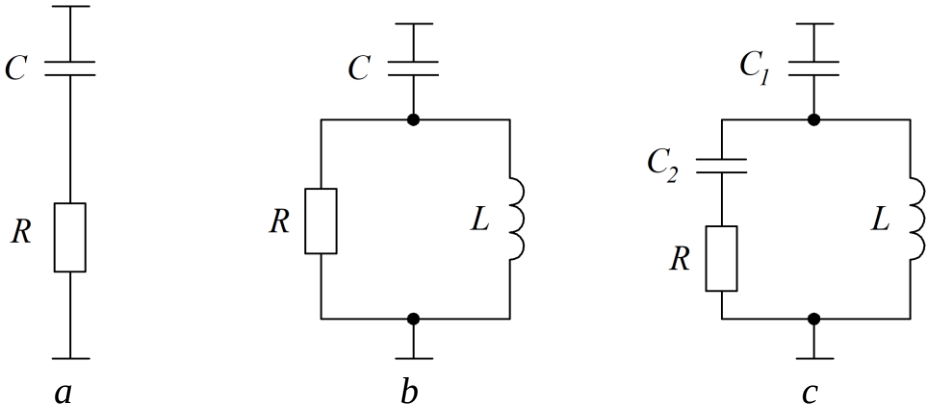

Figure 1.9 – Schematic implementation of passive filters:
a – 1st order; *b* – 2nd order; *c* – 3rd order

Despite in-depth studies aimed at improving the filtering properties, passive filters used to compensate for higher harmonics of the network current and increase the power factor have a number of significant disadvantages, among them:

– high weight and dimensions of filters;

– static AFR, designed only for certain frequencies, does not filter non-canonical harmonics in the network;

– discrete connection of static components to the power supply network does not cause full compensation of reactive currents, but in some cases the generation of additional reactive currents in the power supply system; and

– in transient modes, resonant phenomena with the network may occur, which leads to surges and, as a result, accidents in the power supply system.

The above-mentioned shortcomings makes it possible to conclude that this method is insufficient to achieve the specified goals of improving EMC.

The development of a modern element base of power electronics allows developing a new class of converters that can actively control the form of consumed current, namely, active power filters and active rectifiers with power factor compensation. The use of converters of this type makes it possible to comprehensively improve the quality of consumed electrical energy and EMC in general.

The use of this filter type greatly improves the EMC performance.

The active power filter (APF) is a semiconductor converter that compensates higher harmonics and active power factor. This converter type is able to maintain a given angle between the input voltages and currents and shape the current consumed from the network close to a sinusoidal form. The APF power circuit can be built on the basis of circuits of autonomous voltage inverter (AVI), autonomous current inverter or Vienna rectifier. The APF diagram based on the AVI has become the most widespread.

The connection method for the APF can be serial, parallel, or serial-parallel (combined). When connected in parallel, the APF forms a predetermined form of the consumed current. To form a sinusoidal form of the consumed current from the network, the APF must consume phase currents that repeat the form of higher harmonics of the load shifted by 180°. As a result, the total current of the APF and the load becomes strictly sinusoidal. The parallel connection of the APF to the network is shown in fig. 1.10. The principle of forming the sinusoidal consumed current of the parallel APF is shown in fig. 1.11. As follows from fig. 1.10, the use of the parallel-type APF based on the AVI makes it possible to obtain a complete PFC and form the sinusoidal current consumed by the rectifier unit from the power supply network with the total harmonic distortion (THD) less than 5 %.

In the case of connecting the APF to the high-voltage network, it is advisable to use the APF based on multilevel inverters, in which the voltage applied to the switch is less compared to a two-level active voltage rectifier (AVR). The diagram of the three-level APF is shown in fig. 1.12.

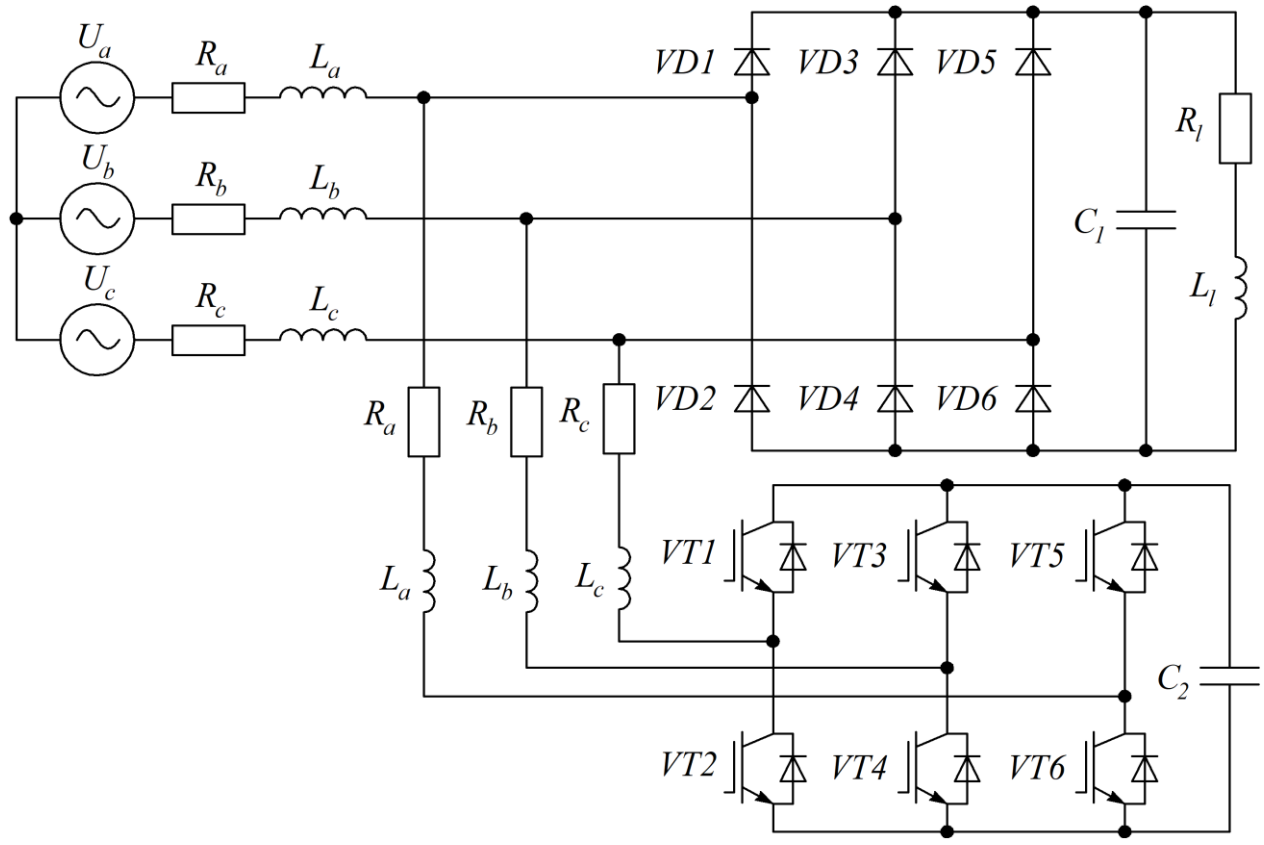

Figure 1.10 – Diagram of parallel connection of APF to network

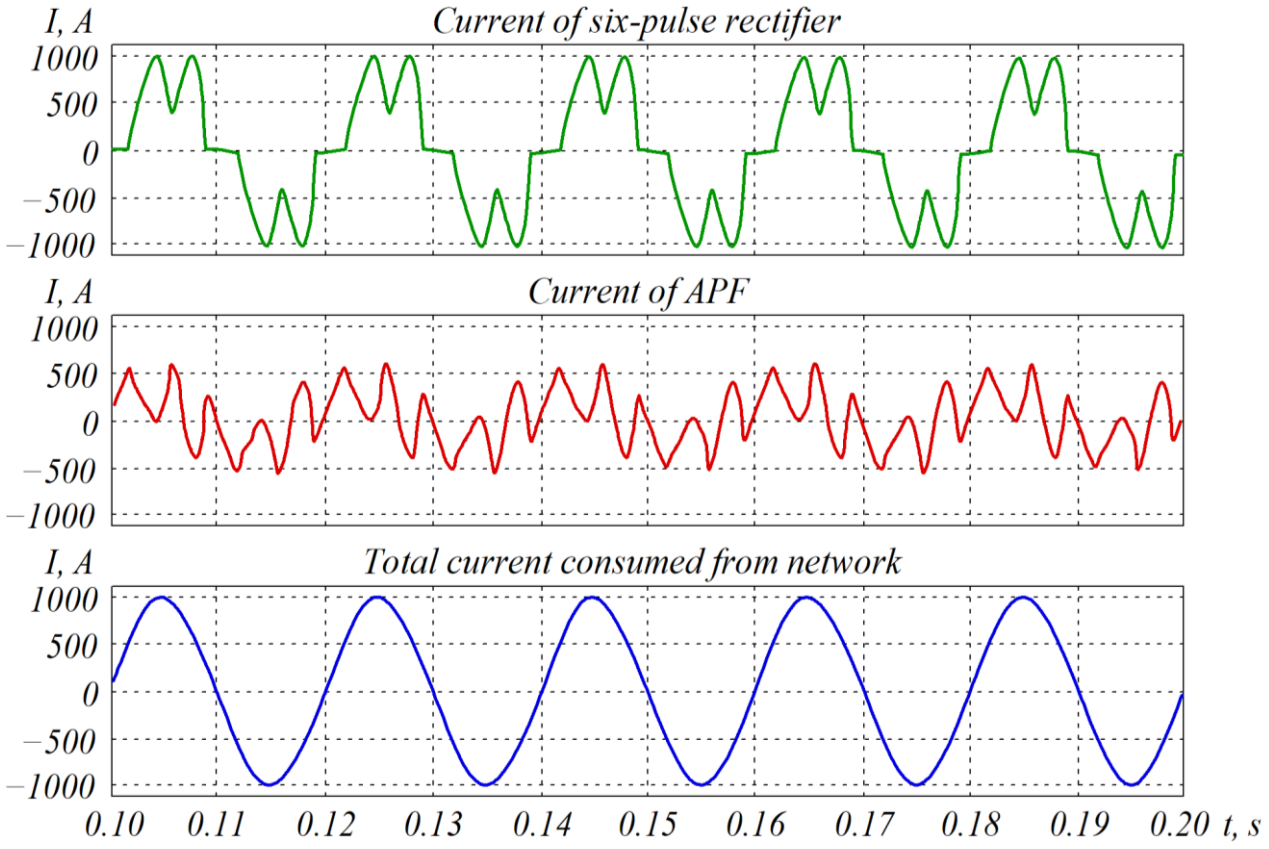

Figure 1.11 – Formation of sinusoidal network current

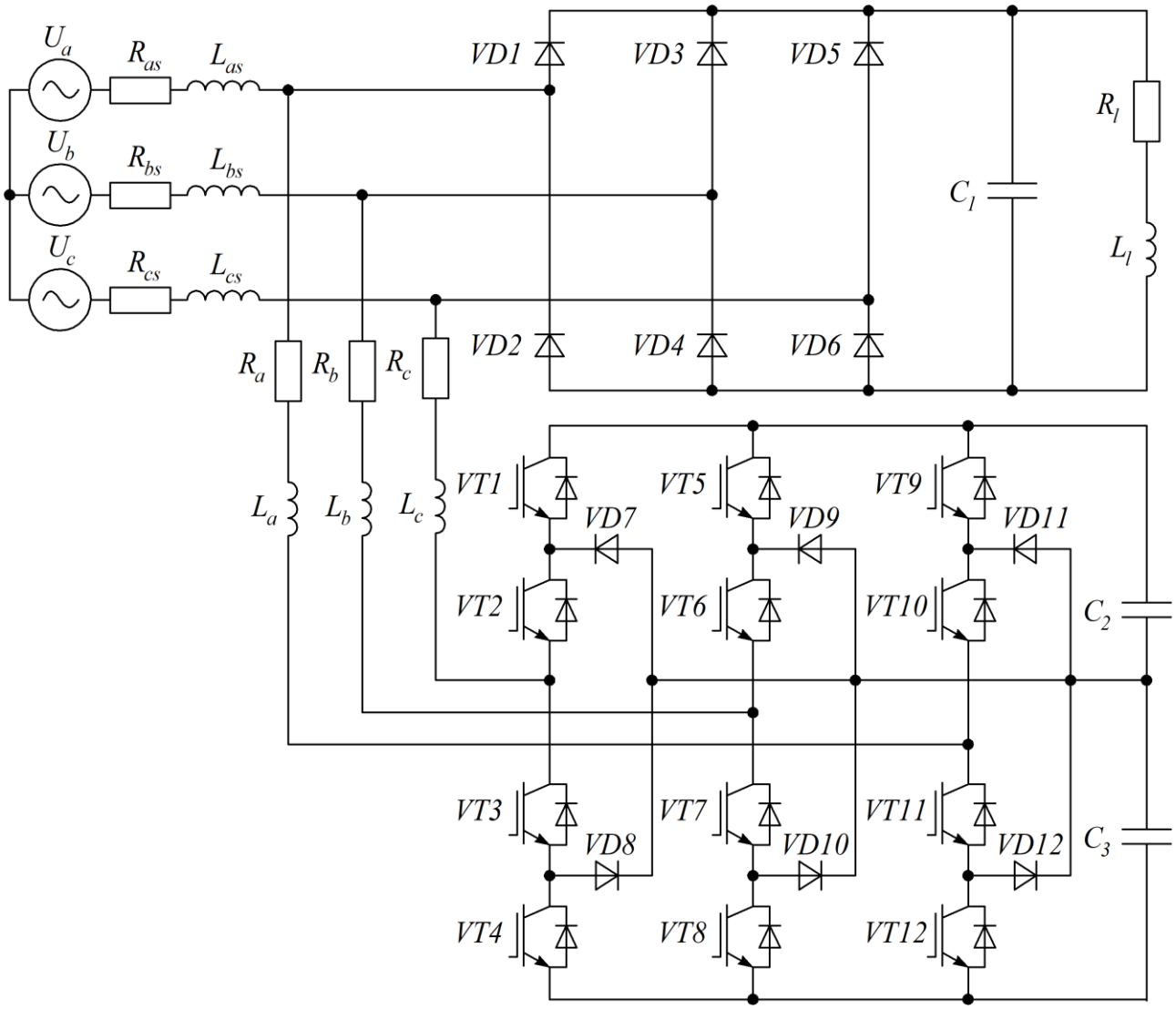

Figure 1.12 – Diagram of three-level APF

The serial-type APF operates in the voltage source mode and eliminates distortions of the supply network voltages by forming higher voltage harmonics in the opposition to the higher voltage harmonics of the network due to which the higher harmonics are compensated. The application of the serial-type APF connected to the input circuits of the PS is shown in fig. 1.13.

The use of a serial-type APF provides compensation for the higher voltage harmonics of the mains, however, it does not provide compensation for the higher harmonics of the consumed current of the PS, and the power factor obtained remains quite low. It is better to apply the serial-type APF in the output circle of a six-pulse rectifier to compensate for higher harmonics of the output voltage. It is possible to build in the output circle the hybrid filter consisting of the APF and the passive filter.

The main advantage of APFs is that they, unlike passive filters, are simultaneously able to provide a low content of higher current and voltage harmonics,

which makes it possible to obtain a high power factor. In addition, in contrast to passive filters tuned to certain frequencies, the APF is able to compensate for dynamically variable higher harmonics in a wide range of frequencies and amplitudes.

Comparative characteristics of passive and active power filters are given in table 1.1.

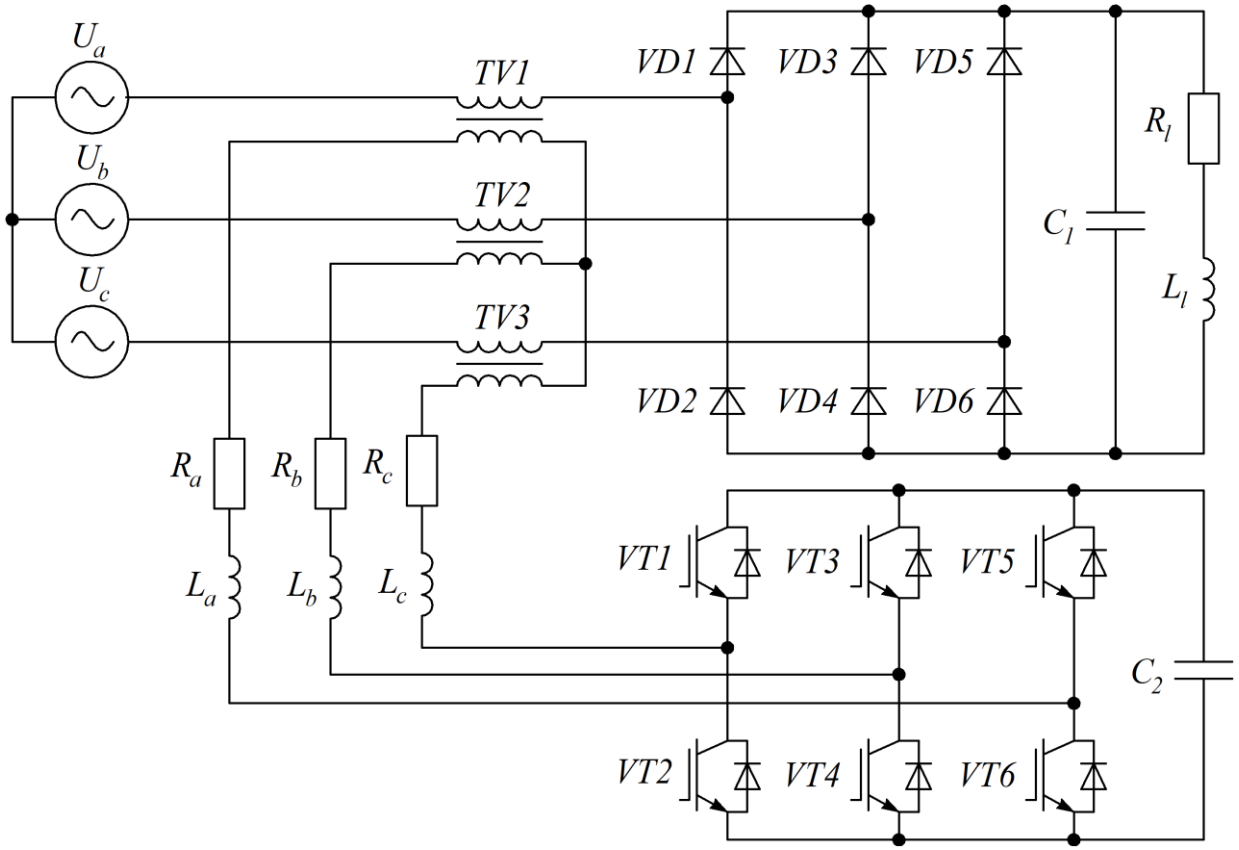

Figure 1.13 – Diagram of series connection of APF to network

Table 1.1 – Comparative characteristics of active and passive filters

Description	Active filter	Passive filter
Compensation for reactive power	Compensates	Compensates
Resonant phenomena in network caused by filter	None	Possible
Suppression of non-canonical harmonic current components	Suppresses	Non-suppressive
Suppression of low-frequency current components	Suppresses	Non-suppressive
Dimensions	Relatively small	Relatively large
Cost	More expensive	Less expensive

The comparative analysis demonstrates significant advantages of power active filters over passive ones. However, the use of APFs is not devoid of disadvantages, namely, it causes additional losses in the power supply system, which reduces the overall efficiency factor. Losses in the system increase in proportion to the switching frequency of the AVI power switches.

The increased switching frequency of the AVI power switches is the reason for the occurrence of high-frequency pulse interference, as a result of an increase in the first derivatives of switched currents. This complicates the EMC between the rectifier system elements as well as between the rectifier system and the network.

In terms of technical feasibility, both for consumers and for producers of electric energy, it is necessary to be very careful when using static capacitor batteries for PFC.

Firstly, the reactive power can be compensated to the level at which the value of the static voltage stability factor in normal mode and post-emergency conditions will not be less than the minimum standardized value.

Secondly, the reactive power of the load can be compensated to the level at which the value of the static stability factor for active power in normal and post-accident modes will not be less than the minimum standardized value, and the power factor of the generators should be close to the nominal value.

Thirdly, in networks with the capacitive series compensation of the reactance of the stator circles the PFC of the load by means of static capacitor batteries should not lead to self-excitation.

1.4. Analysis of exact and approximating dependences of the active resistance of the conductor on the current frequency based on the skin effect

The operation of semiconductor power converters, which are part of TSs, frequency-controlled electric drives and other powerful non-linear loads, causes a significant emission of higher current harmonics to electric networks [12]. According to [13] analytical expressions describing the dependence of the active and impedance of the electrical network on the current frequency are determined.

Higher current harmonics in electric networks cause a complex negative effect on the energy efficiency of the network. Such negative phenomena include:

– the possibility of resonances in the electric network at current harmonics frequencies, which can lead to emergency modes;

– accelerated aging of insulation of electrical wires and cables;

– increased power losses in the resistance of electric networks; and

– EMC problems of power lines with automation systems and data transmission systems.

The increased power losses in the active resistance under the action of higher harmonics occur due to an increase in the root mean square (RMS) of the current and the skin effect.

Additional losses of active power in the three-phase ETL P_{harm}, caused by the higher current harmonics flows are determined by the skin effect and can be calculated as the sum of losses from each harmonic:

$$P_{harm} = m \cdot \sum_{v=2}^{v=n} I_v^2 \cdot R_{dc} \cdot k_{rv}, \tag{1.9}$$

where m – the number of phases; v – the number of harmonics studied; n – the number of harmonics included; I_v – the RMS of the v-th harmonic; R_{dc} – the active resistance of the DC line; k_{rv} – the coefficient including the increase in resistance under the surface effect.

Studies [14, 15] provide equations for determining additional power losses in the active resistance of electrical conductors from higher current harmonics caused by the skin effect.

The coefficient k_{rv} determines the value of the electrical network resistance for the specific frequency of higher harmonics. The value of the coefficient k_{rv} in the function on the current frequency is described by the equation:

$$k_{rv} = 0.47 \cdot \sqrt{v}, \tag{1.10}$$

where $v = f / 50$.

Studies [16, 17] provide equations describing the dependence of the specific resistance of the conductor on the current frequency including the skin effect and the proximity effect.

$$r_{0v} = r_0 \cdot \left(k_{pv} + k_{0v} \right), \tag{1.11}$$

where r_0 – the specific resistance of the DC conductor; k_{pv} – the coefficient including the skin effect on the v-th harmonic; k_{ov} – the coefficient including the proximity effect on the v-th harmonic.

The coefficient k_{pv}, which determines the growth of the active resistance of the conductor at higher frequencies from the surface effect, for copper wires is:

$$k_{pv} = 0.021 \cdot \sqrt{f}, \tag{1.12}$$

where f – the current frequency.

The coefficient k_{pv} for aluminium wires k_{pv} is:

$$k_{pv} = 0.01635 \cdot \sqrt{f}. \tag{1.13}$$

The coefficient k_{0v} including the proximity effect is determined by the expression:

$$k_{0v} = \frac{1.18 + k_{pv}}{k_{pv} \cdot 0.27} \cdot \left(\frac{d}{a}\right)^2, \tag{1.14}$$

where d – the conductor diameter, mm; a – the distance between the core centres, mm.

In a number of publications [18, 19], the coefficient k, which includes the increase in active resistance under the skin effect, has a greater value and is defined as:

$$k_r = \sqrt{v}. \tag{1.15}$$

Publications [20, 21] on the basis of experimental studies provide empirical dependences of active resistance on frequency for different types of wires, as shown in table 1.2.

Table 1.2 – Approximated dependencies of the coefficient k_{rv2}, which includes the skin effect for different cable types

Conductor type	Value k_{rv2}
Cable type AC-400	$0.3 \cdot v$
Cable type A-400	$0.15 \cdot v$
Copper conductor	$0.06 \cdot v$
Aluminium conductor	$0.06 \cdot v$

The dependences of the values of the coefficients k_{rv}, k_{rv2} and k_{pv}, which include the surface effect on the increase in active resistance, and, accordingly, on the power losses in copper conductors from the current frequency of higher harmonics are shown in fig. 1.14. It should be noted that the values of the coefficients k_{rv}, k_{rv2} and k_{pv} correspond to the resistance of DC conductors.

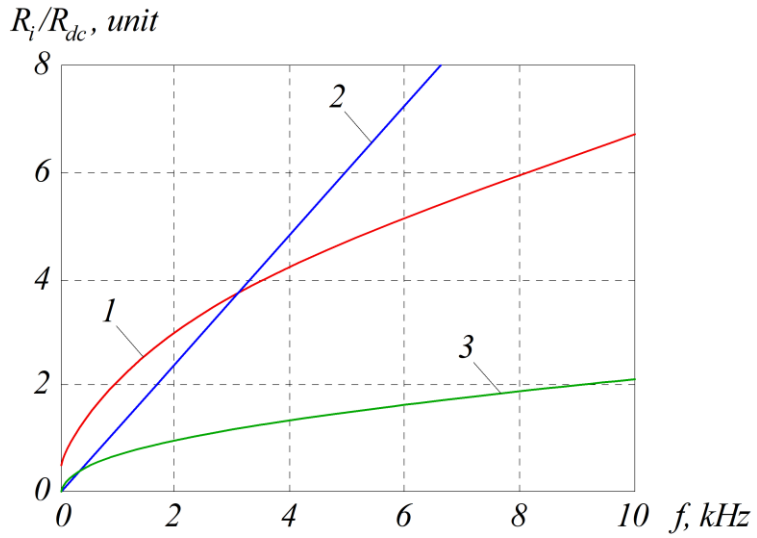

Figure 1.14 – Dependence of conductor resistance on frequency:
1 – k_{rv}; *2* – k_{rv2}; *3* – k_{pv}

Thus, it can be concluded from the analysis that the existing dependences of the active resistance of conductors of electrical networks on the frequency of higher harmonics are quite controversial and give different results while calculating the power losses. It should be noted that the given ratios do not include the geometric properties of the wires, which affect the intensity of current displacement in the conductor during the skin effect. In addition, according to expressions (1.10) and (1.12) and table 1.2, up to a certain frequency, the coefficients k_{rv}, k_{rv2} and k_{pv} become less than one, which indicates a decrease in the network resistance relative to the DC resistance, that is, a certain "superconductivity" of conductors at a frequency of 50 Hz, which is erroneous.

Thus, in the process of the analysis of studies [22, 23], it has been found that the existing empirical dependences of the active resistance of conductors on the current frequency are contradictory, inaccurate and have restrictions in use.

The exact analytical dependence of the active resistance of the conductor on the frequency as a result of the skin effect can be obtained by expressing the first Maxwell equation in a cylindrical coordinate system.

Let us consider the alternating harmonic current I passing along a rectilinear cylindrical wire and determine the electromagnetic field inside the wire. Let us align the axis z of the cylindrical coordinate system with the axis of the wire (fig. 1.15). If the conductor is not affected by the fields of other conductors, the current density is distributed symmetrically about the conductor axis and there is no proximity effect:

$$\left(rot\bar{H} = \bar{J} + \frac{d\bar{D}}{dt} \right), \tag{1.16}$$

where H – the magnetic strength vector; J – the electric current density; D – the electric displacement vector; $d\bar{D}/dt$ – the displacement current density.

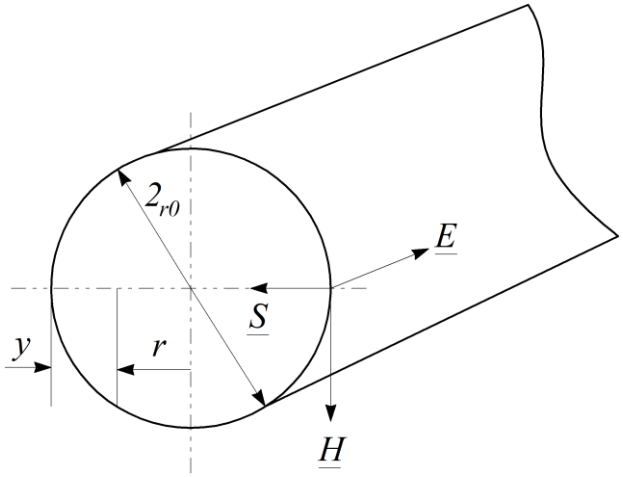

Figure 1.15 – Positive directions of field vectors

Let us consider the alternating fields in conductive environments in the frequency range for which the displacement current density in the right-hand side of Maxwell's first equation can be neglected $d\bar{D}/dt$ compared to the conductive current, that is, assume that $\bar{J} >> d\bar{D}/dt$. A system of main equations describing electromagnetic processes in this case can be described as:

$$\begin{cases} rot\bar{H} = \bar{J}; \\ rot\bar{E} = -\mu \cdot \mu_0 \cdot \dfrac{d\bar{H}}{dt}; \\ div\bar{E} = 0; \\ div\bar{H} = 0. \end{cases} \tag{1.17}$$

One of the field vectors $\bar{E}$ or $\bar{H}$ can be excluded from this system. In order to exclude the vector $\bar{E}$, it is sufficient to calculate *rot* of the right and left parts of the first equation:

$$rot\left(rot\left(\bar{H}\right)\right) = rot\left(\bar{J}\right) = rot\left(\sigma\bar{E}\right) = \sigma \cdot rot\left(\bar{E}\right), \tag{1.18}$$

substitute the right part of the resulting expression from the second equation with the value $rot\left(\bar{E}\right)$, and convert the left part according to the known rule:

$$\left(rot\left(rot\bar{H}\right) = grad\left(div\bar{H}\right) - \nabla^2\bar{H}\right), \tag{1.19}$$

keeping in mind that $div\bar{H} = 0.$ After these transformations we will get:

$$\nabla^2\bar{H} - \sigma \cdot \mu \cdot \mu_0 \frac{\partial\bar{H}}{\partial t} = 0. \tag{1.20}$$

Excluding the vector $\bar{H},$ we get an absolutely similar equation for the vector $\bar{E}$:

$$\nabla^2\bar{E} - \sigma \cdot \mu \cdot \mu_0 \frac{d\bar{E}}{dt} = 0, \tag{1.21}$$

where ∇ – the Nabla operator; σ – the conductivity of the current-carrying part.

The Nabla operator ∇ is defined as a vector differential operator the components of which are partial derivatives of coordinates. For a three-dimensional Euclidean space in a rectangular Cartesian coordinate system, the Nabla operator is determined by the following expression:

$$\nabla = \frac{d}{dx}\vec{i} + \frac{d}{dy}\vec{y} + \frac{d}{dz}\vec{k}, \tag{1.22}$$

where $\vec{i}, \vec{y}, \vec{k}$ – the single spatial vectors along the axes *x*, *y* and *z*, respectively.

In view of this, expression (1.21) in the cylindrical coordinate system will take the following form:

$$\frac{1}{r} \cdot \frac{d}{dr} \cdot \left(r \frac{d\underline{E}}{dr} \right) - j\omega \cdot \mu \cdot \mu_0 \cdot \sigma \cdot \underline{E} = 0. \tag{1.23}$$

By differentiating and replacing variables, we obtain:

$$\eta = r\sqrt{j\omega \cdot \mu \cdot \mu_0 \cdot \sigma} = r\sqrt{-\gamma^2} = jr \cdot \gamma, \tag{1.24}$$

we get the equation:

$$\frac{d^2\underline{E}}{d\eta^2} + \frac{1}{\eta} \cdot \frac{d\underline{E}}{d\eta} + \underline{E} = 0. \tag{1.25}$$

Equation (1.21) is a separate case of the Bessel equation at $n = 0$.

$$\frac{d^2y}{dx^2} + \frac{1}{x} \cdot \frac{dy}{dx} + \left(1 + \frac{n^2}{x^2}\right) \cdot y = 0. \tag{1.26}$$

Let us consider the passage of the alternating harmonic current I along a rectilinear cylindrical wire and determine the electromagnetic field inside the wire. The axis z of the cylindrical coordinate system lies in the wire axis.

The solution for $\bar{H}$ can be found from Maxwell's second equation:

$$\underline{\bar{H}} = -\frac{1}{j\omega \cdot \mu \cdot \mu_0} \cdot rot\,\underline{\bar{E}} = \left[\frac{1}{j\omega \cdot \mu \cdot \mu_0} \cdot \frac{dE_z}{dr}\right] \cdot \bar{e}_\alpha. \tag{1.27}$$

The electric field vector $\vec{E}$ is calculated by the expression:

$$\vec{E} = \frac{J}{\sigma} = \frac{k \cdot \dot{I}}{2 \cdot \pi \cdot a \cdot \sigma} \cdot \frac{J_0 \cdot (k \cdot r)}{J_1 \cdot (k \cdot a)}, \tag{1.28}$$

where $J_0(Z)$ – the Bessel function of the first kind of zero order; $J_1(Z)$ – the Bessel function of the first kind of first order; r – the radius of the current surface; a – the maximum radius of the wire; σ – the specific conductivity, cm/m.

The first-order Bessel functions denoted by $J_\alpha(z)$ are partial solutions of the Bessel differential equation for the endpoints $x = 0$ with the integer or integral α (α determines the function order). The general view of the Bessel function of the first kind of the α-th order is as follows:

$$J_\alpha(z) = \frac{z}{2} \cdot \sum_{n=0}^{n=\infty} \frac{(-1)^n}{n!(n+1+\alpha)!} \cdot \left(\frac{z}{2}\right)^{2n+\alpha}. \tag{1.29}$$

The Bessel functions of the first kind of zero-order are determined as:

$$J_0(z) = \frac{z}{2} \cdot \sum_{n=0}^{n=\infty} \frac{(-1)^n}{n!(n+1)!} \cdot \left(\frac{z}{2}\right)^{2n}. \tag{1.30}$$

The Bessel functions of the first kind of zero-order are determined as:

$$J_1(z) = \frac{z}{2} \cdot \sum_{n=0}^{n=\infty} \frac{(-1)^n}{n!(n+2)!} \cdot \left(\frac{z}{2}\right)^{2n+1}. \quad (1.31)$$

The solution of these Bessel functions in a complex plane is simplified by the possibility of their solving in MathCad using the built-in functions "$J_0(z)$" and "$J_1(z)$".

The distribution of the complex current density will be equal to:

$$J = \frac{k \cdot \dot{I}}{2 \cdot \pi \cdot a} \cdot \frac{J_0 \cdot (k \cdot r)}{J_1 \cdot (k \cdot a)}. \quad (1.32)$$

The dependence of the active resistance on the higher harmonic frequency is determined by solving the Bessel functions.

The magnetic field strength is determined by the following expression:

$$H = \frac{\dot{I}}{2 \cdot \pi \cdot a} \cdot \frac{J_0 \cdot (k \cdot r)}{J_1 \cdot (k \cdot a)}. \quad (1.33)$$

The power dissipated by the cylindrical conductor P can be determined by Joule-Lenz's law in vector form:

$$P = \vec{J} \cdot \vec{E} = \gamma \cdot E^2; \quad (1.34)$$

$$dP = I^2 \cdot R dt, \quad (1.35)$$

where $\vec{J}$ – the electric current density vector; $\vec{E}$ – the electric field strength; γ – the medium conductivity; R – the conductor resistance; I – the current passing through the conductor.

At the same time, the scattering power can be found using Pointing's theorem, which describes the law of conservation of energy for electromagnetic fields.

$$\frac{du}{dt} + \nabla \cdot S = -J \cdot E, \quad (1.36)$$

where u – the energy density; ∇ – the Nabla operator; S – the Pointing vector; J – the current density; E – the electric field strength.

The Pointing vector S is the vector of density of the electromagnetic field, the components of which are part of the pulse energy of the electromagnetic field, which can be determined through the vector product of two vectors:

$$S = \left[E \times H\right], \tag{1.37}$$

where E and H – the strength vectors of electric and magnetic fields, respectively.

Pointing's theorem in integral form is as follows:

$$\frac{d}{dt} = \int_V u \cdot dV + \oint_{dV} S \cdot dA = -\int_V J \cdot E \cdot dV, \tag{1.38}$$

where dV – the surface limiting the volume V; J – the complex current density; E – the electric field strength; S – the Pointing vector.

According to Pointing's theorem, the dissipating power can be expressed as:

$$P = \oint_S [\vec{E} \cdot \vec{H}]\, dS. \tag{1.39}$$

This boils down to the expression:

$$Z = \frac{\oint_S [\vec{E} \cdot \vec{H}]\, dS}{I^2}. \tag{1.40}$$

By equating expressions (1.39) and (1.40), we get:

$$I^2 \cdot Z = \oint_S [\vec{E} \cdot \vec{H}]\, dS. \tag{1.41}$$

As a result, the complex resistance is expressed as follows:

$$Z = \frac{\oint_S [\vec{E} \cdot \vec{H}]\, dS}{I^2}, \tag{1.42}$$

where J – the complex current density; H – the magnetic field strength, A/m; E – the electric field strength; I – the complex current.

Given that the lateral surface area of the cylindrical conductor is equal to S, and the surface radius is equal to the wire radius $r = a$, we obtain an expression that determines the resistance of the conductor:

$$Z = \frac{\oint\limits_S \left[\vec{E} \cdot \vec{H}\right] dS}{I^2} = \frac{\dfrac{k \cdot \dot{I}}{2 \cdot \pi \cdot a \cdot \sigma} \cdot \dfrac{J_0 \cdot (k \cdot r)}{J_1 \cdot (k \cdot a)} \cdot \dfrac{\dot{I}}{2 \cdot \pi \cdot a} \cdot \dfrac{J_1 \cdot (k \cdot r)}{J_1 \cdot (k \cdot a)} \cdot 2\pi a}{I^2} \cdot l =$$

$$= \frac{q}{2 \cdot \pi \cdot r_0 \cdot \gamma} \cdot \frac{J_0 \cdot (q \cdot r_0)}{J_1 \cdot (q \cdot r_0)}; \qquad (1.43)$$

$$\bar{Z} = R + i \cdot X = \frac{q}{2 \cdot \pi \cdot r_0 \cdot \gamma} \cdot \frac{J_0 (q \cdot r)}{J_1 \cdot (q \cdot r)} \cdot l, \qquad (1.44)$$

where X – the reactance of the conductor; R – the active resistance of the conductor; i – the complex component; q – the wave number of the wire; r – the radius of the wire; l – the length of the wire; $J_0(Z)$ – the Bessel function of the first kind of 0-order; $J_1(Z)$ – the Bessel function of the first kind and the first order.

The active wire resistance R is a valid part of the complex resistance Z.

The wave number of the wire q is a complex variable determined according to the thickness of the skin layer Δ:

$$\Delta = \sqrt{\frac{2}{\gamma \cdot \mu \cdot 2 \cdot \pi \cdot f}}, \qquad (1.45)$$

where f – the AC frequency, Hz; γ – the specific electric conductivity, $\gamma = 1/\rho$; ρ – the specific resistance of the conductor ($\text{Ohm}^{-1} \cdot \text{m}^{-1}$), for copper it is $1.72 \cdot 10^{-8}$; for aluminium – $2.7 \cdot 10^{-8}$; μ – the absolute magnetic permeability.

$$\mu = \mu_0 \cdot \mu_r, \qquad (1.46)$$

where μ_0 – the magnetic permeability of vacuum, $\mu_0 = 1.25663706 \cdot 10^{-6}$ N/A; μ_r – the relative magnetic permeability of the material (μ/μ_0 is a dimensionless value), for copper it is 0.999992; for aluminium it is 1.000022.

The obtained dependences of the relative active resistance of a 10-km-long copper wire with different diameters on the frequency, calculated in accordance with Bessel equation (1.19), are shown in fig. 1.16.

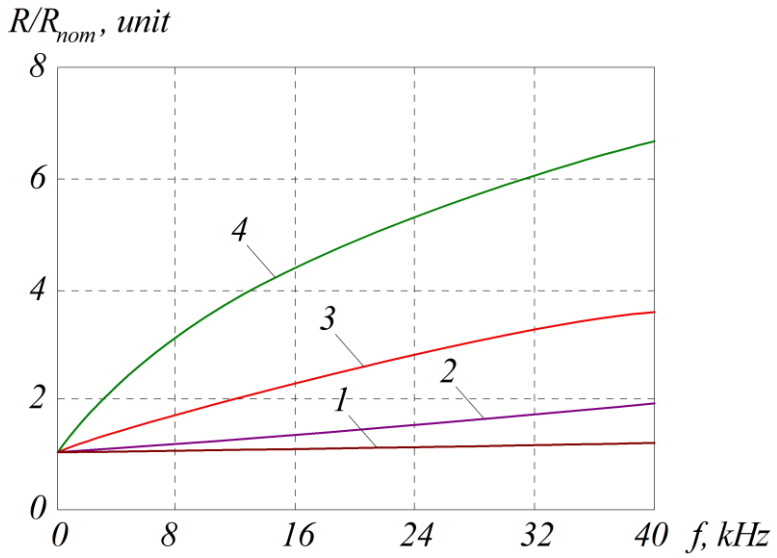

Figure 1.16 – Dependence of active resistance of wire on frequency at diameter: *1* – 0.5 mm; *2* – 1 mm; *3* – 2 mm; *4* – 4 mm

It can be concluded from fig. 1.16 that the value of the wire diameter significantly affects the skin-effect.

To confirm the obtained analytical expressions in Ansys Electronics–Maxwell 3D using computer modelling, a study into the distribution of current density in a copper conductor with a diameter of 8 mm under a current of 50 Hz (fig. 1.17, *a*), 10 kHz (fig. 1.17, *b*) and 32 kHz (fig. 1.17, *c*) was performed.

As can be seen from the results of the skin effect simulation, the increase in the current frequency significantly affects the distribution of the current density and, as a result, the value of the equivalent resistance of the conductor.

Simplified calculation of additional power losses due to the skin effect can be performed by means of simplified empirical dependencies given in the International Standard IEC 60287-1-1-2009 “Electric Cables. Calculation of the Rated Current Load”.

This Standard presents empirical dependences that determine the growth of the active resistance of cables on the current frequency. According to Article 2.1 of this Standard, the resistance of the AC core *R*, Ohm/m, per unit length in all cases, except for cables laid in pipelines, is determined by the expression:

$$R = R' \cdot \left(1 + y_s + y_p\right), \tag{1.47}$$

where R' – the DC core resistance at the maximum operating temperature, Ohm/m; y_s – the surface effect coefficient; y_p – the proximity effect coefficient.

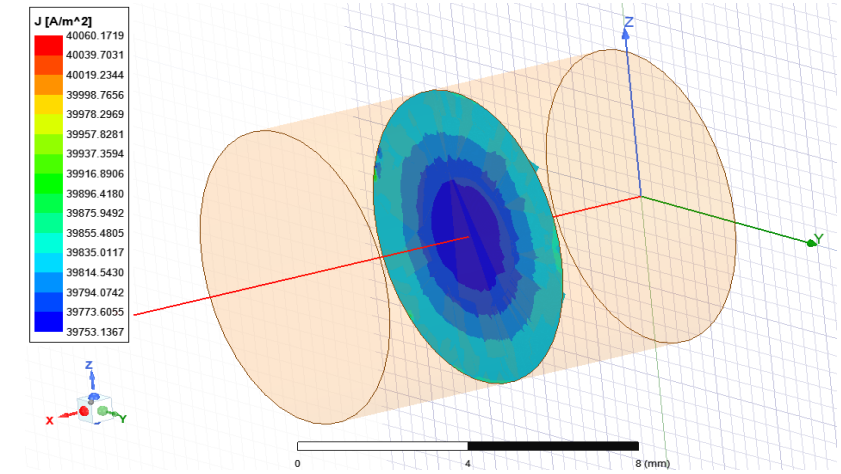

a

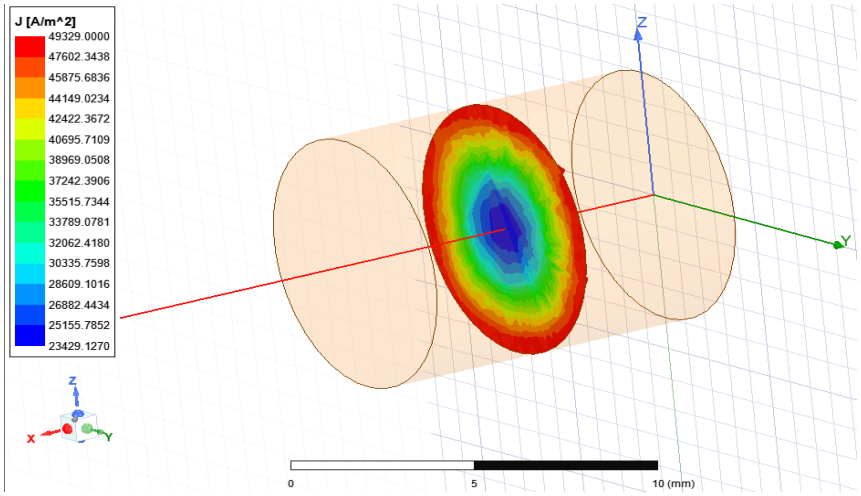

b

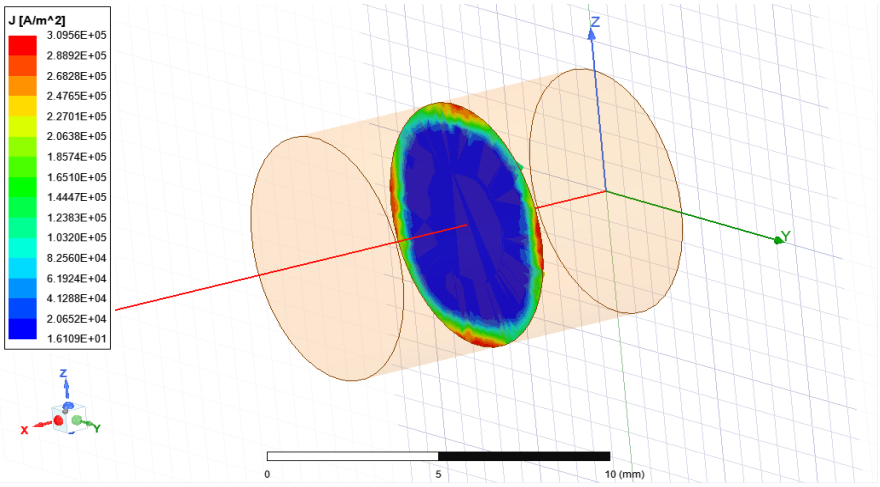

c

Figure 1.17 – Distribution of current density at frequency:
a – 50 Hz, *b* – 10 kHz; *c* – 32 kHz

This stage of the research included only an analysis of the skin effect. The proximity effect will be investigated in a further publication, therefore, the proximity coefficient was not included in the calculation.

The resistance of the DC core per unit length with consideration of the conductor diameter is determined by:

$$R' = \frac{\rho}{\pi \cdot r^2}, \tag{1.48}$$

where ρ – the specific resistance of the conductor; r – the radius of the conductor.

The surface effect coefficient is determined according to the expression:

$$y_s = \frac{x_s^4}{192 + 0.8 \cdot x_x^4}, \tag{1.49}$$

where x_s – the Bessel argument defined as:

$$x_s = \sqrt{\frac{8 \cdot \pi \cdot f}{R' \cdot 10^7}} \cdot k_s. \tag{1.50}$$

The coefficient k_s for single-core, multi-core and segment wires becomes 1 (according to table 2 of IEC 60287-1-1-2009).

At the same time, Article 2.1.2 of IEC 60287-1-1-2009 states that expression (1.19) is accurate if the Bessel argument x_s does not exceed a value of 2.8.

Given that the Bessel argument x_s depends on the frequency and radius of the wire, and for the correct calculation it should not exceed 2.8, then it is possible to determine the critical frequency value F_{crit}. This dependency is defined by the expression:

$$F_{crit} = \frac{\rho \cdot 10^7 \cdot 2.8^2}{8 \cdot \pi^2 \cdot r^2}. \tag{1.51}$$

Graphically, the dependence of the critical frequency F_{crit} on the conductor radius is shown in fig. 1.18. Given that the spectrum of higher current harmonics in electric networks is regulated to a frequency of 2 kHz, as well as semiconductor converters generate an even larger spectrum of higher harmonics of input currents, the use of expressions (1.17)...(1.19) is quite limited.

Let us analyse the convergence of the calculations of the network resistance in accordance with Bessel expression (1.21) and expressions (1.17)…(1.19) given in IEC 60287-1-1.

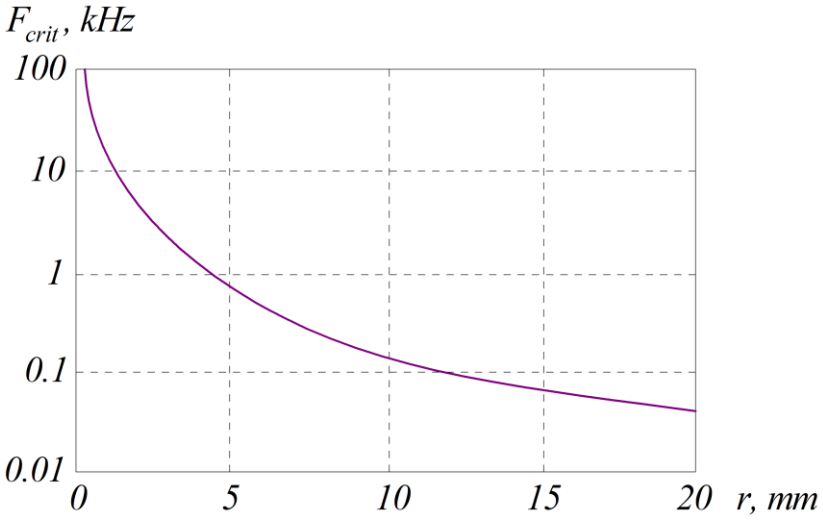

Figure 1.18 – Dependencies of critical frequency on wire radius

On the same coordinate planes, let us build the dependences of the relative active resistance of conductors with a core radius of 10, 4 and 2 mm, solved in accordance with the Bessel equations and ones presented in IEC 60287-1-1. The obtained dependencies are shown in fig. 1.19.

Fig. 1.19 shows: *1* – the characteristic according to Bessel equations; *2* – the approximating dependence according to IEC. From the dependencies obtained, it can be seen that the convergence of the approximating dependence in the Standard IEC 60287-1-1-2009 with the results obtained by means of Bessel functions actually indicates that it is possible to apply the approximating function to the frequency at the value $x_s = 3.529$, at which the discrepancy between the actual and approximating functions is 0.798 %.

From the dependencies in fig. 1.19, it can be seen that the dependence given in the Standard is true for a rather limited frequency range. In addition, at the same frequency, the higher the cross-section of the conductor, the more intense is the discrepancy between the actual and empirical dependencies.

Having analysed the function of expression (1.51) based on the Bessel functions, at a frequency range above the critical frequency F_{crit}, at which $x_s > 2.8$, it is concluded that it behaves as a classical parabolic function $k\sqrt{f}$, and its amplitude depends on the frequency.

It is proposed for the high frequency range above F_{crit}, at which $x_s > 2.8$, the use of the following approximating function to determine the impact of the surface effect:

$$y_{s2} = \pi \cdot r \cdot \sqrt{\frac{f}{\rho \cdot 10^7}} - 0.735. \qquad (1.52)$$

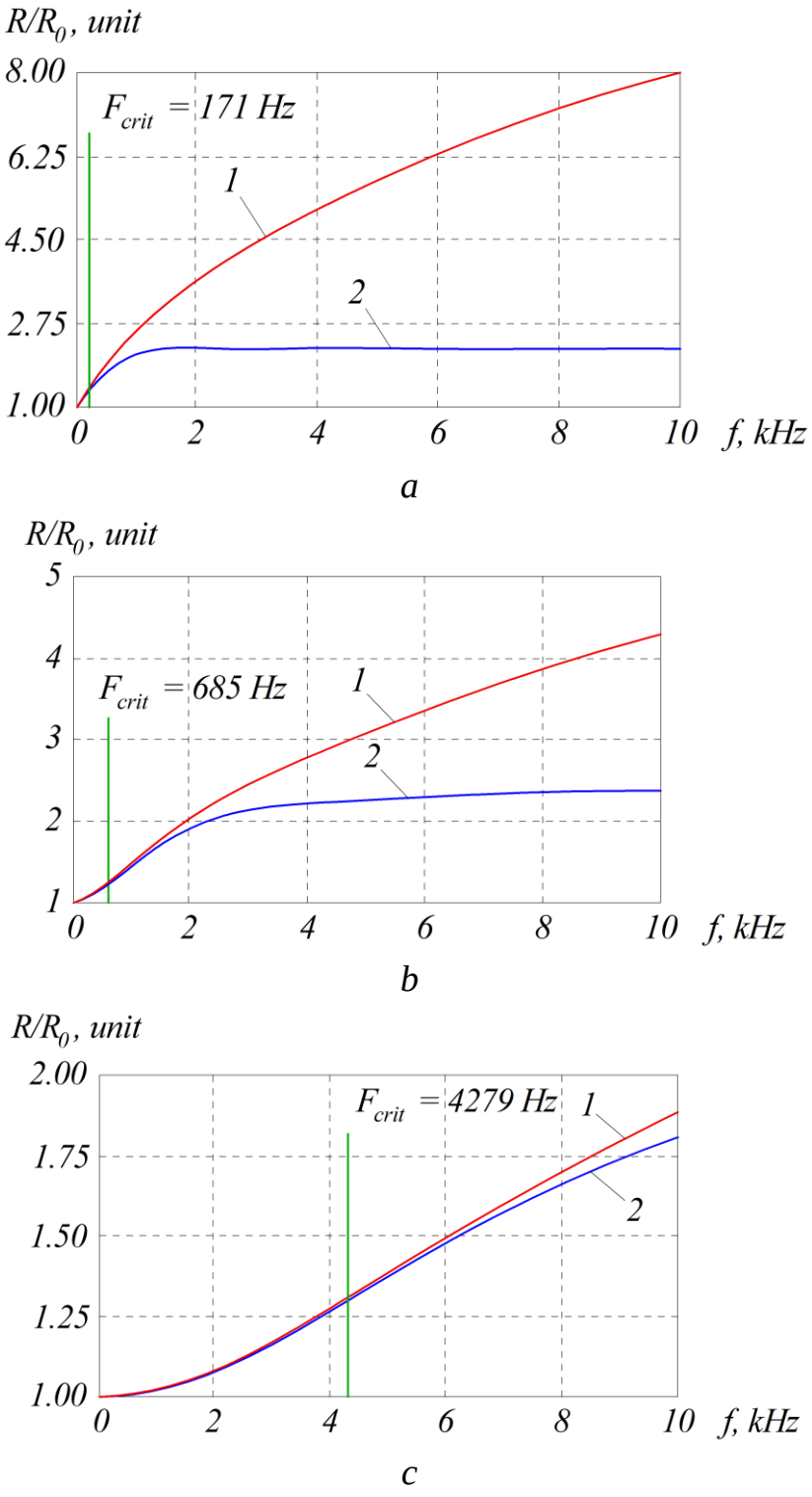

Figure 1.19 – Dependence of active resistance of wire on frequency at diameter: *a* – 10 mm; *b* – 5 mm; *c* – 2 mm

The convergence of proposed approximated expression (1.52) and the dependence of Bessel functions (1.51) for wires with a core radius of 5 and 2 mm is shown in fig. 1.20 (*1* – according to Bessel expression, *2* – according to approximated expressions).

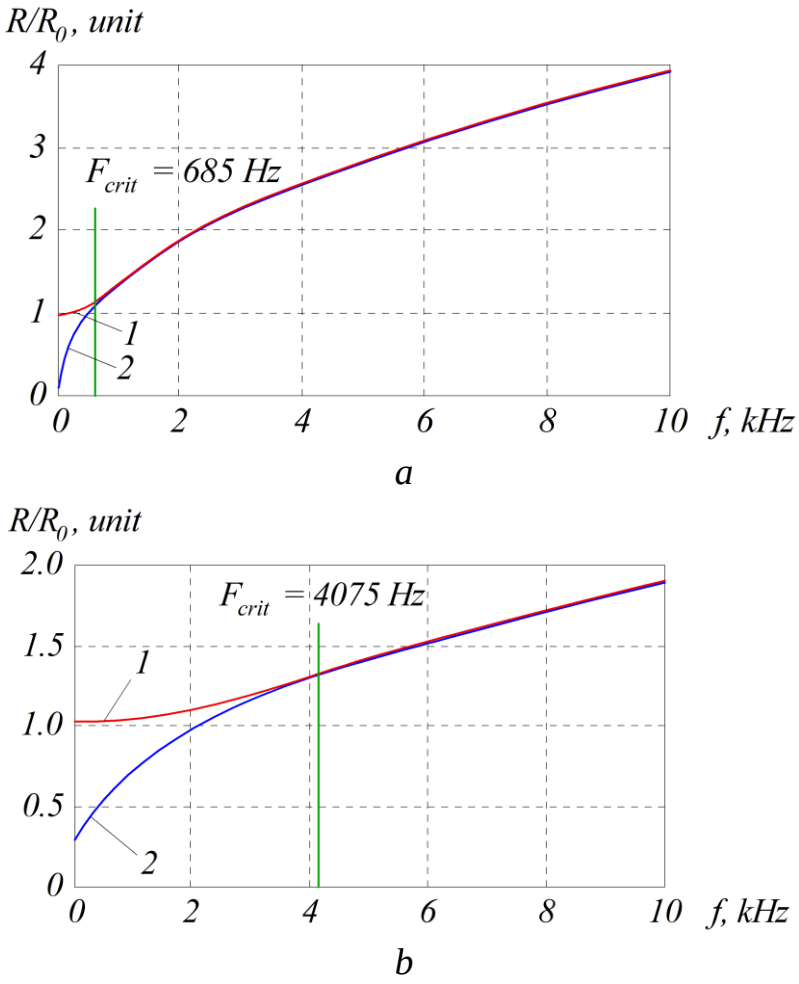

Figure 1.20 – Dependence of active resistance of wire on frequency at diameter: *a* – 5 mm; *b* – 2 mm

Fig. 1.20 shows: *1* – the characteristic according to the Bessel expression; *2* – the characteristic according to approximated expressions. It can be seen from the dependencies obtained that proposed approximated expression (1.52) for the frequency range above F_{crit} makes it possible to obtain a close convergence of the active resistance of the conductor including the skin effect, without solving quite complex equations of the dependence between resistance and frequency according to the Bessel equations.

The research also included an analysis of the error in calculating the resistance by means of Bessel equations applying the approximation method in accordance with IEC in the low and high frequency zone, and the analysis of its convergence. The convergence of the resistance of a single copper wire with a cross-section of 8 mm according to Bessel expression (1.51) by the IEC method (1.16)...(1.19) and the proposed approximated expression (1.52) were analysed. Under this condition, the solution, in accordance with Bessel expression, is taken as the reference. The results of the calculation are given in table 1.3.

Table 1.3 – Analysis of the convergence of the resistance by Bessel expressions using the IEC method and approximated expression

Frequency, Hz	Bessel function x_s (1.18)	Relative increase in resistance R/R_0 according to IEC (1.16)	Relative increase in resistance R/R_0 according to proposed approximated expression (1.52)	Relative increase in resistance R/R_0 according to Bessel equation (1.51)	Relative calculation error in accordance with IEC, %	Relative error of proposed approximation, %
100	0.855998236	1.002790100	0.567641079	1.00279024	1.39496E-05	43.3938369
200	1.210564315	1.011086165	0.692999118	1.01108682	6.47979E-05	31.4599791
300	1.482632436	1.024670371	0.789189725	1.02467263	0.000220453	22.9812818
400	1.711996472	1.043195369	0.870282158	1.04320306	0.000737249	16.5759581
500	1.914070245	1.066205860	0.941726025	1.06622942	0.002209646	11.6769799
600	2.096758899	1.093165272	1.006316218	1.09322751	0.005693057	7.94997300
700	2.264758456	1.123484767	1.065713031	1.12362808	0.012754494	5.15428994
800	2.421128630	1.156551914	1.120998236	1.15684631	0.025448189	3.09877582
900	2.567994709	1.191756789	1.172923236	1.19230762	0.046198772	1.62578712
1000	2.706904100	1.228513933	1.222035122	1.22946870	0.077656887	0.60461707
F_{crit} = 1070.96	2.799994961	1.254860122	1.254947712	1.25621029	0.107479442	0,10050690
1200	2.965264873	1.304562036	1.313379450	1.30695874	0.183380235	–0.49127104
1400	3.202852124	1.381018974	1.397379228	1.38603808	0.362118931	–0.81824216
1600	3.423992945	1.455183877	1.475564315	1.46438361	0.628232421	–0.76350930
1800	3.631692945	1.525283246	1.548997354	1.54052732	0.989536098	–0.54981397
2000	3.828140490	1.590309992	1.618452050	1.61366966	1.447611503	–0.29636734
2200	4.014987618	1.649830090	1.684512485	1.68348334	1.999024835	–0.06113190
2400	4.193517799	1.703803650	1.747632436	1.74994611	2.636793206	0.13221399
3000	4.688495432	1.835181499	1.922633457	1.93119721	4.971823219	0.44344272
3200	4.842257260	1.870148904	1.976996472	1.98647896	5.856093018	0.47735152
3400	4.991284538	1.901427726	2.029685572	2.03964939	6.776736483	0.48850643
3800	5.276727514	1.954515058	2.130604904	2.14058806	8.692611393	0.46637447
4000	5.413808199	1.977033557	2.179070245	2.18874901	9.672897703	0.44220535
4400	5.678049942	2.015521279	2.272493809	2.28123272	11.64771306	0.38307846
4600	5.805662503	2.031988685	2.317611663	2.32579797	12.63262282	0.35197844
5000	6.052821575	2.060395874	2.404995591	2.41204688	14.57894573	0.29233633
5400	6.290276698	2.083849642	2.488948655	2.49492506	16.47646354	0.23954249
5600	6.405704247	2.094051414	2.529758456	2.53523976	17.40223361	0.21620457
5800	6.519088346	2.103381291	2.569845788	2.57486438	18.31098728	0.19490703
6000	6.630533827	2.111931305	2.609247716	2.61383660	19.20186192	0.17556125
6400	6.847985890	2.127005459	2.686128630	2.68995336	20.92779410	0.14218573
6600	6.954162545	2.133663485	2.723667747	2.72715433	21.76227573	0.12784694
6800	7.058742287	2.139811801	2.760642269	2.76381689	22.57765670	0.11486366
7000	7.161795070	2.145499452	2.797076930	2.79963270	23.36496670	0.09128948

Most of the current flows near the outside of the wire. Assuming a sinusoidal current in a rectilinear cylindrical wire of infinite length, the distribution of current in the cross-section is formulated with Bessel functions, which is determined by the properties of the material, the frequency and the diameter of the wire.

Fig. 1.21 shows the surface effect for a wire with a diameter of 1 mm.

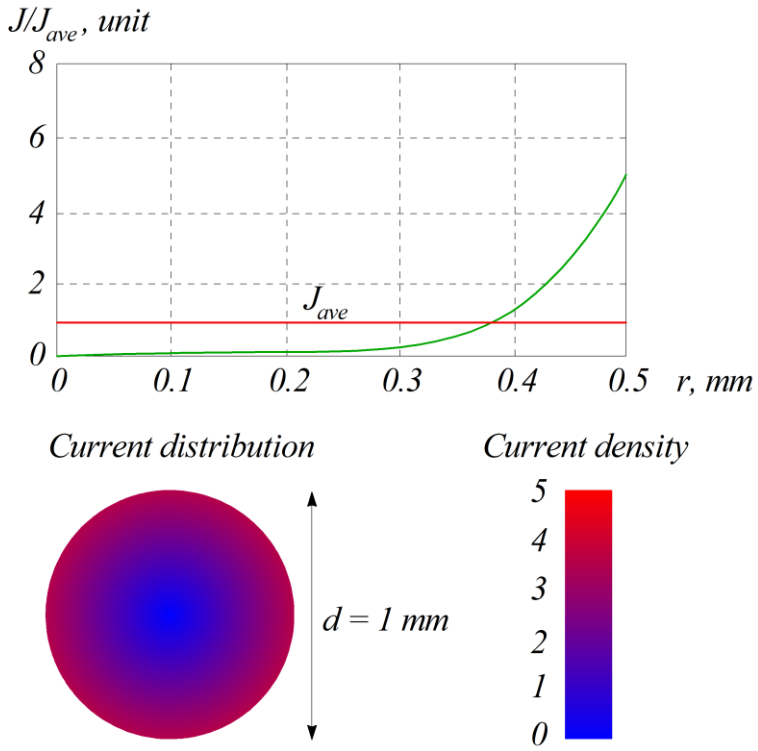

Figure 1.21 – Surface effect of wire

The maximum relative error in calculating the relative resistance of a copper wire with a cross-section of 8 mm was less than 0.9 %, which can be used for engineering calculations.

1.5. Determination of additional power losses in the power supply system from higher current harmonics

Improving energy efficiency is a priority area for power engineering and power supply systems. To realize the maximum energy efficiency of power supply systems, a clear numerical understanding of the components of power losses and methods for their elimination is required. In particular, it is necessary to understand the share of power losses from higher harmonics of the load current in the value of the total losses. This is important, because in recent decades there has been an increase in the number of impulse electricity consumers belonging to both household and industrial appliances.

This leads to an increased amount of the higher current harmonics in power supply systems, and, accordingly, to increased power losses associated with higher

harmonics, which necessitates the use of active rectifiers and active filter-compensating devices [24, 25]. All this makes the problem of determining additional power losses in the power supply system caused by the higher harmonics of the load currents, urgent.

Study [26] presents the results of research into the influence of higher harmonics of the load current on power losses in the electrical network.

The issues of the negative impact of higher harmonics and inactive components of load currents on power supply systems received considerable attention in [27, 28]. However, it should be noted that the results of calculations of additional losses in the active resistance of electrical networks caused by higher current harmonics significantly differ in a number of publications [29, 30].

The AC flow is accompanied by an electromagnetic field around the conductor, which leads to the displacement of electrical charges (of the same current) from the centre of the conductor to its surface. This effect is called the surface effect, or the skin effect. As a result of this effect, the current density over the cross-sectional area of the wire becomes heterogeneous. The volume current density is maximum near the conductor surface. And away from the surface, the volume density decreases exponentially and at the depth Δ it becomes less by *e* times [31, 32].

The dependence of the skin-layer thickness of copper and aluminium wire on the frequency *f* is given in fig. 1.22.

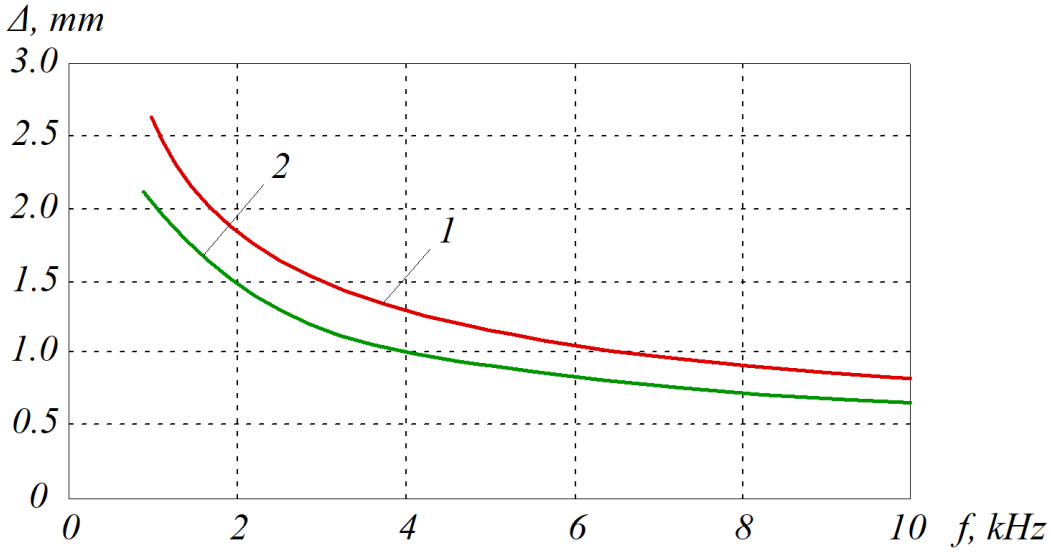

Figure 1.22 – Dependence of skin-layer thickness on current frequency:
1 – for aluminium; *2* – for copper

Thus, at a fairly high frequency of *f* = 10 kHz, the skin-layer thickness becomes meagre (0.66 mm).

For alternating voltage, the current density J from the surface to the centre of the cylindrical conductor is an exponentially decreasing function described by the expression:

$$J = J_s \cdot e^{-\frac{r_k}{\Delta}}, \tag{1.53}$$

where J_s – the conductor conductivity corresponding to the direct current; r_k – the distance from the conductor surface to the centre.

As a result of the exponential reduction of the current density, practically the entire current is concentrated in a layer with a thickness of several Δ. As an example, we give a graph of the distribution of the relative current density in a wire with a thickness of 3Δ (fig. 1.23).

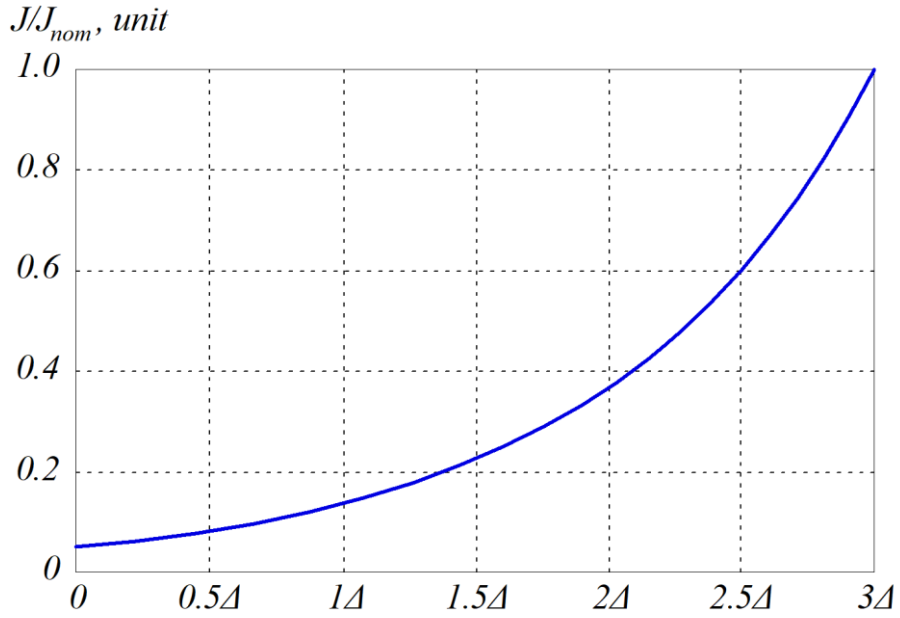

Figure 1.23 – Dependence of relative current density distribution

Thus, the current density decreases by 100 times at a depth of ≈ 4.6·Δ. Thus, the impact of the skin effect on the displacement of the current is determined by the number of skin layers in the wire radius r_0/Δ. This heterogeneity of the current density leads to an increase in its specific resistance.

When the wire radius is greater than the skin-layer thickness, the dependence of the complex wire resistance Z on the current frequency can be described with Bessel function determining the field propagation in a cylindrical coordinate system.

The solution of Bessel functions in a complex plane is simplified by the possibility to solve them in MathCad using the built-in functions "$J_0(z)$" and "$J_1(z)$".

The calculation was made in accordance with expressions (1.30) and (1.31).

The active wire resistance R is a valid part of the complex resistance Z from expression (1.53). The dependences of the active resistance of a 10-km-long copper wire with different diameters on the frequency calculated in accordance with expression (1.29) are presented in fig. 1.24.

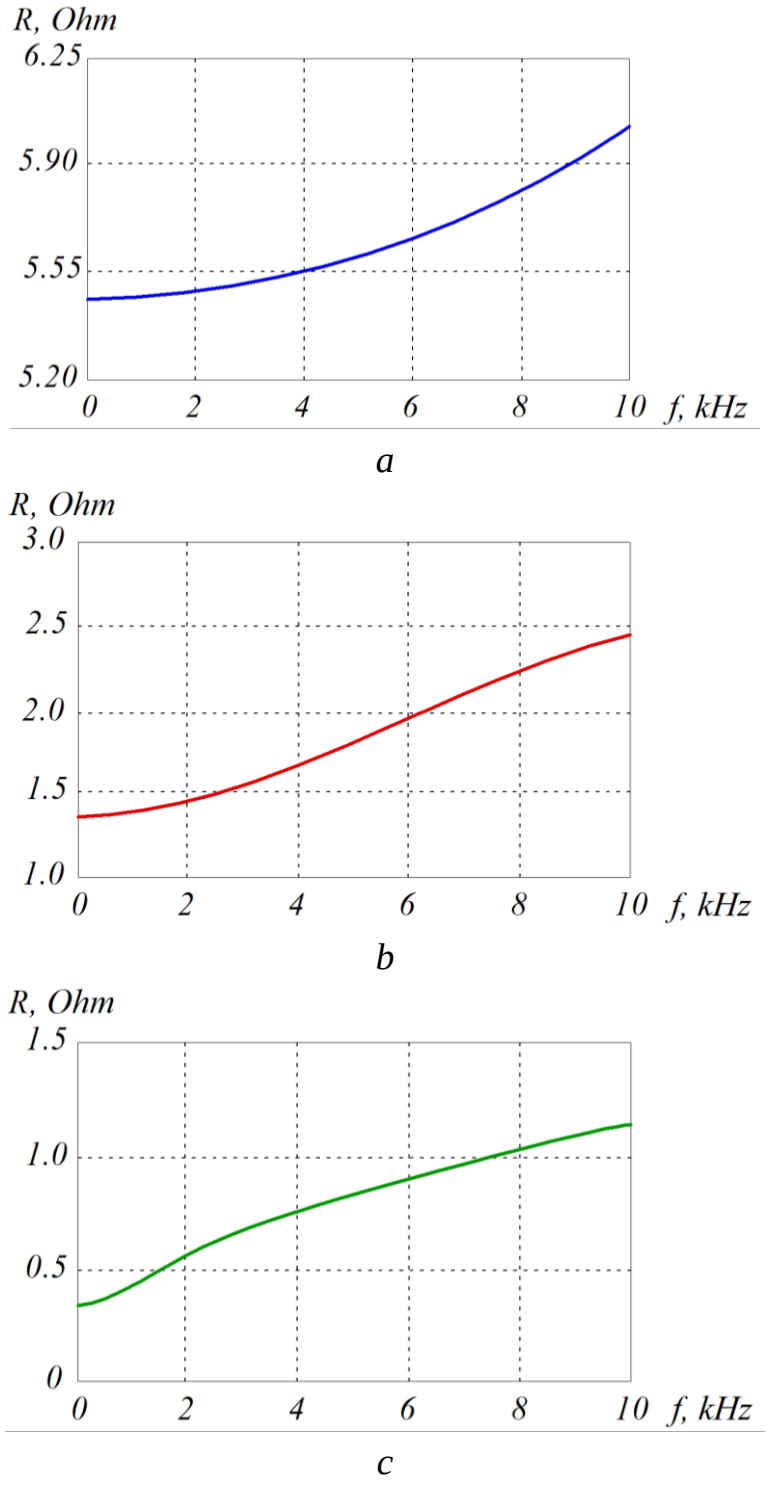

Figure 1.24 – Dependence of active resistance of wire on frequency at diameter: a – 1 mm; b – 2 mm; c – 4 mm

The advantage of the proposed method of resistance calculation is the convergence of the resistance values at the frequency close to zero and the DC resistance:

$$Z\left(f=0\right)=R_{DC}=\frac{L}{\gamma\cdot S}. \tag{1.54}$$

As a result of transformation of the dependencies between the resistances (fig. 1.24) and the frequency into relative values, the graphs of the dependence of the resistances in relative values were obtained (fig. 1.25).

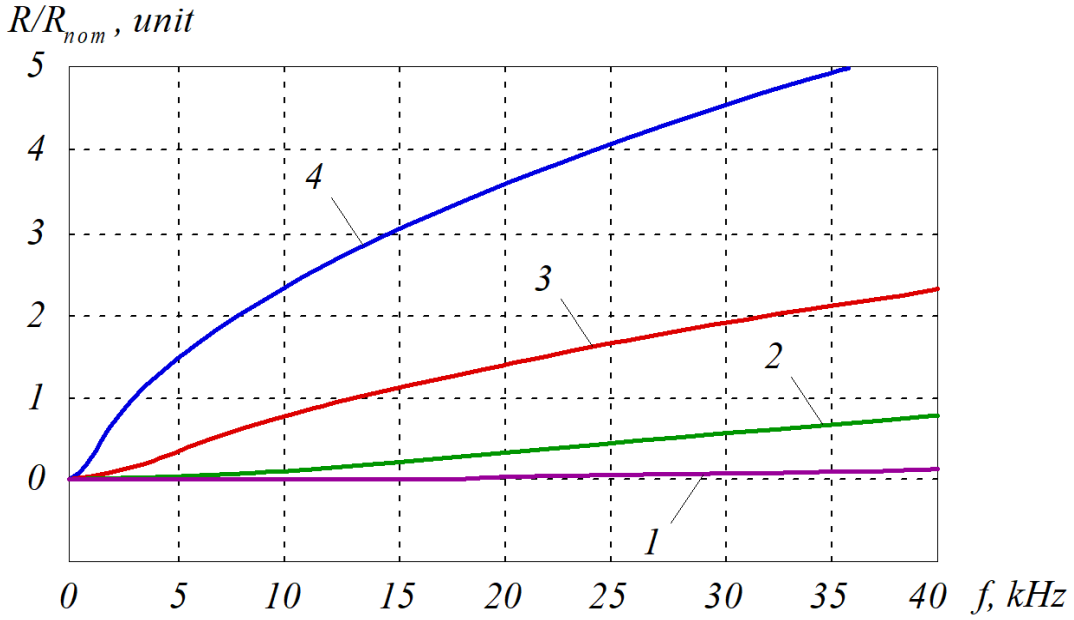

Figure 1.25 – Dependence of active resistance of wire on frequency at diameter:
1 – 0.5 mm; *2* – 1 mm; *3* – 2 mm; *4* – 4 mm

As can be seen from fig. 1.25, the diameter of the conductor core largely affects the current displacement and, as a result, the value of the active resistance at a given frequency.

The skin effect makes the active resistance of the network frequency-dependent and the resistance of the network increases with an increase in frequency, which leads to higher power losses in the power supply system. It can be seen from the above-mentioned characteristics that at the same higher harmonic frequency the larger the radius of the conductor is, the higher power losses will be. Thus, taking into account the power losses from higher harmonics under the skin effect it is especially important for single-core power supply systems with large wire radii, for example, for single-core

contact wires used by the railway power supply systems. At the same time, the use of a multi-core cable eliminates the negative impact from the skin effect on losses in the conductors of the power supply system from higher current harmonics in a fairly wide frequency range. However, even without the skin effect, higher harmonics cause an increase in additional power losses in the conductors of the networks as a result of an increase in RMS of the current.

Studies [33, 34] propose a method for determining additional heat losses in DC and AC electrical networks from higher harmonics, which are unambiguously determined according to the resulting THD of the network current. This method can be used if the skin effect impacts the resistance of a network with a limited spectrum of higher current harmonics is insignificant. In this case, the additional losses in the DC and AC electrical networks from higher harmonics can be calculated taking into account the RMS of the current, and, consequently, the increase in losses in quadratic dependence on the RMS of the current.

As known, THD coefficients for direct THD_{DC} and alternating THD_{AC} currents are determined as:

$$THD_{DC} = \frac{\sqrt{\sum_{m=1}^{m=\infty} I_m^2}}{I_{DC}}; \tag{1.55}$$

$$THD_{AC} = \frac{\sqrt{\sum_{m=2}^{m=\infty} I_m^2}}{I_1}, \tag{1.56}$$

where I_m – the RMS of the m-th harmonic; I_{DC} – the constant component value.

For further expressions, the THD value is given in relative terms, i.e. from 0 to 1.

The effective RMS of alternating (or direct pulse) current is equal to the value of such direct current, which, for a time equal to one period of alternating current, will perform the same work (thermal or electrodynamic effect) as the considered alternating current:

$$I_{RMS} = \sqrt{\frac{1}{T} \cdot \int_0^T i^2(t) \cdot dt}. \tag{1.57}$$

The RMS of the alternating current can also be expressed through the higher harmonics spectrum:

$$I_{RMS\_AC} = \sqrt{I_1^2 + \sum_{m=2}^{m=\infty} I_m^2}. \quad (1.58)$$

From expression (1.54) it is possible to determine the sum of the squares of higher harmonics:

$$\sum_{m=2}^{m=\infty} I_m^2 = \left(THD_I \cdot I_I\right)^2. \quad (1.59)$$

Then the RMS of DC and AC can be presented as follows:

$$I_{RMS\_AC} = \sqrt{I_1^2 + \left(THD_I \cdot I_1\right)^2} = \sqrt{I_1^2 \cdot \left(1 + THD_I^2\right)}; \quad (1.60)$$

$$I_{RMS\_DC} = I_{DC} \cdot \sqrt{\left(1 + THD_{DC}^2\right)}. \quad (1.61)$$

The dependence of the RMS of current on the THD value is given in fig. 1.26, in which the RMS value of the first current harmonic is taken as 100 %.

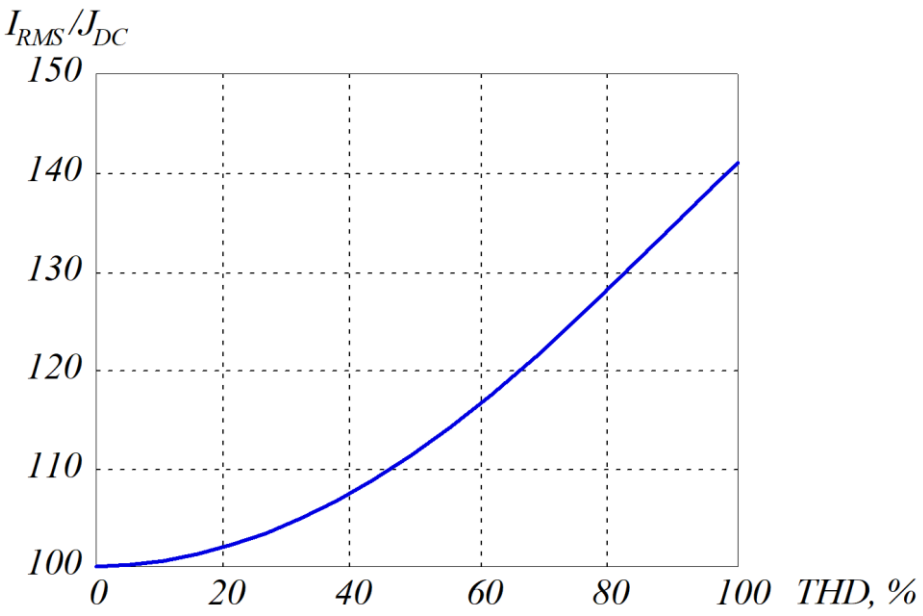

Figure 1.26 – Dependence of RMS on THD

Thus, an unambiguous relationship was established between the THD of the consumed current and the percentage of additional power losses. The dependence of the relative value of additional losses on the value of THD is shown in fig. 1.27, in

which the losses caused by the fundamental harmonic are taken as 100 %, or for the DC network of the constant current component.

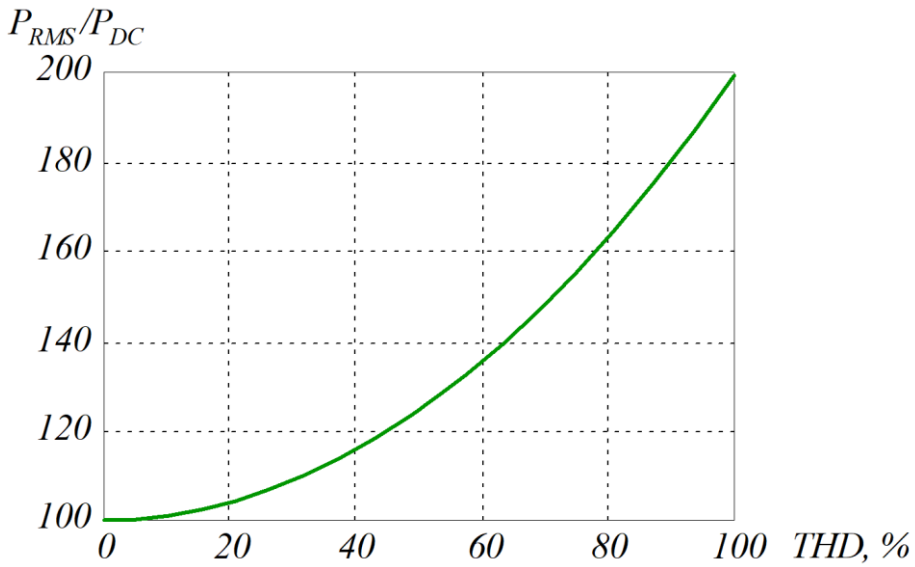

Figure 1.27 – Dependence of additional losses on THD

The ratios shown in fig. 1.27 make it possible to determine additional losses in the power supply system according to the load current. It can be seen from fig. 1.27 that the distortion of the mains current with *THD* = 50 % causes an increase of power losses in the electrical network by about 25 %.

Simulation modelling was used to study power losses in the resistance of the electrical network from the higher harmonics of the three-phase diode rectifier and a reduction in losses when connecting the APF. The simulation model is shown in fig. 1.28.

The parameters of the simulation model are as follows: mains supply voltage – 3×380 V; mains active resistance – 0.2 Ohm, mains inductance – 50 μH, APF throttle inductance – 5 mH; diode rectifier inlet throttle inductance – 0.1 mH; rectifier filter capacity – 12 mF; rectifier load resistance – 3 Ohm. The maximum relative error of calculations of the Matlab system is 0.1 %. The APF control system (CS) is built on the principle of hysteresis modulation and pqr power theory. The APF operates in the mode of antiphase generation of higher harmonics of the load current. This provides mutual compensation of the higher harmonics of the load current by the APF current, which makes it possible to provide the THD of the mains current below 3 %.

The results of the simulation modelling, namely: input current of the three-phase diode rectifier (without the AFA), the current generated by the APF, the resulting network current during the operation of the APF, are shown in fig. 1.29.

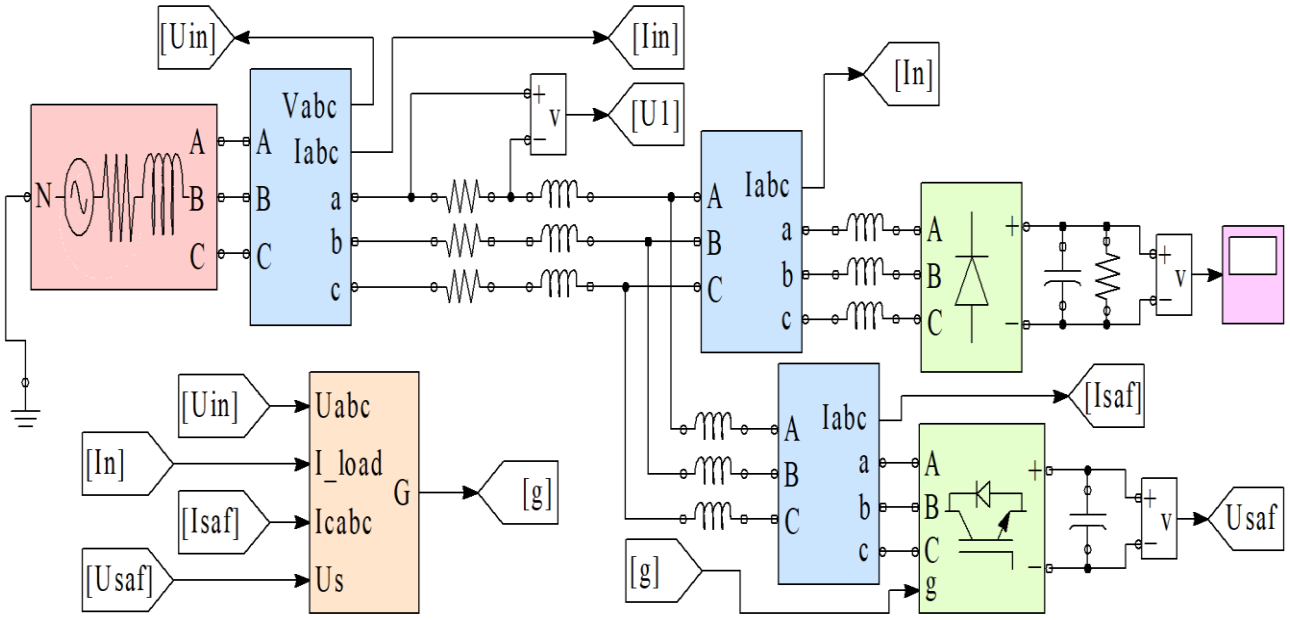

Figure 1.28 – Simulation model of electrical network with three-phase diode rectifier and APF

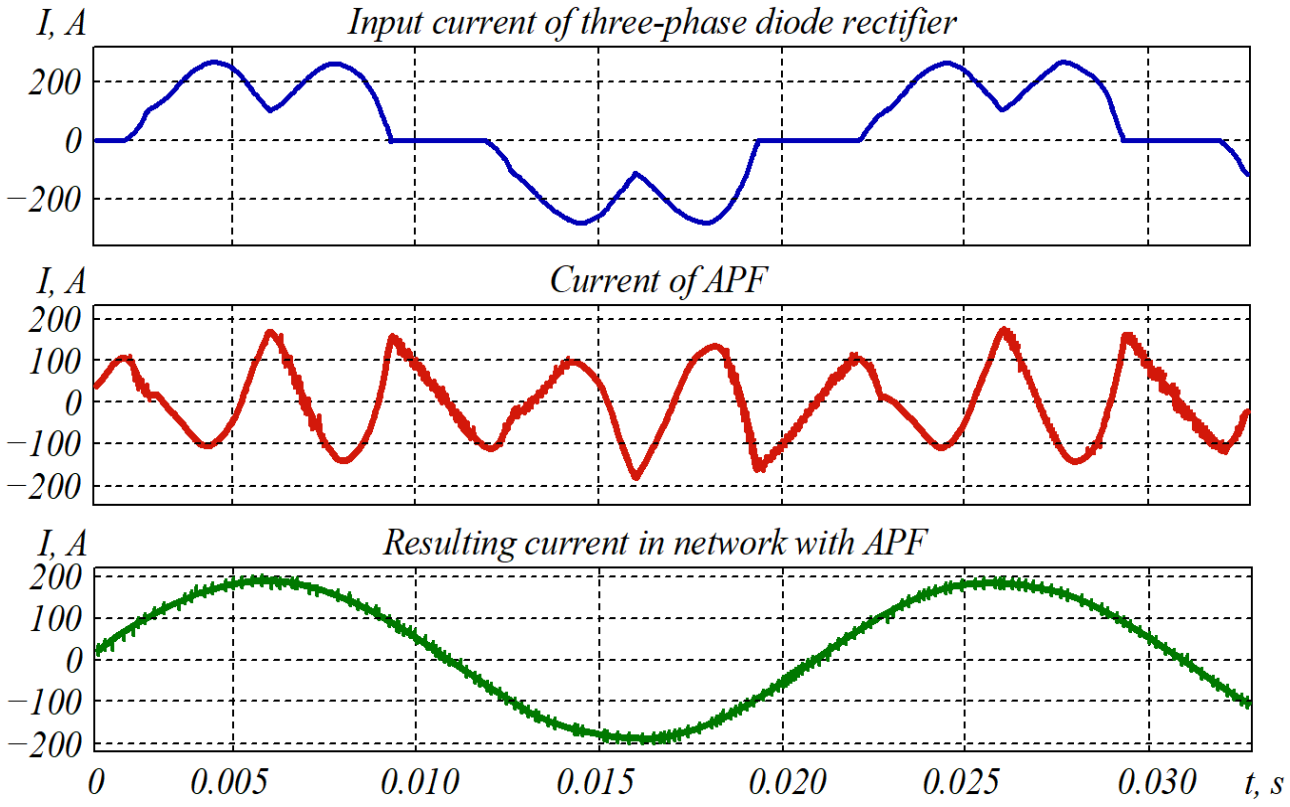

Figure 1.29 – Oscillograms obtained during simulation modelling

The results of Fourier analysis of the mains current with the APF on and off performed in Matlab are shown in fig. 1.30.

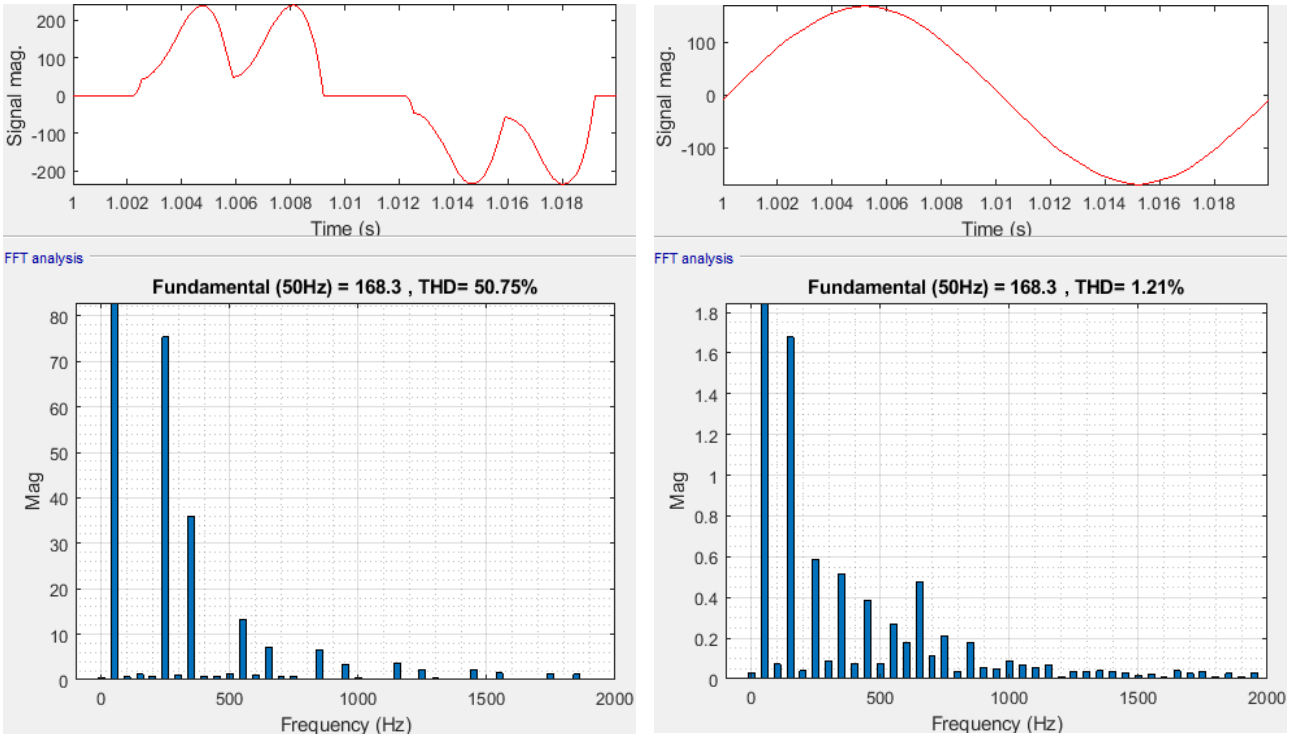

a *b*

Figure 1.30 – Fourier analysis results:
a – for input current of diode rectifier; *b* – for mains current with APF

Numerical results of simulation modelling are given in table 1.4.

Table 1.4 – Results of simulation modelling

Parameter	Values before filtration	Values after filtration
First harmonic of mains current, A	119.006	119.006
THD of mains current, %	50.75	1.21
RMS of mains current, A	133.45	119.014
Power of losses in active network resistance caused by first current harmonic, kW	2.8324	2.8324
Total power losses in active network resistance, kW	3.5617	2.8332

The simulation demonstrates that the APF enables to significantly reduce the content of higher harmonics in the network, reduce the RMS of the network current, and, accordingly, losses in the active resistance of the electrical network. The simulation showed that the use of APF reduces the losses in the active resistance of the network from a specific consumer from 3.56 to 2.83 kW, which coincides with the analytical ratios shown in fig. 1.27.

The increase in power losses in the active resistance of the network from higher harmonics of load currents is determined as the sum of the power losses from each harmonic. With the skin effect an increase in the frequency of higher harmonics results in an increase in the active resistance of the network. The available ratios that determine the values of the active resistance from the frequency of higher harmonics are mutually exclusive. In addition, for the low frequency range, these expressions are erroneous, because they determine the values of the active resistance of the network for a current with a frequency of 50 Hz, and for a harmonic of 150 Hz they are significantly lower than those for a direct current.

If the spectrum of higher harmonics is limited and an increase in the active resistance of the network in this frequency range grows insignificantly, the influence of the skin effect can be neglected. Here, the impact of higher harmonics of the load current on the power losses in the electrical network can be determined on the basis of the RMS of the load current. The study provides analytical dependencies of the relative increase of power losses on the THD of the mains current. The above-mentioned dependencies are confirmed by simulation modelling in Matlab on the example of a three-phase power supply system with a diode rectifier and an APF.

The results of this study can be used for calculating power losses in:

– AC and DC power supply systems; and

– the electrical network from a specific consumer, as a factor in the feasibility study of the use of APFs and other filter-compensating devices designed to reduce the content of higher harmonics.

1.6. Calculation of static and dynamic losses in power IGBTs using polynomial approximation of basic energy characteristics

Power losses and efficiency are among the most important indicators in semiconductor converters of electricity [35]. “Manual” calculation of power losses in semiconductor converters with different modulation types is quite a complex task and requires the search for a new technique.

Study [36] proposes a calculation technique that makes it possible to determine with high accuracy the static and dynamic losses in power IGBTs for any type of semiconductor converter with any control law.

The applications for automatic calculation of power losses in power IGBTs are quite common, namely: MelcoSim, Semisel, Iposim, etc. These programs are quite convenient tools, however they can perform automatic calculation of power losses only

for “standard” topologies (step-up and step-down DC voltage converter, three-phase AVI) with “standard” pulse-width modulation (PWM) control algorithms: PWM with constant fill factor, sinusoidal PWM, spatial-vector PWM. The disadvantages of the existing programs are that they cannot model “non-standard” topologies, namely: APF, active rectifiers with power factor correction, multi-level converters, and many other topologies, or standard topologies with non-standard control algorithms [37].

Matlab / Simulink is one of the most popular programs for studying semiconductor converters; it can be used for modelling virtually any converter topology with any CS. However, a disadvantage of this application is that it does not include dynamic power losses in IGBTs. In addition, the IGBT volt-ampere characteristic is presented as a linear function (fig. 1.31).

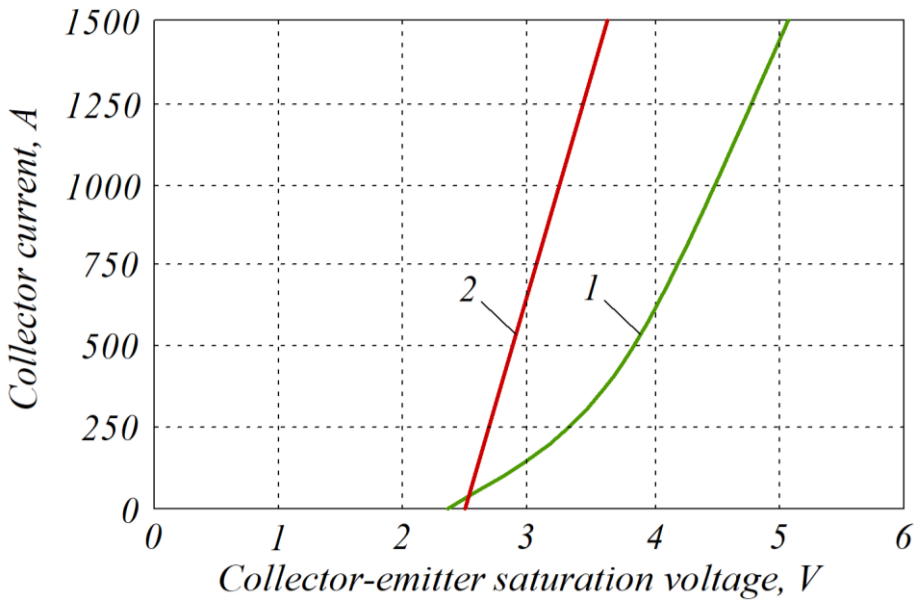

Figure 1.31 – Current-voltage characteristic:
1 – actual transistor; *2* – transistor in Matlab environment

In the SPICE schematic modelling programs, namely, Multisim, LT-spice, TINF and MicroCap, simulation of volt-ampere processes is more accurate [38]. The models of transistors in the SPICE-simulation include the on and off times of the transistors and the dynamic losses in them [39]. However, the above-mentioned programs make it possible to model exclusively low-power transistors, since they simply do not have models of high-voltage power IGBTs.

Study [40] provides a calculation of the power losses in IGBTs and a calculation of the temperature of the switch. However, this publication does not specify the transistor which characteristics were used in the calculation. Furthermore, it is not specified how dynamic power losses were taken into account.

Studies [41, 42] describe the methods for modelling dynamic losses in IGBTs. However, the technique presented has disadvantages:

– the dependencies of the switch-on energy E_{on} and the switch-off energy E_{off} on the emitter current in the IGBT are represented by linear dependencies, although in reality these characteristics have the form close to the parabola;

– no power loss in the by-pass diode of the transistor is taken into account.

Determination of power losses in IGBTs can be performed by calculating the static and dynamic losses in the IGBT *VT* and parallel diodes *VD*, respectively, by the expressions [43]:

$$\Delta P = P_{VT} + P_{VD}; \tag{1.62}$$

$$P_{VT} = P_{VT.DC} + P_{VT.SW}; \tag{1.63}$$

$$P_{VD} = P_{VD.DC} + P_{VD.SW}, \tag{1.64}$$

where $P_{VT.DC}$ – the static losses in IGBT; $P_{VT.SW}$ – the dynamic losses in IGBT; $P_{VD.DC}$ – the static losses in parallel diodes; $P_{VD.SW}$ – the dynamic losses in parallel diodes.

The switching of current and voltage in the IGBT-switch and the graphical distribution of static and dynamic losses are shown in fig. 1.32.

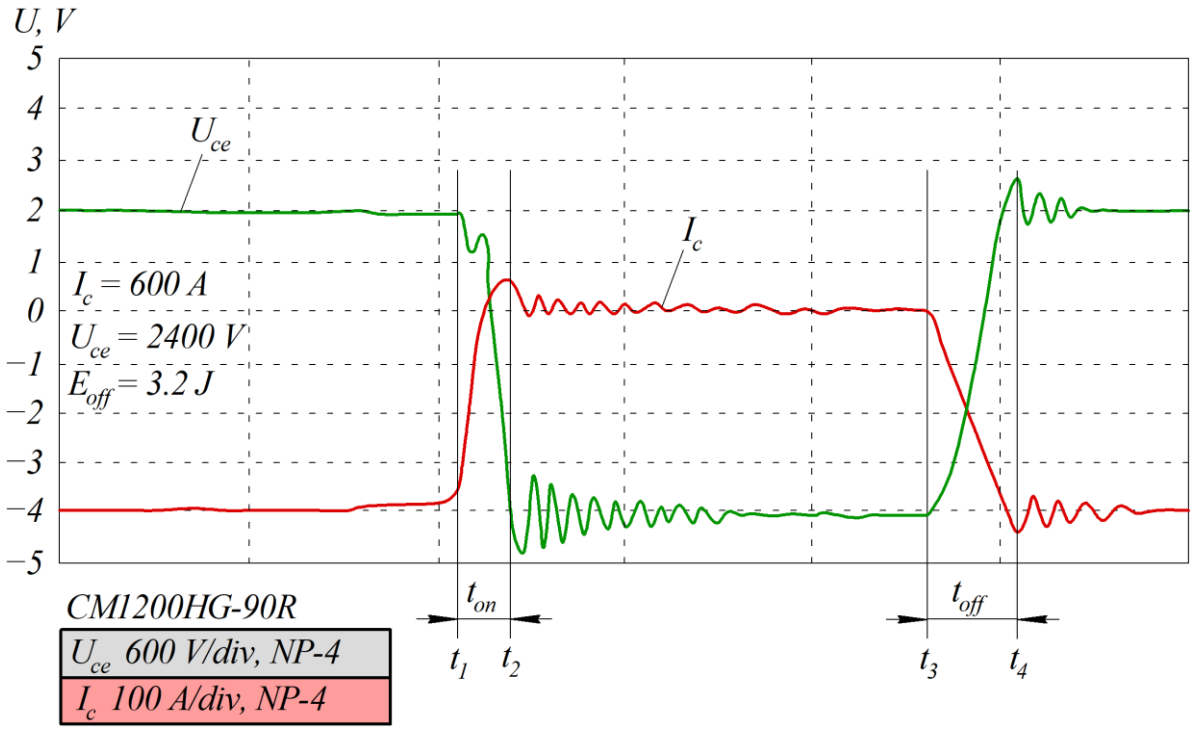

Figure 1.32 – Current and voltage switching in IGBT

Static losses in IGBT P_{DC} are determined according to the following expression:

$$P_{DC} = \frac{1}{2\pi} \cdot \int_0^{\pi} \left(I_c \cdot V_{ce}\left(I_c\right) \cdot D_{on} \right) \cdot dt, \tag{1.65}$$

where I_c – the collector current; $V_{ce}(I_c)$ – the voltage between the collector and the emitter, which depends on the collector current value; D_{on} – the PWM fill factor.

Dynamic losses in IGBT P_{SW} are determined from the expression:

$$P_{SW} = \frac{1}{2\pi} \cdot \int_0^{\pi} \left[\left(E_{on}\left(I_c\right) + E_{off}\left(I_c\right) \cdot f \right) \right] \cdot dt, \tag{1.66}$$

where f – the PWM frequency; $E_{on}(I_c)$ – the energy dissipated in the transistor when turned on, which depends on the magnitude of the collector current; $E_{off}(I_c)$ – the energy dissipated in the transistor when turned off, which depends on the magnitude of the collector current.

Power losses in the by-pass diode of the power transistor consist of conduction losses and losses associated with the power loss for recovery. Calculation of power losses in the by-pass diode is carried out in accordance with the expressions:

$$P_{VD} = P_{DC.VD} + P_{SW}; \tag{1.67}$$

$$P_{SW} = E_{rec} \cdot f; \tag{1.68}$$

$$P_{DC.VD} = U_{fwd} \cdot I. \tag{1.69}$$

When determining the IGBT power losses, the following dependencies are basic [44]:

– dependence of the voltage between the collector and the emitter on the collector current (current-voltage characteristic (CVC) of the transistor);

– CVC of the by-pass diode; and

– dependence of the switching-on and switching-off energy of the transistor, as well as the recovery energy of the by-pass diode on the current of the transistor emitter.

The energy characteristics of IGBT of the type CM750HG-130R (*1* – passport; *2* – after approximation) are shown in fig. 1.33. It is worth noting that the energy characteristics of the transistor at temperatures of 25 and 125 °C vary considerably and with an increase in temperature the losses in the transistor increase.

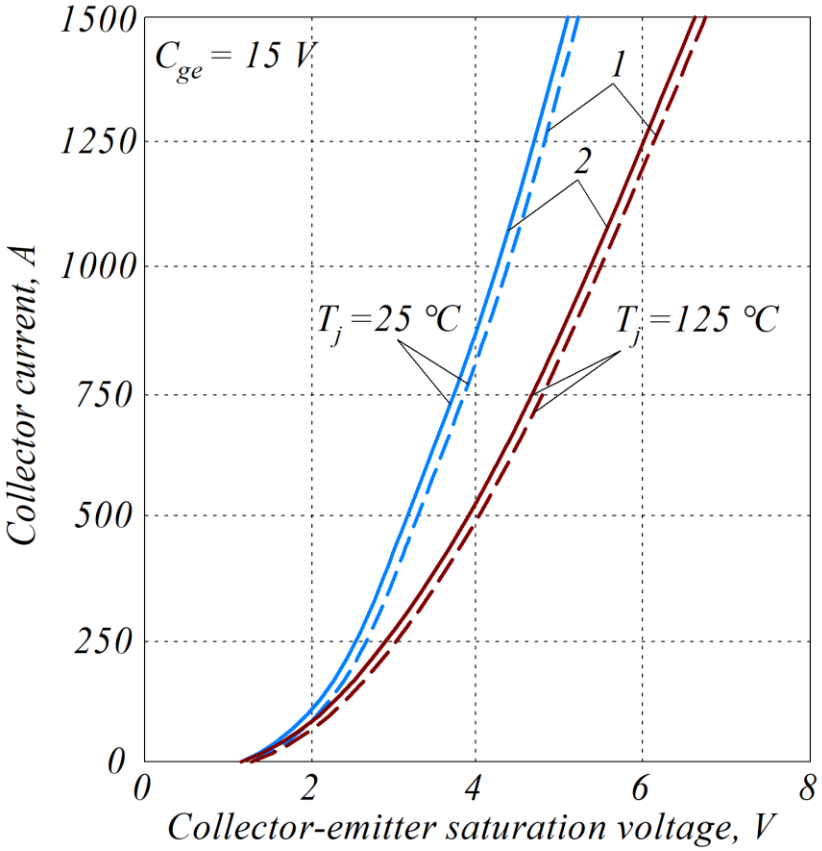

a

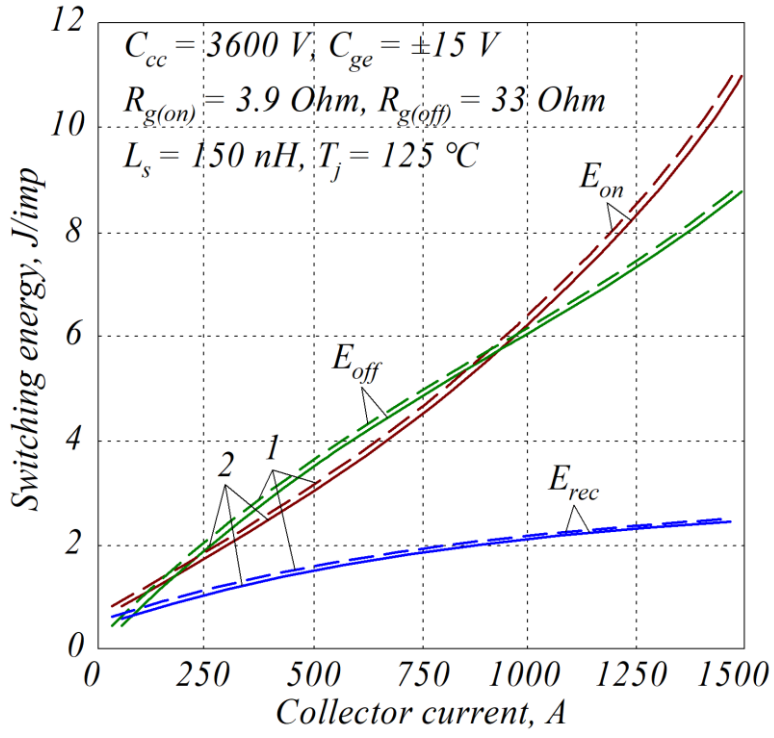

b

Figure 1.33 – Energy characteristics of IGBT series CM750HG-130R: *a* – CVC of transistor $V_{ce}(I)$; *b* – dependencies of switching-on, switching-off and recovery energies of by-pass diode on current

The energy dependencies of the transistor shown in fig. 1.33 are transferred to the tabular data (table 1.5).

Table 1.5 – Energy characteristics of the CM1200HG-90R transistor

Collector current, kA	Switch-on energy E_{on}, J/imp	Switch-off energy E_{off}, J/imp	Energy of recovery E_{rec}, J/imp	CVC of the transistor $V_{ce}(I_{ce})$, V	CVC of the diode, V
0	0.31	0.32	0.5	1.0	0.7
0.1	0.75	0.8	0.7	1.65	1.02
0.2	1.1	1.15	0.9	2.15	1.36
0.3	1.45	1.5	1.1	2.5	1.6
0.4	2.0	1.95	1.25	2.75	1.76
0.5	2.4	2.25	1.5	3.0	1.9
0.6	2.75	2.5	1.7	3.2	2.04
0.7	3.125	2.75	1.9	3.4	2.2
0.8	3.65	3.1	2.0	3.65	2.32
0.9	4.0	3.4	2.15	3.825	2.44
1.0	4.5	3.725	2.25	4.05	2.58
1.1	5.0	4.0	2.35	4.2	2.66
1.2	5.5	4.25	2.45	4.4	2.8
1.3	6.0	4.55	2.5	4.55	2.9
1.4	6.5	4.85	2.55	4.75	3.0
1.5	7.05	5.1	2.6	4.9	3.1
1.6	7.75	5.45	2.65	5.05	3.2
1.7	8.3	5.7	2.65	5.2	3.3
1.8	9.0	6.0	2.65	5.375	3.4
1.9	9.75	6.25	2.65	5.6	3.5
2.0	10.45	6.6	2.65	5.7	3.6

If there is an error in the source tabular data (roughly transferred), it is inappropriate to use the interpolation method to analyse them and find an approximate function exactly passing through all points of the given source tabular function. In such a case, an approximating function which passes in proximity to the setpoints and closer to the initial points should be built. The approximation smoothes the processed experimental data containing deviations, i.e., it is a way of finding intermediate values according to the available discrete set of known values [45].

The main task of interpolation is to replace the tabular function with a simple analytical function and then find its approximate values at those points inside the interval where the initial function is not specified.

There are different types of approximation: linear, partial-linear, static, exponential, and polynomial [46]. In addition, there are various mathematical methods for performing approximation.

The purpose of approximation is to determine the mathematical functions that most accurately describe the obtained tabular dependencies $E_{on}(I)$, $E_{off}(I)$, $E_{rec}(I)$, $U_{ce}(I)$, $U_{VD}(I)$.

In order to automatically calculate power losses in power IGBT-switches, the current-voltage characteristics of the transistor and the dependencies of the switching-on and switching-off energy on the load current were approximated by the least squares method.

The mathematical approximation was performed in Wolfram Mathematica.

If we remove the requirement for the mandatory passage of the approximating function through the nodal points and replace it with the requirement for a minimum sum of squared differences between the values of the approximating function and the function approximated in the nodes, then the least squares method will come out, which does not ignore errors in the values of the approximating function, but tries to average their influence on the result of approximation.

The least squares method is based on minimizing the function of:

$$F = \sum_{i=0}^{n} \left(\varphi(x_i) - y_i \right)^2 \to \min, \tag{1.70}$$

where n – the number of measurement points.

In this method, the approximating function $f(x)$ is a polynomial of order k:

$$\varphi(x) = a_0 + a_1 \cdot x + ... + a_k \cdot x^k, \tag{1.71}$$

or with substitution

$$F = \sum_{i=0}^{n} \left(a_0 + a_1 \cdot x + ... + a_k \cdot x^k - y_i \right)^2 \to \min. \tag{1.72}$$

To find unknown coefficients, derivatives from this function are determined by the corresponding coefficient and equated to zero:

$$\begin{cases} \dfrac{\partial F}{\partial a_0} = 2 \cdot \sum\limits_{i=0}^{n} \left(a_0 + a_1 \cdot x + ... + a_k \cdot x^k - y_i \right) = 0; \\ \dfrac{\partial F}{\partial a_1} = 2 \cdot \sum\limits_{i=0}^{n} x_i \cdot \left(a_0 + a_1 \cdot x + ... + a_k \cdot x^k - y_i \right) = 0; \\ \vdots \\ \dfrac{\partial F}{\partial a_k} = 2 \cdot \sum\limits_{i=0}^{n} x_i^k \cdot \left(a_0 + a_1 \cdot x + ... + a_k \cdot x^k - y_i \right) = 0. \end{cases} \quad (1.73)$$

After the transformations, we get a system of equations:

$$\begin{cases} n + \sum\limits_{i=0}^{n} x_i + ... + \sum\limits_{i=0}^{n} x_i^k = \sum\limits_{i=0}^{n} y_i; \\ \sum\limits_{i=0}^{n} x_i + \sum\limits_{i=0}^{n} x_i^2 + ... + \sum\limits_{i=0}^{n} x_i^{k+1} = \sum\limits_{i=0}^{n} x_i \cdot y_i; \\ \vdots \\ \sum\limits_{i=0}^{n} x_i^k + \sum\limits_{i=0}^{n} x_i^{k+1} + ... + \sum\limits_{i=0}^{n} x_i^{2 \cdot k} = \sum\limits_{i=0}^{n} x_i^k \cdot y_i. \end{cases} \quad (1.74)$$

By solving the resulting system of equations, we can find the coefficients a_0, a_1, …, a_k of polynomial functions to describe the energy characteristics of each particular power transistor. The approximation of energy characteristics is automated using Wolframe Matematica. The results of approximation of the energy characteristics of high-voltage power IGBTs manufactured by Mitsubishi are given in table 1.6. For convenience, the coefficients in approximated functions depending on the current are described in kiloamperes. The approximation results correspond to the output characteristics of the IGBT of the type CM750HG-130R. As can be seen from fig. 1.26, the obtained mathematical dependencies almost perfectly describe the output dependencies from the Datasheet transistor. The advantage of polynomial approximation is a fairly accurate description of the tabular data in the specified range. However, outside the tabular range, the resulting function may behave indefinitely.

When the current through the transistor exceeds the permissible values, the transistor physically breaks [47, 48]. Graphically, this effect is shown in fig. 1.34.

Therefore, polynomial approximation makes it possible to describe quite accurately the energy dependencies of power transistors in a given range, but outside this range the function will behave incorrectly, which imposes restrictions on the application of this method, namely, the losses are calculated correctly only in a given current limitation range.

Table 1.6 – Results of approximation of energy characteristics of power IGBTs of different classes

Transistor	Results of approximation
CM750HG-130R (6600 V, 750 A)	$U_{ce}(I) = 2.3774 \cdot I^5 - 10.499 \cdot I^4 + 17.946 \cdot I^3 - 15.401 \cdot I^2 + 9.7617 \cdot I + 1.3188;$ $U_{VD}(I) = 2.4376 \cdot I^5 - 10.013 \cdot I^4 + 15.671 \cdot I^3 - 12.144 \cdot I^2 + 7.2184 \cdot I + 0.7822;$ $E_{rec}(I) = 0.0101 \cdot I^4 + 0.1402 \cdot I^3 - 1.0272 \cdot I^2 + 2.4108 \cdot I + 0.4976;$ $E_{on}(I) = 0.1699 \cdot I^4 + 0.5074 \cdot I^3 + 0.4161 \cdot I^2 + 4.577 \cdot I + 0.5697;$ $E_{off}(I) = 0.0139 \cdot I^4 + 1.2829 \cdot I^3 - 3.7047 \cdot I^2 + 8.4595 \cdot I - 0.0041.$
CM1200HG-90R (4500 V, 1200 A)	$U_{ce}(I) = 0.7622 \cdot I^5 - 4.4108 \cdot I^4 + 9.6859 \cdot I^3 - 10.245 \cdot I^2 + 7.1998 \cdot I + 1.0169;$ $U_{VD}(I) = 0.33 \cdot I^5 - 1.9618 \cdot I^4 + 4.4951 \cdot I^3 - 5.1124 \cdot I^2 + 4.1169 \cdot I + 0.6899;$ $E_{rec}(I) = 0.2203 \cdot I^4 - 0.9136 \cdot I^3 + 0.513 \cdot I^2 + 1.9475 \cdot I + 0.4954;$ $E_{on}(I) = 0.0367 \cdot I^4 + 0.2901 \cdot I^3 - 0.2417 \cdot I^2 + 4.1088 \cdot I + 0.3115;$ $E_{off}(I) = -0.1981 \cdot I^4 + 1.0595 \cdot I^3 - 2.0282 \cdot I^2 + 4.5203 \cdot I + 0.3366.$
CM800HC-66H (3300 V, 800A)	$U_{ce}(I) = -6.09 \cdot I^6 + 31.87 \cdot I^5 - 65.31 \cdot I^4 + 66.62 \cdot I^3 - 35.96 \cdot I^2 + 12 \cdot I + 0.63;$ $U_{VD}(I) = 0.6245 \cdot I^3 - 2.1404 \cdot I^2 + 3.7624 \cdot I + 0.76;$ $E_{rec}(I) = -0.5676 \cdot I^2 + 2.269 \cdot I + 0.9238;$ $E_{on}(I) = 0.001201 \cdot I + 0.121;$ $E_{off}(I) = 0.4111 \cdot I^3 - 1.1164 \cdot I^2 + 1.677 \cdot I + 0.2012.$
CM1200HB-50H (2500 V, 1200 A)	$U_{ce}(I) = 0.0586 \cdot I^4 - 0.3132 \cdot I^3 + 0.2529 \cdot I^2 + 1.6165 \cdot I + 1.2544;$ $U_{VD}(I) = -0.001 \cdot I^3 - 0.2254 \cdot I^2 + 1.5294 \cdot I + 0.8259;$ $E_{rec}(I) = -0.1089 \cdot I^2 + 0.3528 \cdot I + 0.2666;$ $E_{on}(I) = -0.0182 \cdot I^3 + 0.1893 \cdot I^2 + 0.5797 \cdot I + 0.1952;$ $E_{off}(I) = -0.017 \cdot I^3 - 0.1293 \cdot I^2 + 1.0389 \cdot I + 0.2487.$
CM1200DC-34S (1700 V, 1200 A)	$U_{ce}(I) = -0.1623 \cdot I^4 + 0.9421 \cdot I^3 - 2.0092 \cdot I^2 + 2.7468 \cdot I + 0.5729;$ $U_{VD}(I) = -0.1856 \cdot I^4 + 1.0545 \cdot I^3 - 2.1711 \cdot I^2 + 2.7352 \cdot I + 0.6813;$ $E_{rec}(I) = 0.0054 \cdot I^5 - 0.0368 \cdot I^4 + 0.1002 \cdot I^3 - 0.16 \cdot I^2 + 0.2309 \cdot I + 0.0227;$ $E_{on}(I) = 0.2406 \cdot I^2 - 0.006 \cdot I + 0.0496;$ $E_{off}(I) = 0.0587 \cdot I^2 + 0.1842 \cdot I + 0.0547.$

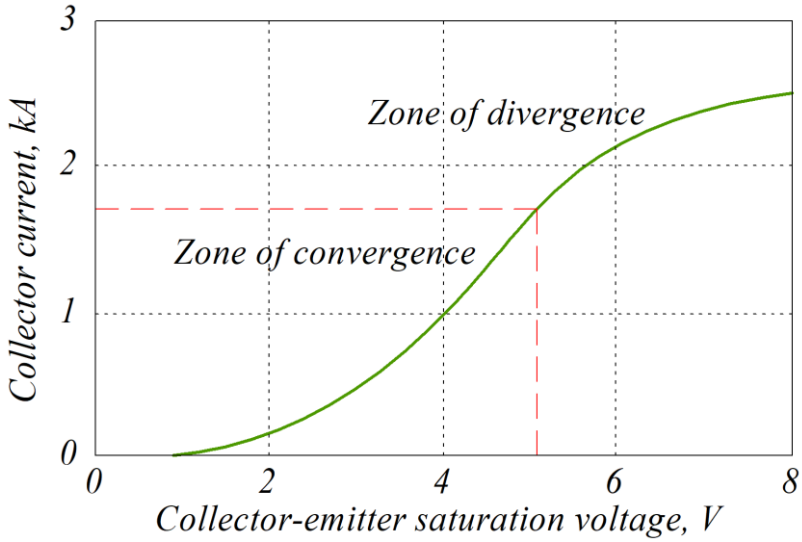

Figure 1.34 – Zone of convergence and divergence of IGBT

The output signals for determining the static and dynamic power losses in Matlab are the transistor control signal and the transistor current signal. The static losses are determined as the instantaneous power integral by the expression:

$$P_{stat} = \int I_c \cdot U_{ce}\left(I_c\right) \cdot dt. \tag{1.75}$$

An example of the simulation model for calculating power losses in a IGBT of the type CM800HC-66H is shown in fig. 1.35.

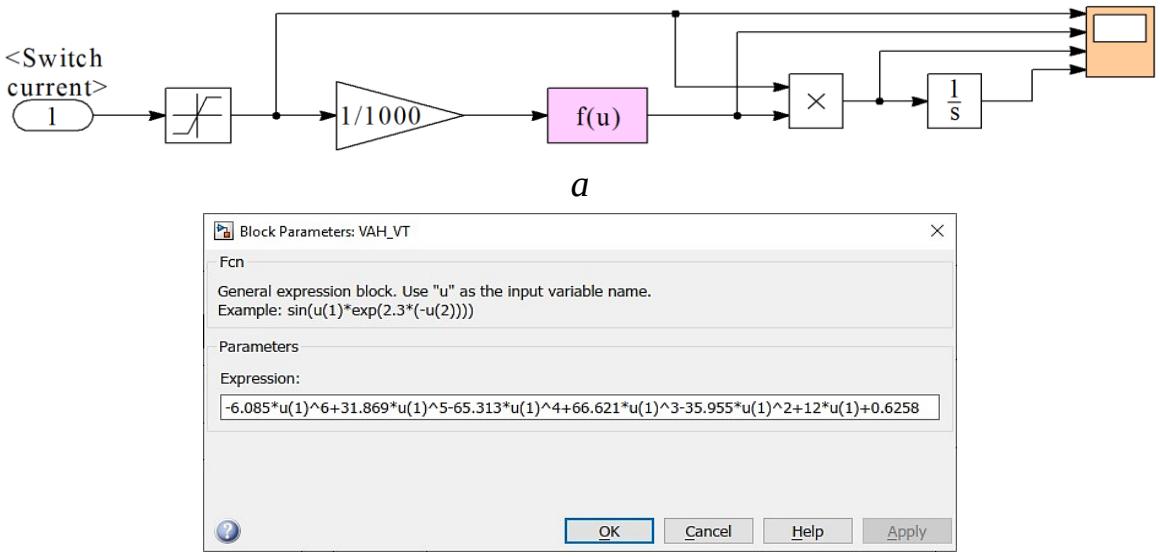

a

b

Figure 1.35 – Sub-model for calculating static power losses in IGBT:
a – model type; *b* – given approximating dependence between voltage and current

Mathematically, the dependence $U_{ce}(I_c)$ is introduced into the “Fcn” block, which makes it possible to set the dependence approximated.

The results of the simulation of static power losses are shown in fig. 1.36. The calculation of dynamic losses is more complicated. Fig. 1.37 shows a simulation model for calculating dynamic power losses in an IGBT module with a by-pass diode.

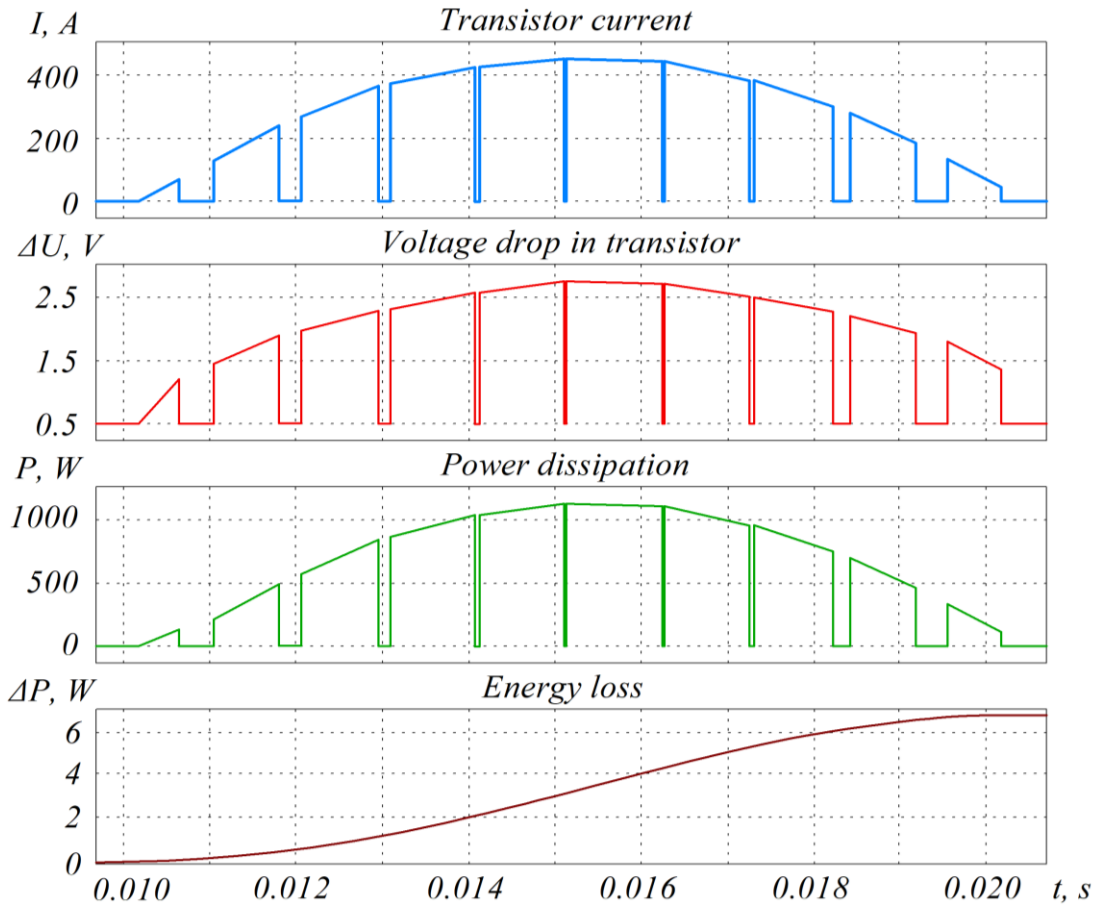

Figure 1.36 – Results of simulation of static power losses

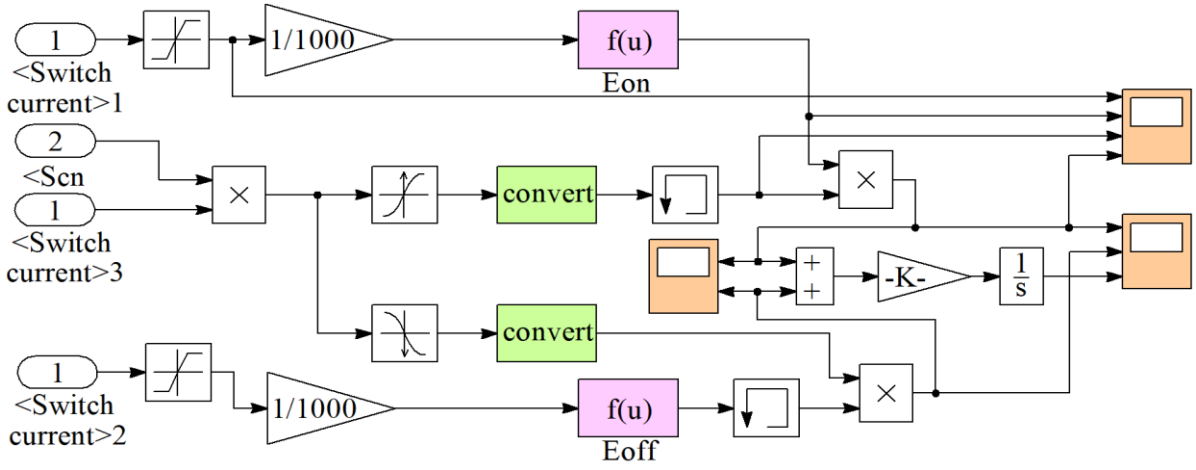

Figure 1.37 – Simulation model for calculating dynamic power losses

The results of dynamic loss modelling are shown in fig. 1.38.

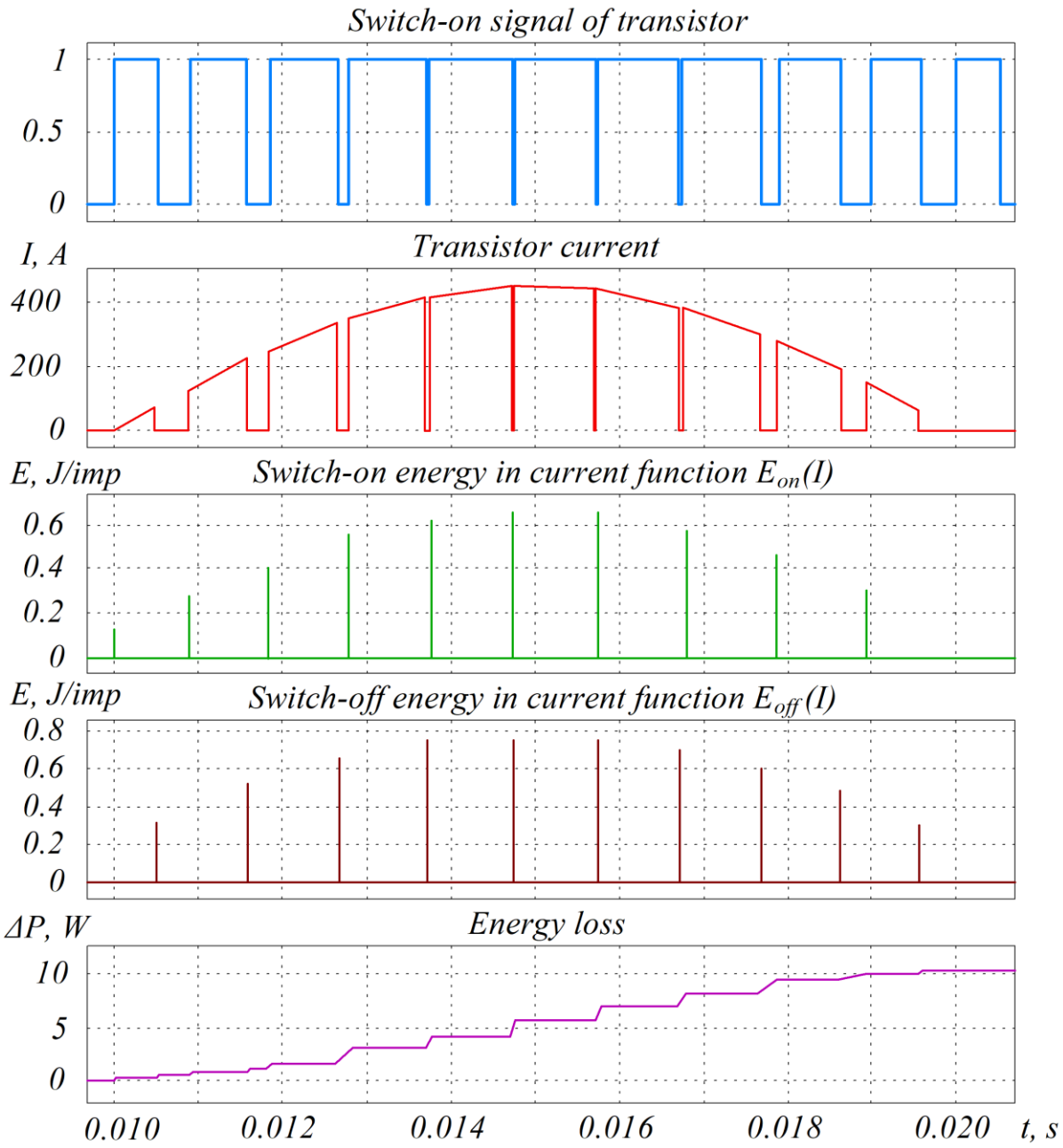

Figure 1.38 – Results of modelling dynamic power losses

As can be seen from fig. 1.38, the switch-on and switch-off energy depend on the magnitude of the transistor current. To simulate dynamic losses, it is necessary to set the simulation method with a constant calculation step.

The developed technique for determining power losses in power IGBTs was verified. The calculations of power losses performed in MelcoSim 5.1 for a three-level AVI with *RL*-load (fig. 1.39) and those performed in Matlab were compared with the above-described technique.

The output calculation data: diagram of a three-phase AVI; voltage in the DC circle – 2800 V; PWM frequency – 2 kHz; RMS of the output current – 934.5 A; active load resistance – 1 Ohm; load inductance – 1 mH; cosφ = 0.954.

The analysis of the convergence of the calculation in Matlab and MelcoSim is given in table 1.7. A number of studies have shown that the discrepancy between the calculation of power losses of the model developed in Matlab and that performed by MelcoSim 5.1 does not exceed 2.1 %.

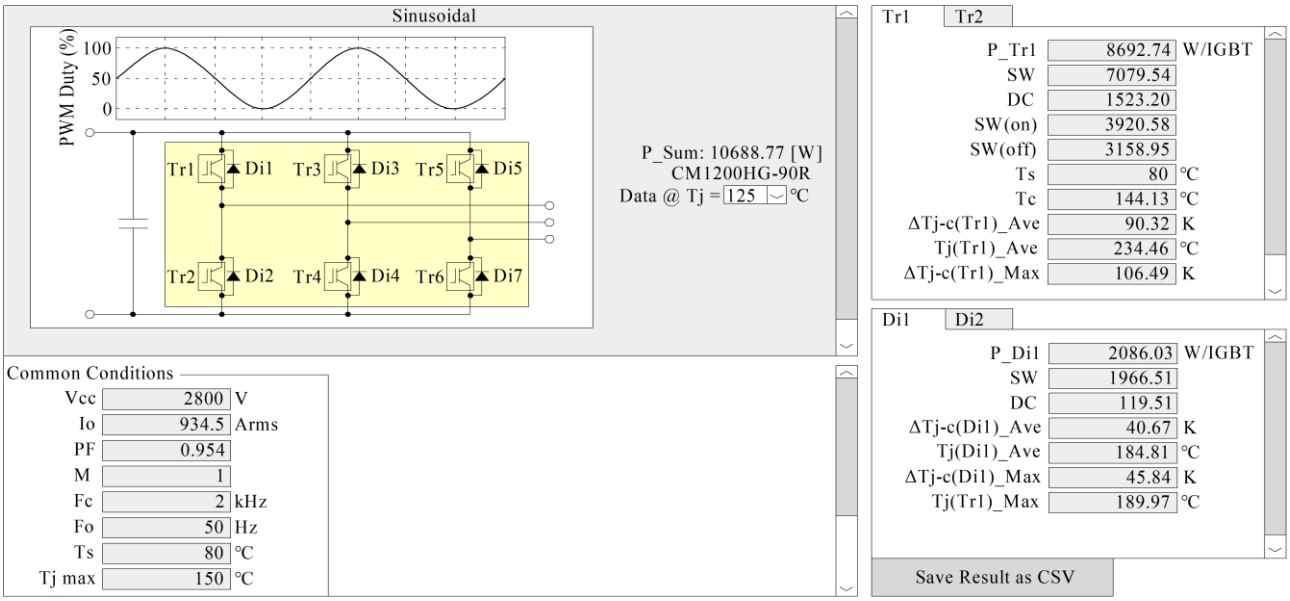

Figure 1.39 – Interface of MelcoSim 5.1

Table 1.7 – Results of power loss calculation in IGBT series CM1200HG-90R

Parameter	Calculation in Matlab, W	Calculation in Melcosim, W	Relative calculation error, %
Dynamic losses in transistor, W	7079.54	7094.94	0.217
Static losses in transistor, W	1523.20	1519.14	0.266
Dynamic losses in by-pass diode, W	1966.51	2005.68	–1.992
Static losses in by-pass diode, W	119.51	121.93	–2.024
Cumulative power losses, W	10688.77	10771.96	0.778

Table 1.7 shows the deviation of the calculation results in MelcoSim, the disadvantage of which is that for the AVI this program calculates the switching of a purely sinusoidal current without distortion, i.e., it takes the current value during

switching, taking into account the sinusoidal function. For high-voltage switches with low switching frequency, the form of the load current may differ significantly from the sinusoidal, resulting in distorted calculation.

Fig. 1.40 shows the ideal and real shapes of the inverter output current.

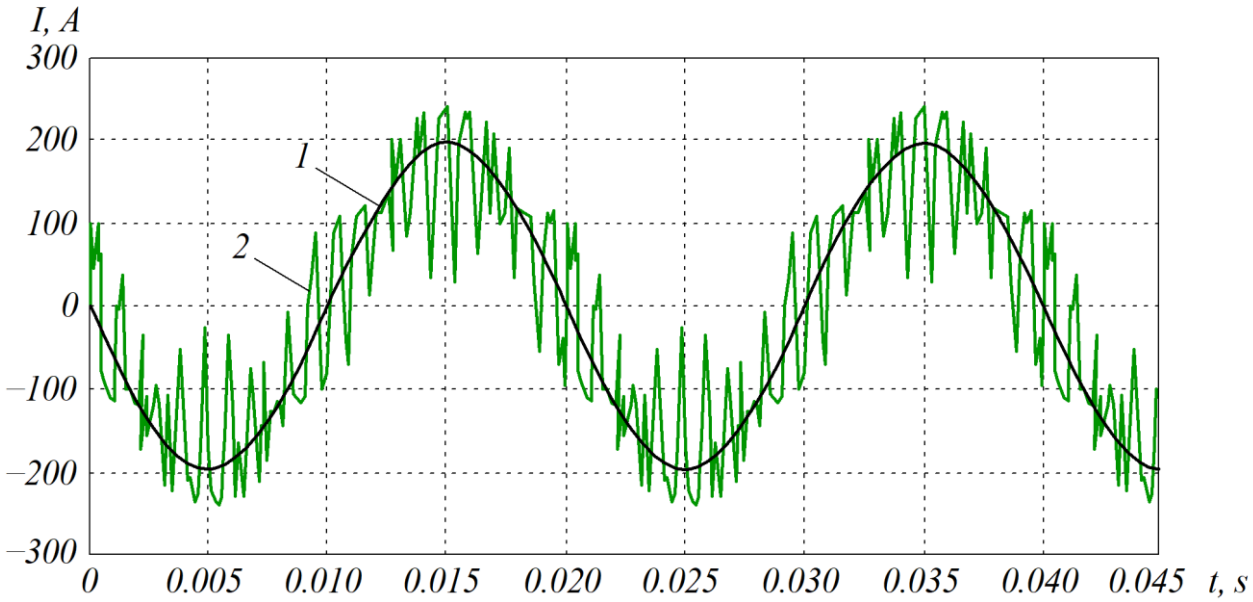

Figure 1.40 – Ideal (*1*) and actual (*2*) forms of output current of inverter

As can be seen from fig. 1.40, the form of the real output current of the inverter differs significantly from the ideal sinusoidal shape at switching moments.

The method proposed for calculation makes it possible to determine with fairly high accuracy the static and dynamic losses in power IGBTs for any type of semiconductor converter with any control law in Matlab. The method consists of polynomial interpolation of IGBT energy characteristics by the least squares method.

1.7. Approximation of IGBT energy characteristics taking into account the temperature

According to [49, 50], the results of the 3D-approximation of the energy voltage drops between the collector and the emitter depending on the magnitude of the current flowing and the temperature of the switch for a CM600DX-24T power transistor are given. The expressions presented enables to determine the static and dynamic losses in power switches of semiconductor converters of different topologies with different CS [51, 52] with computer modelling. The CM600DX-24T power transistor was selected for the research; its characteristics are given in table 1.8.

Table 1.8 – Boundary power characteristics of CM600DX-24T transistor

Parameters	Rating
Collector-emitter voltage U_{ces}, V	600
Gate-emitter voltage U_{ges}, V	±20
Collector current I_c, A	150
Collector power dissipation P_c, W	500
Junction temperature T_j, °C	+150
Storage temperature T_s, °C	–40 to +125
Isolation voltage U_i, VAC	2500
Screw Torque M, Nm	3.5
Zero gate voltage collector current I_{ces}, mA	1
Gate-emitter leakage current I_{ges}, nA	200
Gate-emitter threshold voltage $U_{ge(t)}$, V	6.7
Collector-emitter saturation voltage $U_{ge(s)}$, V	2.3
Input capacitance C_e, nF	12
Switch-on time T_{on}, μs	0.4
Switch-off time T_{off}, μs	0.5
Forward on voltage U_f, V	1.8
Reverse recovery time T_r, μs	0.35
Lead resistance R_l, mΩ	1.39
Thermal resistance R_t, °C/W	0.25
Contact thermal resistance R_c, °C/W	0.05

The basic energy dependencies in the current function and temperature of the module 2MBI150U2A-060 are shown in fig. 1.41.

As can be seen from fig. 1.41, *a*, with a switch current of 400 A, the voltage drop between the collector and the emitter lies in the range from 1.3 to 1.45 V.

By approximating the energy characteristics with the least squares method, the following polynomial dependencies were obtained for the characteristics of the switch at temperatures of 25 and 125 °C. For graphs describing the energy characteristics at a temperature of 25 °C:

$$U_{ce}\left(I_c; 25\,^{\circ}\mathrm{C}\right) = -754.78 \cdot I_c^4 + 495.27 \cdot I_c^3 - 112.56 \cdot I_c^2 + 15.67 \cdot I_c + 0.65; \quad (1.76)$$

$$U_{fw}\left(I_f; 25\,^{\circ}\mathrm{C}\right) = -544.87 \cdot I_f^4 + 388.92 \cdot I_f^3 - 96.72 \cdot I_f^2 + 13.04 \cdot I_f + 0.77; \quad (1.77)$$

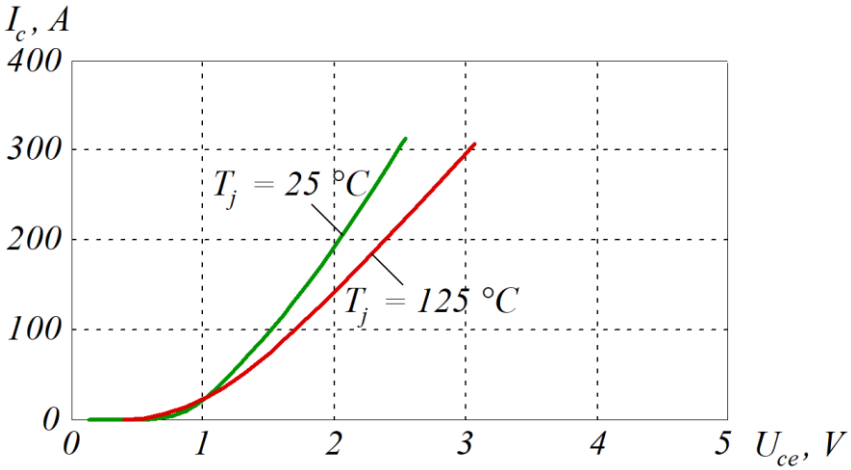

a

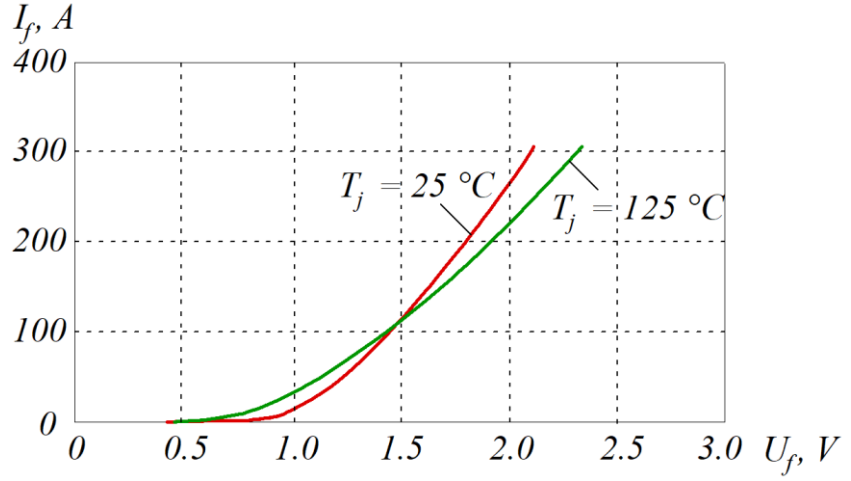

b

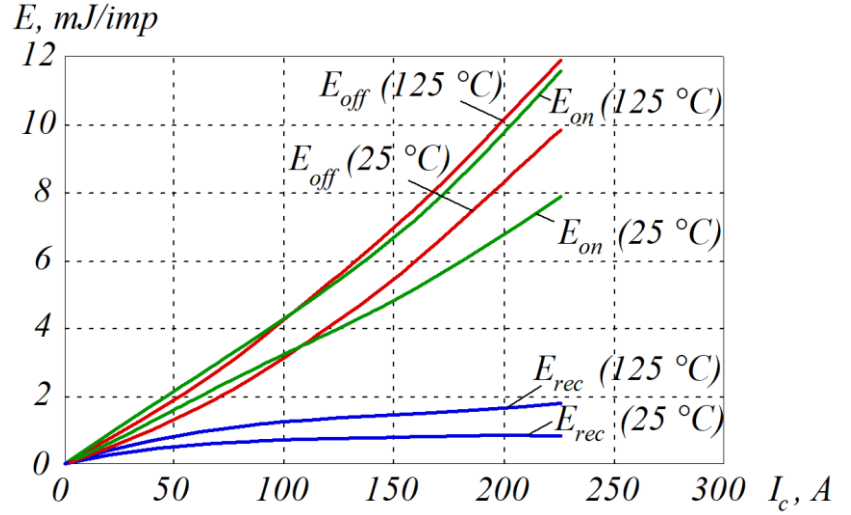

c

Figure 1.41 – Energy characteristics of module 2MBI150U2A-060:
a – CVC of transistor; *b* – CVC of by-pass diode; *c* – dependences of switch-on energy E_{on}, switch-off energy E_{off} and recovery energy of by-pass diode E_{rr} on switched current

$$E_{on}\left(I_c;25\,^{\circ}\mathrm{C}\right)=147.2\cdot I_c^3-23.618\cdot I_c^2+32.7\cdot I_c+0.0182; \quad (1.78)$$

$$E_{off}\left(I_c;25\,^{\circ}\mathrm{C}\right)=-41.523\cdot I_c^3+112.92\cdot I_c^2+20.687\cdot I_c+0.0216; \quad (1.79)$$

$$E_{rec}\left(I_f;25\,^{\circ}\mathrm{C}\right)=149.31\cdot I_f^3-74.937\cdot I_f^2+12.939\cdot I_f+0.0017. \quad (1.80)$$

For graphs describing the energy characteristics at a temperature of 125 ℃, the following expressions will be true:

$$U_{ce}\left(I_c;125\,^{\circ}\mathrm{C}\right)=-1005.9\cdot I_c^4+677.07\cdot I_c^3-156.39\cdot I_c^2+21.41\cdot I_c+0.53; \quad (1.81)$$

$$U_{fw}\left(I_f;125\,^{\circ}\mathrm{C}\right)=-798.78\cdot I_f^4+568.49\cdot I_f^3-141.58\cdot I_f^2+18.77\cdot I_f+0.48; \quad (1.82)$$

$$E_{on}\left(I_c;125\,^{\circ}\mathrm{C}\right)=394.34\cdot I_c^3-56.97\cdot I_c^2+44.487\cdot I_c+0.0153; \quad (1.83)$$

$$E_{off}\left(I_c;125\,^{\circ}\mathrm{C}\right)=55.074\cdot I_c^3+64.019\cdot I_c^2+35.379\cdot I_c-0.0127; \quad (1.84)$$

$$E_{rec}\left(I_f;125\,^{\circ}\mathrm{C}\right)=221.79\cdot I_f^3-107.46\cdot I_f^2+20.898\cdot I_f+0.0094. \quad (1.85)$$

The limitation of the obtained mathematical dependencies is that they describe energy characteristics only in the nominal range of currents. After interpolating the obtained dependencies for the graphs describing the energy characteristics at a temperature of 125 ℃, the following expressions will be true:

$$\begin{aligned}U_{ce}\left(I_c;t,^{\circ}\mathrm{C}\right)&=-1005.9\cdot I_c^4\cdot\left(2.496\cdot10^{-3}\cdot t+0.688\right)+\\&+677.07\cdot I_c^3\cdot\left(2.685\cdot10^{-3}\cdot t+0.664\right)-156.39\cdot I_c^2\cdot\left(2.81\cdot10^{-3}\cdot t+0.649\right)+\\&+21.408\cdot I_c\cdot\left(2.679\cdot10^{-3}\cdot t+0.665\right)+0.5288\cdot\left(-2.288\cdot10^{-3}\cdot t+1.286\right); \quad (1.86)\end{aligned}$$

$$\begin{aligned}U_{fw}\left(I_f;t,^{\circ}\mathrm{C}\right)&=-798.78\cdot I_f^4\cdot\left(3.178\cdot10^{-3}\cdot t+0.603\right)+\\&+568.49\cdot I_f^3\cdot\left(3.159\cdot10^{-3}\cdot t+0.605\right)-141.58\cdot I_f^2\cdot\left(3.168\cdot10^{-3}\cdot t+0.604\right)+\\&+18.764\cdot I_f\cdot\left(3.049\cdot10^{-3}\cdot t+0.619\right)+0.4792\cdot\left(-6.127\cdot10^{-3}\cdot t+1.766\right); \quad (1.87)\end{aligned}$$

$$E_{on}(I_c;t,°C)=394.34\cdot I_c^3\cdot(6.27\cdot10^{-3}\cdot t+0.22)-$$
$$-56.97\cdot I_c^2\cdot(5.85\cdot10^{-3}\cdot t+0.27)+44.487\cdot I_c\cdot(2.649\cdot10^{-3}\cdot t+0.669)+$$
$$+1.53\cdot10^{-2}\cdot(-1.895\cdot10^{-3}\cdot t+1.237); \quad (1.88)$$

$$E_{off}(I_c;t,°C)=55.07\cdot I_c^3\cdot(1.754\cdot10^{-2}\cdot t-1.19)+64.02\cdot I_c^2\cdot(-7.64\cdot10^{-3}\cdot t+1.95)+$$
$$+35.379\cdot I_c\cdot(4.152\cdot10^{-3}\cdot t+0.48)-1.27\cdot10^{-2}\cdot(2.71\cdot10^{-2}\cdot t-2.376); \quad (1.89)$$

$$E_{rec}(I_f;t,°C)=221.79\cdot I_f^3\cdot(3.27\cdot10^{-3}\cdot t+0.59)-107.46\cdot I_f^2\cdot(3.03\cdot10^{-3}\cdot t+0.62)+$$
$$+20.898\cdot I_f\cdot(3.81\cdot10^{-2}\cdot t+0.524)+9.4\cdot10^{-3}\cdot(1.18\cdot10^{-2}\cdot t-0.476). \quad (1.90)$$

The results of calculating the current-voltage characteristics at intermediate temperatures of 25, 50 and 125 °C are shown in fig. 1.42.

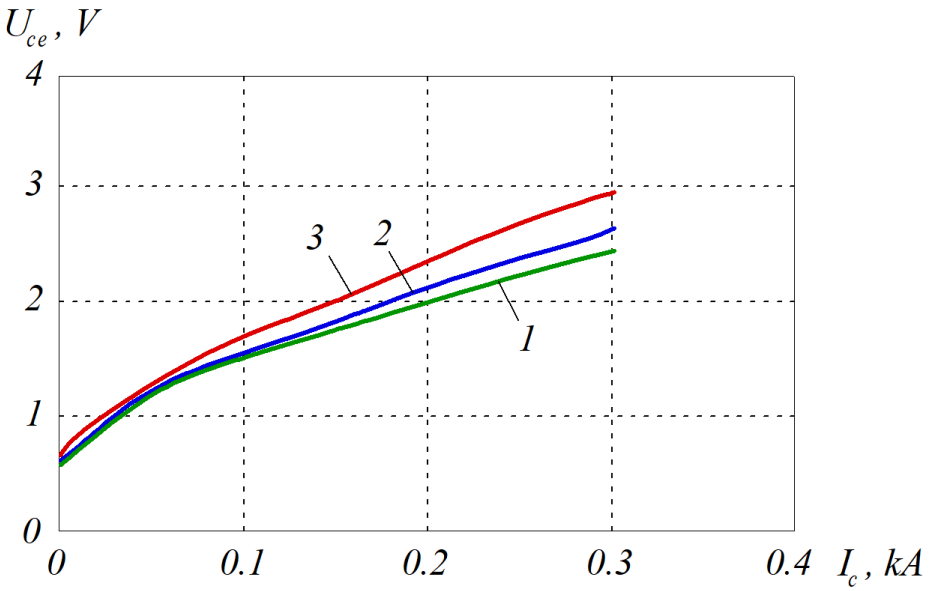

Figure 1.42 – Current-voltage characteristics by temperature:
1 – 25 °C; *2* – 50 °C; *3* – 125 °C

To numerically estimate the effect of temperature on power losses in the frequency converter, a model was built in Matlab; this model is presented in fig. 1.43.

The main parameters of the model are given in table 1.9.

The content of the sub-module for calculating static and dynamic power losses in the transistor part and the by-pass diode is shown in fig. 1.44.

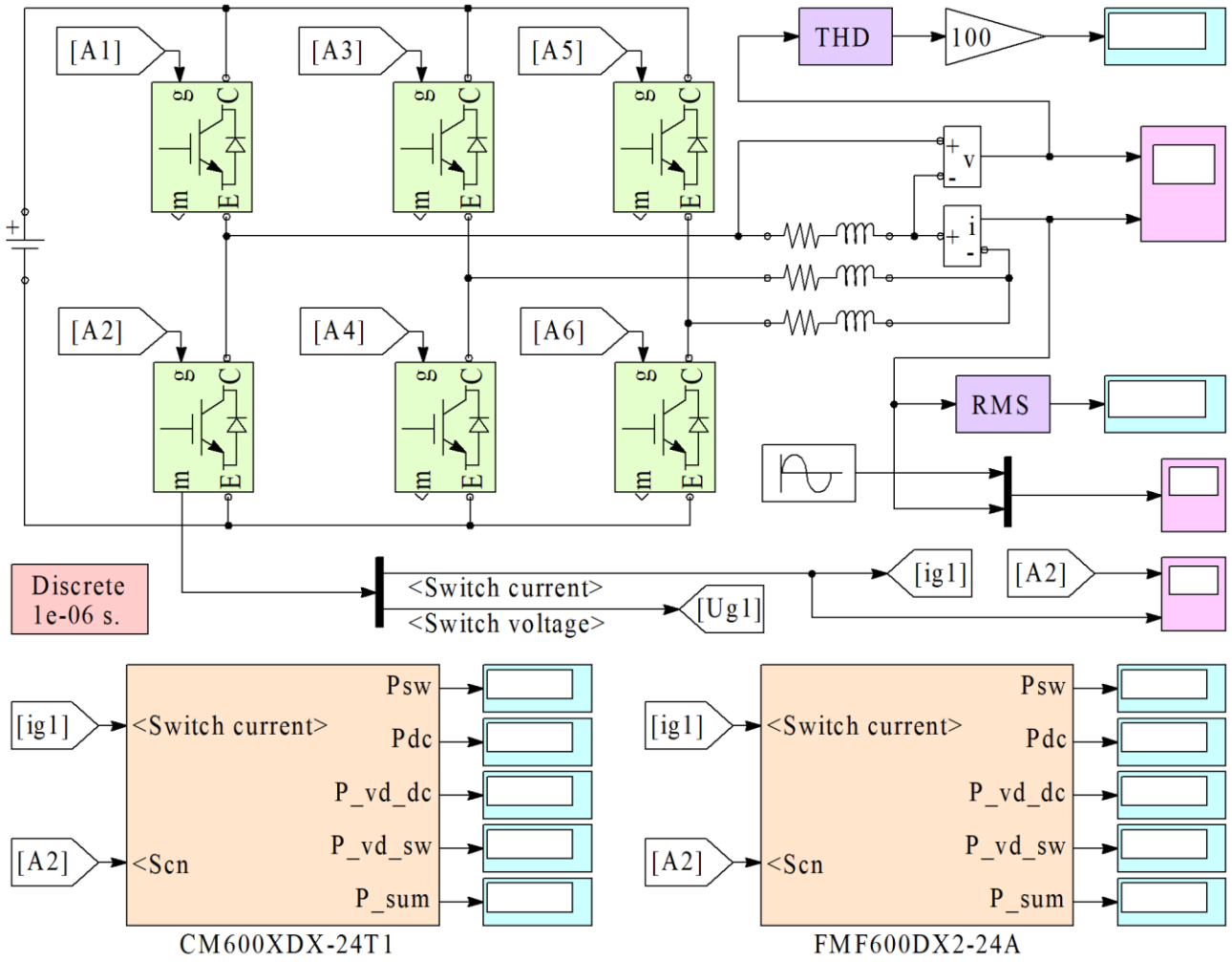

Figure 1.43 – AVI model with loss calculation module

Table 1.9 – Main parameters of the frequency converter model

Parameter	Value
Voltage in DC circuits, V	600
Active load resistance, Ohm	0.617
Load inductance, mH	1
Modulation type	Sinusoidal PWM
Modulation frequency, kHz	1…16

The results of modelling power losses at temperatures of 25 and 125 ℃ are given in table 1.10.

The results of modelling losses in the frequency converter at a temperature of 125 ℃ are given in table 1.11.

Graphical dependences of the total power losses in the power switches of the inverter depending on the switching frequency at temperatures of 25 and 125 ℃ are shown in fig. 1.45.

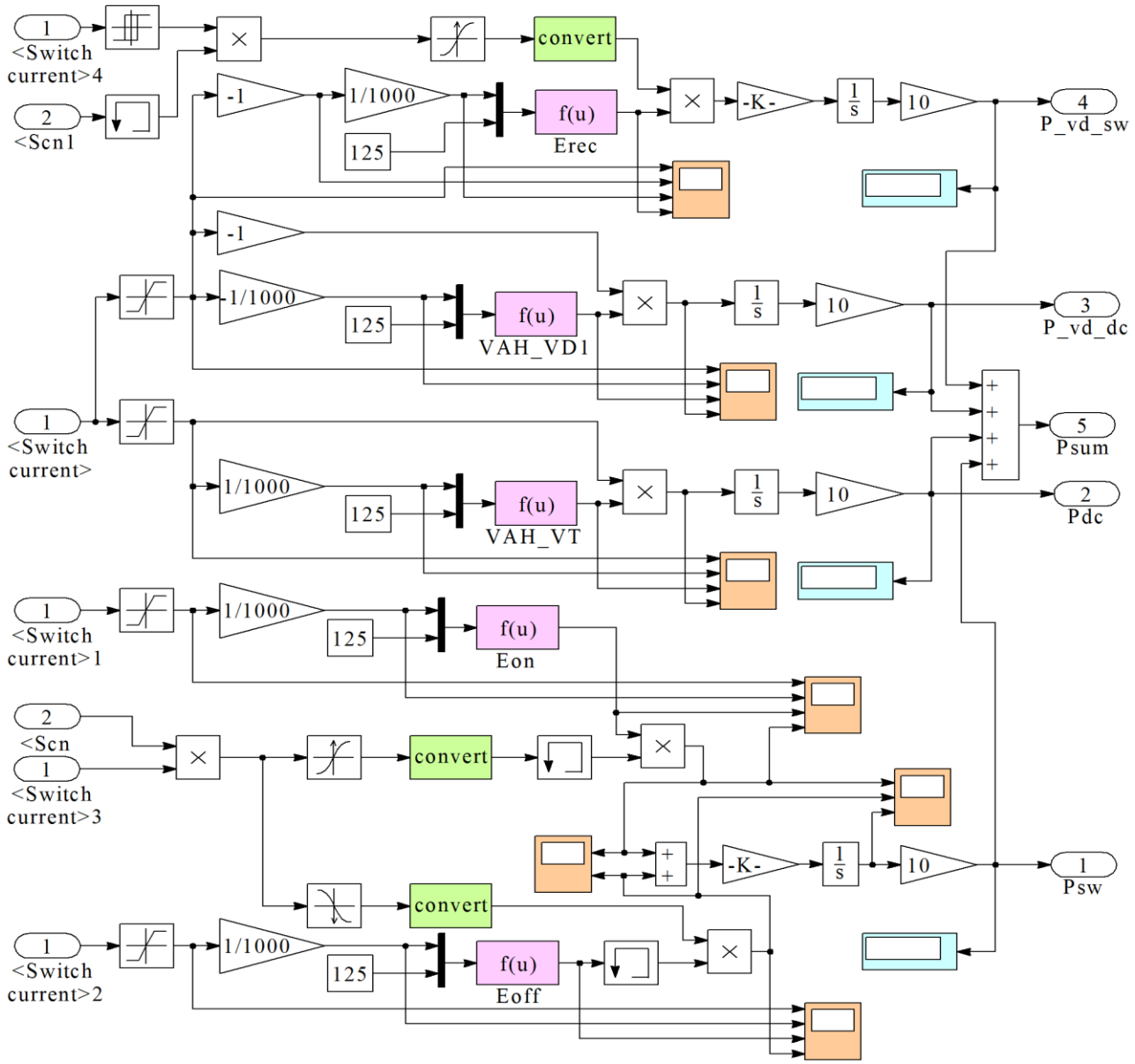

Figure 1.44 – Sub-module for calculating static and dynamic power losses

Table 1.10 – Dependence of power losses in power switches

f, kHz	I_{RMS}, A	P_{VT}, W			P_{VD}, W			P_{Σ}, W	P_{loss} inverter	P_{in}	Efficiency
		SW	*Con.*	*T*, °C	*SW*	*Con.*	*T*, °C				
1	150	4.97	108.68	53.40	0.35	15.73	32.39	129.69	778.17	47902	98.375
2	150	9.87	108.57	54.61	0.68	15.76	32.56	134.87	809.24	47832	98.308
4	150	19.64	108.35	57.00	1.33	15.76	32.86	145.08	870.50	47801	98.179
6	150	29.46	108.45	59.48	1.98	15.80	33.18	155.69	934.14	47801	98.045
8	150	39.29	108.47	61.94	2.63	15.78	33.47	166.18	997.07	47844	97.916
10	150	49.06	108.51	64.39	3.28	15.78	33.77	176.63	1059.79	47860	97.785
12	150	58.45	108.49	66.73	3.90	15.79	34.06	186.63	1119.76	47795	97.657
14	150	67.34	108.67	69.00	4.52	15.83	34.36	196.35	1178.13	47871	97.539
16	150	78.36	108.21	71.64	4.93	15.72	34.50	207.21	1243.28	47796	97.398

Table 1.11 – Losses in three-phase AVI at switch temperature 125 °C

P_{VT}, W			P_{VD}, W			P_{Σ}, W	P_{loss} inverter	Efficiency
SW	*Con.*	*T*, °C	*SW*	*Con.*	*T*, °C			
6.50	124.80	–	0.70	15.90	–	147.90	887.39	98.147
12.95	124.72	–	1.34	15.95	–	154.96	929.75	98.056
25.84	124.45	–	2.63	15.95	–	168.87	1013.21	97.880
38.78	124.56	65.84	3.92	15.99	34.16	183.25	1099.52	97.699
51.74	124.60	69.09	5.20	15.97	34.74	197.52	1185.09	97.523
64.62	124.62	72.31	6.50	15.97	35.34	211.71	1270.28	97.345
76.99	124.60	75.40	7.72	15.98	35.90	225.30	1351.81	97.171
88.73	124.82	78.39	8.94	16.02	36.48	238.51	1431.08	97.010
103.24	124.27	81.88	9.73	15.90	36.79	253.15	1518.88	96.822

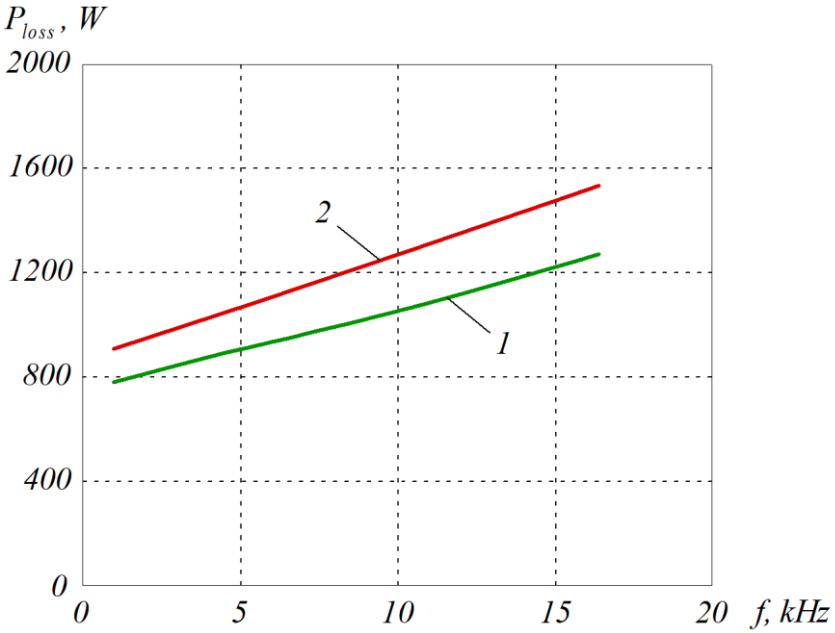

Figure 1.45 – Dependence of power losses on temperature:
1 – 25 °C; *2* –125 °C

The modelling showed that depending on the temperature mode, the power losses in the switches change quite significantly – 14...22 %. Thus, it is demonstrated that the effect of the temperature mode on the accurate calculation of power losses is rather important.

CHAPTER 2

ACTIVE FOUR-QUADRANT RECTIFIERS WITH POWER FACTOR COMPENSATION

2.1. Combined operation of a three-phase diode and active rectifiers

At present, DC traction power supply systems are physically and morally obsolete. Most often, such systems include two step-down traction rectifiers, three-phase diode or thyristor rectifiers and passive output filters (fig. 2.1).

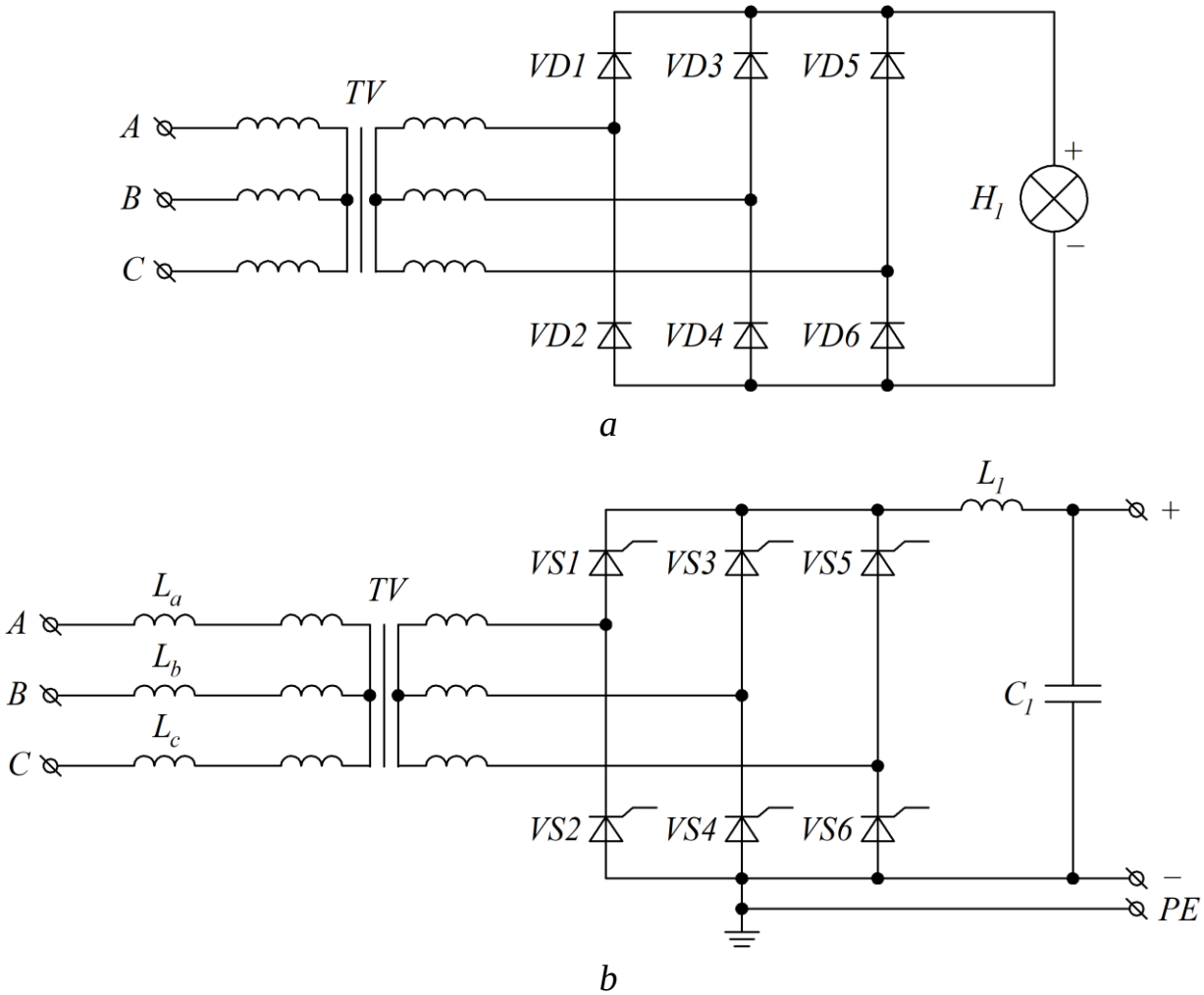

Figure 2.1 – Diagram of DC traction power supply:
a – with three-phase diode rectifier; *b* – with three-phase thyristor rectifier

To reduce the ripple of the rectified voltage, a reactor with an inductance of 4.5 mH and a filter device consisting of resonant circuits at 300, 400, 600, 900, 1200 Hz are provided.

Existing DC traction power supply systems are characterized by a number of disadvantages, among which are: low power factor, significant level of emission of higher harmonics of the current to the power supply network, lack of possibility of voltage stabilization, as well as lack of regeneration energy from the traction network to the general industrial network. Each of the above-mentioned factors leads to significant economic costs.

Thus, higher current harmonics cause additional losses in the active resistance of the conductors [53]. Low power factor (estimated value from 0.75 to 0.8) leads to additional reactive power costs. And the lack of possibility to adjust and stabilize the voltage level in the overhead system leads to voltage drops. Under this condition, the consumer (electric locomotive), when the supply voltage is reduced, consumes a higher current to ensure a given speed, which leads to higher additional power losses in the catenary.

To stabilize the voltage in the contact network of the DC traction power supply system, thyristor voltage boosters (VB) are used. The voltage booster is a power converter device connected in series with the load, which provides an additional voltage added to the voltage of the main power supply, in case of its subsidence, or subtracted from it when it rises during the regeneration [54].

The series connection of the three-phase diode rectifier and the VB makes it possible to stabilize the overhead line. In addition, an increase in the electrical energy quality is provided. The disadvantages of such a technical solution include the lack of possibility of energy regeneration at PSs, as well as an insufficiently high value of the power factor. The VB regulates voltage from 0 to 450 V. It is possible to increase the value of the power factor of the PS by adding a three-phase APF on the side of alternating current (fig. 2.2). The advantage of this technical solution is the almost complete elimination of reactive power and higher current harmonics in the consumed energy. However, the disadvantage of such a solution is the lack of voltage stabilization in the overhead system and lack of possibility of energy regeneration.

A rather promising technical solution is the replacement of diode and thyristor rectifiers with active voltage rectifiers with power factor compensation. The advantage of such a technical solution is the provision of the most complete functionality, namely: the provision of a power factor close to one, a low level of emission of higher harmonics of the current to the power supply network, the possibility of regulating and stabilizing the voltage in the overhead system. However, the disadvantage of such a technical solution is the higher cost (compared to other technical solutions) and the need to provide a rather high switching frequency of power switches (from one to several kilohertz), which leads to a relatively low efficiency (estimated value is 0.95).

Each of the above-mentioned technical solutions has its drawbacks and cannot be considered as a complete solution to the existing technical problem. The combined operation of a three-phase diode rectifier and an APF is promising.

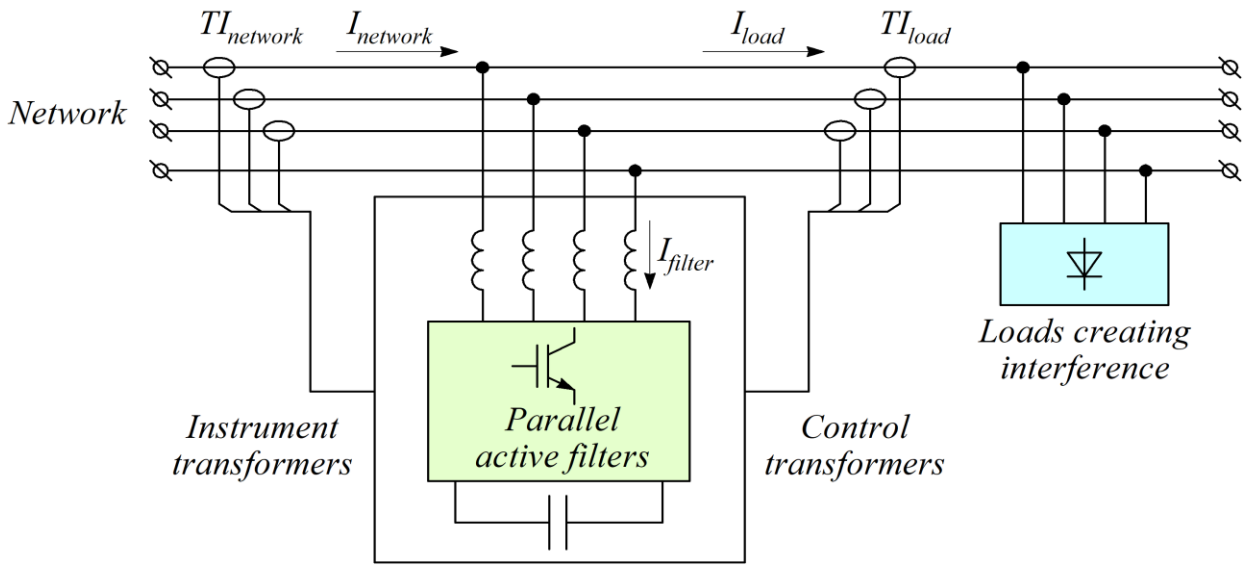

Figure 2.2 – APF connection diagram

To improve the electric energy quality and reduce the losses from voltage drop of the power supply system built on a six-pulse diode rectifier, it will be advisable to use the combined operation of the APF, which additionally operates in the mode of a voltage booster (fig. 2.3).

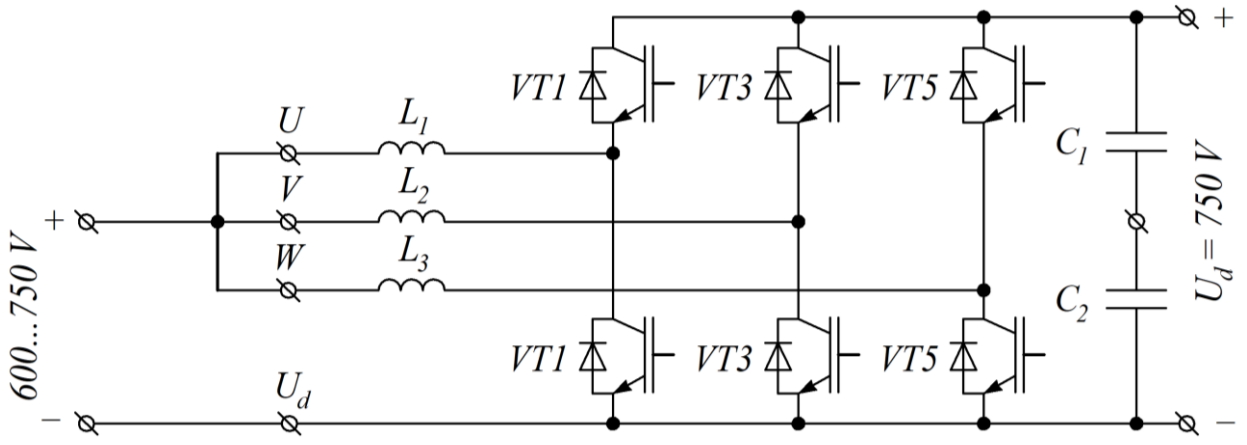

Figure 2.3 – Circuit of combined operation of APF

This technical solution combines the advantages of the VB and the APF. Most of the energy (about 20 %) to the overhead network is supplied through a three-phase diode rectifier that has high efficiency.

Since a six-pulse diode rectifier has a high efficiency (≈ 99 %), but a low power factor (≈ 76 %), and an AVR, on the contrary, has a low efficiency (≈ 96 %), but a high power factor (≈ 99 %), this combination in the power supply system will significantly increase the efficiency and power factor of the power supply system. The AVR increases the voltage, thereby making it possible to provide bi-directional power transmission without changing the polarity of the output voltage, which is a significant advantage for the converter.

The structural diagram of the combined automatic control system VB–APF is shown in fig. 2.4.

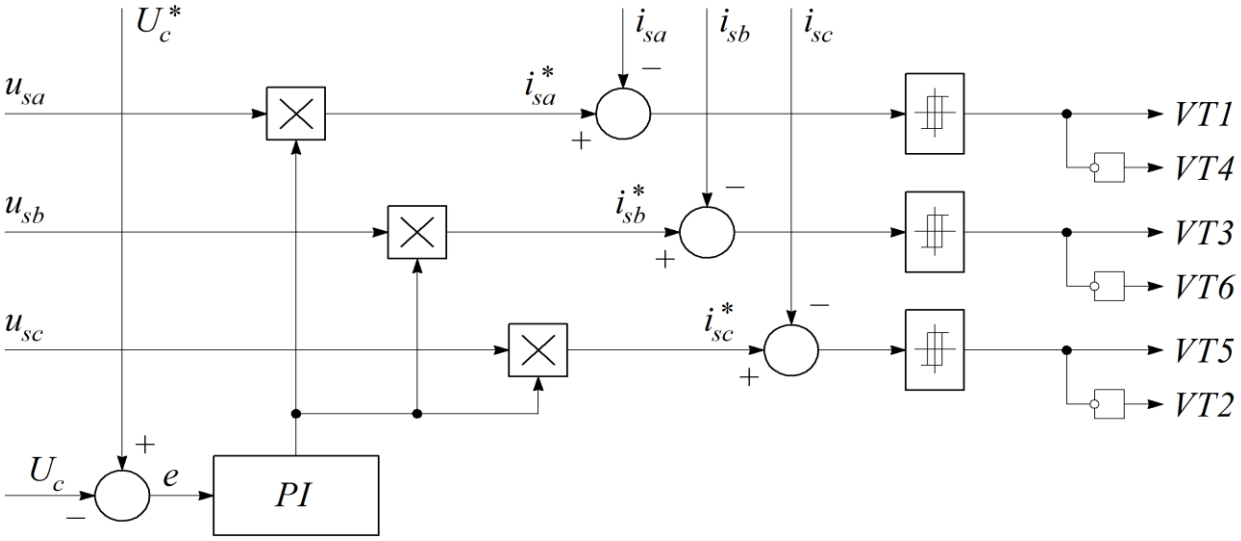

Figure 2.4 – Circuit of automatic control system of VB–APF

To confirm the effectiveness of the proposed solution, a simulation model of a PS built on a diode bridge connected as a VB of the active voltage rectifier was developed in Matlab.

The developed model consisted of the following components: three-phase power supply network, six-pulse rectifier, input filter, smoothing device, VB, R-load, voltage and current meter.

The PS model with VB is shown in fig. 2.5.

Parameters of the simulation model of a PS with a VB are given in table 2.1.

The CS uses feedbacks on the output current and output voltage with the use of a regulator to obtain a signal on the switch-on of the VB and regeneration. Feedback signals with the task signal are supplied to the output voltage regulator.

The task signal in the CS is formed directly in the system of *abc*-coordinates by extracting the first harmonics of phase voltages or by applying the transformations of the coordinate systems *abc* to other coordinate systems: *αβ0*, *pqr*, *dqo*.

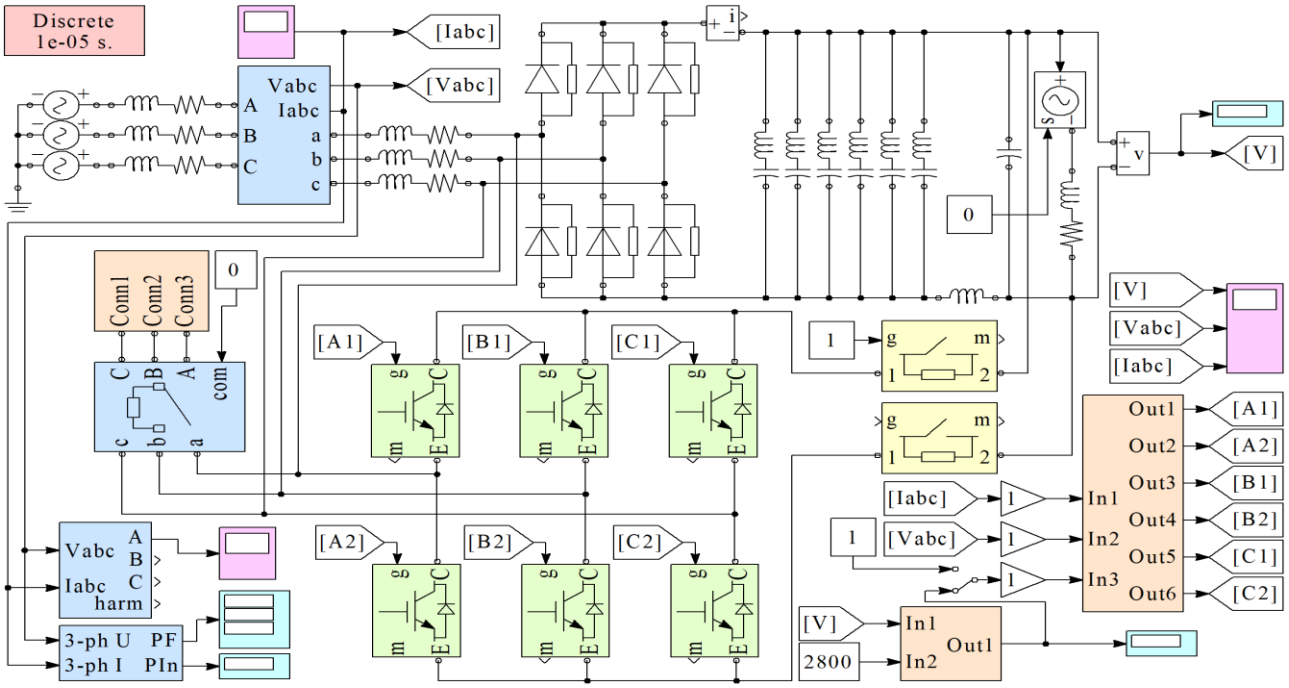

Figure 2.5 – PS model with VB

Table 2.1 – Parameters of simulation model of PS with VB

Parameter	Value
Mains voltage, V	3300
Power, kV·A	10000
Average rectification voltage, V	4000
Inlet throttle inductance, mH	0.9
Inlet throttle resistance, Ohm	0.04
Pulsatility	6
Equivalent active load resistance, Ohm	3
Equivalent load inductance, mH	3.3

In the CS of the VB with PWM the inconsistency signal Δi, obtained between the phase current task signal and the phase voltage of the network, are compared with a sawtooth signal of the PWM, the frequency of which exceeds the frequency of the network by several orders of magnitude. The sawtooth signal has a constant amplitude and frequency, which leads to the operation of the switches at a fixed switching frequency. The form of signals in the CS is shown in fig. 2.6. The forms of input phase voltages and phase currents of the six-pulse rectifier with and without the VB connection are shown in fig. 2.7. Also, the use of the VB in the mode of operation of the AVR makes it possible to carry out bi-directional energy transfer. Oscillograms of phase voltages and currents in the regeneration mode are shown in fig. 2.8.

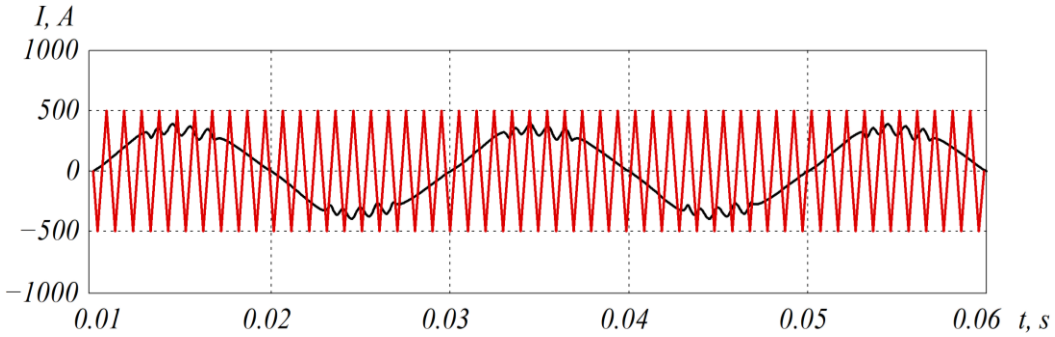

Figure 2.6 – Form of signals in CS

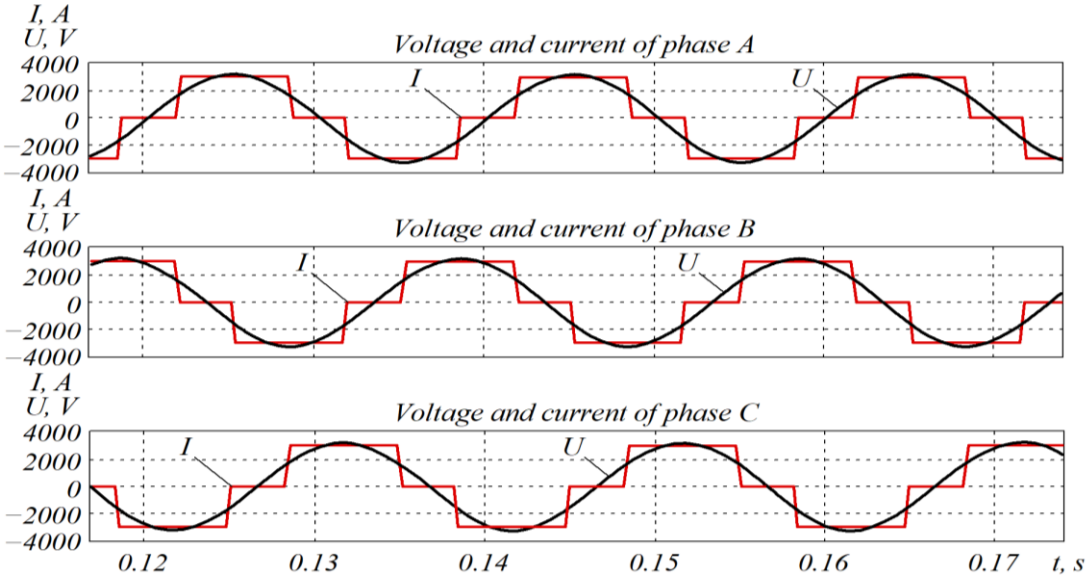

a

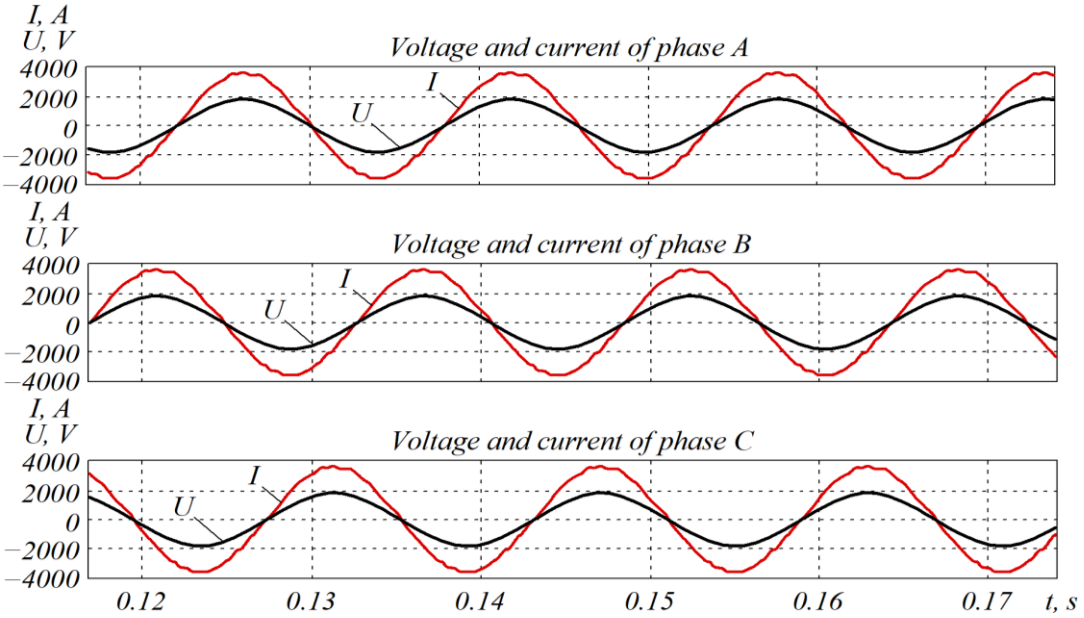

b

Figure 2.7 – Forms of input phase voltages and currents:
a – without VB; *b* – with VB

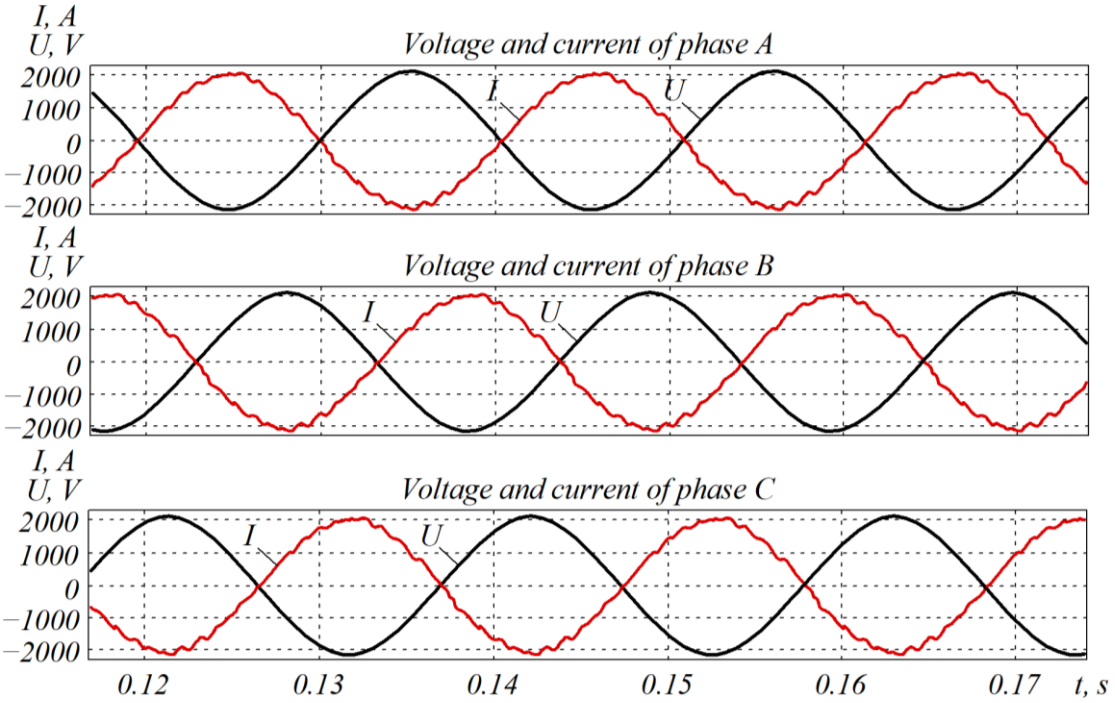

Figure 2.8 – Forms of input phase voltages and currents in the regeneration mode

Output voltage oscillograms with and without the VB connection are shown in fig. 2.9.

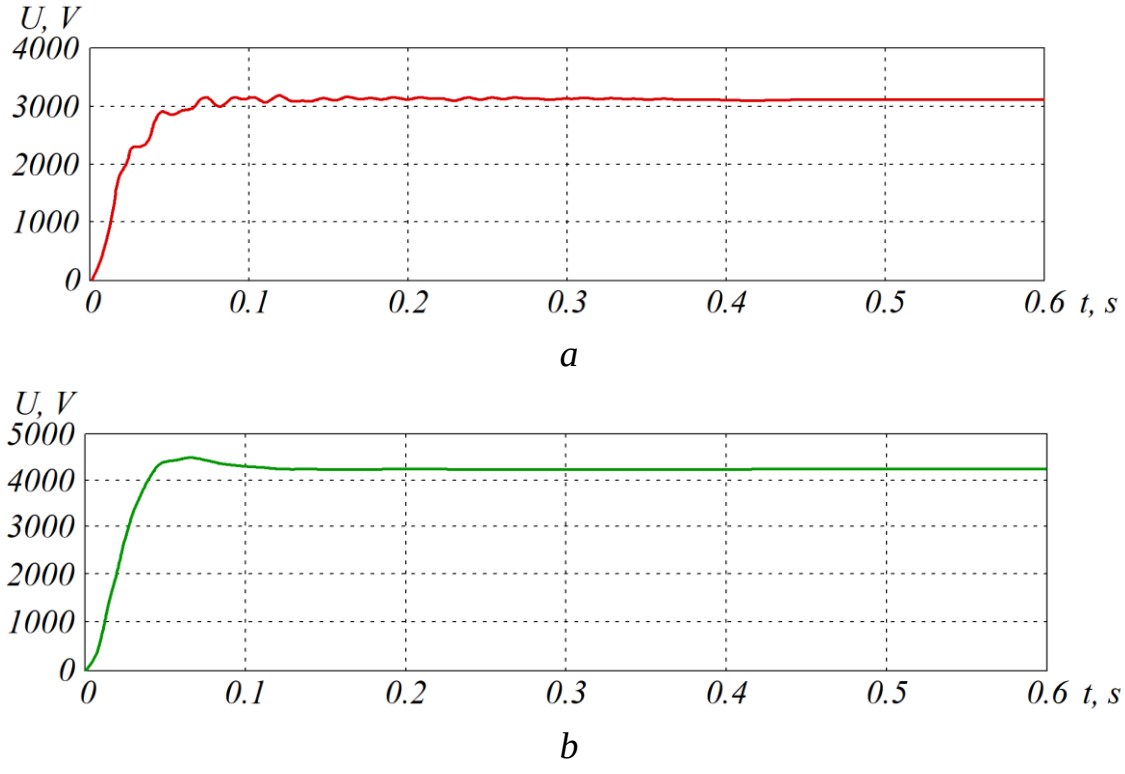

Figure 2.9 – Oscillograms of output voltage:
a – without VB; *b* – with VB

In the process of simulation, the dynamic mode and the EMC parameters were studied: power factor and the THD of phase current. The THD of the input currents with and without the VB connection is shown in fig. 2.10. Ripple factors of the output voltage with and without the VB connection are shown in fig. 2.11.

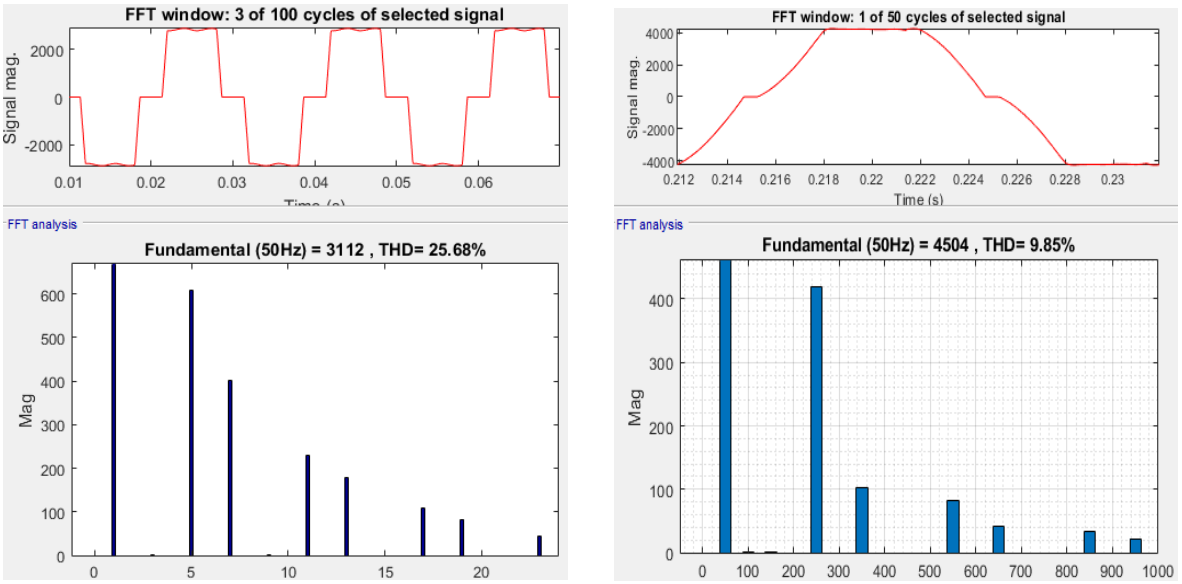

a *b*

Figure 2.10 – THD of input current:
a – without VB; *b* – with VB

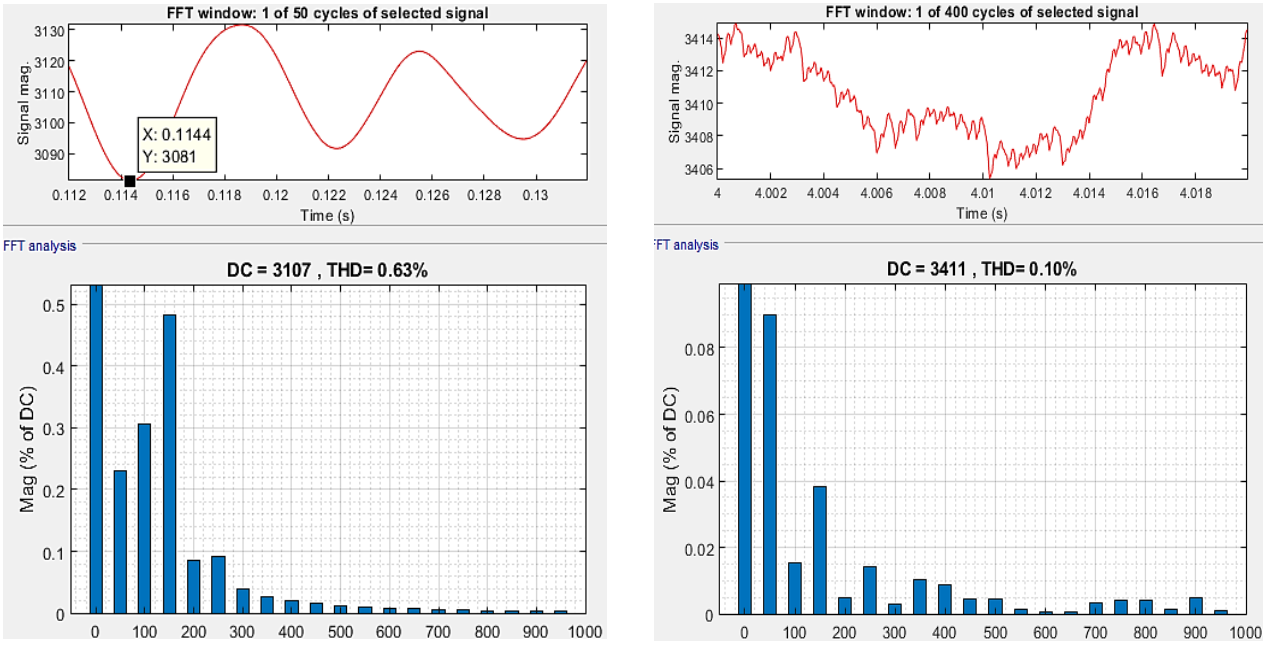

a *b*

Figure 2.11 – THD of output voltage:
a – without VB; *b* – with VB

Taking into account the higher harmonics in the phase voltage and current, the power factor is calculated according to the expression:

$$PF = \frac{I_{1RMS}}{I_{RMS}} \cdot \frac{U_{1RMS}}{U_{RMS}} \cdot \cos\varphi. \qquad (2.1)$$

In the simulation model, the power factor meter is made in accordance with expression (2.1) and implemented in the subsystem shown in fig. 2.12.

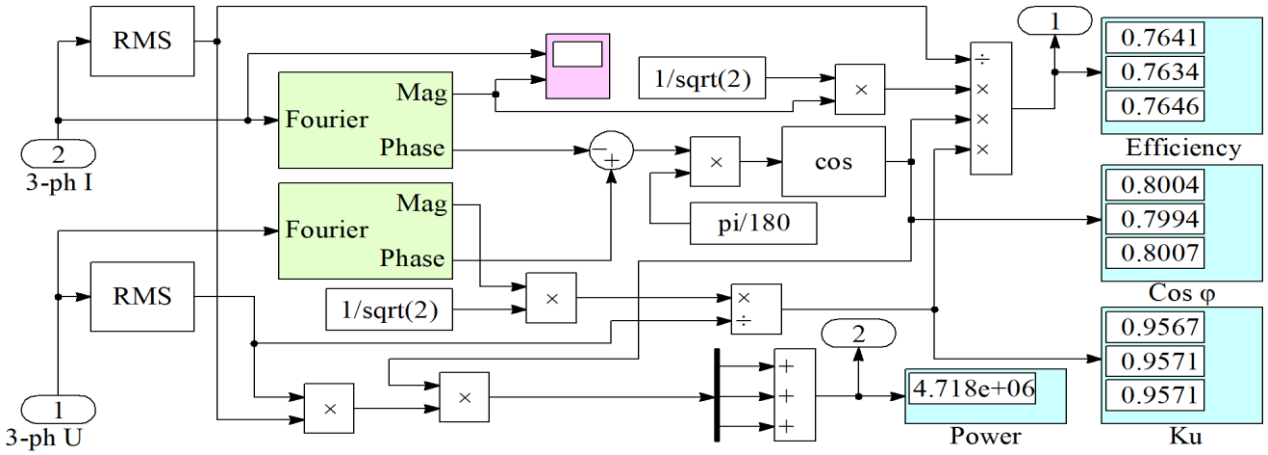

a

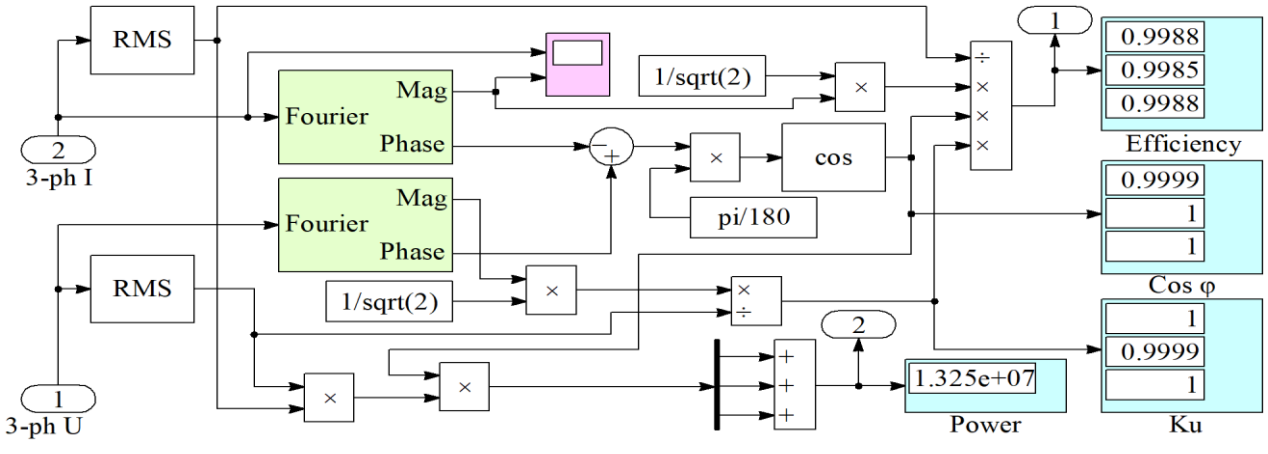

b

Figure 2.12 – Subsystem of power factor calculation:
a – without VB; *b* – with VB

The measured power factor with the VB connection reaches 99.88 %, and without a VB – 76.41 %. To calculate the efficiency of the power supply system, the losses of the existing power supply system were estimated and calculated using the AVR as the VB. Calculation of losses of all components of the power supply system at S_n = 10 MV·A, U_{DC} = 3.3 kV, I_{DC} = 3150 A, cosφ = 0.8 is given in table 2.2.

Table 2.2 – Losses of existing power system using AVR as VB

Components of losses	Active power losses of existing power system		Active power loses of upgraded power system	
	ΔP, kW	ΔP, %	ΔP, kW	ΔP, %
ETL 110 (AC-70)	209.09	4.3	209.09	2.2
Transformer 110/10 kV (TDN-10000/110)	58	1.19	58	0.91
Transformer 10/3.3 kV (TMPU-16000/10GY)	73	1.505	73	0.98
Traction rectifier UVKE-1	66	1.36	66	1.03
AVR with IGBT series CM750HG-130R	–	–	286.01	2.5
Overhead system 3.3 kV (AC-240)	1804	29.21	1804	12.39
Smoothing device	27	0.55	27	0.42
Electric locomotive (1100 A, 3 Ohm)	2611	62	3780	80
Total	4848.09	100	5867.09	100

The efficiency of the power supply system is calculated by the expression:

$$\eta = \frac{P_c - \Delta P_{pl} - \Delta P_i - \Delta P_{t1} - \Delta P_{t2} - \Delta P_{cn} - \Delta P_{ERS}}{P_c}, \quad (2.2)$$

where P_c – the total power, kW; ΔP_{pl} – the power loss in the 110 kV ETL (total in industry), kW; ΔP_i – the power loss in the rectifier, kW; ΔP_{t1} – the power loss in the transformer (110/10 kV), kW; ΔP_{t2} – the power loss in the transformer (10/3.3 kV), kW; ΔP_{cn} – the power loss in the overhead line (3.3 kV), kW; ΔP_{ERS} – the power loss in the electric rolling stock (ERS), kW.

Calculation of efficiency for the existing power supply system:

$$\eta_1 = \frac{10000 - (4848.09 - 2611)}{10000} \cdot 100 = 77.63\,\%. \quad (2.3)$$

Calculation of the efficiency for the power supply system with the AVR connected as the VB:

$$\eta_2 = \frac{10000 - 209.09 - 58 - 73 - 66 - 286.01 - 1804 - 27}{10000} \cdot 100 = 98\,\%. \qquad (2.4)$$

Thus, with the use of the VB, additional active power losses for switching IGBT switches are added – 2.5 %, but additional losses for voltage drop are reduced, and 80 % of the power is transferred to the load (electric locomotive), as a result of which the efficiency of the power system increases.

Table 2.3 shows a comparative characteristic of the existing energy system with a six-pulse rectifier and the energy system with the AVR connected as the VB.

Table 2.3 – Comparative characteristics of energy systems

Parameter	Existing power system with six-pulse rectifier	Energy system with AVR as VB
Efficiency of power supply system, %	78	98
Rectifier efficiency, %	99	97
THD of PS input current, %	25.68	9.85
Voltage ripple coefficient in overhead network, %	0.63	0.20
Power factor of PS, %	76.41	99.8
Ripple amplitude of output voltage, V	51	1.8
Possibility of regeneration	None	Possible
THD in regeneration mode, %	–	3.23
Power factor in regeneration mode, %	–	–99.8
Electrical energy transmission	Unidirectional	Bi-directional

The application of VBs is economically and technically advantageous, as the voltage drop losses are reduced, the quality of electrical energy is improved and the efficiency of the power supply system is increased.

2.2. Three-phase active compensation rectifiers with power factor compensation

There are quite a few ways to improve the EMC of rectifier plants with power supply networks [55, 56]. Among them two directions are fundamentally noted: the creation of new rectifier converters that provide higher EMC performance, and the

modernization of existing rectifiers with additional technical devices. Such technical devices are passive, active and hybrid filters, voltage booster converters, etc. Among promising rectifier installations that provide higher EMC performance are active rectifiers with power factor compensation.

At the same time, there are quite a number of options for the circuit implementation of active rectifiers: single-switch circuits, Vienna-rectifier circuit, active current rectifiers and active voltage rectifiers. The most promising of them are active voltage rectifiers.

The most common CS of AVRs are based on hysteresis modulation (fig. 2.13). Hysteresis modulation provides quite high EMC characteristics with a power supply network and an overhead network, but causes quite high switching frequencies of switches, from a few tens to hundreds of kilohertz.

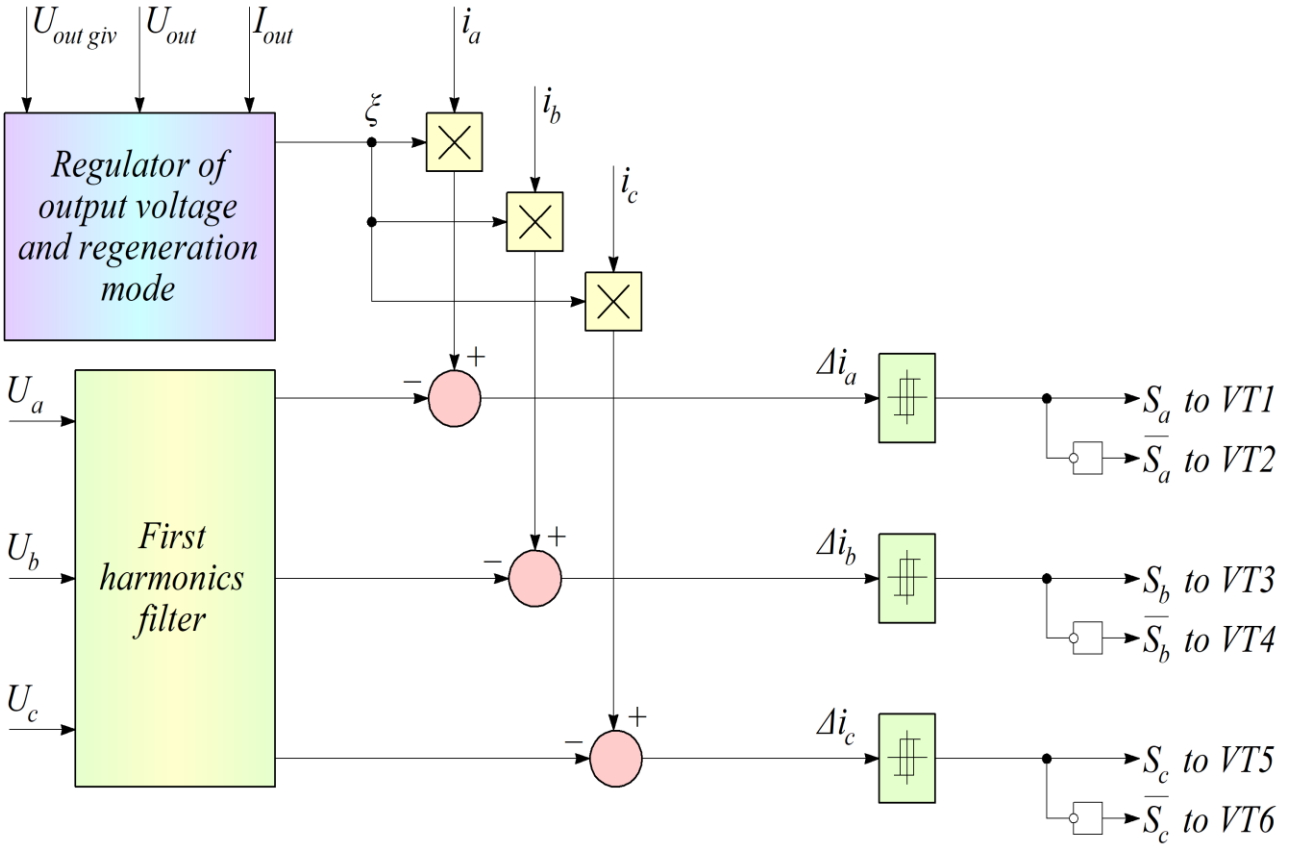

Figure 2.13 – CS of AVR with hysteresis modulator

The advantage of the AVR with hysteresis CS is the implementation of a high EMC level: *THD* < 5 %; power factor *PF* > 99 %, two-way transmission, as well as the possibility to adjust the output voltage [57, 58]. However, this CS causes a high switching frequency (from several tens to hundreds of kilohertz), which changes and is unknown at the design stage.

A significant advantage of the CS of the AVR based on PWM is the implementation of significantly lower switching frequencies (fig. 2.14).

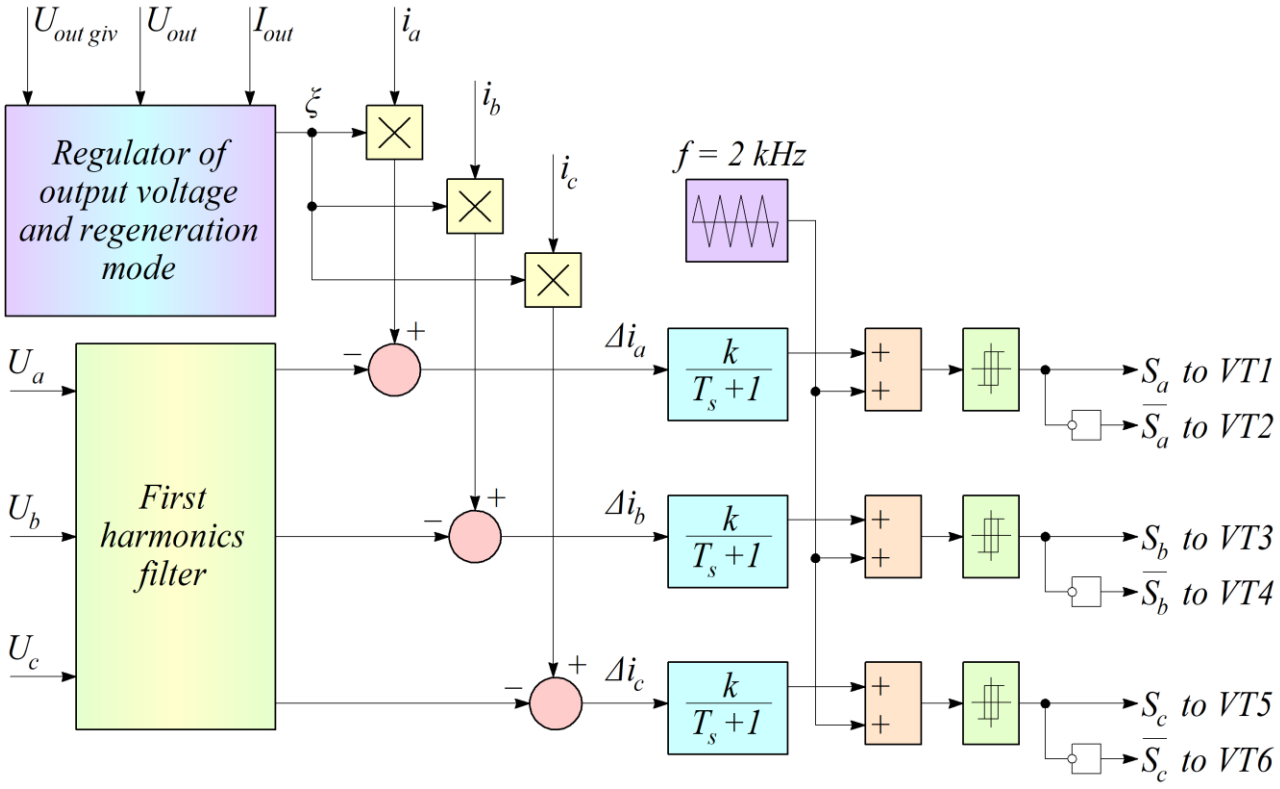

Figure 2.14 – CS of AVR with PWM

There are a number of electromechanical systems in which several rectifier units are powered from a single AC mains [59, 60]. Such systems are DC PSs, electric locomotive traction drives, etc. For these systems, the use of compensators is promising (fig. 2.15, 2.16).

The CS of the compensatory AVR is shown in fig. 2.17, in which the channels are synchronized with individual bridges with the shift of the PWM reference signal at an angle of ψ.

This makes it possible to mutually compensate higher harmonics of phase currents and output voltage of individual bridges, which improves the power quality indicators.

A significant advantage of the compensatory AVR is better indicators of electricity quality and reduced switching frequency of the switches.

The concept of compensation of higher harmonics in the phase current with individual bridges is shown in fig. 2.18.

Fourier analysis of the compensation AVR currents, consisting of two bridges, with a switching frequency of 2 kHz is shown in fig. 2.19.

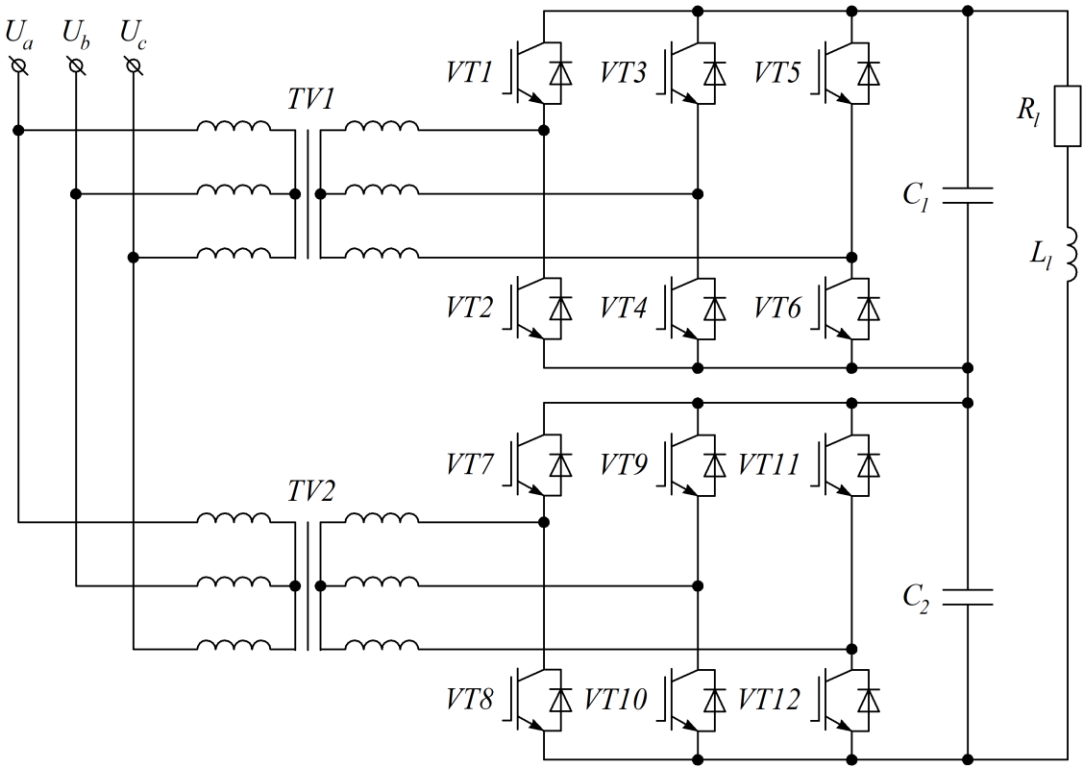

Figure 2.15 – Compensation AVR with series connection of bridges

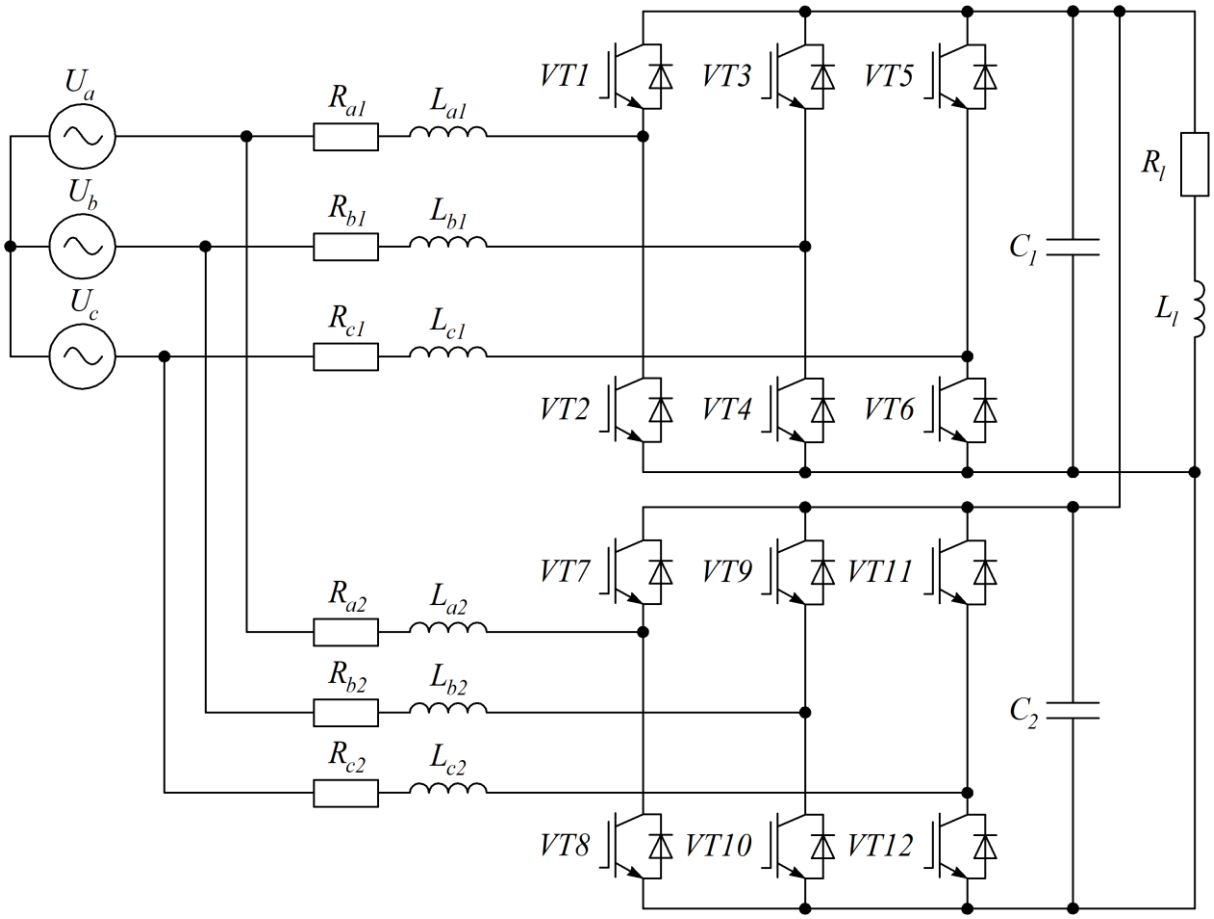

Figure 2.16 – Compensation AVR with parallel connection of bridges

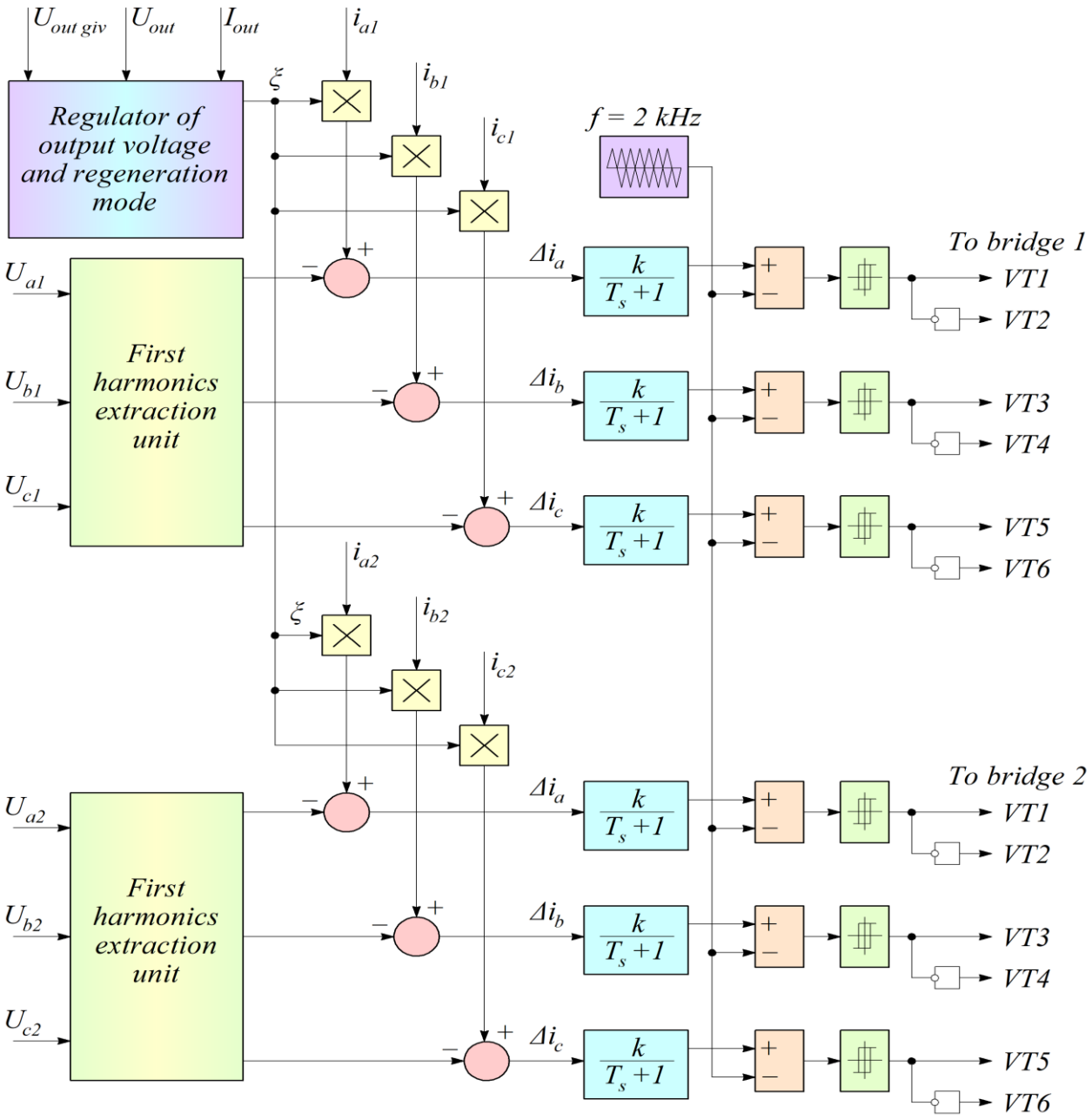

Figure 2.17 – CS of compensatory AVR

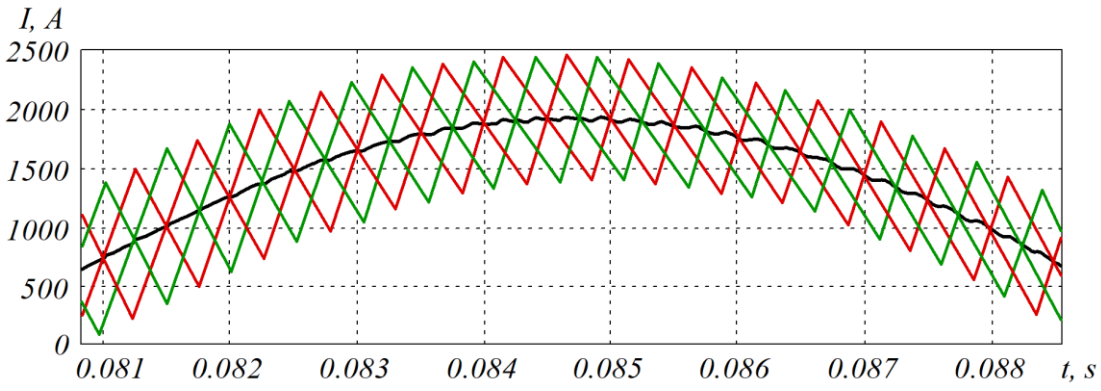

Figure 2.18 – Oscillogram of current consumed by individual bridges

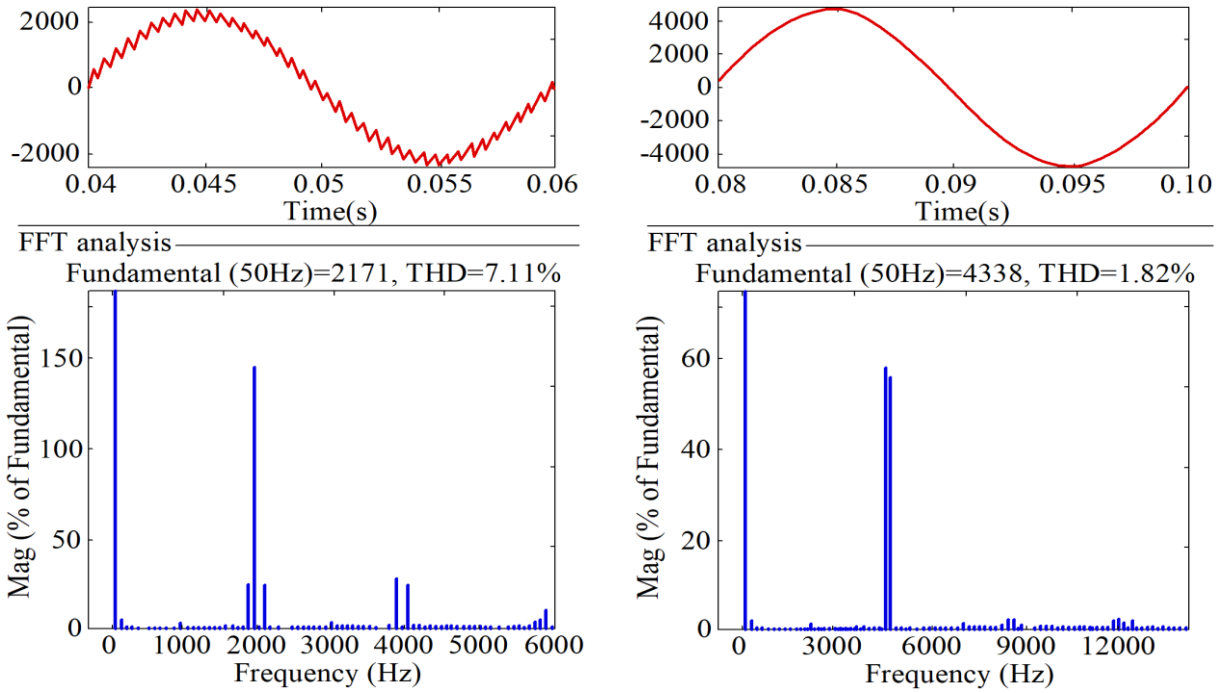

Figure 2.19 – Fourier analysis of currents of compensation AVR:
a – phase current of one bridge; *b* – total consumed current

Table 2.4 shows the EMC parameters of compensation active rectifiers at different number of parallel bridges.

Table 2.4 – EMC parameters of compensation active rectifiers

Electricity quality indicators	Value								
Number of bridges of compensation AVR	2	3	4	2	3	4	2	3	4
Switching frequency, kHz	0.5			1			2		
Power factor, %	99.48	99.59	99.62	99.57	99.63	99.69	99.59	99.64	99.72
THD of phase current of bridge, %	27.91	37.94	46.23	9.06	19.52	23.73	7.11	9.85	12.73
THD of total current, %	7.03	3.45	1.48	2.82	1.75	0.8	1.82	0.89	0.44
Ripple coefficient U_{out}, %	0.13	0.05	0.18	0.11	0.9	0.25	0.5	0.48	0.11

It can be seen from table 2.4 that with an increase in the number of parallel bridges, the electricity quality indicators improve.

Fig. 2.20 shows the equivalent circuit of the active three-phase rectifier with power factor compensation. This converter includes six fully controlled IGBT switches with parallel diodes (*VT1*…*VT6*); three inlet throttles L_a, L_b, L_c; output capacitor C; three input resistances R_a, R_b, R_c.

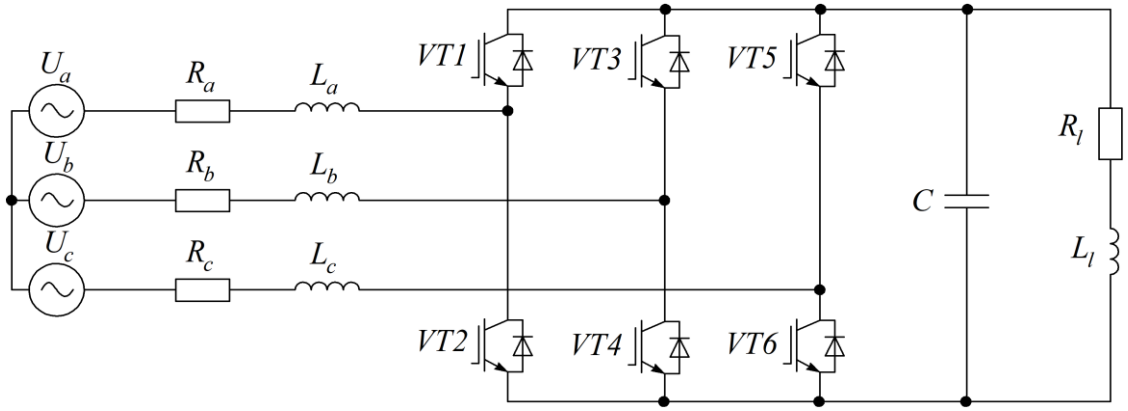

Figure 2.20 – Equivalent circuit of active step-up rectifier

There are several fundamentally different CSs of the AVR, one of which is the hysteresis CS, which implements high energy indicators and a power factor close to one, both in the rectification mode and in the regeneration mode. The structural diagram of the proposed CS is shown in fig. 2.21.

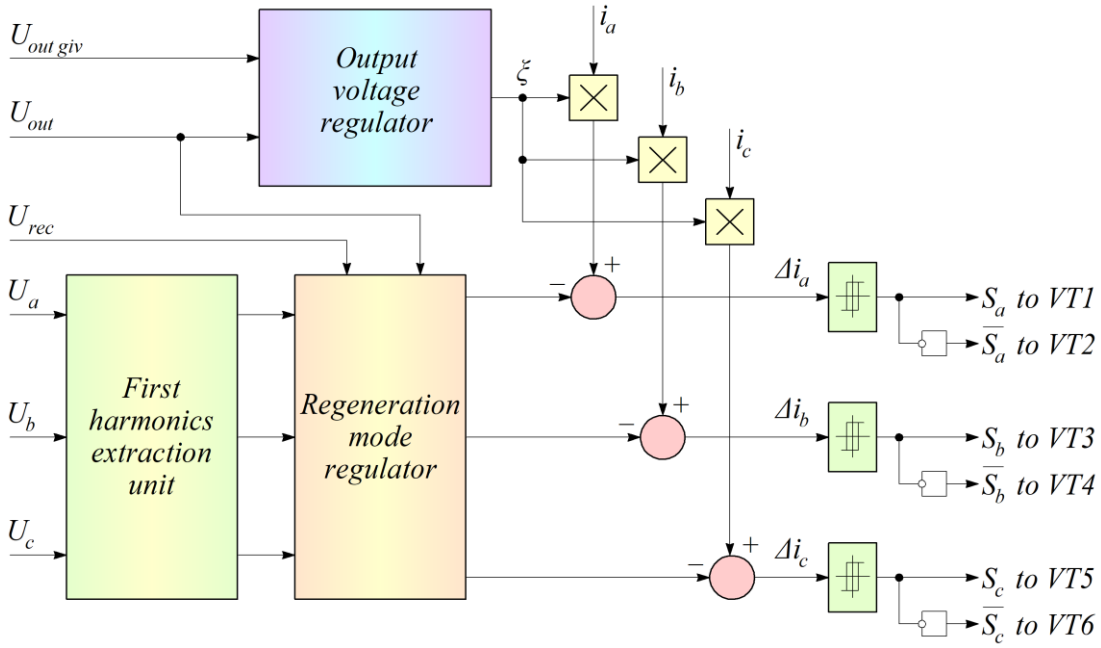

Figure 2.21 – CS of three-phase active rectifier

The CS forms a controlling influence on the AVR switches. Under this condition, the concept of switching functions is introduced. The switching function describes the position of the converter connection switches. If the switching function equals one, then the anode group switch is enabled, and if the switching function is zero, then the cathode group switch is enabled. The switching positions of the switches of the active rectifier are shown in fig. 2.22.

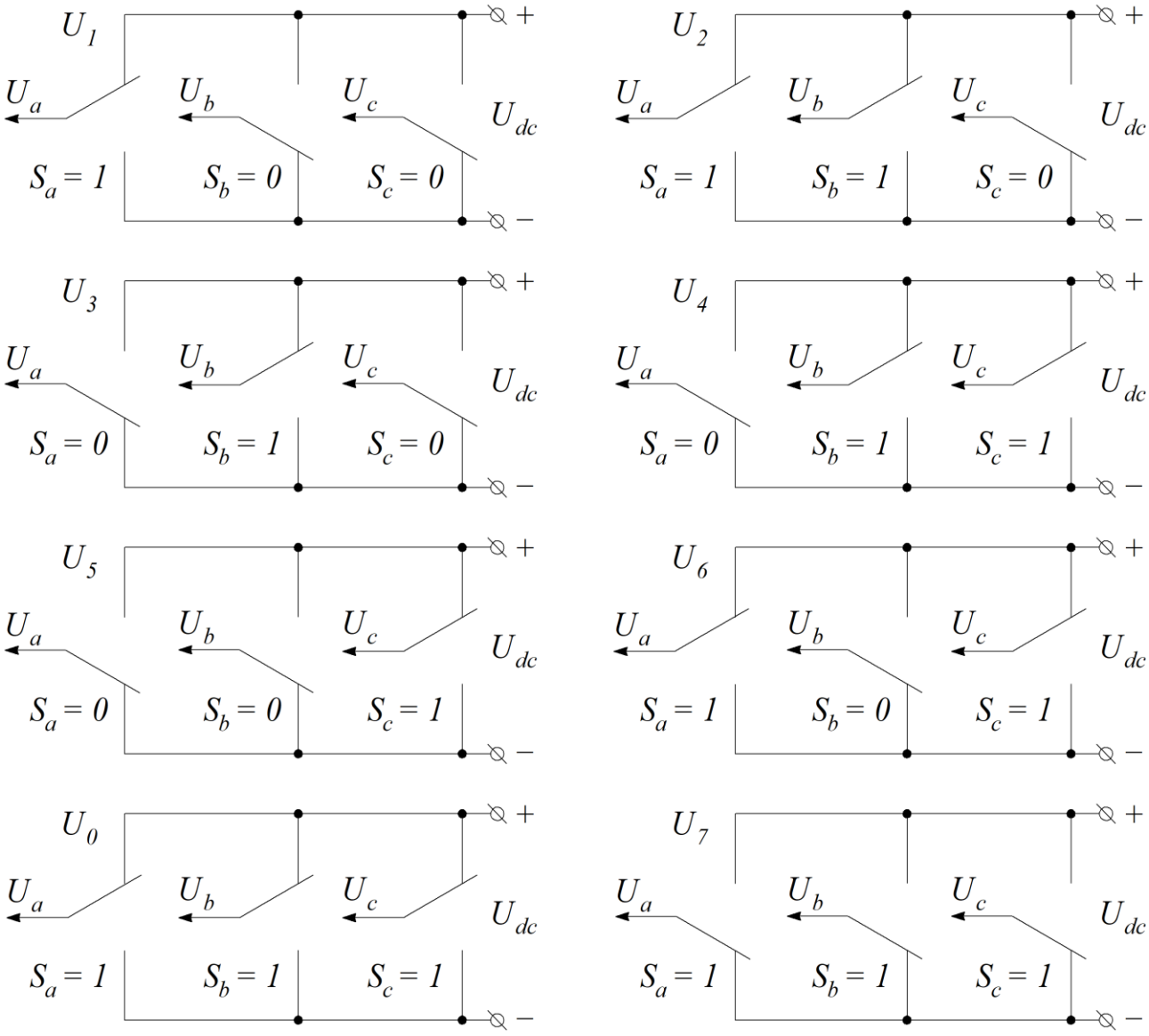

Figure 2.22 – Switching positions of active rectifier switches

In view of the switching positions of the AVR switches, a dynamic model of the active three-phase rectifier is given (fig. 2.23).

A discrete dynamic AVR model was developed in Matlab with the following parameters: L_a = 0.2 mH; R_a = 0.01 Ohm; C = 6 μF; R_n = 2 Ohm; L_n = 20 mH (fig. 2.24).

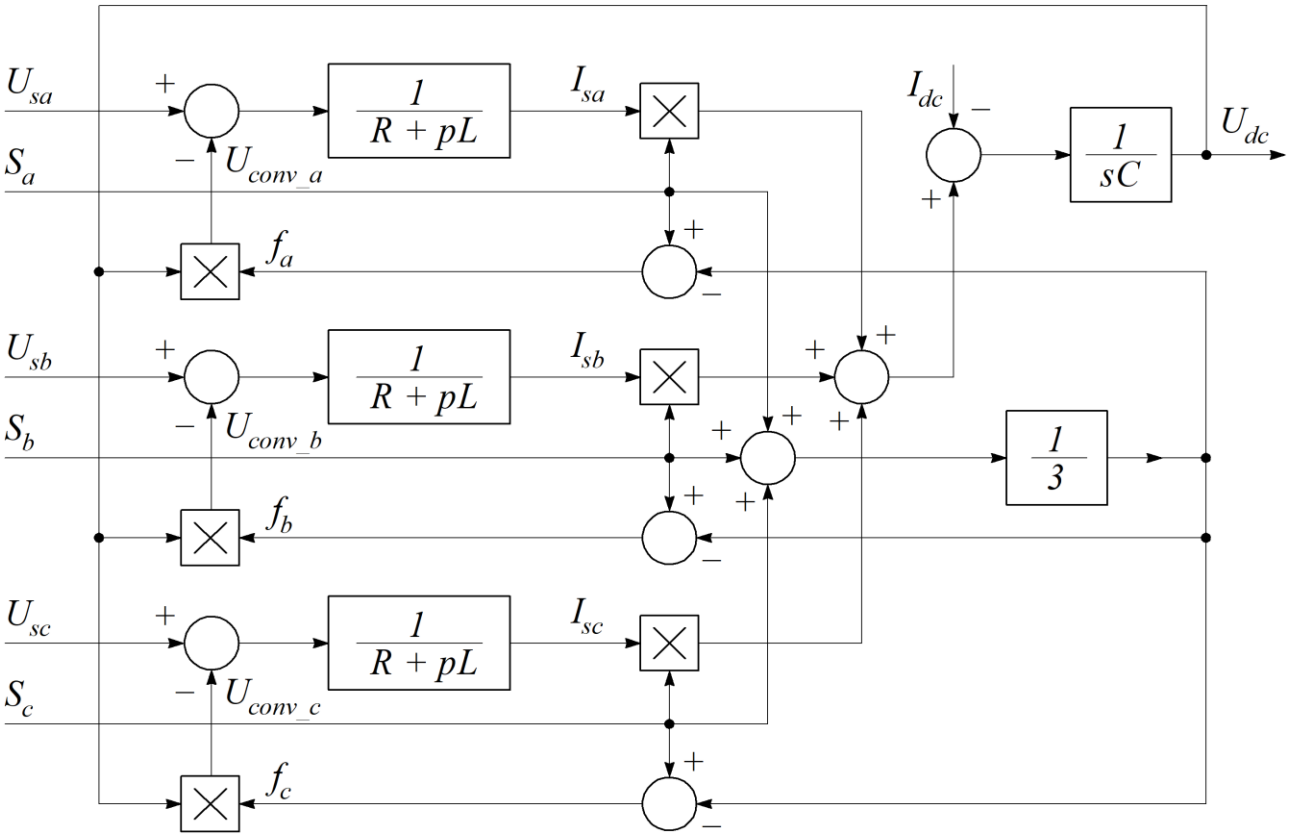

Figure 2.23 – Dynamic model of active three-phase rectifier

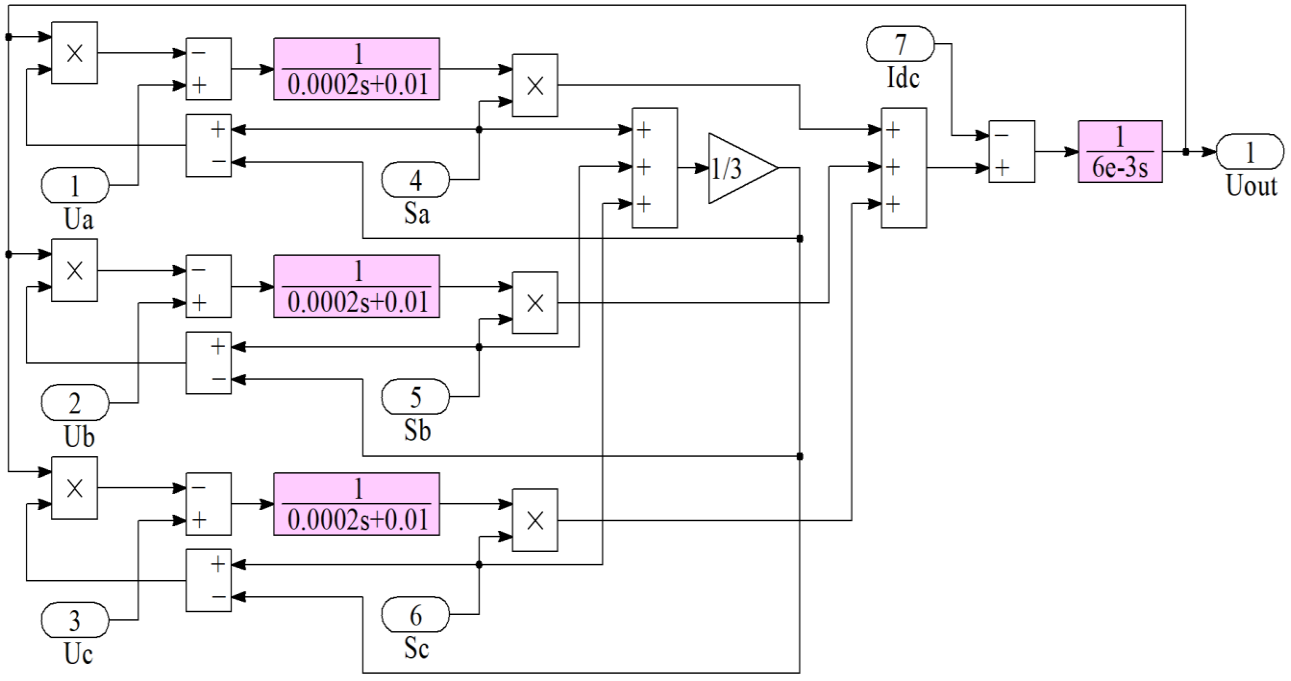

Figure 2.24 – Discrete dynamic AVR model

The results of simulation of phase currents and voltages of the AVR during mathematical and simulation modelling are shown in fig. 2.25.

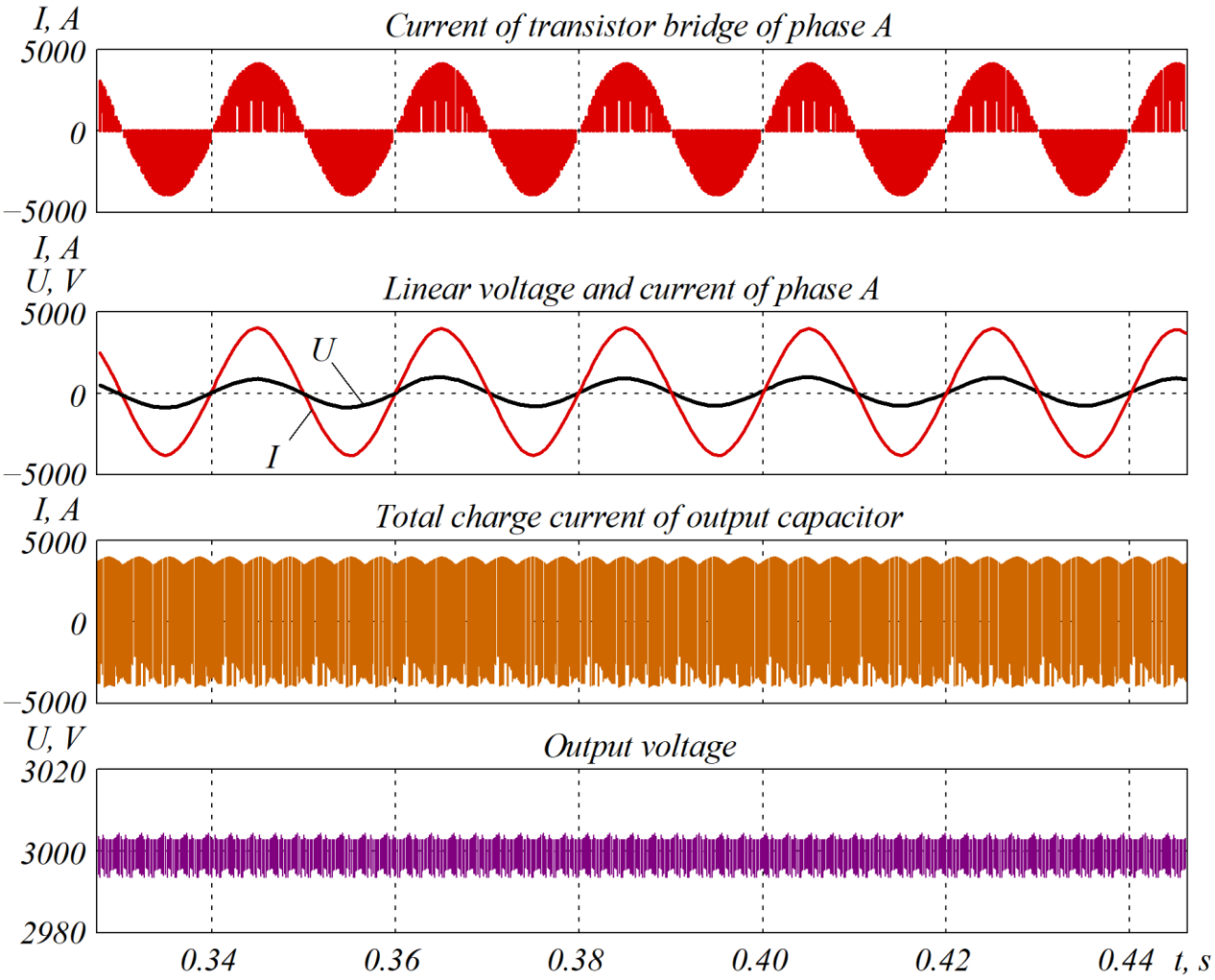

Figure 2.25 – Results of simulation of AVR phase currents and voltages

It can be seen from the simulation that the active rectifier provides power factor compensation in the rectification mode, and the amplitude of the output voltage ripples is less than 10 V.

2.3. Investigation of electromagnetic processes in compensation active voltage rectifiers

The modern element base of IGBT power modules has limited parameters of voltage, current and switching frequency, which must be taken into account when designing AVRs, the power of which is several megavolt-amperes. The railway DC PS has a capacity of more than 10 MV·A. At this time, *Infineon*, an advanced Mitsubishi company, produces a large scale IGBT modules of the 66th class with rated currents up to 1200 A [61]. Current limitation requires the parallel connection of switches in the

converter connections, which leads to complication of the topology of the power part and negatively affects the cost and the total losses. One of the ways to solve the problem to reduce the load of the active rectifier switches by current and voltage when implementing the same output power is the parallel or series compensation AVRs [62].

By analogy with the classic 12-pulse diode rectifier, circuits of compensation active rectifiers with series connection of bridges can be constructed. Under this condition, the number of bridges operating in parallel can differ. The compensation diagram of an active rectifier with the series connection of two bridges operating on one load is shown in fig. 2.15. A prerequisite for this circuit implementation of the compensation rectifier is the galvanic isolated power supply of each bridge.

In a classic 12-pulse diode circuit, the harmonic composition is improved by means of shifted supply voltage with individual bridges from a transformer with star-triangle winding connection. In the diagram shown in fig. 2.15, the 12-pulse mode is carried out using a certain algorithm controlling the power switches of bridges.

The advantage of this circuit is the lower voltage applied to the switches, which makes it possible to use a higher power converter. Disadvantages of this solution are the need to use galvanic isolated transformers, which makes the system more expensive and reduces the overall efficiency. Therefore, in a number of cases, it will be more appropriate to use the parallel connection of the AVR bridges.

Another way to reduce the operating currents of the AVR is to use a parallel bridge connection in the multi-pulse active rectifier. The diagram of the compensatory AVR with parallel connection of two bridges is shown in fig. 2.16. With the symmetry of the voltages and parameters of the bridges, half of the output load current will flow through each AVR bridge, which reduces the current requirements for the switches. The number of parallel bridges in the compensation active rectifier may vary.

The advantage of parallel connection of AVR bridges is the need to use galvanic isolated power supply of individual bridges.

The disadvantage of the multi-pulse AVR with parallel connection of bridges, unlike the AVR with series connection, is the lack of reduction of load requirements for switches by voltage. The voltage applied to the switches is equal to the output voltage. Which of these two circuit solutions is more economical and energy efficient will depend on the cost and efficiency of the galvanic isolated transformer and the cost of the lower class IGBT switches. In compensation active rectifiers with serial or parallel connection of bridges, different CS with active rectifiers can be used [63, 64]. It is possible to use CSs based on both hysteresis modulation and PWM.

Schematic implementation of the compensation AVR with parallel and serial connections of bridges makes it possible to obtain an improved harmonic composition

of phase currents and output voltage. This is achieved by synchronizing the CS with individual bridges and shifting the reference PWM signals in the control channels of each bridge relative to each other, which makes it possible to implement mutual compensation of higher harmonics of the input currents and output voltage.

At the same time, it should be noted that the mutual compensation of higher harmonics of individual bridges of 4QS-converters during hysteresis modulation is a much more difficult task, which is due to the fact that the switching frequency during hysteresis modulation is variable.

In terms of mutual compensation of higher harmonics of the input current and output voltage the most optimal is the application of the CS based on two-way PWM. Therefore in the control channel of each bridge in the compensation 4QS-converter, the sawtooth reference signals of the PWM must be synchronized and shifted in time relative to each other by an angle ψ. The indicated principle is shown in fig. 2.26.

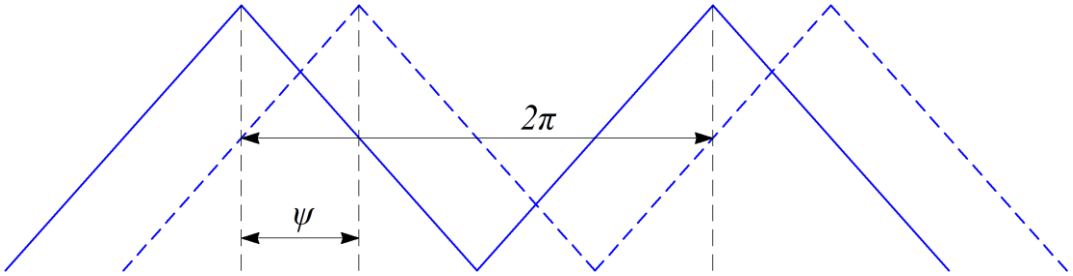

Figure 2.26 – Reference signals of bridges of compensation AVR with PWM

Thus, *n*-pulse AVRs can be implemented. At the same time, the shift angle of the reference signal depends on the number of parallel-connected bridges of the active rectifiers. In the course of research, it was determined that the optimal shift angle of the reference PWM signals will depend on the number of bridges of the compensation AVR and is determined by the expression:

$$\psi = \frac{360}{n}, \tag{2.5}$$

where n – the number of multi-pulse AVR bridges.

The CS of the compensation active rectifier shown in fig. 2.17 consists of two channels, each repeats the CS with a six-pulse AVR. However, the reference PWM signals of the individual channels are shifted by an angle of 180°. The time diagrams of signals acting in the CS of the compensation AVR with a shift of the reference PWM signals are shown in fig. 2.27.

At the same time, it should be noted that the implementation of mutual compensation of higher harmonics requires fulfilment of the condition of value equality for the input inductances of the bridges in the compensation 4QS-converter.

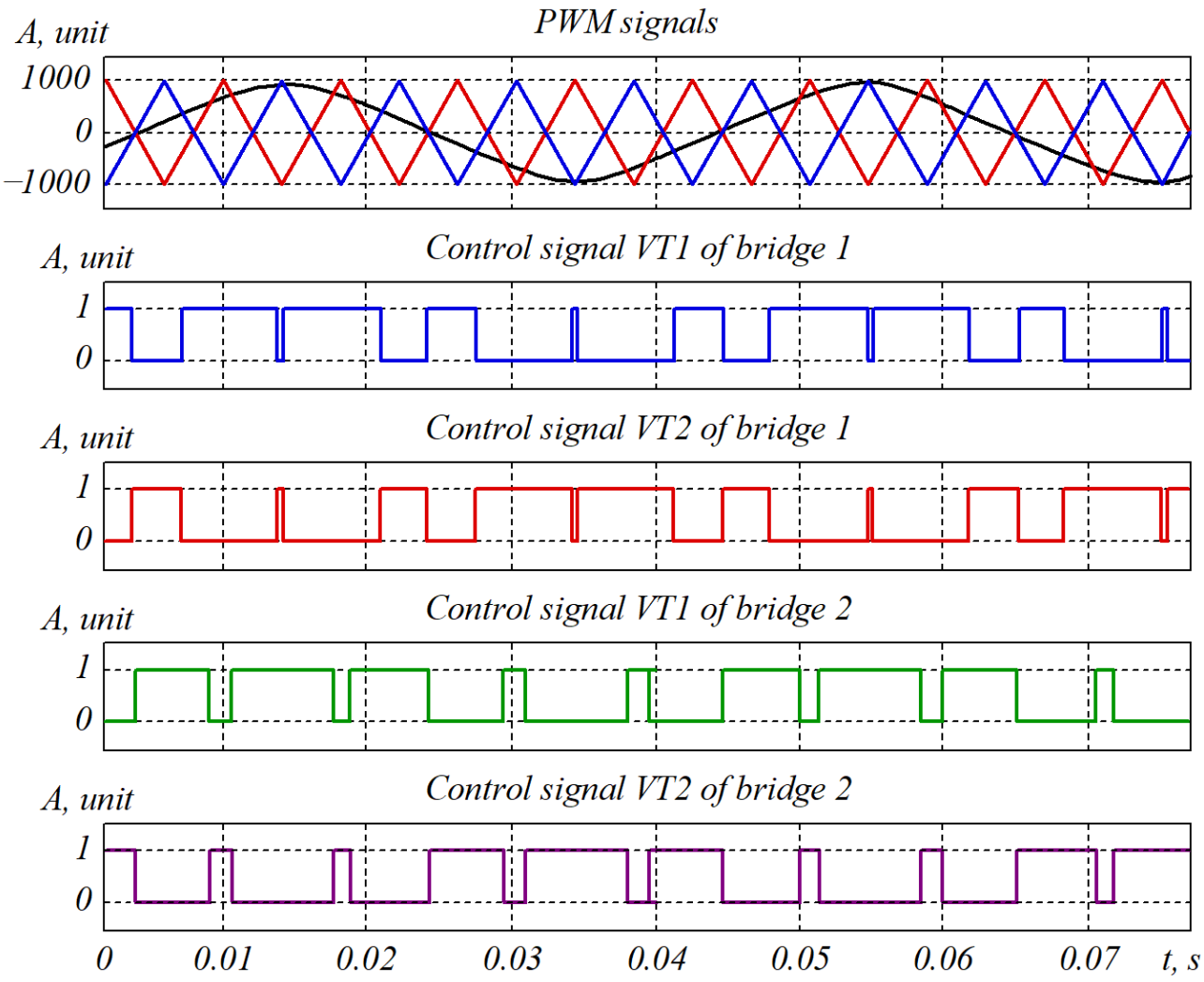

Figure 2.27 – Modulation with phase shift of carrier signals

The application of the above-mentioned control principle over the compensation AVR makes it possible to implement improved EMC indicators, reduce operating switching frequencies, and apply lower-class switches with smaller rated currents.

The electromagnetic processes in the compensation active rectifier and the processes of mutual compensation of higher harmonics and EMC indicators have been studied by means of a simulation model developed in Matlab (fig. 2.28).

The compensation active rectifier consists of two parallel bridges powered by one network and operates on one equivalent *RL*-load. The CS in fig. 2.28 is marked with sub-blocks Control System1 and Control System2.

Parameters of the simulation model are given in table 2.5.

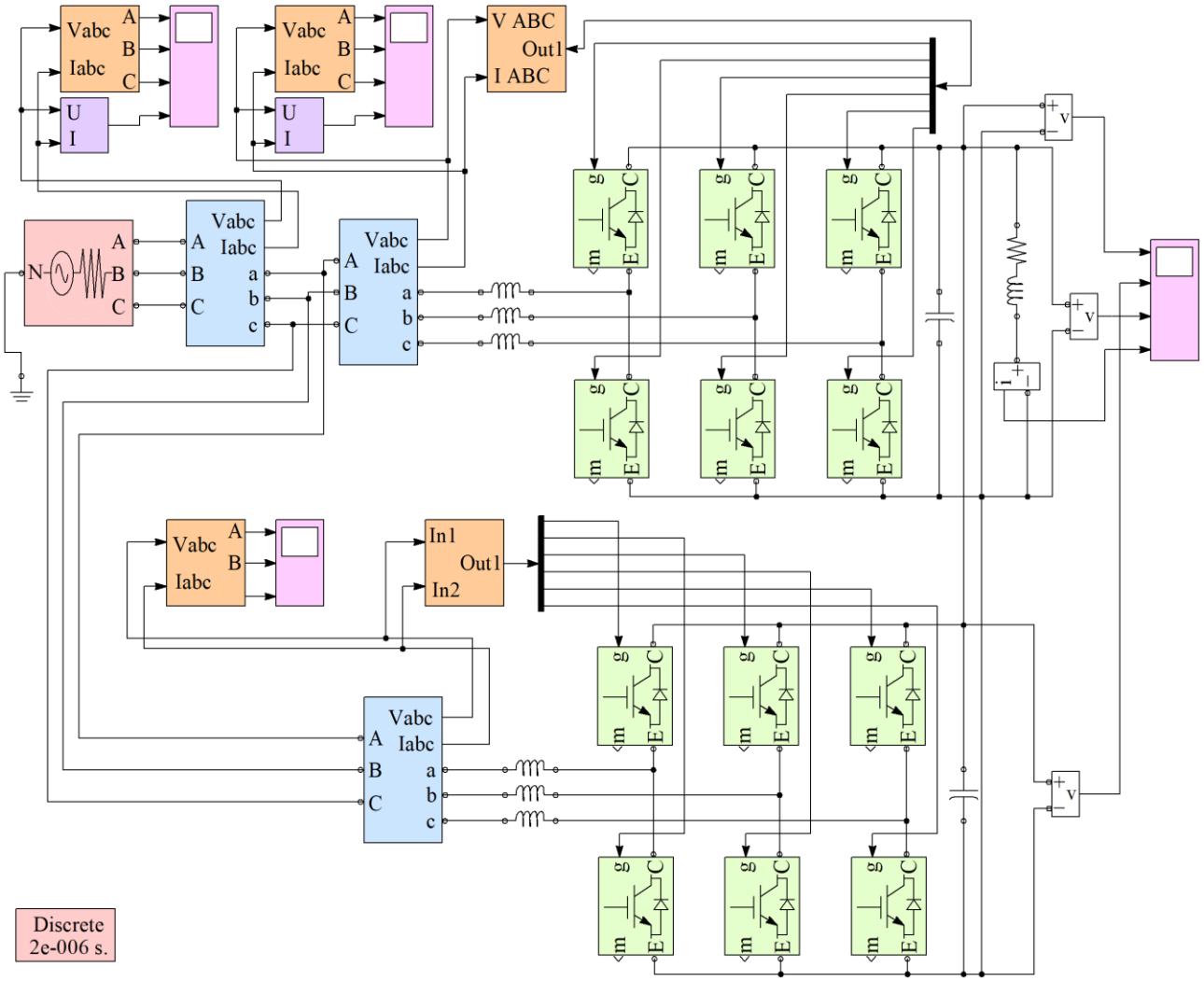

Figure 2.28 – Simulation model of compensation AVR with parallel connection of bridges

Table 2.5 – Parameters of simulation model of compensation active rectifier

Parameter	Value
Phase-to-phase voltage of three-phase network, V	1200
Active mains resistance, Ohm	0.2
Inductive network resistance, mH	0.1
Inductance of input filters, mH	0.8
Capacitance of the output capacitor, mF	12
Active load resistance, Ohm	1…12
Inductive load resistance, mH	0.1…5
Load voltage, V	3300

The simulation model of the CS of the compensation AVR has two channels of reference voltage formation (fig. 2.29).

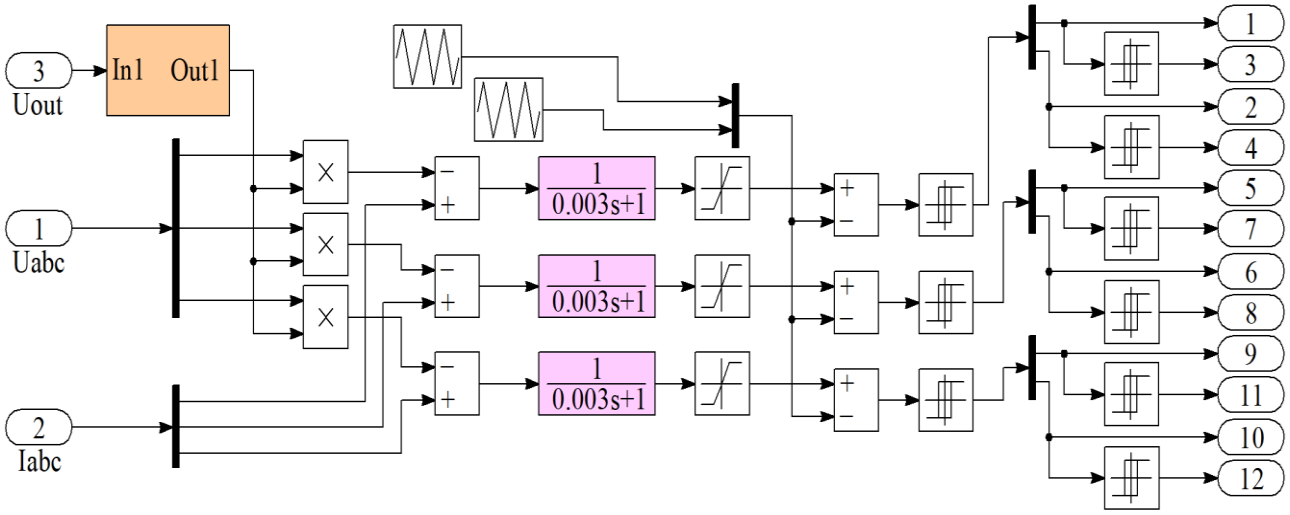

Figure 2.29 – Sub-model of CS of compensation AVR

The processes in the CS during synchronization of the PWM carrier signals with a shift of the carrier signal by 180° are shown in fig. 2.30.

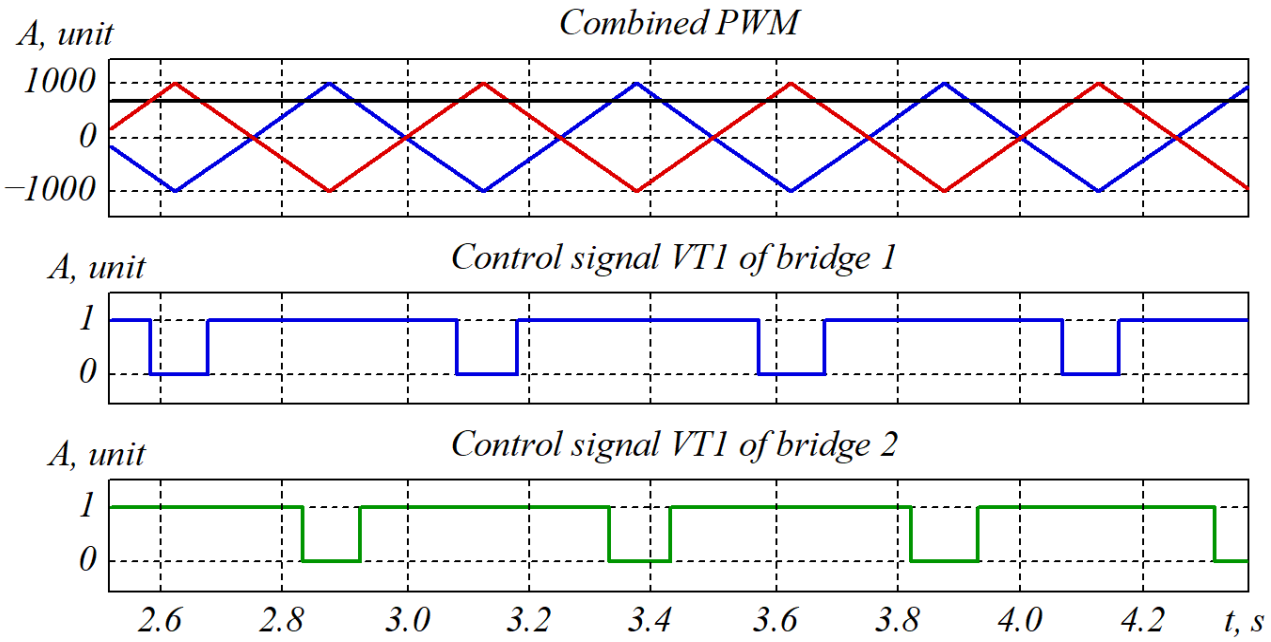

Figure 2.30 – Generation of control signals

By means of the simulation of electromagnetic processes, the following oscillograms were obtained: input currents and voltages of the compensation AVR, charge current of the output capacitor and the output voltage.

The special feature of the input current formation is the sequential operation of two AVR bridges. When the instantaneous value of the input current of the first bridge increases, the instantaneous value of the input current of the second bridge decreases.

Thus, in the total consumed current, ripples with a modulation frequency are compensated. The instantaneous values of the phase currents of the AVR bridges and the total consumed current are shown in fig. 2.31.

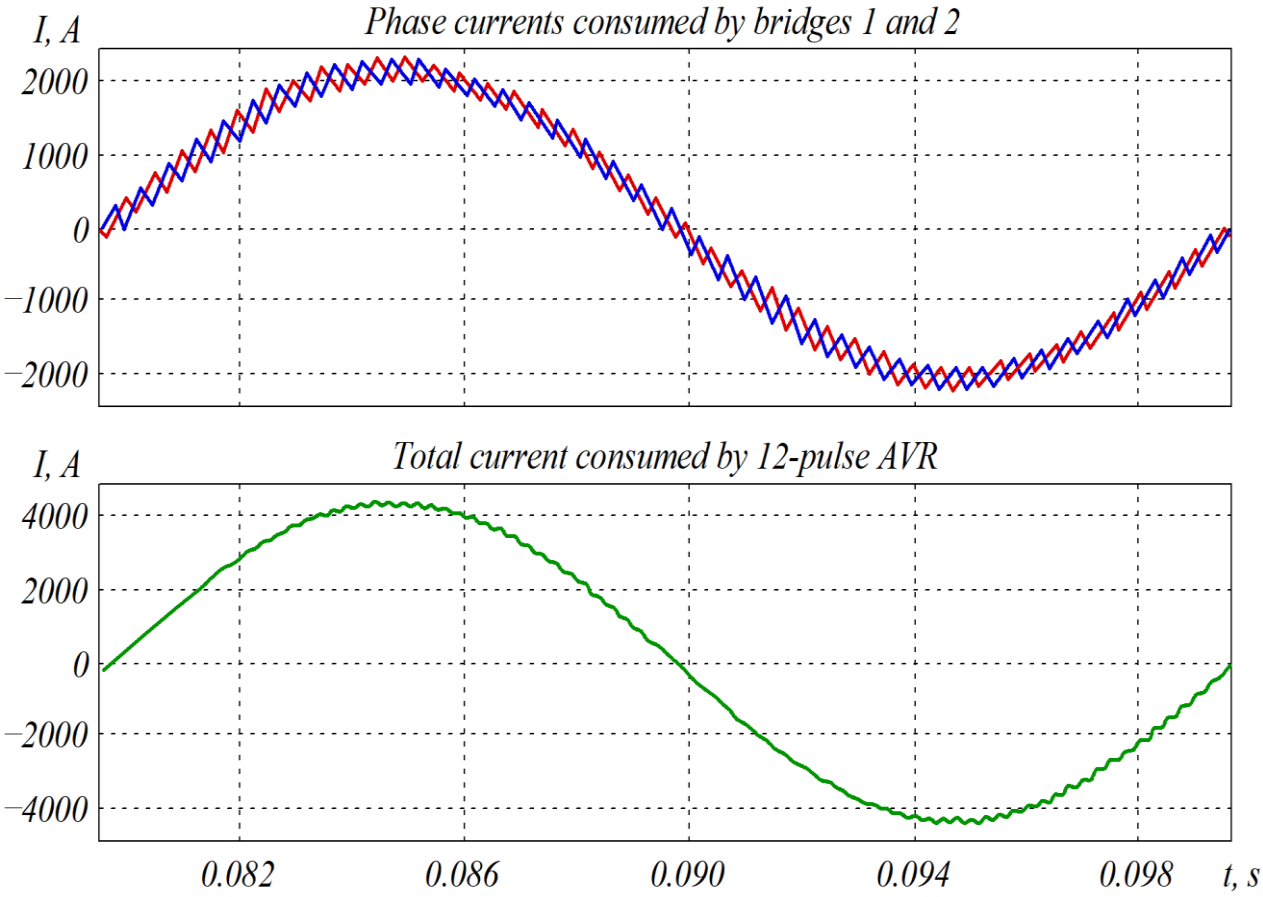

Figure 2.31 – Compensation of higher harmonics of input current

Fig. 2.32 shows the instantaneous values of the sum of the higher current harmonics of two bridges of the compensation AVR, obtained by subtracting the phases of their first harmonics from the current signal.

As follows from fig. 2.32, the higher harmonics amplitudes in the resulting input current have significantly decreased. However, the fundamental harmonic frequency of the spectrum of higher harmonics of the resulting input current has doubled.

The formation of the output voltage is influenced by the charge of the output capacitor through two parallel AVR bridges.

Fig. 2.33 shows the charge currents of the output capacitor formed by the bridges of the compensation AVR and the shape of the output voltage.

Under these circumstances, the ripple frequency of the output voltage of the compensation AVR, caused by higher harmonics, if compared to the six-pulse AVR, has doubled.

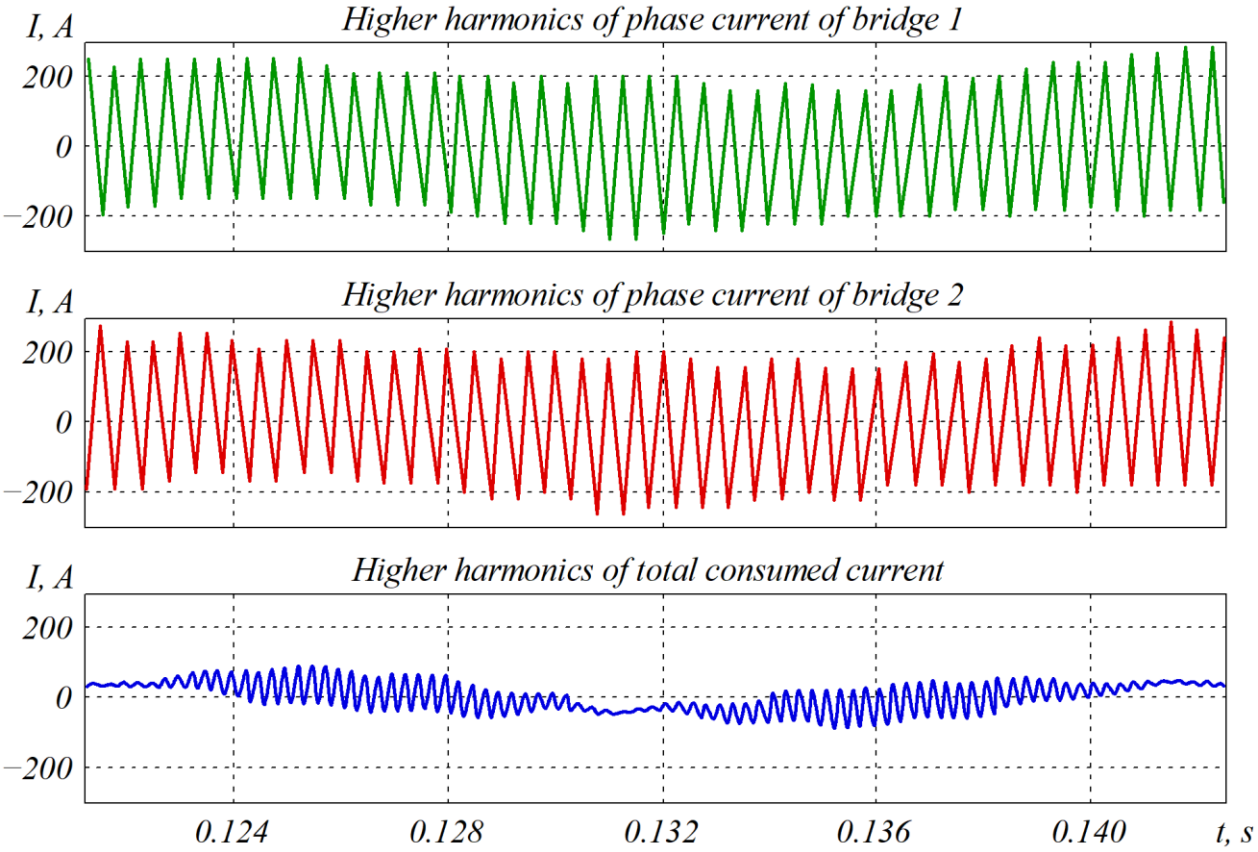

Figure 2.32 – Instantaneous values of higher harmonics of AVR bridges

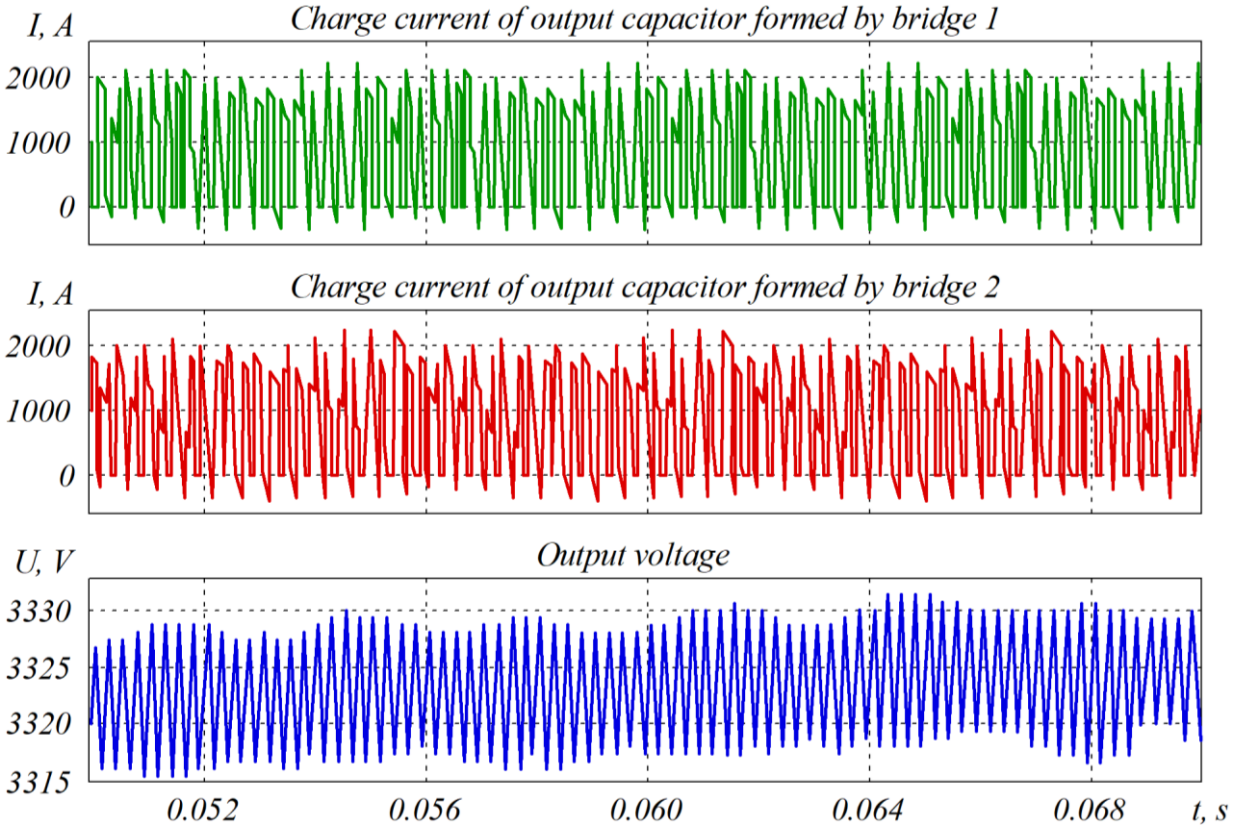

Figure 2.33 – Charging of output capacitor with two bridges

The oscillograms of the input phase voltage and currents, and the oscillogram of the output voltage of the compensation AVR are shown in fig. 2.34.

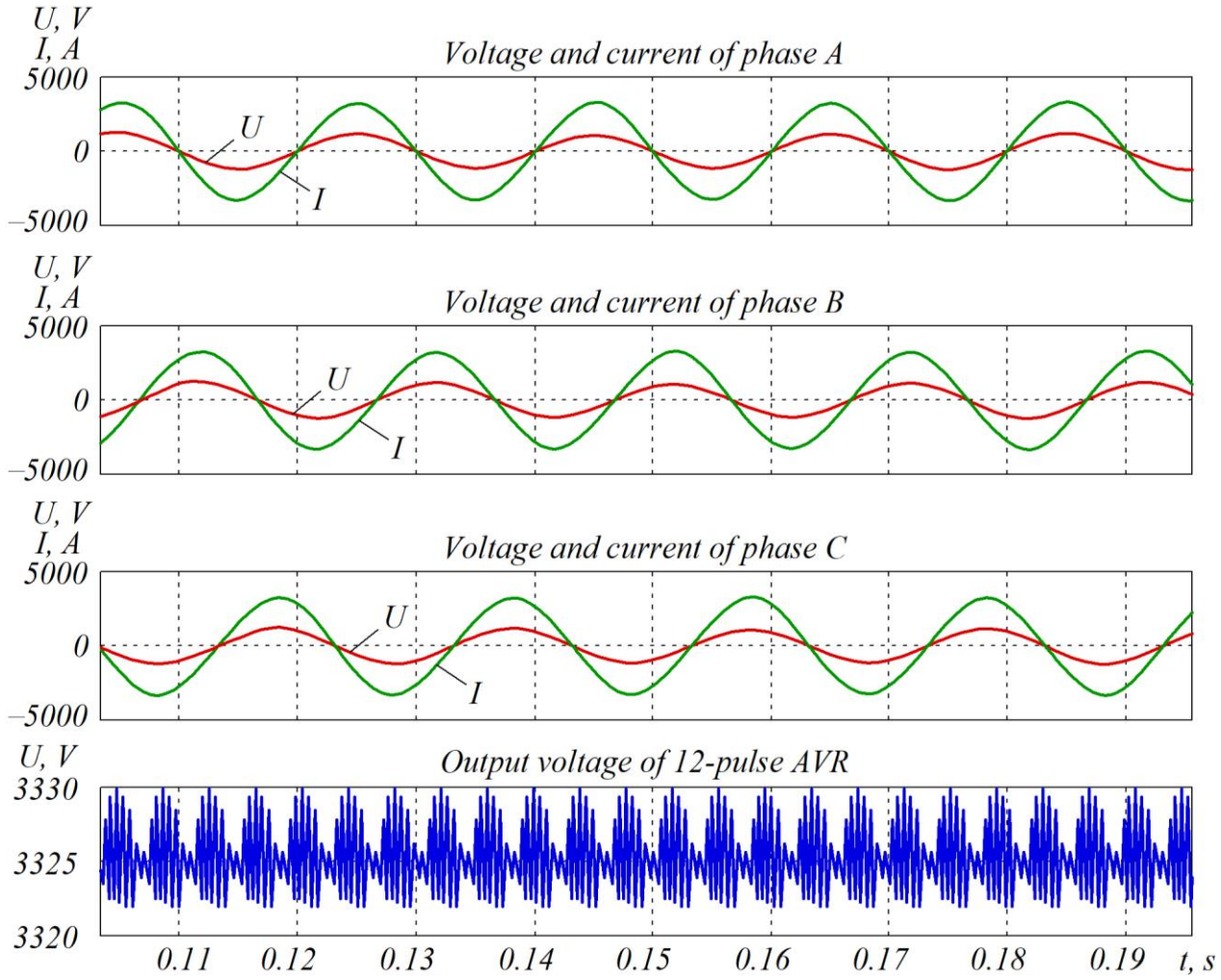

Figure 2.34 – Form of phase voltage and current of compensation AVR

As follows from fig. 2.34, the proposed CS implements the phase currents similar to sinusoidal, cosφ close to one, a small amplitude of output voltage ripples.

The simulation model of the compensation 4QS-converter with PWM developed in Matlab was used for studying the following EMC parameters: power factor, THD of phase current, ripple factor of output voltage, interference voltage value.

Fourier analysis of the current consumed by one bridge of the compensation AVR is shown in fig. 2.35.

The spectrum of current harmonics consumed by one bridge of the compensation AVR repeats the spectrum of the six-pulse AVR, but the phase shift of the higher current harmonics, multiple to the modulation frequency, provides their compensation. Fourier analysis of the total consumed current of the compensation active rectifier is shown in fig. 2.36.

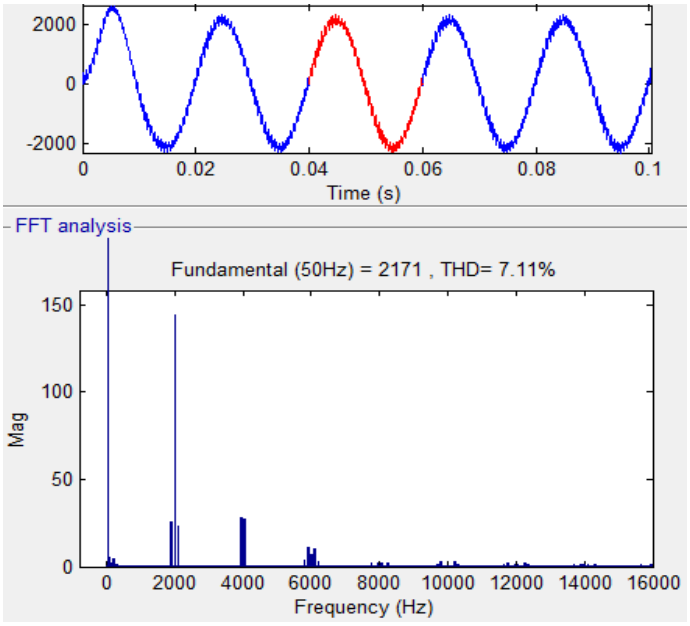

Figure 2.35 – Fourier analysis of current of one bridge of compensation AVR

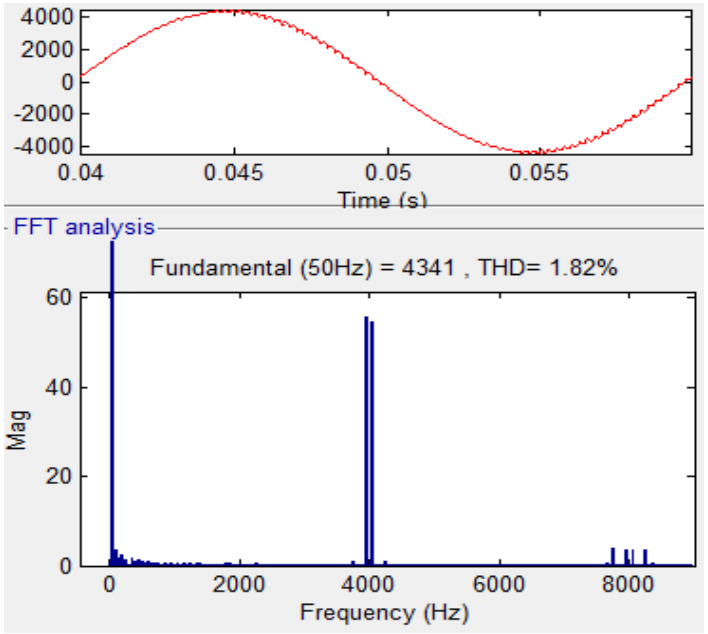

Figure 2.36 – Fourier analysis of total consumed current of compensation AVR

As follows from fig. 2.35 and fig. 2.36, in a parallel connection of bridges in the compensation AVR with a shift of the reference PWM signal in the CS, higher harmonics are compensated, which leads to an improvement in the THD of the total consumed current. The THD of the phase current of the compensation AVR is 1.82 %.

The following higher harmonic spectrum is typical for the compensation AVR:

$$f_I = (2 \cdot f_m \mp f_n) + (2 \cdot f_m \mp 5 \cdot f_n) + (4 \cdot f_m \mp f_n) + (4 \cdot f_m \mp 5 \cdot f_n) + (4 \cdot f_m \mp 7 \cdot f_n), \quad (2.6)$$

where f_m – the PWM frequency; f_n – the power supply network frequency.

The quality of the output voltage is determined by the following indicators: ripple amplitude, ripple coefficient and interference voltage value.

Fourier analysis of the output voltage form of the compensation converter is shown in fig. 2.37.

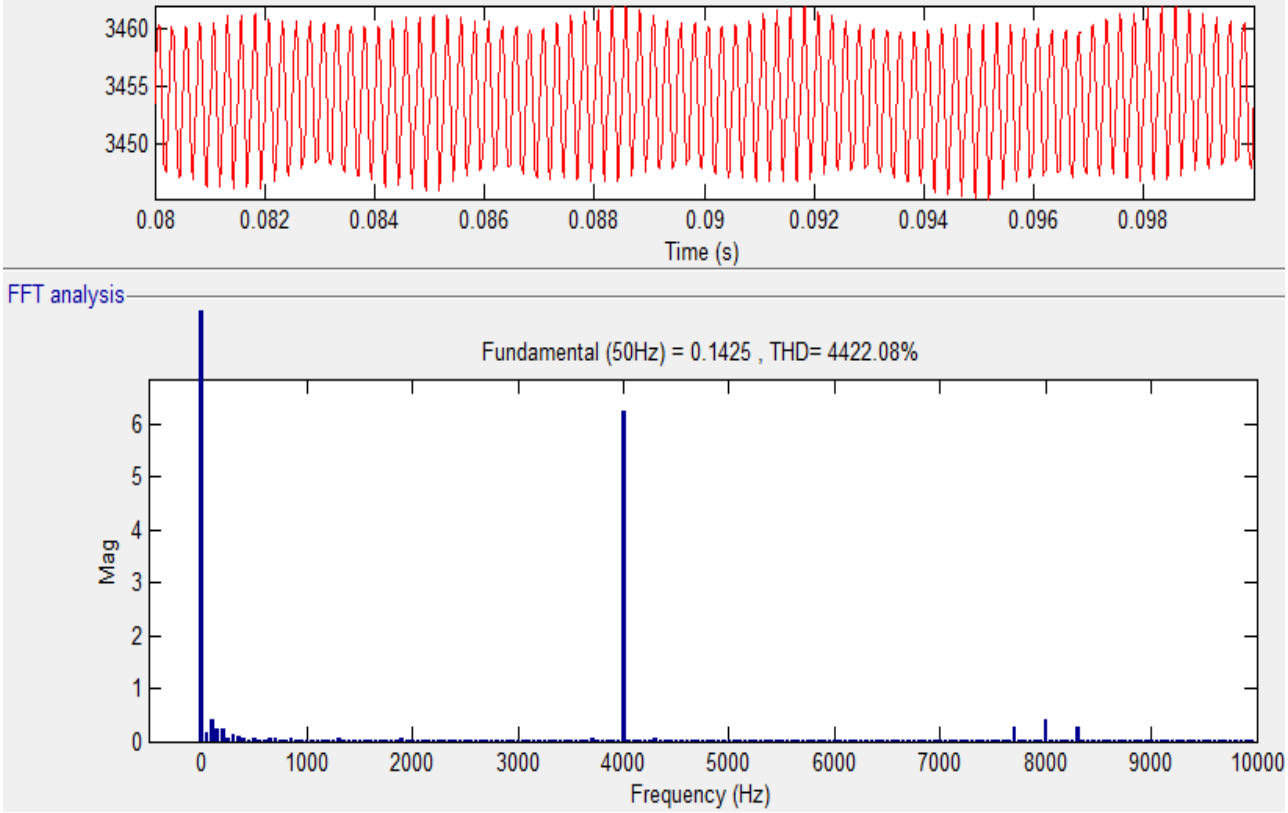

Figure 2.37 – Fourier analysis of output voltage of compensation AVR

The spectrum of higher harmonics of the output voltage depends on the switching frequency and the network frequency as follows:

$$f_U = (2 \cdot f_m) + (2 \cdot f_m + 2 \cdot f_m \mp 6 \cdot f_n) + (4 \cdot f_m + 4 \cdot f_m \mp 6 \cdot f_n) + \ldots . \qquad (2.7)$$

As follows from fig. 2.36 and fig. 2.37, the compensation active rectifier with PWM can significantly improve the harmonic composition of the output voltage and input current.

The voltage ripple coefficient of the compensation AVR equals:

$$k_{pulse} = \frac{\sqrt{V_2^2 + V_3^2 + V_4^2 + V_5^2 + V_6^2 + \ldots}}{V_{DC}}, \qquad (2.8)$$

$$k_{pulse} = \frac{4422.08 \cdot 0.1425}{3455} = 0.1824\,\%.$$

The voltage value of interference is an integral indicator characterizing the level of higher harmonics in the output voltage of the PS rectifier, which affect the communication lines and railway automation devices.

The voltage interference in the compensation AVR model was measured with the subsystem shown in fig. 2.38.

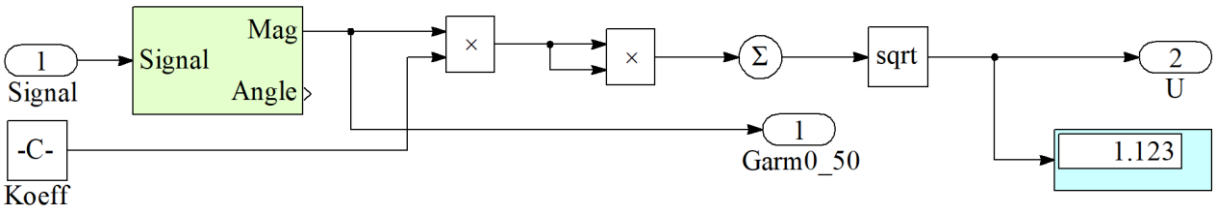

Figure 2.38 – Subsystem for measuring interference voltage of compensation AVR

The interference voltage is determined by measuring RMS of higher harmonics in the output voltage. When measuring the interference voltage, 80 higher harmonics of the AVR output voltage can be analysed.

In the simulation model, the power factor was calculated with the subsystem for calculation of power factor, input capacity, and THD, which is given in fig. 2.39.

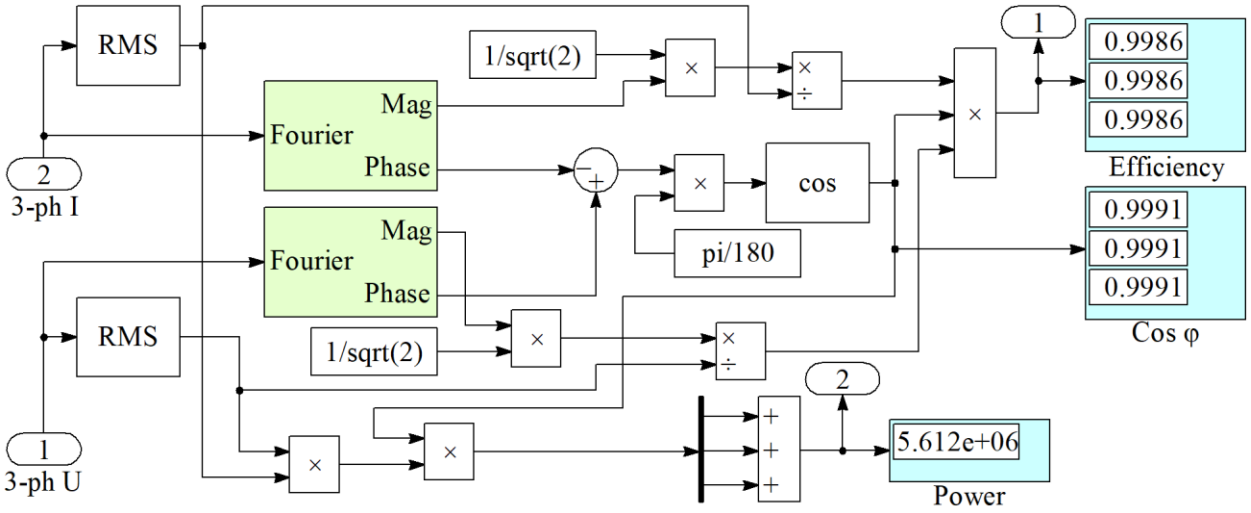

Figure 2.39 – Subsystem for calculating parameters of compensation AVR

As a result of the simulation, a power factor equal to 0.9986 was obtained; it meets the International and Ukrainian Standards.

The results of simulation of the active rectifier structures studied are given in table 2.6.

Table 2.6 – Comparative analysis of EMC indicators of structures of active rectifiers studied

Parameter	2-level AVR with hysteresis	2-level AVR with PWM	3-level AVR with PWM	12-pulse AVR with PWM
Switching frequency, kHz	≈41.2	2	2	2
Power factor, %	99.74	99.51	99.81	99.86
THD of input current, %	2.13	2.27	2.95	1.82
Ripple coefficient U_{out}, %	0.101	0.143	0.1211	0.1824
Interference voltage, V	3.803	3.764	2.362	1.123

On the basis of a comparative analysis of the structures of active rectifiers, the use of compensation active rectifiers is an optimal approach.

2.4. Reduction of dynamic losses in the active one-phase four-quadrant converter with power factor compensation with an improved hysteresis modulation algorithm

Diode and thyristor four-zone rectifiers used for AC ERS cause a significant emission of higher current harmonics and have a rather low power factor lying within 0.65...0.85, which significantly reduces the energy efficiency of both the ERS and the entire traction power supply system. In turn, a significant reactive power component in the traction electric network requires to use rather expensive reactive power compensators made by a passive or active topology [65].

The application of active four-quadrant power factor-corrected rectifiers, known as 4QS-converters, for the ERS is promising. Unlike traditional thyristor rectifiers, 4QS-converters have a number of significant advantages:

– provide a consumed current form similar to the sinusoid;

– implement a power factor close to one;

– provide a low level of higher current harmonics emission into the power supply network (THD can be provided below 5 %);

– implement two-way electric energy transmission; and

– ensure regulation and stabilization of the DC circle voltage.

Study [66] presents a description and substantiation of the use of the proposed CS with the power switches of the active single-phase four-quadrant rectifier, which makes it possible to reduce dynamic power losses, increase the converter efficiency and improve the sinusoidality of the input current.

The power circuit of the traction electric drive of AC ERS with the 4QS-converter, feeding an AVI and a traction asynchronous motor, is shown in fig. 2.40.

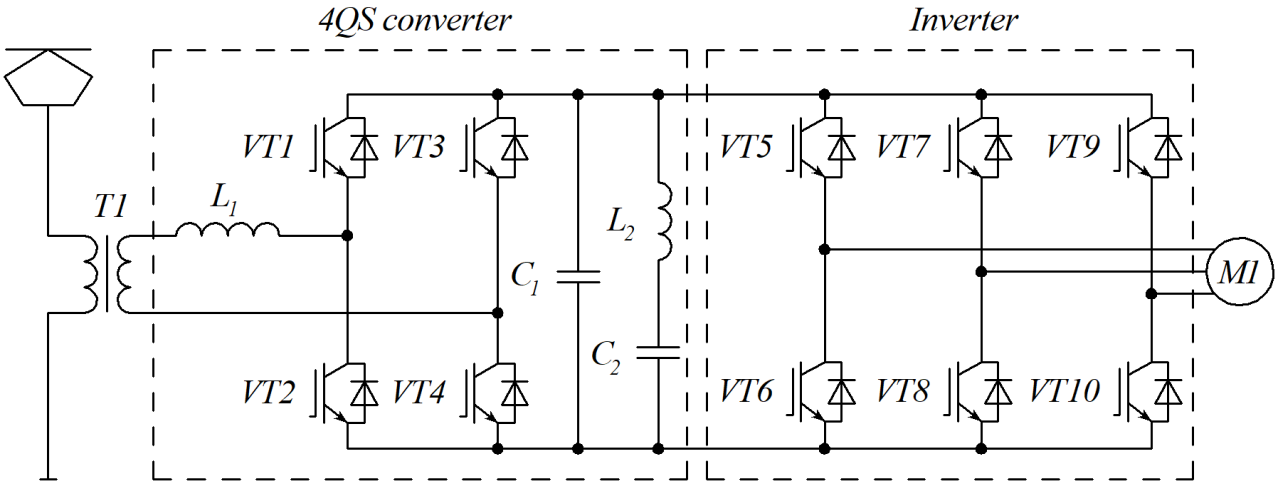

Figure 2.40 – Power circuit of ERS electric drive with 4QS-converter

Fig. 2.40 presents the active four-quadrant rectifier consisting of throttle L_1, which acts as a buffer reactor to increase the output voltage, IGBT *VT1–VT4*, capacitive filter C_1, designed to reduce the amplitude of the output voltage ripples, and rejection filter C_2–L_2, which is used to suppress harmonics of 100 Hz in the output voltage. In 4QS-converters the most widespread are CSs based on PWM and hysteresis modulation [67]. Each of these systems has its advantages and disadvantages.

The advantage of the CS based on PWM is the possibility of setting a constant modulation frequency, but there are also disadvantages, namely: a decrease in the range of output voltage regulation and deteriorated indicators of the electrical energy quality. The advantage of hysteresis CSs is their relative simplicity and the possibility of implementing quite high indicators of the electrical energy quality. The disadvantage of the existing hysteresis CSs is their rather high and variable switching frequency of power switches, which causes high dynamic losses in the converter [68, 69]. In this case, the switching frequency of the 4QS-converter with the hysteresis CS depends on many factors: value of the input inductance of the converter, load current, and value of the hysteresis setpoint. The structural diagram of the basic hysteresis CS is shown in fig. 2.41, which has the following marks: u_{in} – the instantaneous value of the input voltage; u_{out} – the RMS of the output voltage; i_{in} – the instantaneous value of the input

current; i^*_{in} – the task signal of the instantaneous value of the input current; u_{out_set} – the task signal of the output voltage; ξ – the adjusting coefficient of the CS, i_{out} – the RMS of the output current; S_{VT1}, S_{VT2}, S_{VT3}, S_{VT4} – the control signals for the corresponding transistors.

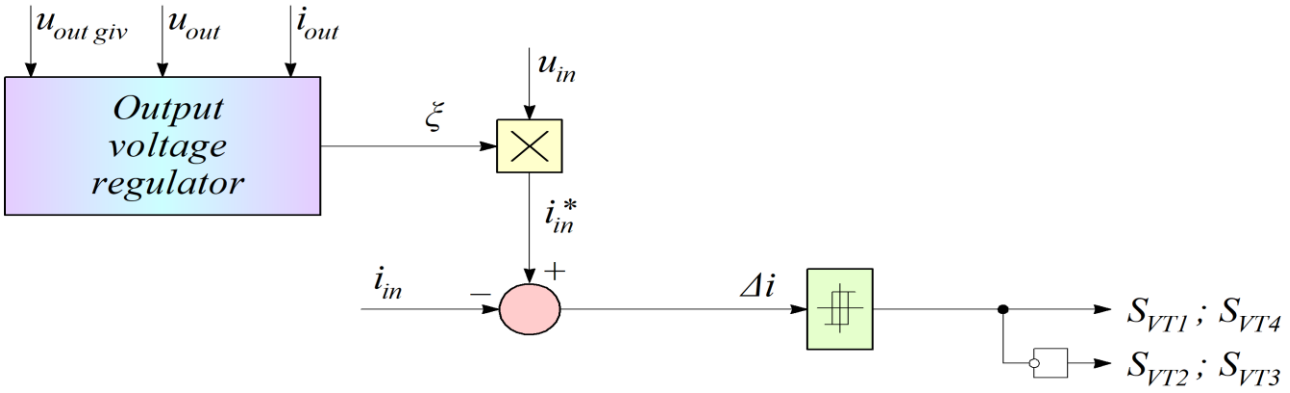

Figure 2.41 – Structural diagram of basic hysteresis CS

The principle of formation of the sinusoidal input current of the 4QS-converter with the basic (known) hysteresis CS (fig. 2.42) is comparing the task signal of the input current i^*_{in}, obtained as the instantaneous value of the input voltage u_{in} scaled with the regulating coefficient ξ, with the instantaneous value of the input current i_{in} and obtaining the error signal Δi. Later on, the hysteresis modulator unit compares the error signal Δi with the hysteresis setpoint h.

Provided that $\Delta i > h$, that is, when the instantaneous value of the current exceeds its task signal by the value h, then the CS provides actuating signals to the pair of power transistors *VT1* and *VT4*, which causes the switching of the input current with a drop (decrease) in its instantaneous value. Then, if $\Delta i < -h$, that is, the value of the instantaneous input current relative to its task signal by the value h, the CS sends actuating signals to the pair of power transistors *VT2* and *VT3*, which causes the instantaneous increase in the value i_{in}. Thus, the sinusoidal current corridor is formed [70, 71].

When the pair of transistors *VT1* and *VT4* is switched on, a DC voltage $+U_{out}$, which is higher than the amplitude value of the input voltage, is applied to the inlet throttle from the active converter. This causes the instantaneous value of the input current to drop. And conversely, switching-on the pair of transistors *VT2* and *VT3* causes the instantaneous value of the input current to rise. Thus, in the case of each input current switching, all four power switches are commutated, which, under the condition of a fairly high switching frequency, causes quite significant dynamic losses in the converter.

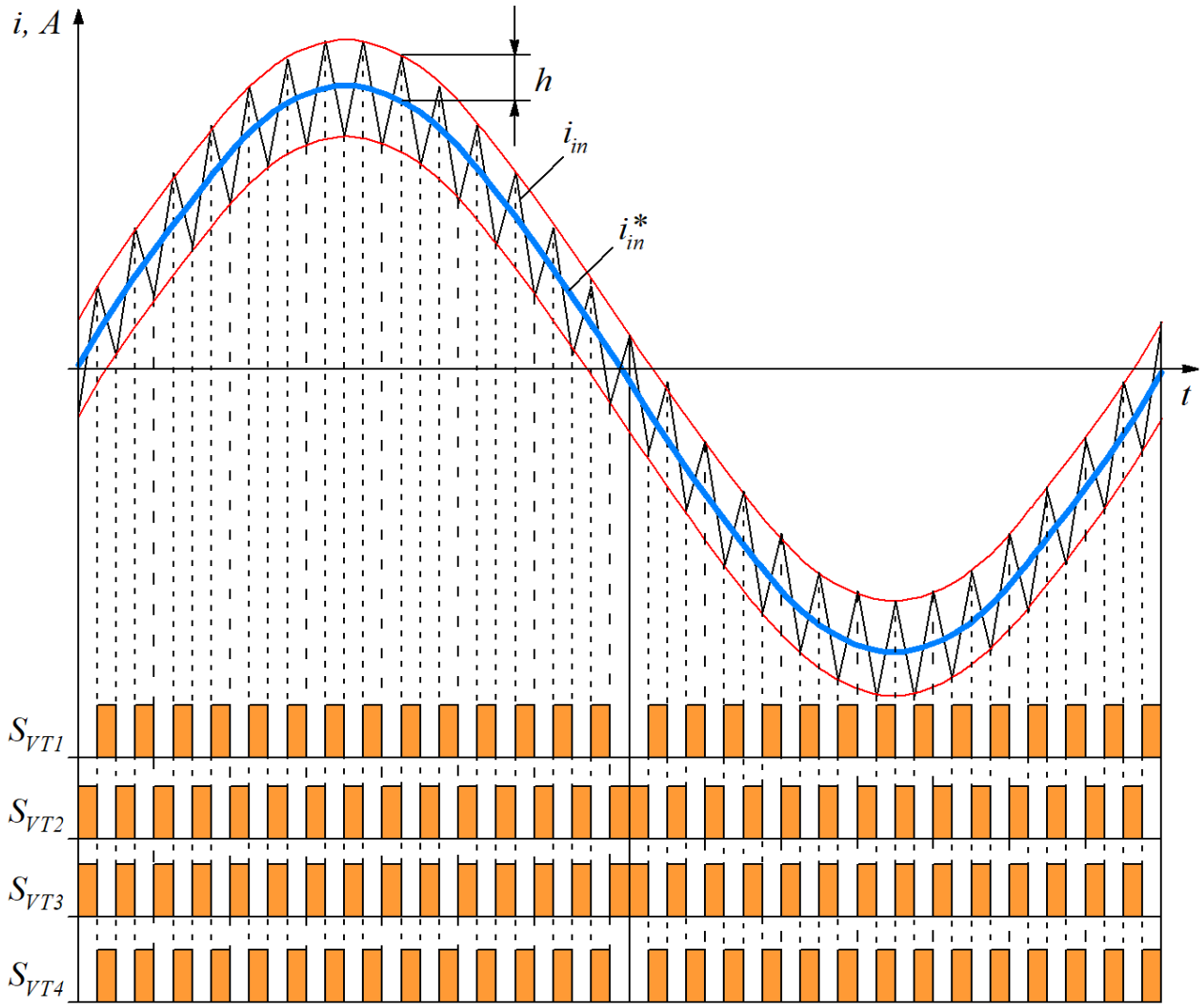

Figure 2.42 – Formation of 4QS-converter current with basic hysteresis CS

An improved hysteresis modulation algorithm in an active four-quadrant converter is synthesized, which makes it possible to reduce the number of power switch commutations and, thereby, reduce dynamic losses in the converter. It is proposed to add the switching positions of simultaneous switching-on the pair of transistors *VT1* and *VT3* and the pair *VT2* and *VT4* to the sequence of power switch commutations. These switching positions under positive polarity of the input voltage cause an increase in the instantaneous value of the input current, and in the case of a negative input voltage polarity, contribute to the drop in the input current. This makes it possible to switch from the switching position *VT1–VT4* to the position *VT1–VT3* during the positive half-wave of the input voltage. In this case, the instantaneous value of the input current changes from the descending position to the ascending one, but unlike the basic switching algorithm only two power switches are switched. In case of negative polarity U_{in} short-circuited positions can also be used: switching from switching position *VT2–VT3* in *VT1–VT3*.

The proposed improved switching algorithm for power switches consists of six switching positions, shown in table 2.7, where the grey colour shows the stages of input current switching, in which the corresponding power switches are not switched.

The principle of forming the sinusoidal input current of the 4QS-converter with the proposed hysteresis CS is shown in fig. 2.43.

Table 2.7 – Sequence of power switch commutation at enhanced hysteresis modulation

Power switch	Switching positions of power switches at input voltage positive polarity				Switching positions of power switches at input voltage negative polarity			
VT1	0	1	1	1	0	1	0	0
VT2	1	0	0	0	1	0	1	1
VT3	0	0	1	0	1	1	1	0
VT4	1	1	0	1	0	0	0	1
$I_{in}(t)$	Growing	Drops	Growing	Drops	Drops	Growing	Drops	Growing
Step	Step 1	Step 2	Step 3	Step 4	Step 1	Step 2	Step 3	Step 4

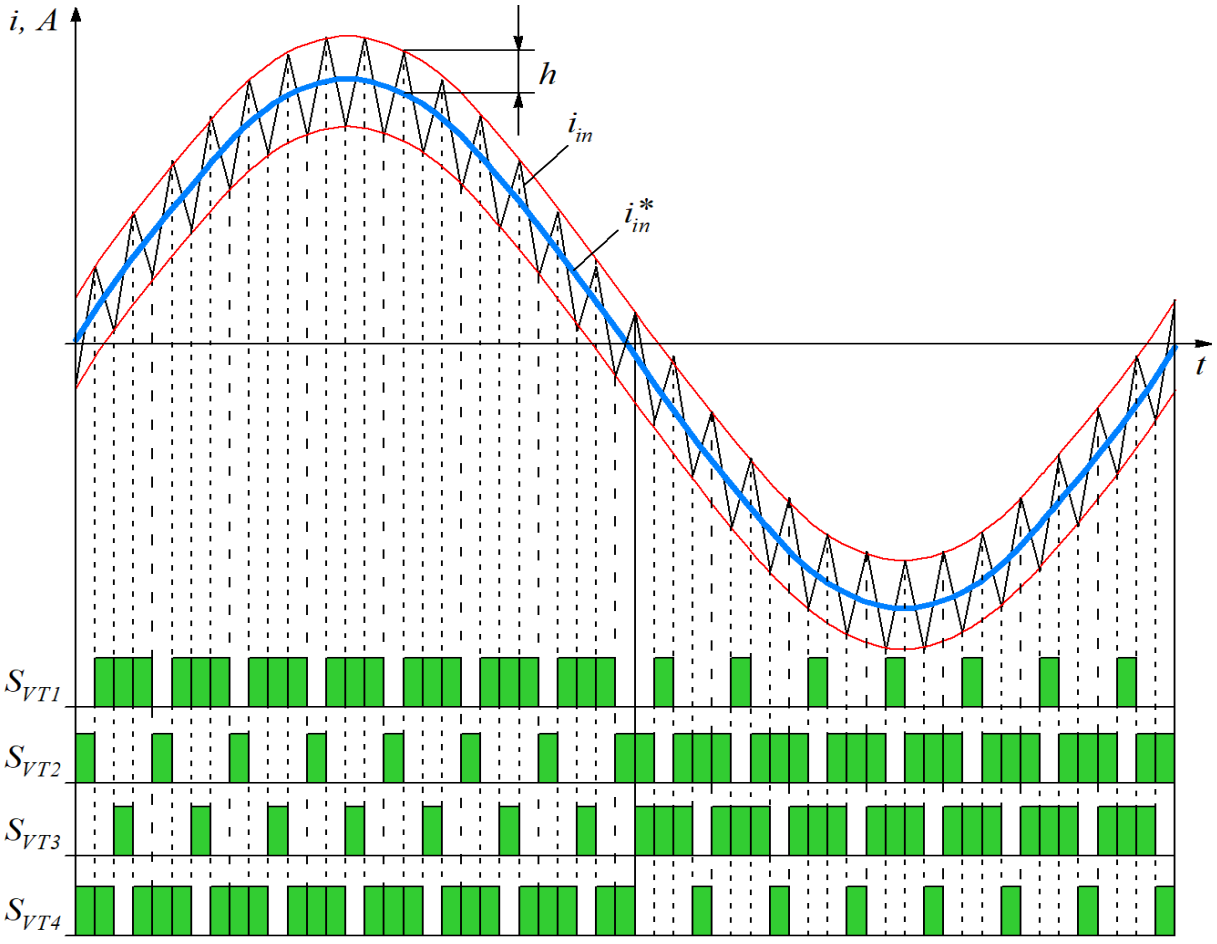

Figure 2.43 – Formation of 4QS-converter current with proposed hysteresis CS

It is worth noting that the advantage of the proposed algorithm is that all four switches of the modulation algorithm have the same dynamic losses.

As can be seen from fig. 2.43 and table 2.7, the proposed switching algorithm makes it possible to reduce the number of switches, which reduces the total dynamic losses in the switches of the 4QS-converter with the hysteresis CS up to 50 %, which increases its efficiency. The energy-saving effect of the introduction of an improved hysteresis modulation algorithm was determined by means of the calculation of power losses in the active four-square converter at its output voltage of 3000 V.

The calculation was performed with power IGBTs with a nominal voltage of 4500 V of series CM1200HG-90G [72, 73]. The basic parameters of the CM1200HG-90G transistor are given in table 2.8.

Table 2.8 – Boundary parameters of CM1200HG-90G transistor

Parameter	Value
Voltage between collector and emitter, V	4500
Gate-emitter voltage, V	±20
Permissible DC load current, A	1200
Permissible pulse current, A	2400
Insulation voltage, V	10200
Permissible transistor temperature, °C	–50…150

The actual oscillograms of the current and voltage switching of the power IGBT CM1200HG-90G are shown in fig. 2.44. In the calculations, the total power losses in power transistors are divided into two components: static and dynamic losses.

The power losses in IGBTs can be calculated with static P_{DC} and dynamic P_{SW} losses in IGBTs and parallel diodes [74, 75]:

$$P = P_{DC} + P_{SW}, \tag{2.9}$$

where P_{DC} – the static losses in the IGBT; P_{SW} – the dynamic losses in the IGBT.

Static power losses P_{DC} in power IGBTs are determined in accordance with the expression:

$$P_{DC} = U_{ce} \cdot I_c \cdot \alpha, \tag{2.10}$$

where U_{ce} – the voltage drop between the collector and the emitter of the transistor; I_c – the current of the transistor collector; α – the fill factor during modulation.

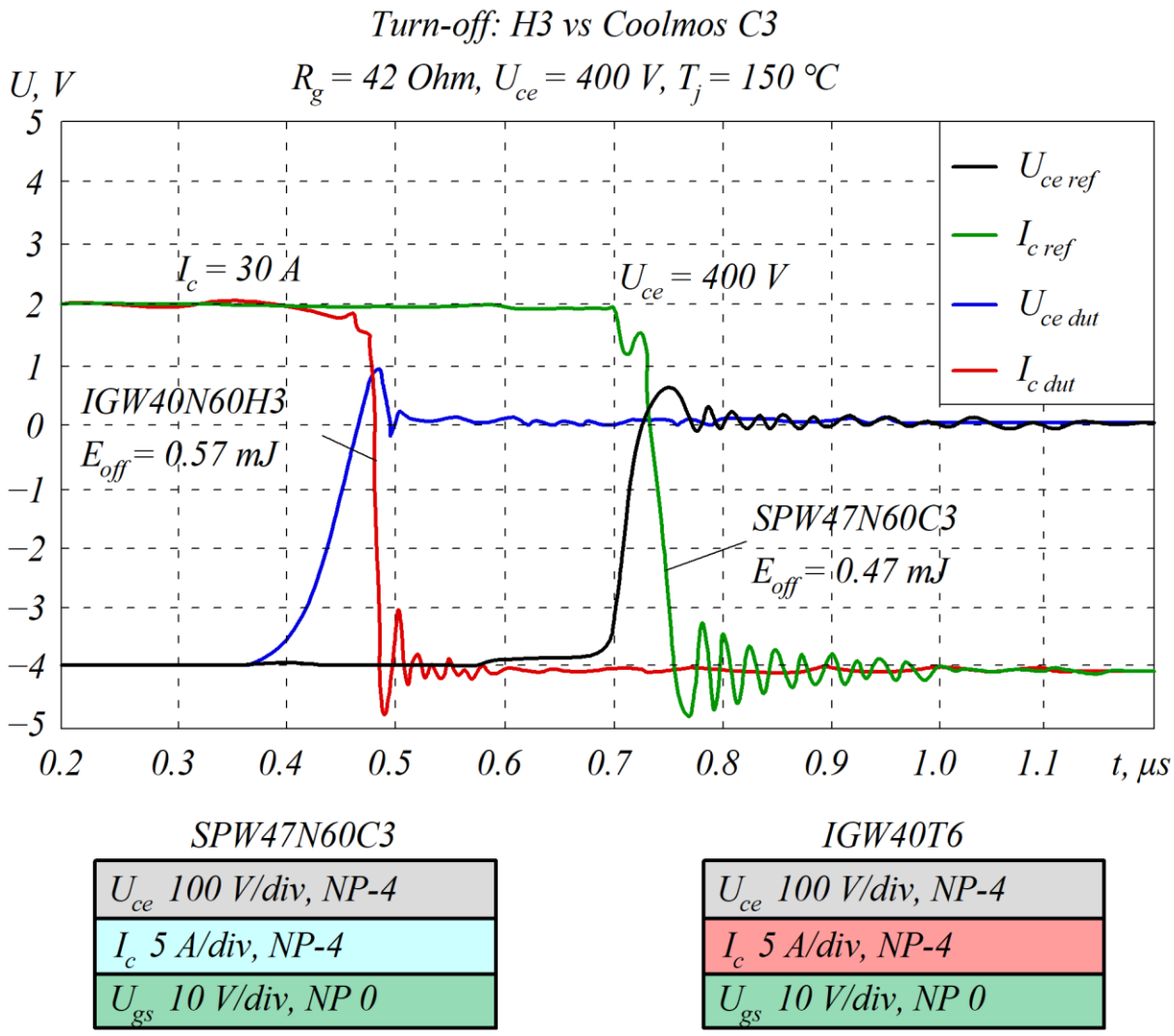

Figure 2.44 – Current and voltage switching

Fig. 2.45 shows the dissipation of the power IGBT during switching.

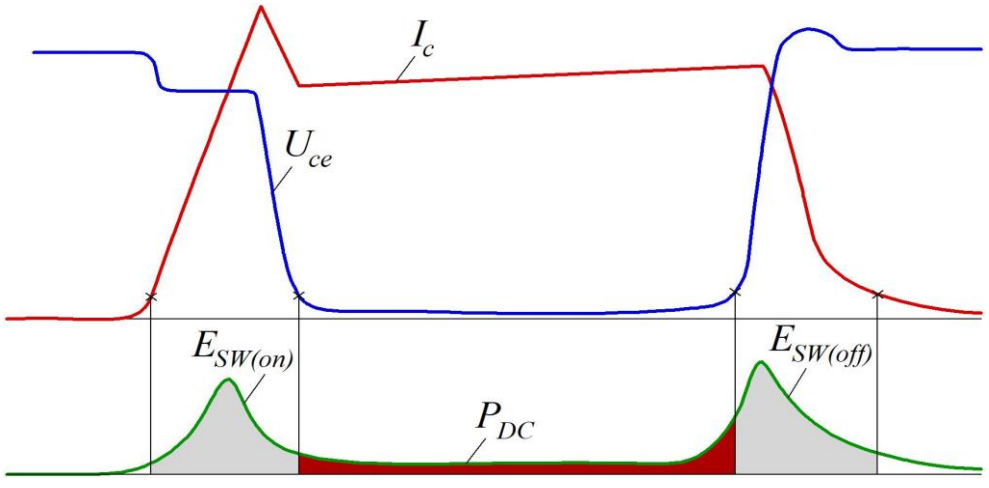

Figure 2.45 – Power dissipation of power IGBT

Dynamic power losses P_{SW} in power IGBTs are determined from the expression:

$$P_{SW} = \left(E_{on} + E_{off}\right) \cdot f, \tag{2.11}$$

where E_{on} – the energy dissipated in the transistor when turned on; E_{off} – the energy dissipated in the transistor when turned off; f – the switching frequency of the power switches.

$$E_{on} = \int_{t1}^{t2} U_{ce} \cdot I_c \cdot dt; \tag{2.12}$$

$$E_{off} = \int_{t3}^{t4} U_{ce} \cdot I_c \cdot dt. \tag{2.13}$$

The results of the calculations were used for building the basic energy characteristics of the CM1200HG-90G power transistor. Fig. 2.46 shows the dependence of the voltage between the collector and the emitter on the load current. Fig. 2.47 shows the dependence of the switching energy of the transistor on the load current.

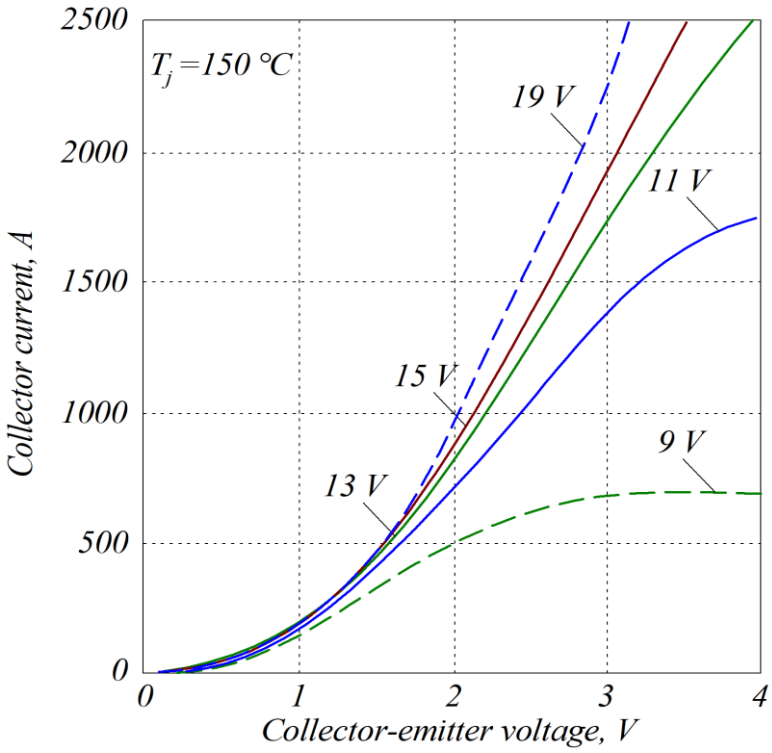

Figure 2.46 – Dependence of voltage between collector and emitter on load current

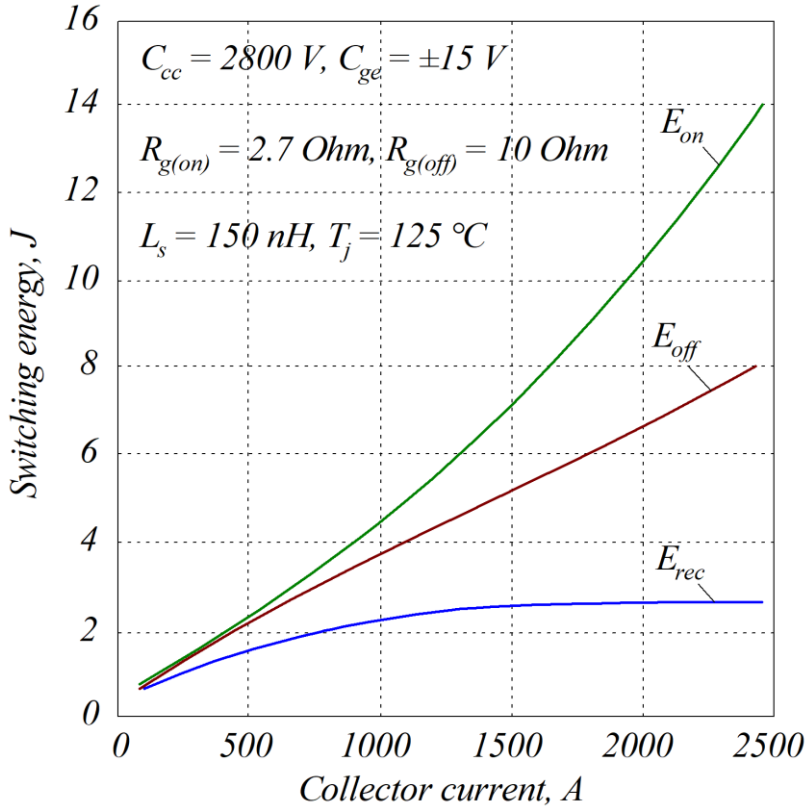

Figure 2.47 – Dependence of switching energy of transistor on load current

Practically power losses are determined according to the documentation for each specific power IGBT.

An automated calculation of power losses in power IGBTs was conducted by means of the current voltage characteristics of the transistor and the dependence of the switching-on and switching-off energy on the load current, which were approximated by the least squares method.

The least squares method is based on the principle of minimizing the sum of squared errors of functions on the sought variables.

The approximation can be performed using polynomials of different orders. The greater the degree of polynomial describing the equation order, the higher is the accuracy.

At the same time, a higher polynomial degree complicates the calculation and makes the simulation time longer.

The result of the approximation of the current voltage characteristic $U_{ce}(I)$ of the power IGBT CM1200HG-90R with polynomial functions of degrees 5, 4 and 3 is given in the following expressions:

$$U_{ce5}(I) = 0,762 \cdot I^5 - 4,411 \cdot I^4 + 9,686 \cdot I^3 - 10,245 \cdot I^2 + 7,199 \cdot I + 1,017; \quad (2.14)$$

$$U_{ce4}(I) = -0{,}5901 \cdot I^4 + 2{,}9832 \cdot I^3 - 5{,}311 \cdot I^2 + 5{,}8917 \cdot I + 1{,}0803; \quad (2.15)$$

$$U_{ce3}(I) = 0{,}5776 \cdot I^3 - 2{,}3224 \cdot I^2 + 4{,}6356 \cdot I + 1{,}1783. \quad (2.16)$$

In the expressions, the current is presented in kiloamperes. The dependence of the approximation reliability R^2 of the relative calculation error $U_{ce}(I)$ on the equation order is given in table 2.9.

Table 2.9 – Approximation accuracy parameters

Degree of polynomial approximation $U_{ce}(I)$	Approximation accuracy R^2
$U_{ce3}(I)$	99.72
$U_{ce4}(I)$	99.89
$U_{ce5}(I)$	99.96

The dependence of the relative calculation error $U_{ce}(I)$ on the equation order is given in table 2.10.

The results of approximation of the current voltage characteristic by the polynomial of degree 5 showed that the relative reduced error does not exceed 1 %, which provides sufficient calculation accuracy. Therefore, the polynomial function of degree 5 was chosen for approximation.

The approximation of dependencies between the energy of switching-on $E_{on}(I)$, and switching-off $E_{off}(I)$ and the restoring energy $E_{rec}(I)$ on the load current is carried out with the expressions:

$$E_{on}(I) = -0.154 \cdot I^5 + 0.847 \cdot I^4 - 1.243 \cdot I^3 + 1.014 \cdot I^2 + 3.693 \cdot I + 0.351; \quad (2.17)$$

$$E_{off}(I) = 0.213 \cdot x^5 - 1.265 \cdot x^4 + 2.935 \cdot x^3 - 3.389 \cdot x^2 + 4.875 \cdot x + 0.321; \quad (2.18)$$

$$E_{rec}(I) = -0.187 \cdot I^5 + 1.156 \cdot I^4 - 2.559 \cdot I^3 + 1.707 \cdot I^2 + 1.636 \cdot I + 0.509. \quad (2.19)$$

The results of approximation of the energy characteristics of the power transistor CM1200HG-90G are shown in fig. 2.48. The above-presented calculations show that the use of the proposed switching algorithm for power switches makes it possible to reduce power losses in power switches.

To confirm the reduction of dynamic power losses and improve the quality of the input current of the active rectifier, a simulation model was developed in Matlab.

Table 2.10 – Dependence of relative calculation error on equation order

Collector current I, A	U_{ce} according to the documentation for transistor, V	U_{ce5}, V	Relative reduced error for calculation of polynomials of degree 5, %	U_{ce4}, V	Relative reduced error for calculation of polynomials of degree 4, %	U_{ce3}, V	Relative reduced error for calculation of polynomials of degree 3, %
0.00	1.01	1.02	–0.68	1.08	–6.96	1.18	–16.66
0.10	1.65	1.64	0.38	1.62	1.86	1.62	1.87
0.20	2.15	2.12	1.50	2.07	3.76	2.02	6.18
0.30	2.50	2.48	0.70	2.45	2.18	2.38	4.98
0.40	2.75	2.77	–0.81	2.76	–0.47	2.70	1.89
0.50	3.00	3.01	–0.48	3.03	–1.15	2.99	0.41
0.60	3.20	3.23	–0.89	3.27	–2.23	3.25	–1.51
0.70	3.40	3.43	–0.82	3.48	–2.46	3.48	–2.45
0.80	3.65	3.62	0.76	3.68	–0.83	3.70	–1.27
0.90	3.83	3.82	0.25	3.87	–1.14	3.89	–1.71
1.00	4.05	4.02	0.77	4.05	–0.10	4.07	–0.47
1.10	4,.20	4.20	–0.04	4.24	–0.99	4.24	–0.86
1.20	4.40	4.39	0.19	4.43	–0.77	4.39	0.12
1.30	4.55	4.57	–0.55	4.63	–1.82	4.55	0.03
1.40	4.75	4.75	0.01	4.84	–1.85	4.70	1.03
1.50	4.90	4.91	–0.28	5.05	–3.04	4.86	0.90
1.60	5.05	5.07	–0.37	5.26	–4.21	5.02	0.68
1.70	5.20	5.22	–0.35	5.48	–5.29	5.18	0.29
1.80	5.38	5.37	0.09	5.68	–5.70	5.37	0.16
1.90	5.60	5.54	1.10	5.87	–4.88	5.56	0.65
2.00	5.70	5.74	–0.72	6.04	–6.03	5.78	–1.42

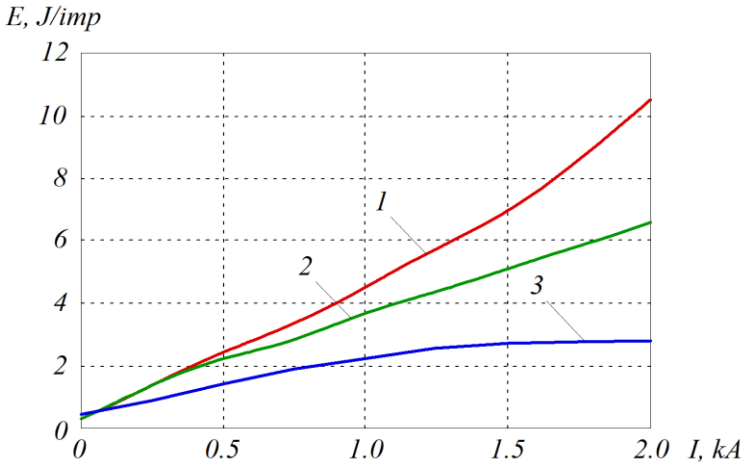

Figure 2.48 – Results of approximation of dependence between switch-on (*1*), switch-off (*2*) and recovery (*3*) energies and load current

The simulation model designed describes the electromechanical system of the main AC electric locomotive DS3, i.e. the 4QS–AVI–AM system. Parameters for the DS3 electric locomotive are given in table 2.11.

Table 2.11 – Parameters of electric locomotive DS3

Parameter	Value
Voltage in the overhead network, kV	25
Output voltage of traction transformer, V	800
Output voltage of 4QS-converter (voltage in DC circuit), V	1400
Input inductance of 4QS-converter, mH	0.5
Capacitance of output capacitor, mF	24
Load current, A	200…1200

The simulation model has a basic and improved hysteresis CS with an active four-quadrant transducer. The main parameters of the simulation model are given in table 2.12. The model describes electromagnetic processes in the active four-quadrant transducer with basic and improved hysteresis modulation of the electromechanical system (fig. 2.49).

Table 2.12 – Main parameters of simulation model

Parameter	Value
Time sampling of simulation model calculation, μs	1
Allowable simulation error, %	0.1
Amplitude value of input voltage of active four-quadrant converter, V	600
Adjustment factor value ξ	1…2.5
Input inductance, mH	0.4…0.8
Active resistance of input inductance, mOhm	15
Filter capacitance in DC circle, mF	3
Voltage in DC circuit, V	600…1500
RMS of load current of active converter, A	590
Parameters of traction motor by type	CTA1200

The modelling was carried out through solving differential equations describing the models by means of the ode23tb operator, which uses the implicit Runge-Kutta method at the beginning and then the method based on the reverse differentiation equations of the 2nd order. The allowable relative calculation error was 0.01 %.

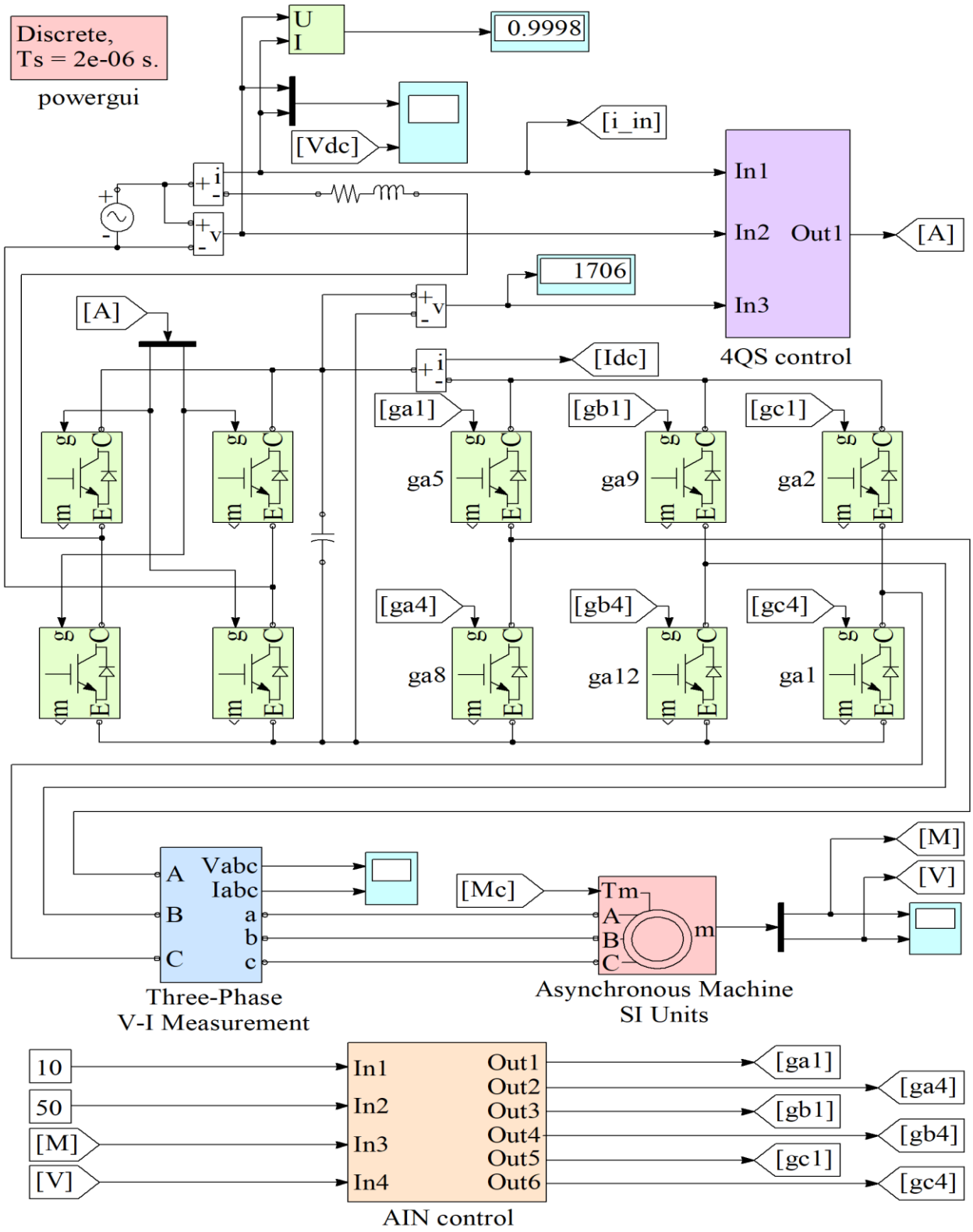

Figure 2.49 – Simulation model of electromechanical system 4QS–AVI–AM

To estimate the dynamic losses in the power transistors of the active four-quadrant converter in the model, a counter of power switch on and off signals is used. It should be noted that the use of the proposed switching algorithm of power switches for the hysteresis modulation leads to a decrease in the higher harmonic amplitudes in

the input current and simultaneous expansion of its spectrum. The results of simulation modelling of the traction electric drive system with an input inductance of 0.4 mH and a hysteresis setpoint of 20 A are shown in fig. 2.50.

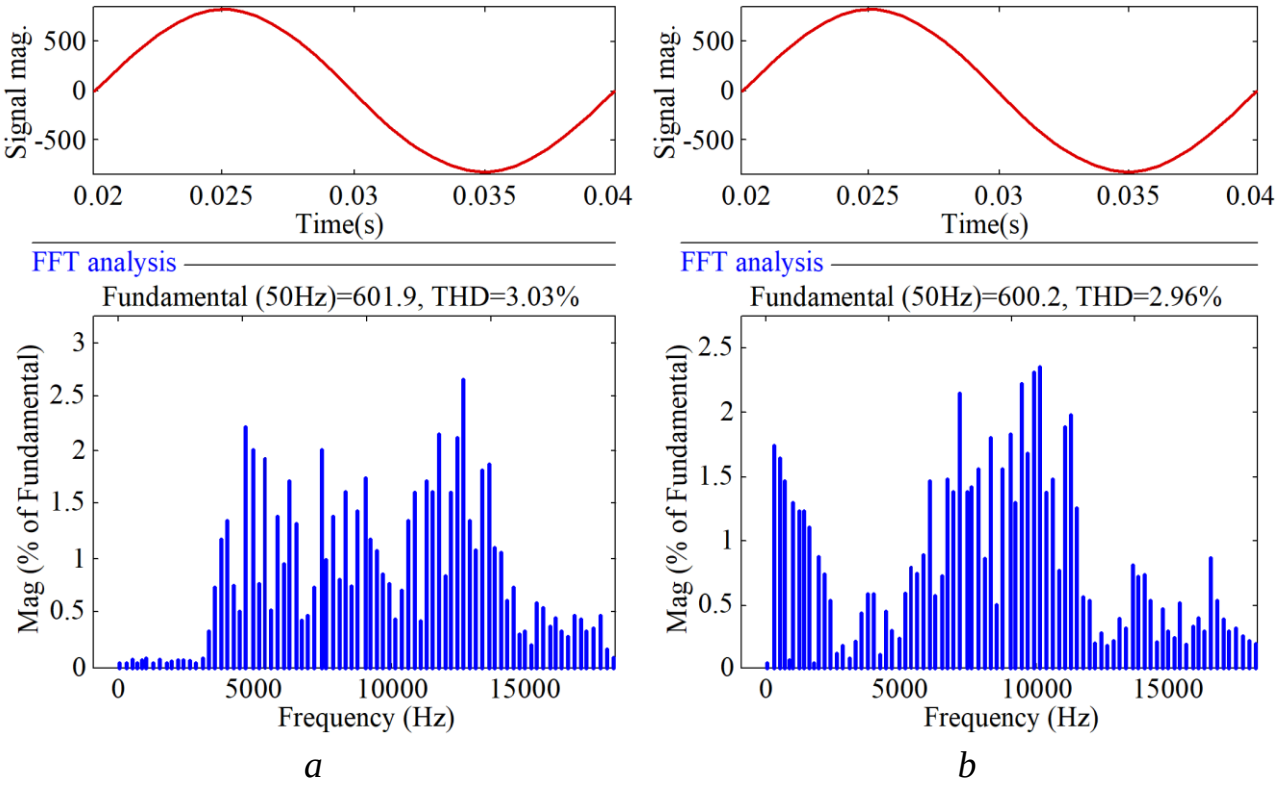

Figure 2.50 – Fourier analysis of input current of active rectifier:
a – with basic hysteresis CS; *b* – with improved hysteresis CS

The results of the simulation modelling obtained confirm a decrease in the number switches of power switches, and, accordingly, a decrease in the dynamic losses. Given that the switching frequency of the power switches is variable, it was evaluated with averaged values at the supply voltage period.

Table 2.13 shows the energy characteristics of the 4QS-converter at different values of the input inductance and different values of the hysteresis setpoints (voltage in the DC circle of 1 kV, load current of 200 A). It can be seen from table 2.13 that the power losses and the THD value for the improved hysteresis CS are significantly lower than those for the classical one, which confirms the feasibility of its use.

The developed simulation model makes it possible to study the rectification and regeneration modes in traction converters. The rectification mode will be carried out at the value of the adjustment coefficient ξ in the positive range of values. Under such conditions, the energy from the overhead network will be transmitted from the power supply network through the input 4QS-converter, through the DC link and the AVI to

the asynchronous traction motor. In the regeneration mode, the asynchronous traction motor switches to the generator mode, and the input 4QS-converter must operate in the negative range of the adjustment factor ξ.

Table 2.13 – Energy characteristics of 4QS-converter

Input inductance, mH	Hysteresis setpoint, A	Classic hysteresis CS			Improved hysteresis CS		
		Average switching frequency at the period, Hz	THD, %	Power losses, kW	Average switching frequency at the period, Hz	THD, %	Power losses, kW
0.4	20	13340	3.26	49.44	7230	2.96	27.76
	30	9400	4.60	35.44	4810	4.36	19.20
	40	7250	5.96	27.84	3740	5.79	15.40
0.6	20	9300	3.07	35.12	5430	2.83	21.40
	30	6440	4.43	24.80	3690	4.20	15.20
	40	4930	5.78	19.60	2790	5.58	12.02
0.8	20	7070	2.99	27.20	4020	2.79	16.38
	30	4850	4.34	19.32	2720	4.28	11.76
	40	3700	5.70	15.28	2060	5.66	9.40

The limitation of the study is that the developed simulation model adequately operates only in nominal modes, and in emergency modes, at which the current and voltage values exceed the nominal values, the model will not adequately reflect. Such a limitation should be taken into account in the practical application when studying start-up and emergency modes.

2.5. Hysteresis control system for active three-phase rectifier with power factor compensation

The diode and thyristor rectifiers used as part of the DC transformer rectifier at the PS do not meet the requirements of the International Standards IEC 61000-3, IEEE 519, EN 61000-3-2 EMC in terms of emission of higher current harmonics. In addition, these rectifier units do not provide the possibility of implementing regeneration energy into the power supply network, which reduces the energy efficiency of these converters.

Analysis of the electromagnetic processes in the AVR requires the creation of a mathematical and dynamic model of the converter. The mathematical model can be used to analyse constant and transient processes, obtain static and dynamic

characteristics of the converter, synthesize closed-loop automatic control systems (ACS), as well as analyse the stability of the converter and its CS [76].

The research into dynamic characteristics of the pulse energy converter can be considered from the standpoint of discrete or continuous ACSs. As known, discrete mathematical models of transducers can be reduced to equivalent continuous models [77]. This approach is based on the presentation of the power part of the converter and its CS in the form of continuous ARS links, which makes it possible to simplify their description. It should be noted that the representation of the converter as a continuous ARS is applicable if the load time constant is much higher than the sampling period of the converter.

The sampling period of the transducer, comparable to the load time constant, when the transducer is presented as a discrete element, is more accurate. Thus, the model may include more realistic reflection of the transient processes running in the converter, besides, this makes it possible to investigate the influence of the CS switching functions on the converter operation. At the same time, according to the automatic control theory, the active rectifier with power factor correction is a nonlinear discrete ARS element.

A mathematical model can be built with the dependence of the output voltage on the input voltage using possible combinations of activation switches for the AVR. This is the concept of switching logic variable switches: S_a, S_b, S_c. The value of the switching logic variables determines the position of the connection switches in the AVR. If the switch of the anode connection group of the phase A is enabled, then $S_a = 1$. If the switch of the cathode connection group of the phase A is enabled, then $S_a = 0$. At the same time, the switches of the anode and cathode groups of the AVR cannot be enabled simultaneously. Only one switch of the converter connection must be in the ON position, otherwise a DC short circuit will occur.

At the same time, the energy stored in the output capacitor will be sufficient to physically destroy the switch structure. Possible combinations of AVR switches are shown in fig. 2.22.

Thus, if the switches of the anode group are enabled, the values of the switching functions are taken equal to “1”. For example: $S_a = 1$; $S_b = 1$; $S_c = 1$. If the switches of the cathode group are enabled, the values of the switching functions are assumed to be “0”. For example: $S_a = 0$; $S_b = 0$; $S_c = 0$.

Thus, eight possible switching positions of the converter switches can be presented as eight spatial voltage vectors in the $\alpha\beta$-coordinate system. The AVR voltage vectors are shown in fig. 2.51. It should be noted that six of them are active vectors, and two vectors are null.

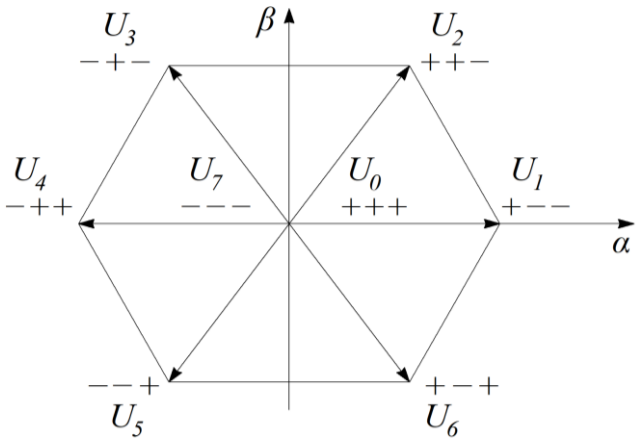

Figure 2.51 – Spatial voltage vectors of AVR

The mains phase voltages, which do not contain higher harmonic components and applied to the inlet throttles from the mains side, are described by the following equations:

$$u_{AN} = E_m \cdot \sin(\omega t); \tag{2.20}$$

$$u_{BN} = E_m \cdot \sin\left(\omega t + \frac{2\pi}{3}\right); \tag{2.21}$$

$$u_{CN} = E_m \cdot \sin\left(\omega t - \frac{2\pi}{3}\right), \tag{2.22}$$

where E_m – the amplitude value of the phase voltage of the network; ω – the circular frequency of the phase voltage.

The AVR forms the sinusoidal phase currents by setting the required voltage modulation law applied to the inlet throttles on the side of the converter.

Fig. 2.52 shows the equivalent circuit of the phase A of the active rectifier with the following notations: U_a – the mains phase voltage; R_0 – the inlet throttle active resistance; U_{conv} – the AVR voltage applied to the inlet throttle from the active rectifier.

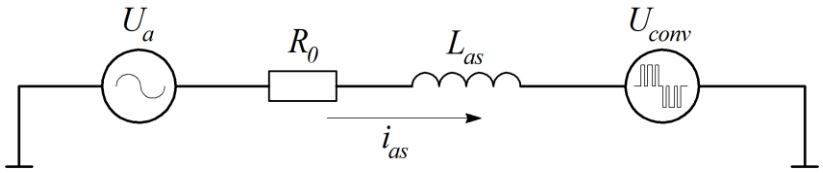

Figure 2.52 – Equivalent circuit of the phase A of the active rectifier

Using Kirchhoff's second law, let us write an equation that links the modulation voltage and the current flow:

$$U_a + U_{conv} = i_{as} \cdot R + L\frac{di_{as}}{dt}. \quad (2.23)$$

Linear voltages applied to the inlet throttles from the active rectifier can be presented as functional dependencies on the switching logic variables and the output voltage value:

$$u_{AB\_conv} = (S_A - S_B) \cdot u_{DC}; \quad (2.24)$$

$$u_{BC\_conv} = (S_B - S_C) \cdot u_{DC}; \quad (2.25)$$

$$u_{CA\_conv} = (S_C - S_A) \cdot u_{DC}, \quad (2.26)$$

where u_{AB_conv}, u_{BC_conv}, u_{CA_conv} – the linear voltage applied to the inlet throttles from the active rectifier; u_{DC} – the output voltage of the AVR.

The ratio of the phase voltages applied to the inlet throttles from the AVR, and the voltage in the DC circle of the converter are expressed by the following equations:

$$u_{A\_conv} = f_a \cdot u_{DC}; \quad (2.27)$$

$$u_{B\_conv} = f_b \cdot u_{DC}; \quad (2.28)$$

$$u_{C\_conv} = f_c \cdot u_{DC}, \quad (2.29)$$

where f_a, f_b, f_c – the switching functions; u_{A_conv}, u_{B_conv}, u_{C_conv} – the phase voltage applied to the inlet throttles from the active rectifier.

Switching functions are determined from the following expressions:

$$f_a = \frac{2 \cdot S_A - (S_B + S_C)}{3}; \quad (2.30)$$

$$f_b = \frac{2 \cdot S_B - (S_A + S_C)}{3}; \quad (2.31)$$

$$f_c = \frac{2 \cdot S_C - (S_A + S_B)}{3}. \quad (2.32)$$

In equations (2.30)…(2.32), the variables f_a, f_b, f_c obtain values of 0, ±1/3, ±2/3.

The vector equation describing the voltage balance in the active rectifier in vector form is given below:

$$\bar{u}_s = R \cdot \bar{l}_s + L \frac{d\bar{l}_s}{dt} + \bar{u}_{conv}, \quad (2.33)$$

where $\bar{u}_s$ – the network voltage vector; $\bar{l}_s$ – the vector of the input phase currents of the AVR formed during modulation; $\bar{u}_{conv}$ – the vector of the voltage applied to the inlet throttle from the active rectifier; R – the active resistance of the inlet throttles; L – the inductance of the inlet throttle.

The output voltage u_{DC} of the AVR is formed by phase currents. The differential equation describing the dependence of the output voltage on the magnitude of the phase currents is as follows:

$$C \frac{du_{DC}}{dt} = S_a \cdot i_a + S_b \cdot i_b + S_c \cdot i_c - i_{DC}, \quad (2.34)$$

where i_{DC} – the load current of the AVR; C – the capacitance of the output capacitor; i_a, i_b, i_c – the phase currents of the AVR.

Fig. 2.23 shows the dynamic model of the power part of the AVR, based on equations (2.20)...(2.34). The input signals of the dynamic model are the phase voltage of the network and switching logic variables S_a, S_b, S_c, obtained from the CS of the AVR. The output signal of the model is the output voltage of the active rectifier.

The advantage of the proposed model, in contrast to those given in works [78,79], is that it provides information on the phase currents being formed, which are intermediate signals in the model, and also takes into account the peculiarities of the processes in the AVR according to the CS applied.

The most important component of active transducers, which enables to realize the effect of power factor compensation, is its CS. At present there are many different CSs of the AVR. The most important differences of the CS are due to the type of regulator used and the type of modulation implemented. They include hysteresis CS, built on hysteresis modulation, and its modification, as well as CS with a constant frequency based on a multitude types of PWV software. Various types of regulators

can be implemented as an output voltage regulator: PI, PID, phase-regulators, and adaptive regulators. Among the above-described systems, the most widespread are hysteresis CSs.

Generally, the CS of the AVR consists of the following components:

– meters of instantaneous values of input phase currents, phase voltages of the network and output voltage of the rectifier; for the regeneration process, the load current of the rectifier must be measured;

– task signal conditioner, which determines the instantaneous value of the first harmonics in the phase voltage;

– output voltage regulator and regeneration mode; and

– delta modulator.

The analysis of the regulatory characteristics of the AVR with hysteresis CS demonstrated that for regeneration the AVR must also be equipped with a load current meter to maintain a given voltage in the regeneration mode.

When implementing a digital CS, it is necessary to consider the structural features of the measuring part and the choice of an analogue-to-digital converter, taking into account the sampling frequency.

The task signal conditioner can be made both in the *abc*-coordinate system and using the principles of the instantaneous power theory, and the task signal formation can be implemented by transforming the coordinate systems *abc-αβ0*, *abc-pqr*, *abc-dqo* [80].

The hysteresis modulation is based on the comparison of the instantaneous value of the input current with the task signal. In terms of this the task signal is a scaled input phase voltage signal. The scaling of the signal of the first harmonic of the phase voltage is carried out by a regulator by setting the required value of the output voltage. Thus, the hysteresis type of modulation is the simplest, though reliable, in addition, it carries out bidirectional energy transfer in the active rectifier [81].

The CS of the AVR with hysteresis modulator is shown in fig. 2.13. The figure has the following notations: U_a, U_b, U_c – the signals of instantaneous values of phase voltages; i_a, i_b, i_c – the signals of instantaneous values of phase currents; U_{out_as} – the output voltage setting signal; U_{out} – the output voltage sensor signal; I_{out} – the load current sensor signal. The difference from the known CSs is the output current sensor, which provides a regeneration mode and maintains a given value of the output voltage.

In the CS, the inconsistency signal Δi is supplied to the hysteresis modulator. If the inconsistency signal Δi is higher than the setting value of the hysteresis modulator, the anode group switch is closed, and the cathode group switch is opened, after which the instantaneous value of the current in the phase decreases. At the moment when the

instantaneous value of the scaled phase current decreases and is less than the instantaneous value of the phase voltage by the hysteresis value, there is a reverse switching of the switches, the anode group switch is opened, and the cathode group switch is closed, after which the instantaneous value of the phase current increases. The form of the task signal and the shaped current of phase A, as well as the control signals to the switches *VT1* and *VT2* of the active rectifier are shown in fig. 2.53. The following notations are used in the figure: I_{sa}^{*} – the phase current shape task signal obtained by scaling the phase voltage; i_{a_am} – the instantaneous value of the shaped phase current; *hyst* – the value of the hysteresis task in the CS.

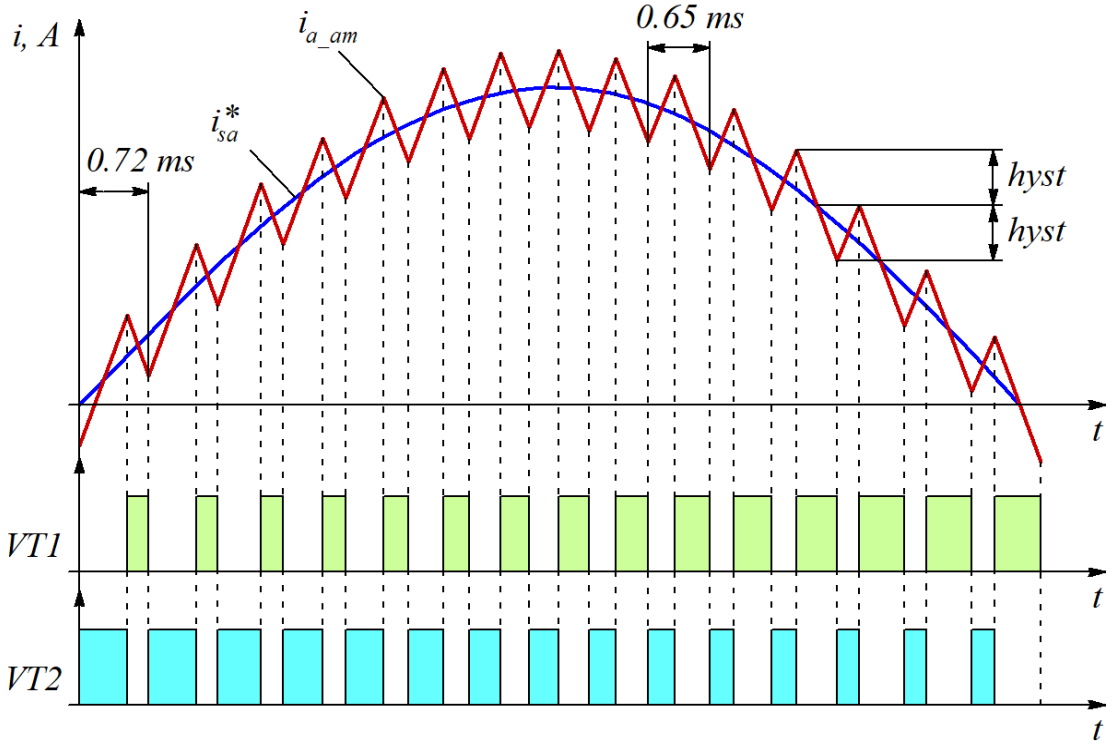

Figure 2.53 – Principle of current formation in hysteresis modulation

Thus, when setting a fairly small value of hysteresis, the CS forms a practically sinusoidal phase voltages. The output voltage is adjusted by setting the required scale of the phase current relative to the phase voltage. Therefore, the greater the magnitude of the shaped phase current, the higher the magnitude of the output voltage will be. However, it is found that this dependence is nonlinear, which is important when designing the regulator. The advantage of this CS is the possibility of implementing the highest power factor, low harmonic level, as well as minimum ripple values of the output voltage by means of inlet throttles of lower rating compared to PWM. However, at the same time, the hysteresis CS has significant disadvantages, namely, a variable and clearly unknown switching frequency. To form a harmonic coefficient lower than

5 %, the frequency can reach nearly a few tens of kilohertz. The existing element base of high-voltage power IGBTs has limited frequency properties, which imposes restrictions on the use of high-power AVRs.

The maximum switching frequency can be limited by embedding D-triggers with the switching resolution clock signal in the CS of AVRs. Under these conditions, the switching of power transistors occurs at a frequency lower than the frequency of the D-trigger clock signal (fig. 2.54). The disadvantage of this method of frequency limitation is the worse characteristics of the EMC and CS stability being implemented.

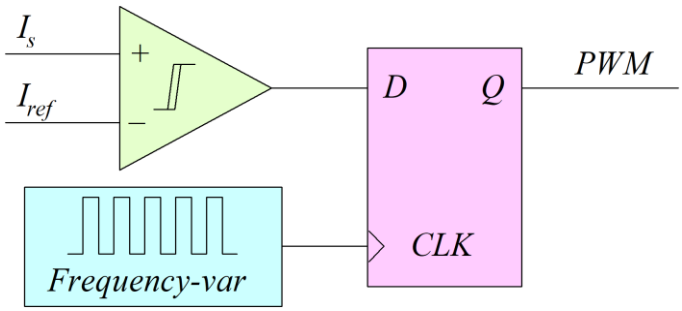

Figure 2.54 – Limitation of active rectifier switching frequency by DQ-trigger

The main advantage of this method of switching frequency limitation is that it is fairly simple and effective to limit the maximum modulation frequency, since only a D-trigger and a clock frequency generator are necessary to limit the switching frequency.

However, with this improved CS, only the maximum switching frequency is determined, the actual frequency is not determined. A significant disadvantage of the proposed method of switching frequency limitation is the deterioration of the shape of the phase currents, which impairs the power factor and the THD.

The mentioned above poses the task of obtaining analytical dependencies that determine the maximum frequency of AVR modulation with the hysteresis CS.

The switching frequency in the hysteresis CS by the active rectifier depends on the value of the hysteresis setpoint and the current increase rate di/dt. At the same time, the current increase rate di/dt depends on the diagram parameters: inductances of the inlet throttle and the network, the active resistance of the inlet throttle and the network, as well as the phase voltage and the output voltage of the rectifier.

The equation given in [82], presenting the maximum switching frequency of the AVR, does not include the load of the converter, the active resistance of the inlet throttle, the value of the output capacitance and supply voltage, and in general, it is of evaluative nature:

$$f_{\max} = \frac{U_d}{4 \cdot h \cdot L_s}, \tag{2.35}$$

where h – the value of the hysteresis band in a percentage of the full current scale; L_s – the inductance of the inlet throttle; U_d – the output voltage of the converter.

In AVR, the switching period is determined by two transient processes associated with an increase and a decrease of the phase current. The maximum switching frequency in the AVR with the hysteresis CS can be determined with the converter equivalent circuits at the intervals of current increase and decrease.

The duration of the transient process at the interval of the current increase is determined on the basis of the equivalent diagram for the state of the AVR switches. The equivalent circuits of AVRs obtained from the switching states of the switches at the current increase interval are shown in fig. 2.55.

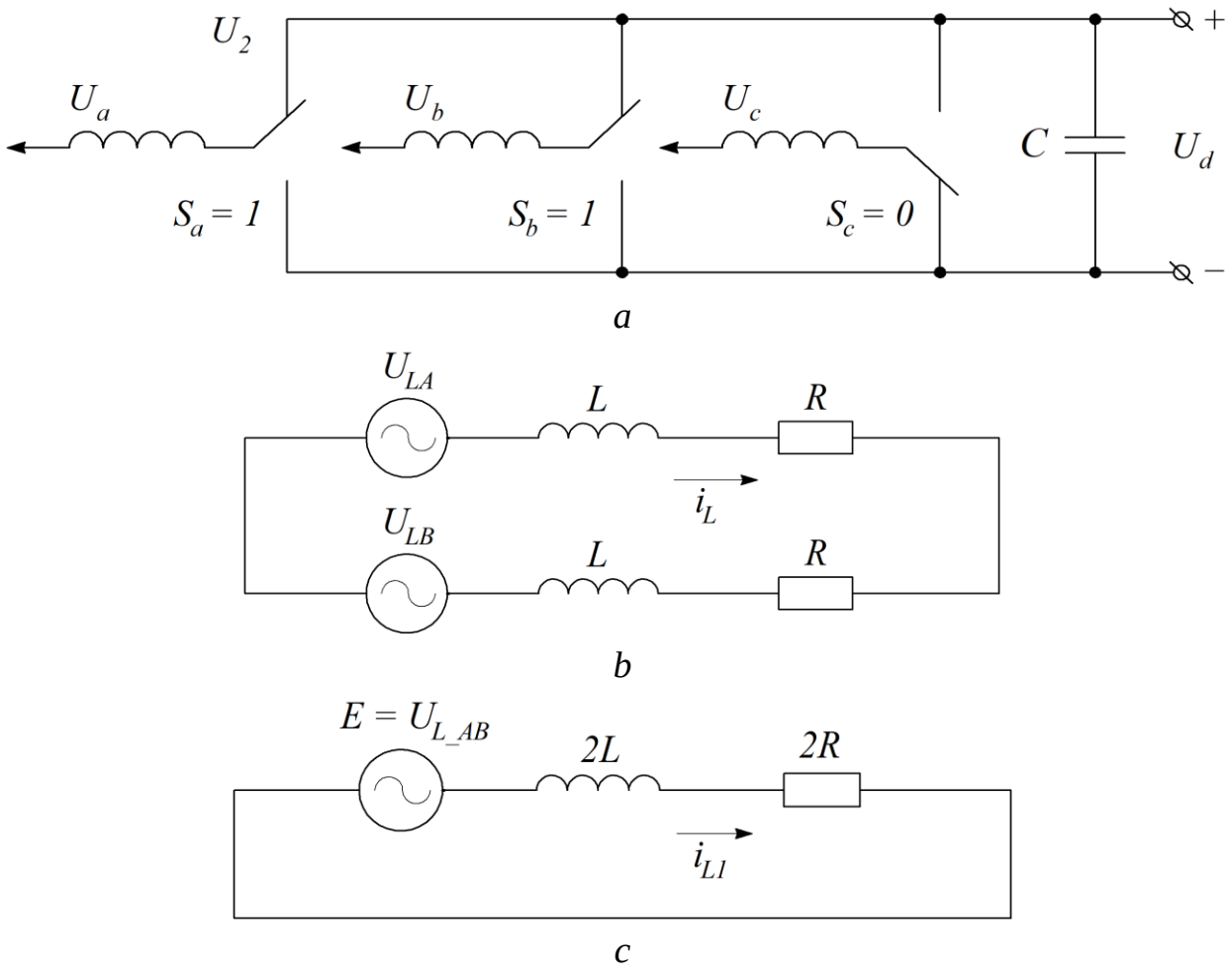

Figure 2.55 – Equivalent circuits for AVR at current increase interval:
a – switching position of AVR switches; *b* – equivalent circuit of AVR input circuit;
c – equivalent circuit at steady added voltage to inlet throttle

The maximum switching frequency is reached at the time when the instantaneous value of the line voltage of the network reaches its maximum value.

When describing the processes at the current switching interval in the hysteresis CS, it is assumed that the mains voltage added to the inlet throttle is stable. This assumption is based on the fact that during the phase current switching (frequency can reach tens and hundreds of kilohertz), the line voltage of the network practically does not change.

The transient process of current increase in the obtained equivalent circuit is determined by the sum of the forced i_{pr1} and the free component i_{sv1}:

$$i_1(t) = i_{pr1} + i_{sv1}. \tag{2.36}$$

The forced component of the transient function is a constant and is defined as:

$$i_{pr1} = \frac{U_L}{2 \cdot R_0}, \tag{2.37}$$

where U_L – the phase voltage of the mains; R_0 – the active resistance of the inlet throttle.

The free component of the transient function is an exponential function of the current increase, which is described by the expression:

$$i_{sv1} = A \cdot e^{pt}. \tag{2.38}$$

To determine the coefficient of the equation using the free component, we write the characteristic equation in the operator form:

$$p \cdot 2 \cdot L + 2 \cdot R_0 = 0. \tag{2.39}$$

The root of the obtained characteristic equation will be equal to:

$$p = -\frac{R_0}{L}. \tag{2.40}$$

Substituting expression (2.37) using equations (2.38) and (2.40), we obtain the expression of determining the coefficient A:

$$A = -i_{pr1} = -\frac{U_L}{2 \cdot R_0}. \tag{2.41}$$

Substituting expressions (2.37) and (2.38) into expression (2.36), taking into account (2.40) and (2.41), we obtain an expression that determines the law of current change at the build-up interval:

$$i_1(t) = \frac{U_L}{2 \cdot R_0} \cdot \left(1 - e^{-\frac{R_0}{L} \cdot t}\right). \tag{2.42}$$

We obtain the time of current increase taking into account the value of the hysteresis setpoint ΔI by solving equation (2.42) relative to the variable t.

$$t_1 = \frac{\ln\left(1 - \frac{\Delta I}{i_{pr1}}\right)}{p} - \frac{\ln\left(1 - \frac{\Delta I}{\frac{U_L}{2 \cdot R_0}}\right)}{-\frac{R_0}{L}}. \tag{2.43}$$

The following are graphical dependences of the time of current increase on the values of the hysteresis setpoint (fig. 2.56), the supply voltage value (fig. 2.57), the value of the inductance of the inlet throttle (fig. 2.58) for other constant values (U_L = 1400 V; R_0 = 0.001 Ohm; L = 2 mH; ΔI = 30 A).

As follows from the dependencies, the current rise time by the value of the hysteresis setpoint mostly depends on the value of the setpoint itself.

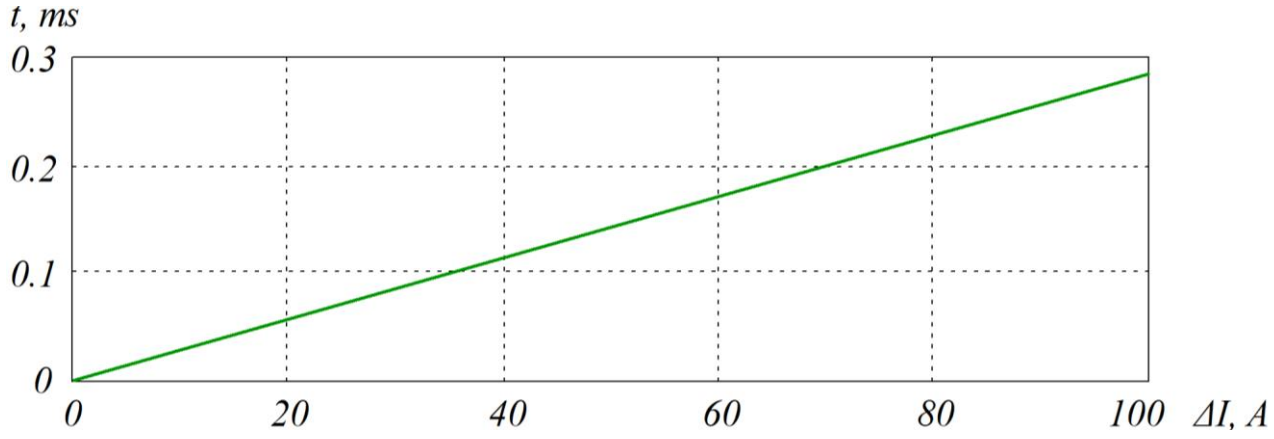

Figure 2.56 – Dependence of current rise time on hysteresis setpoint

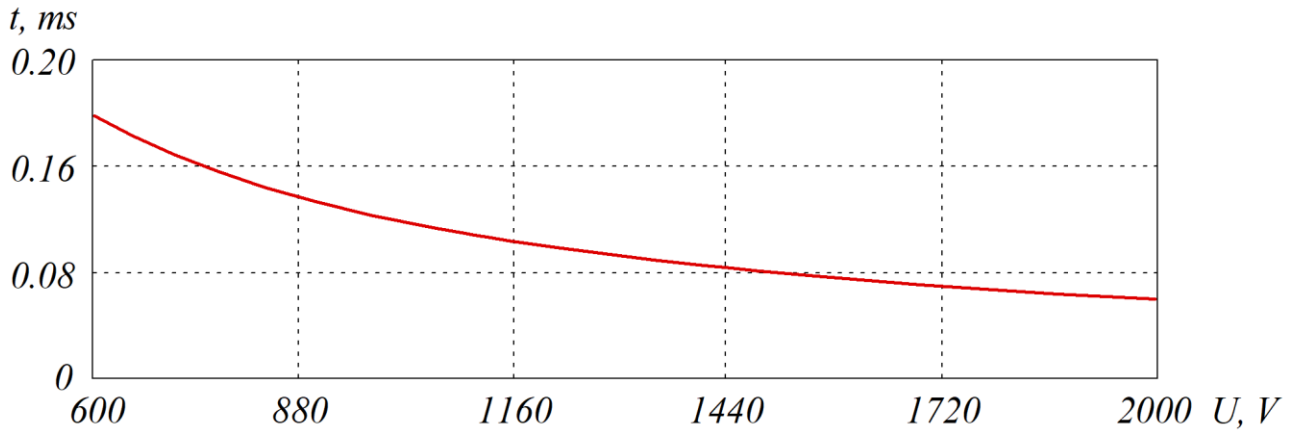

Figure 2.57 – Dependence of current rise time on supply voltage

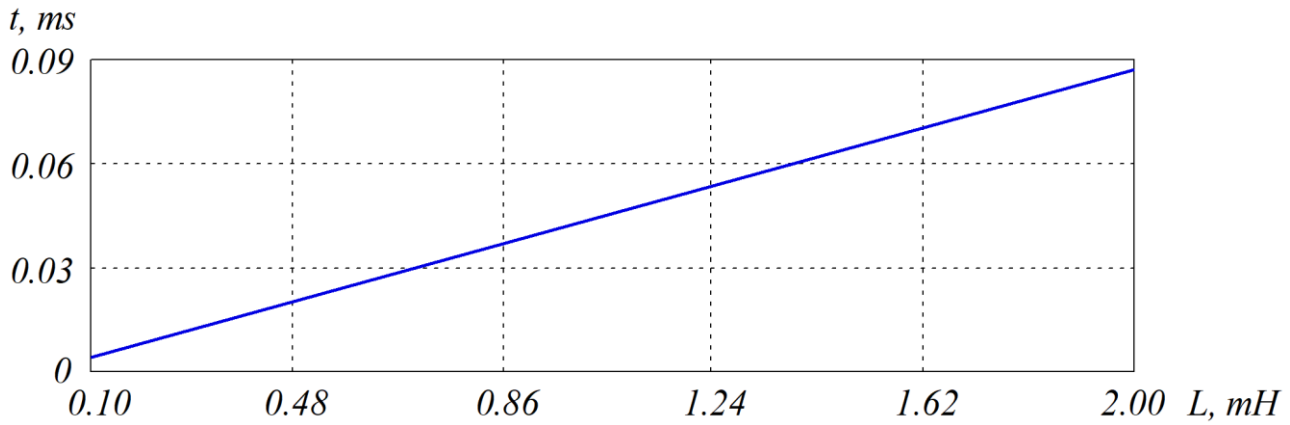

Figure 2.58 – Dependence of current rise time on inlet throttle inductance

The equivalent circuit for the AVR switch positions at the current drop interval is shown in fig. 2.59.

Similarly, the current at the drop interval according to expression (2.36) is determined by the sum of the forced i_{pr2} and the free component i_{sv2}:

$$i_2(t) = i_{pr2} + i_{sv2}. \tag{2.44}$$

When determining the forced component at the current drop interval, it is necessary to take into account the initial non-zero value of the voltage of the output capacitor U_c.

The forced component is described by the following equation:

$$i_{pr2} = \frac{U_c - U_l}{2 \cdot R_0 + R}. \tag{2.45}$$

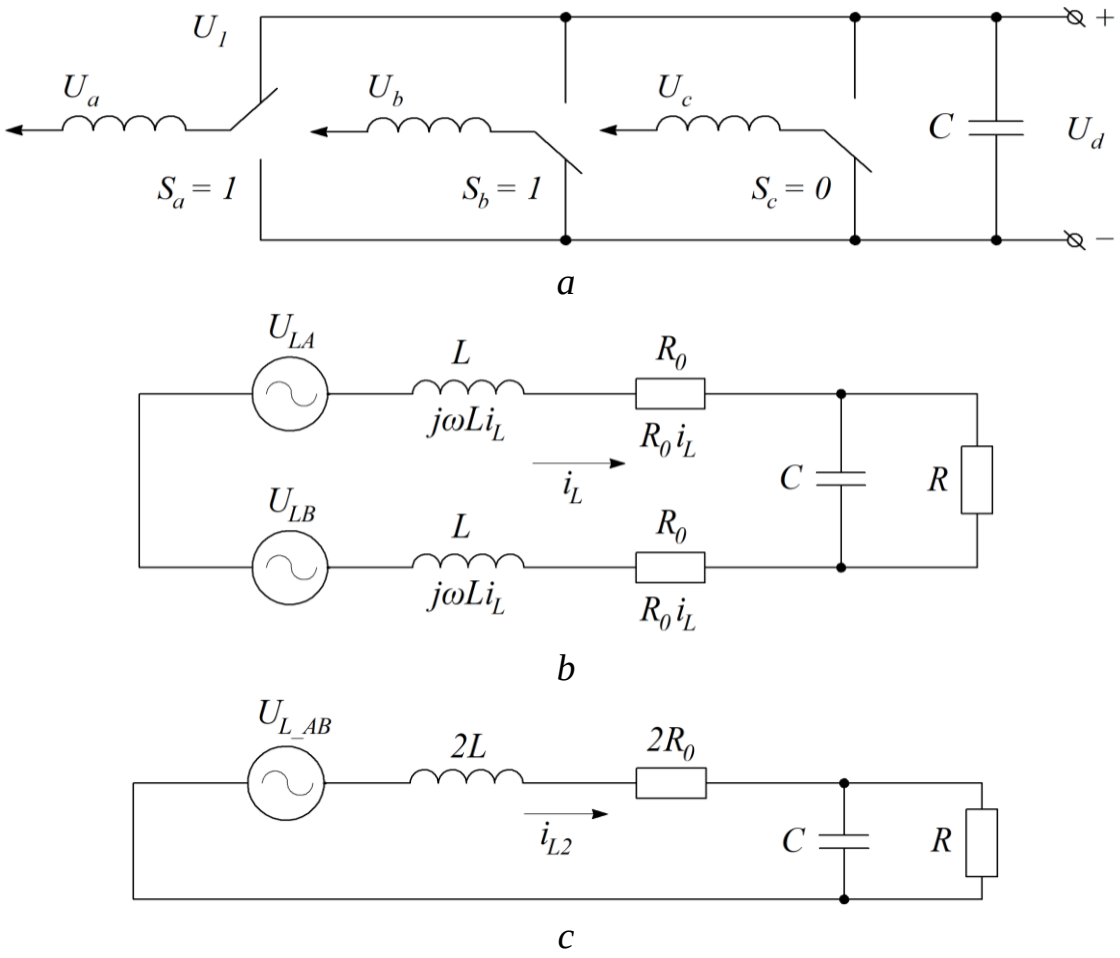

Figure 2.59 – Equivalent circuits of AVR at current rise interval:
a – switching position of AVR switches; *b* – equivalent circuit of input AVR circuit;
c – equivalent circuit at steady added voltage to inlet throttle

The free current component at the drop interval is determined by the equation:

$$i_{sv2}(t) = A_1 \cdot e^{p_1 t} + A_2 \cdot e^{p 2 t}. \tag{2.46}$$

To determine the coefficients A_1 and A_2 with the free component, we write the characteristic equation of the equivalent circuit:

$$2 \cdot R \cdot L \cdot C \cdot p^2 + (2 \cdot L + 2 \cdot R_0 \cdot R \cdot C) \cdot p + 2 \cdot R_0 + R = 0. \tag{2.47}$$

And find the roots of the characteristic equation obtained:

$$p_{1,2} = \frac{-2 \cdot L - 2 \cdot R_0 \cdot R \cdot C \mp \sqrt{(2 \cdot L + 2 \cdot R_0 \cdot R \cdot C)^2 - 4 \cdot R \cdot 2 \cdot L \cdot C \cdot (2 \cdot R_0 + R)}}{2 \cdot R \cdot 2 \cdot L \cdot C}. \tag{2.48}$$

The coefficients A_1 and A_2 can be determined through the equation system:

$$\begin{cases} p_1 \cdot A_1 + p_2 \cdot A_2 = 0; \\ A_1 + A_2 + i_{pr} = 0. \end{cases} \tag{2.49}$$

By solving equation system (2.49), the following expressions for the coefficients A_1 and A_2 can be obtained:

$$A_1 = -A_2 \cdot \frac{p_2}{p_1}; \tag{2.50}$$

$$A_2 = \frac{-i_{pr2}}{1 - \frac{p_2}{p_1}}. \tag{2.51}$$

Substituting expressions (2.45) and (2.46) in (2.44), taking into account (2.48), (2.50) and (2.51), and making the transformation, we obtain an expression defining the current function at the drop interval:

$$i_2(t) = \frac{U_C - U_L}{2 \cdot R_0 + R} + A_1 \cdot e^{p_1 t} + A_2 \cdot e^{p_2 t}. \tag{2.52}$$

Solving equation (2.52) relative to the time t_2 and taking into account the hysteresis setpoint value ΔI, we obtain the dependence of the time of the phase current drop on the hysteresis setpoint value:

$$t_2(\Delta I) = \frac{\ln\left(\frac{\Delta I - i_{pr2}}{A_1 + A_2 \cdot e^{\frac{p_2}{p_1}}}\right)}{p_1}. \tag{2.53}$$

The switching period Δt will be equal to the sum of the two temporary components of the current rise and drop t_1 and t_2.

$$\Delta t = t_1 + t_2. \tag{2.54}$$

Substituting in (2.54) the expressions for t_1 and t_2 in (2.54) and making the transformation, we get an expression that determines the maximum AVR switching frequency:

$$f_{\max} = \frac{1}{\Delta t} = \frac{1}{t_1 + t_2} = \frac{\text{l}}{\dfrac{\ln\left(1 - \dfrac{\Delta I}{\dfrac{U_L}{2 \cdot R_0}}\right)}{-\dfrac{2 \cdot R_0}{2 \cdot L}} + \dfrac{\ln\left(\dfrac{\Delta I - \dfrac{U_C - U_L}{2 \cdot R_0 + R}}{A_1 + A_2 \cdot e^{\frac{p_2}{p_1}}}\right)}{p_1}}. \qquad (2.55)$$

This expression is more accurate compared to (2.35), since it includes all the parameters of the converter equivalent circuit, as well as the hysteresis setpoint magnitude.

Using the above-given calculation technique, it is possible to estimate the value of the maximum AVR switching frequency with the hysteresis CS when setting the circuit parameters and the hysteresis setpoint value.

The graphical dependence of the maximum AVR switching frequency $f_{\max}$ on the hysteresis setpoint values ΔI and the inductance of the inlet throttles L is shown in fig. 2.60.

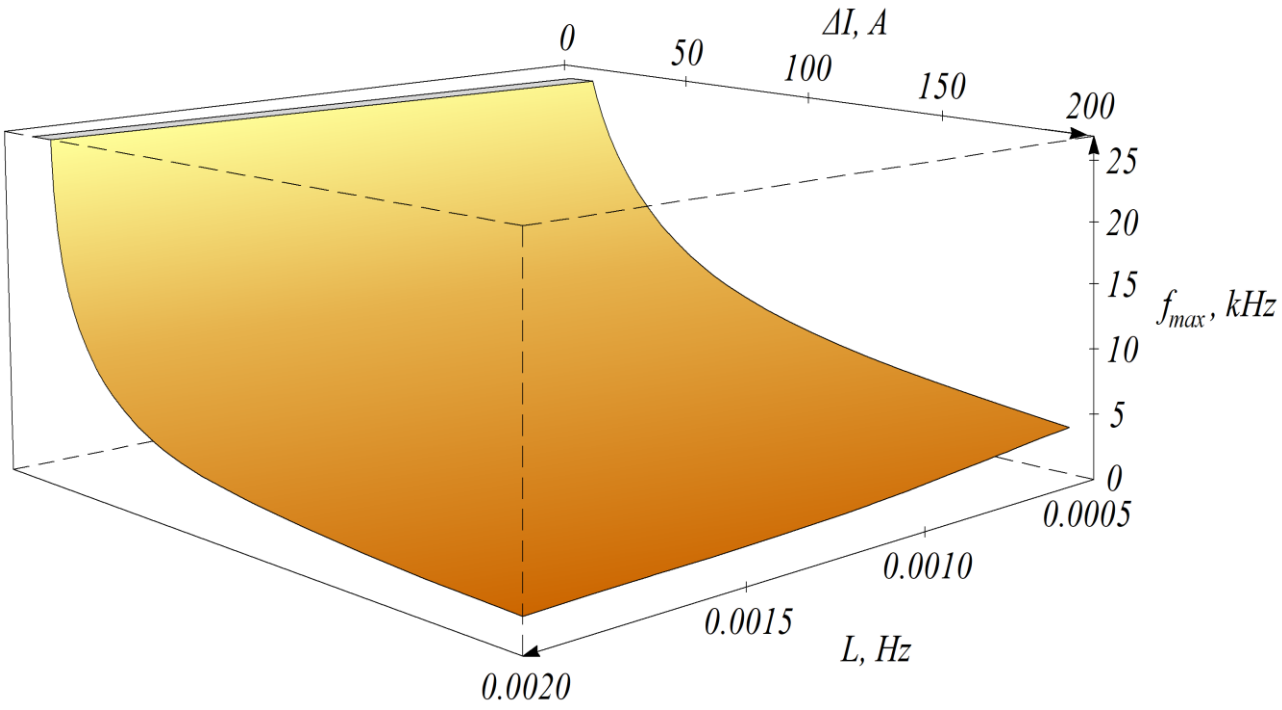

Figure 2.60 – Dependence of $f_{\max}$ of AVR with hysteresis SC on values L and ΔI

The adequacy of the obtained method was confirmed almost completely by the correspondence of the results of the analytical calculation and the results of the simulation experiment carried out in Matlab.

In a number of cases, a limitation or reduction in the switching frequency of active rectifiers with hysteresis modulation is required, which is achieved by reducing the current rise rate *di*/*dt*. The current rise rate can be limited by changing the inductance of the inlet throttles of the active rectifiers or increasing the value of the hysteresis setpoint. Higher inductance of the inlet throttles leads to an increase in the mass and size characteristics of the converter and its cost, and an increase in the hysteresis setpoint leads to a deterioration in the phase current shape.

The adjustment characteristic of the AVR with the hysteresis CS is obtained according to the equation of the power balance in the converter. The output voltage of the AVR in the hysteresis CS is adjusted by scaling (setting the required scale) the current amplitude with respect to the voltage amplitude. The instantaneous power balance in the converter is described by the following equation:

$$3 \cdot U_{in} \cdot I_{in} \cdot \eta = U_{out} \cdot I_{out}, \tag{2.56}$$

where η – the efficiency of the active rectifier; U_{in} – the phase voltage of the network; I_{in} – the shaped phase current of the network; U_{out} – the output voltage of the AVR; I_{out} – the load current of the AVR.

Due to the fact that the hysteresis CS of the AVR forms a current form that repeats the voltage form, with the necessary amplitude, the resulting input current repeats the task signal form, which can be expressed through the adjustment factor and the input voltage as follows:

$$I_{in}^{*} = U_{in}^{*} \cdot \xi, \tag{2.57}$$

where I_{in}^{*} – the phase current task signal; U_{in}^{*} – the phase input voltage of the AVR; ξ – the adjustment factor.

By substituting expression (2.57) into expression (2.58) and performing the transformation, we obtain an expression that determines the adjustment characteristic of the active rectifier and describes the dependence of the output voltage on the adjustment factor and the load current:

$$U_{out}\left(\xi; U_{in}; I_{out}\right) = \frac{3 \cdot U_{in}^{2} \cdot \xi}{I_{out} \cdot \eta}. \tag{2.58}$$

From equation (2.58), we can obtain an equation describing the adjustment characteristic of the AVR, which determines the dependence of the output voltage on the adjustment factor and the load resistance:

$$U_{out}\left(\xi; U_{in}; R_{load}\right) = \sqrt{3 \cdot U_{in}^2 \cdot \xi \cdot R_{load} \cdot \eta}. \qquad (2.59)$$

Fig. 2.61 shows the adjustment characteristic of AVR $U_{out} = f\,(\xi;\, U_{in};\, R_{load})$ at an input voltage of 1400 V.

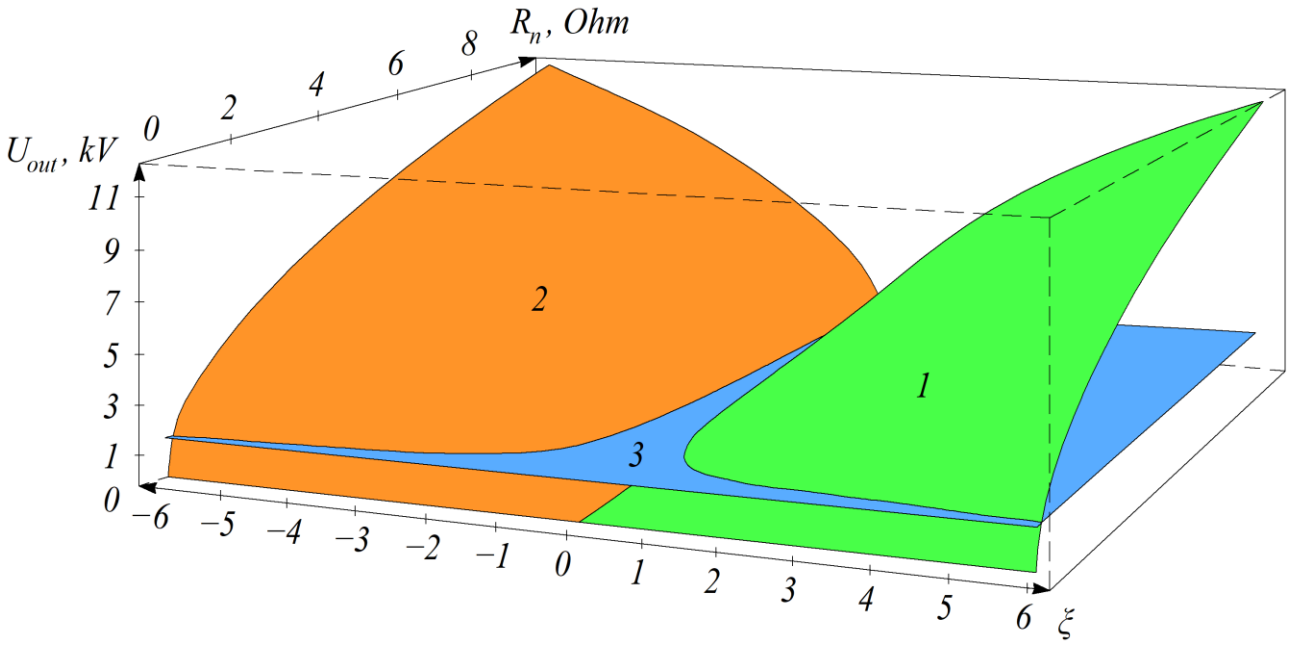

Figure 2.61 – Adjustment characteristic of output voltage of AVR:
1 – in rectification mode; *2* – in regeneration mode;
3 – restriction in regulation of U_{out}

The above-mentioned adjustment characteristic describes the rectification mode of the AVR, which is determined by the positive range ξ, and the regeneration mode, which is determined by the negative range ξ.

The AVR is a step-up converter, so its stability depends on the maintenance of the output voltage above the level of the amplitude value of the phase voltage of the supply network. This stability limit in fig. 2.61 is indicated by the plane at only 1400 V.

It was found that in order to maintain the power factor compensation mode, the output voltage should not be less than

$$U_{out\_\min} \geq U_{line} \cdot \sqrt{2}, \qquad (2.60)$$

where U_{line} – the amplitude value of the line voltage of the network.

The AVR application for traction power supply requires the stabilization of the output voltage. At the same time, it should be noted that the characteristic feature of traction power supply is a sharply changing load. Changes in the PS load are the reason for deviation of the output voltage from the set value. High load current rates cause an oscillatory process, which leads to overvoltage and changes in the harmonic composition of the contact and rail circuits.

Deterioration of the quality of electrical energy in the overhead system negatively affects the ERS and railway automation circles. This circumstance requires the high quality of electric energy received from the AVR in the established and transient modes.

In the AVR, the output voltage is stabilized by applying the automatic regulation laws. According to the results of the analysis of the requirements relating to the quality of voltage in the overhead system, there are requirements for ARS of the output voltage of the AVR. They include the following requirements:

– the error of the output voltage regulation in the established mode should decay to zero;

– the maximum efficiency for a given regulation law; and

– the permissible re-adjustment is slightly more than 20 %.

The value of re-adjustment is determined by the maximum permissible voltage in the railway overhead contact network of 4 kV, at a rated voltage value of 3.3 kV. The peculiarity of the AVR is the need to consider the dynamic processes that occur simultaneously in the system: input inductance, power switch, output capacitor.

The method of dynamic characteristics of the ARS of the AVR output voltage is based on the method of frequency characteristics. This method has relative simplicity and visibility, which makes it possible to synthesize the transfer function of the regulator quite effectively; it ensures the implementation of previously formed requirements for the AVR output voltage control system.

Fig. 2.62 shows the oscillograms of the AVR control signal with the addition of the 55 Hz harmonic component and the response to this control signal in the output voltage. The oscillogram confirms the reliability of the obtained AFR of the AVR.

Table 2.14 shows the results of measurements obtained when taking the AFR of the AVR.

The AFR obtained of the open hysteresis system for regulating the output voltage of the AVR is shown in fig. 2.63.

Fig. 2.64 shows the asymptotic logarithmic amplitude frequency response (LAFR) of the open CS L_{giv}, referred to a single contour transmission coefficient.

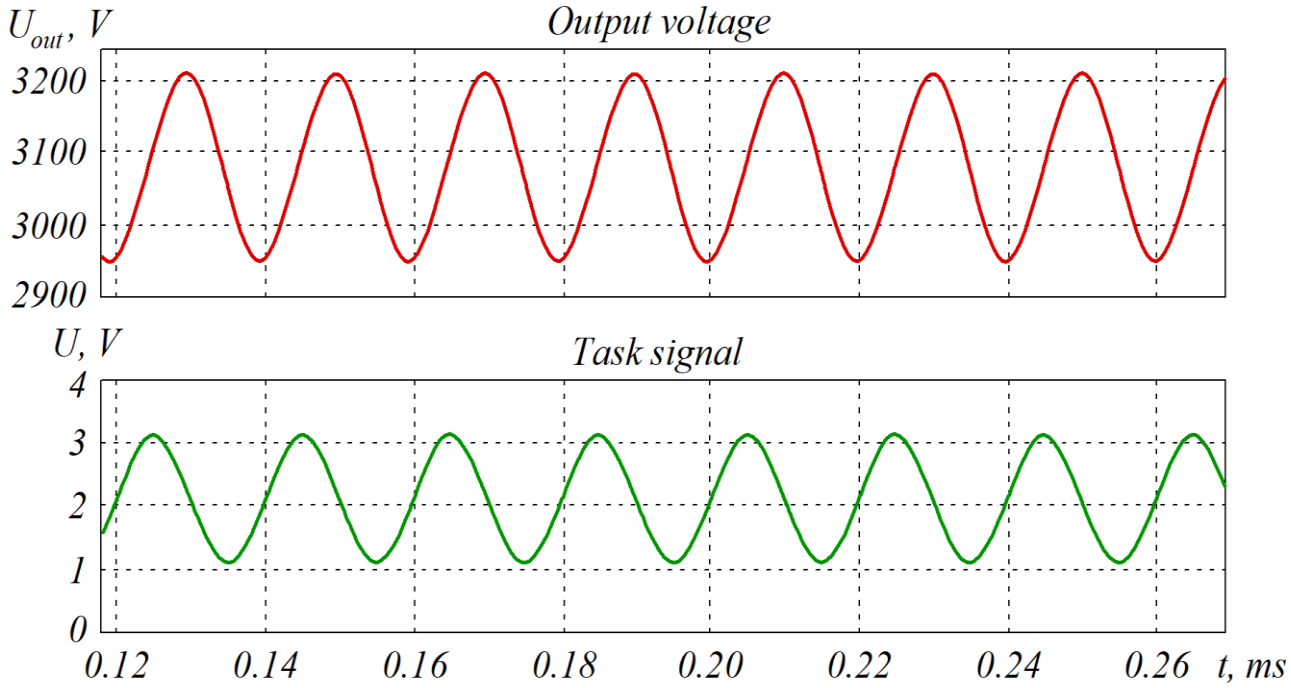

Figure 2.62 – Control signal and output voltage form

Table 2.14 – AFR of AFR with hysteresis CS

Harmonic frequency in control signal	Amplitude of harmonic in output voltage	Signal amplification, dB
10	868	61.74523
40	706	59.95093
80	494	56.84937
300	190	48.54991
600	140	45.89739
1200	124	44.84327
2500	120	44.55846
5000	103	43.23158
10000	69	39.75181
20000	37	34.33887
40000	18	28.08028
80000	8.7	21.76522
160000	3.0	12.51726
200000	1.4	5.897394

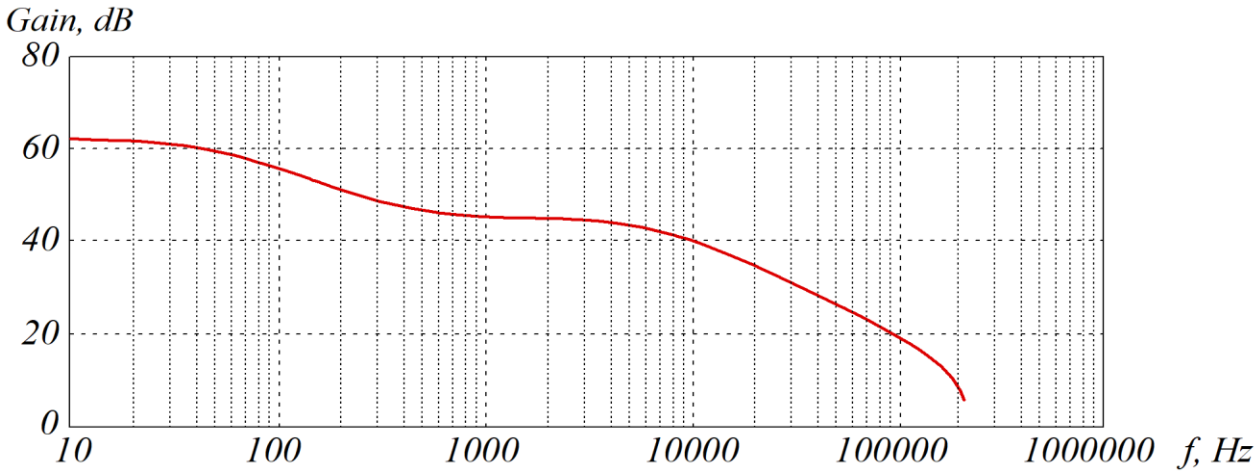

Figure 2.63 – AFR of AVR with hysteresis control system

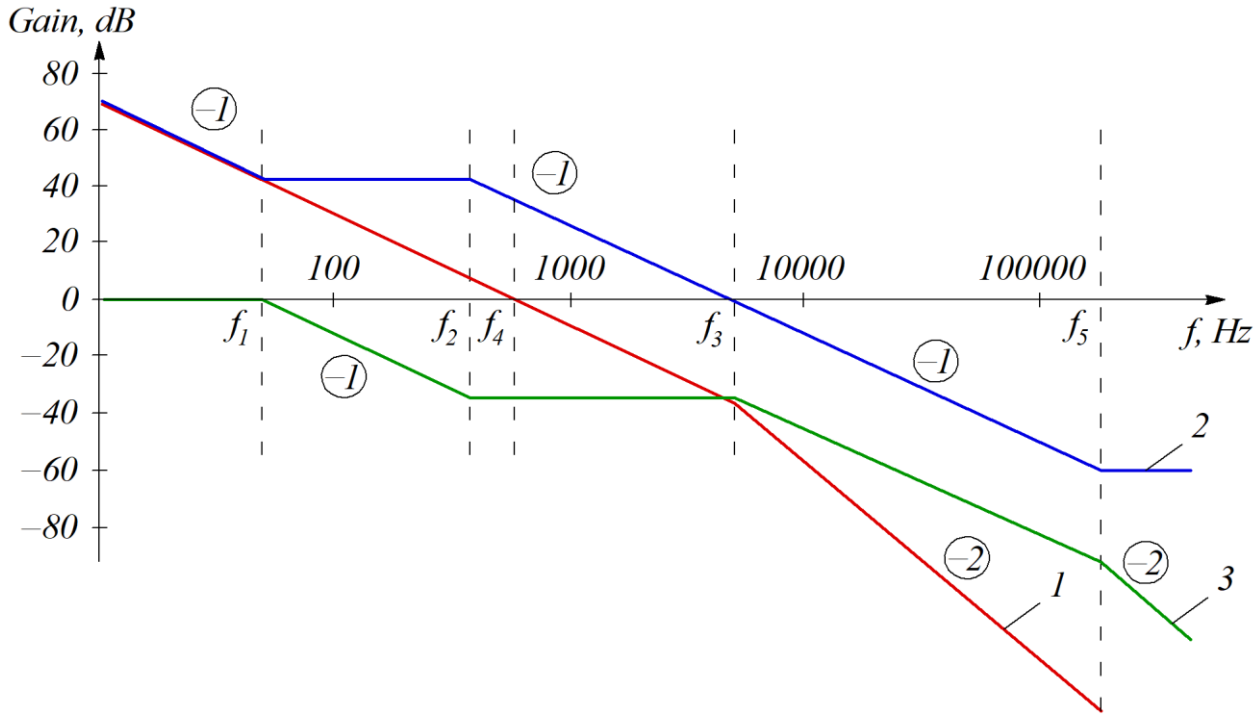

Figure 2.64 – Characteristics of the control system:
1 – asymptotic LAFR L_{giv}; *2* – desired LAFR L_{des}; *3* – LAFR of regulator L_{reg}

The same figure shows the desired LAFR L_{des} and the LAFR of the regulator L_{reg}, associated with the expression:

$$L_{reg} = L_{des} - L_{giv}. \tag{2.61}$$

The time constant T_4, which corresponds to the cut-off frequency of the desired LAFR, is determined according to the expressions:

$$T_4 = \frac{1}{\omega_4}, \tag{2.62}$$

where ω_4 – the circular cut-off frequency of the desired LAFR;

$$\omega_4 = \frac{\pi \cdot \lambda_\delta}{t_r}, \tag{2.63}$$

where t_r – the time of output signal setting; λ_δ – the coefficient determined from the permissible re-adjustment.

The value of the coefficient λ_δ is determined from the permissible value of re-adjustment δ, %. The value of the coefficient λ_δ is shown in fig. 2.65.

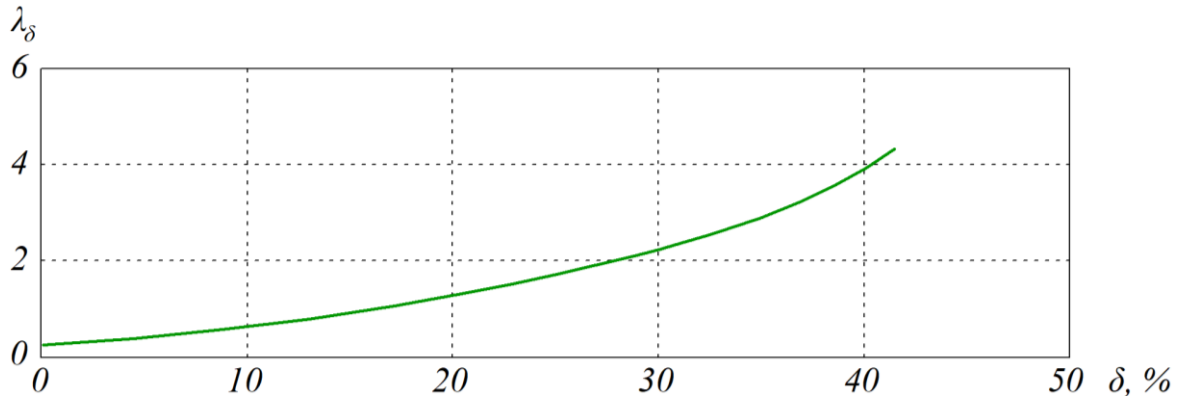

Figure 2.65 – Dependence of coefficient λ_δ on re-adjustment value δ

In the low and medium frequency range, the desired asymptotic LAFR has a slope of –20 dB/dec. The medium frequency range is limited by the connecting frequency:

$$\omega_3 = (2-4) \cdot \omega_4. \tag{2.64}$$

This type of desired LAFR causes first-order astatism in the output voltage and a rather high level of variable component damping. From fig. 2.64, the transmitting function of the closed ARS of the AVR output voltage and the voltage regulator was obtained:

$$W_r(p) = \frac{1}{T_4 p \cdot (T_3 p + 1)}; \tag{2.65}$$

$$H_r(p) = \frac{(T_1 p + 1) \cdot (T_5 p + 1)}{T_4 p \cdot (T_2 p + 1)}, \quad (2.66)$$

where T_1, T_2, T_3, T_4 – the time constants typical to the frequencies f_1, f_2, f_3, f_4 on the asymptotic LAFR of the open CS (see fig. 2. 63).

The transfer function of the output voltage regulator is as follows:

$$H_r(p) = \frac{T_1 \cdot T_5 p^2 + (T_1 + T_5) p + 1}{T_4 p \cdot (T_2 p + 1)} = \frac{1}{(T_2 p + 1)} \cdot \left(\frac{T_1 \cdot T_5 p}{T_4} + \frac{T_1 + T_5}{T_4} + \frac{1}{T_4 p} \right). \quad (2.67)$$

Taking into account expression (2.20), we write down the transfer function of the closed ARS of the AVR output voltage:

$$W_c(p) = \frac{W_r(p)}{1 + W_r(p)} = \frac{1}{T_4 p \cdot (T_3 p + 1) \cdot \left(1 + \frac{1}{T_4 p \cdot (T_3 p + 1)} \right)} =$$

$$= \frac{1}{T_4 p \cdot (T_3 p + 1)} = \frac{1}{T_0^2 p^2 + 2 \cdot g \cdot T_0 p + 1}, \quad (2.68)$$

where $T_0 = \sqrt{T_4 \cdot T_3}$; $g = \frac{1}{2} \cdot \sqrt{\frac{T_4}{T_3}}$ – the damping coefficient.

The dynamic properties of the regulation system can be determined with transfer function (2.68) of the closed system in the form of elementary aperiodic links:

$$W_c(p) = \frac{A_1}{p - p_1} + \frac{A_2}{p - p_2}, \quad (2.69)$$

where $p_{1,2}$ – the transfer function poles.

The transfer function poles are determined according to the expression:

$$p_{1,2} = \frac{-g \pm a}{T_0}; \quad (2.70)$$

$$a = \sqrt{g^2 - 1}. \quad (2.71)$$

The coefficients A_1 and A_2 are defined as the subtraction of the function $W_3(p)$ at special points:

$$A_i = \frac{1}{\frac{dV(p)}{dp}}, \tag{2.72}$$

where $V(p)$ – the characteristic polynomial of the transfer function $W_c(p)$.

By performing the transformation (2.72), we obtain:

$$A_1 = \frac{1}{2 \cdot a \cdot T_0}; \tag{2.73}$$

$$A_2 = -\frac{1}{2 \cdot a \cdot T_0}. \tag{2.74}$$

Taking into account (2.69), (2.73) and (2.74), the expression for the transfer function of the closed-loop output voltage control system takes the form:

$$W_c(p) = \frac{1}{2 \cdot a} \cdot \left(\frac{1}{T_0 + g - a} - \frac{1}{T_0 + g + a} \right). \tag{2.75}$$

To assess the transients of the regulatory system, its transient function is determined.

The image of the transition function looks like:

$$H(p) = \frac{W_c(p)}{p}. \tag{2.76}$$

Applying the decomposition theorem to expression (2.76) and performing the transformation, we obtain:

$$h(t) = 1 - \frac{e^{-g \cdot \frac{t}{T_0}}}{2 \cdot a} \cdot \left[(a+g) \cdot e^{\left(a \cdot \frac{t}{T_0} \right)} + (a+g) \cdot e^{\left(-a \cdot \frac{t}{T_0} \right)} \right]. \tag{2.77}$$

Fig. 2.66 shows the result of the analytical calculation of the ARS transient process of the AVR output voltage. To calculate the transient process, the parameters obtained from the LAFR are used, which is shown in fig. 2.64.

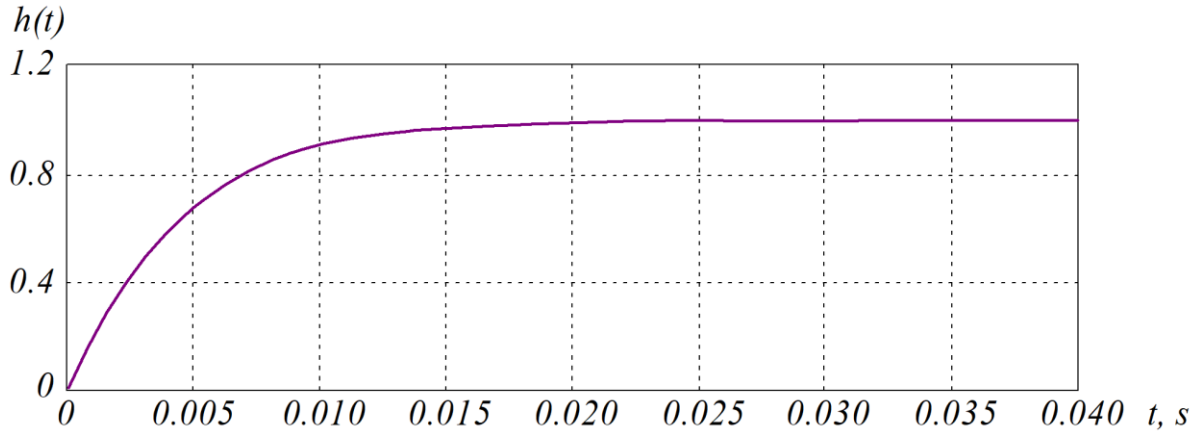

Figure 2.66 – Transient process of ANR output voltage

As follows from fig. 2.66, the transient process duration with high accuracy coincides with the given transient process duration t_r when calculating the time constant T_4 by expression (2.62).

A simulation model of an active rectifier with the hysteresis CS was created in Matlab.

Parameters of the simulation model are given in table 2.15.

Table 2.15 – Parameters of the AVR simulation model

Parameter	Value
Phase-to-phase voltage of three-phase network, V	1400
Inlet throttle inductance, mH	0.2
Active resistance of inlet throttle, Ohm	0.02
Load resistance, Ohm	2…15
Output capacitance, μF	2
Output voltage, V	3300
Current hysteresis setpoint value, A	5…30

The developed model has the following components: three-phase power supply network, meter of input phase voltages and currents, two-level active rectifier, equivalent *RL*-load, and hysteresis CS. The AVR with the hysteresis CS is shown in fig. 2.67.

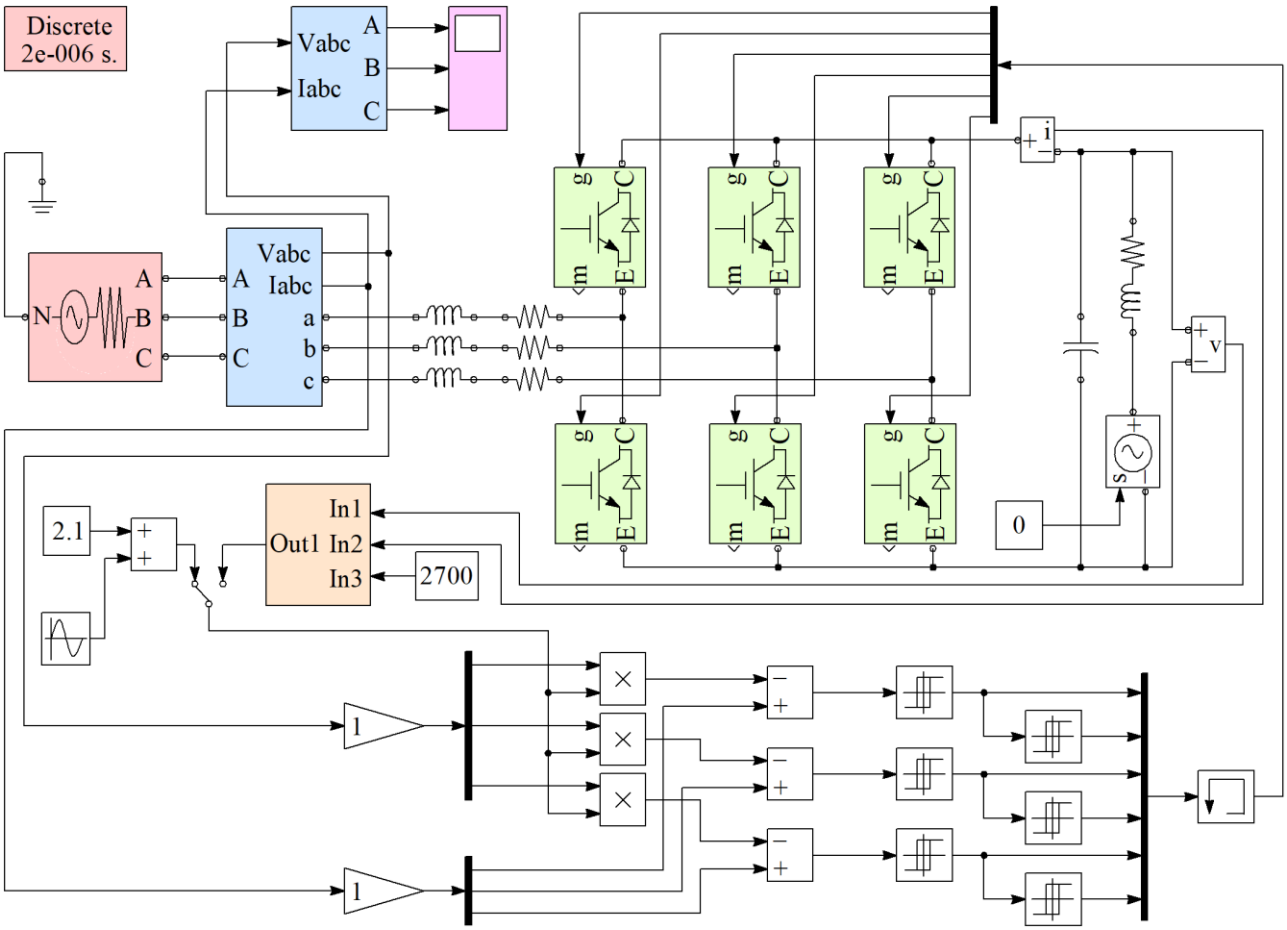

Figure 2.67 – AVR simulation model with hysteresis CS

In the CS, to obtain the rectification and regeneration modes, feedbacks with the output current and output voltage with the use of a regulator are implemented. Feedback signals with the task signal are supplied to the output voltage regulator.

The forms of the input phase voltage and currents, as well as the output voltage of the active rectifier with hysteresis CS during the transient start-up process of the AVR are shown in fig. 2.68. With an active energy source load, which is the ERS for the PS, the energy from the DC circle can be transferred to the power supply network. The oscillogram of the phase voltage and currents of the AVR with hysteresis CS when switching from the rectification mode to the regeneration mode is shown in fig. 2.69.

In the process of simulation, the dynamic mode and EMC parameters were studied: power factor consumed from the network (rectification); THD of phase current; interference voltage magnitude. The result of the Matlab simulation of the AVR with a hysteresis setpoint in the current channel equal to 30 A showed a maximum switching frequency of 41.34 kHz, while the resulting calculation technique gave a result of 41.45 kHz, which confirms the adequacy of the developed technique for calculating the maximum switching frequency.

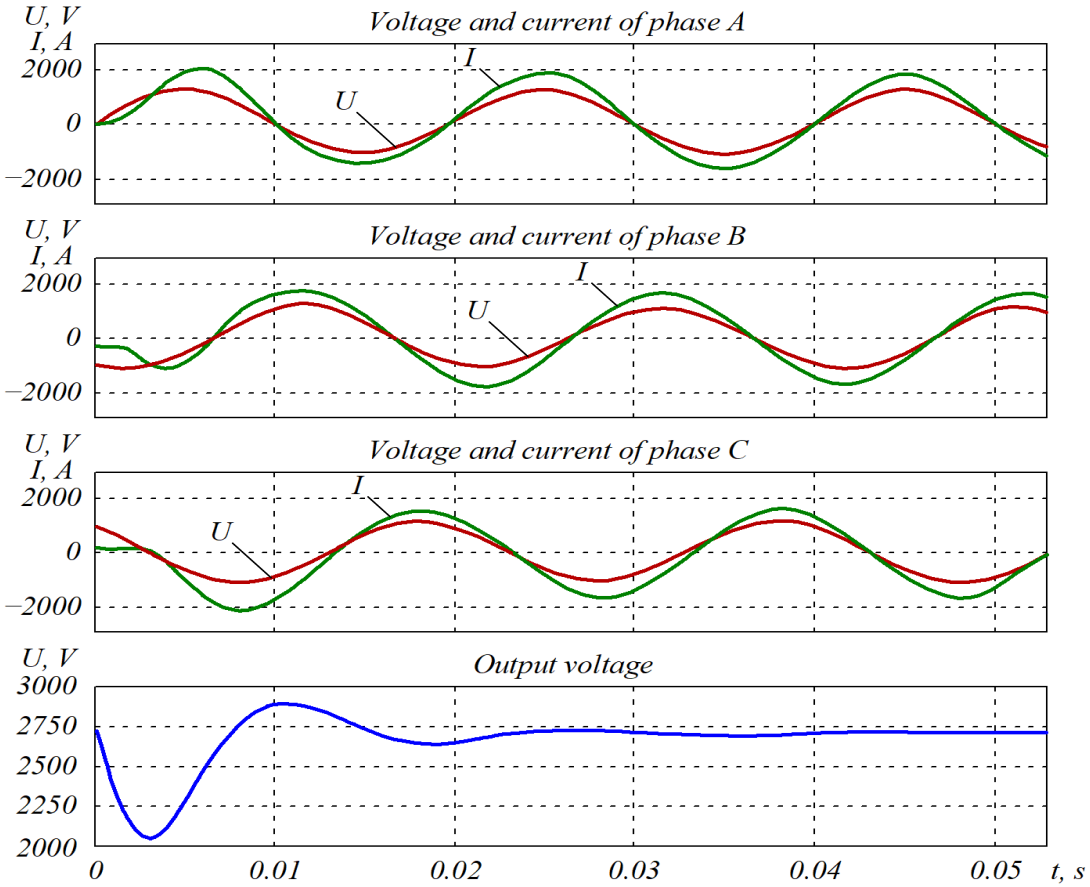

Figure 2.68 – Forms of phase voltages and currents during transient process

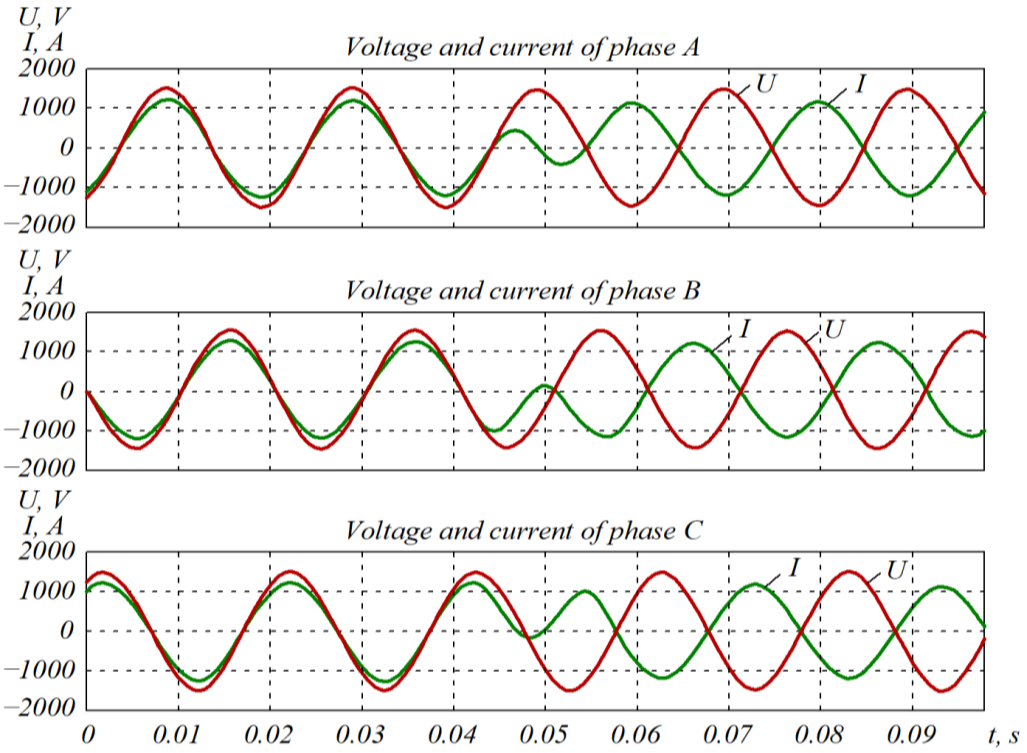

Figure 2.69 – Forms of phase voltages and currents when switching during transient process

Fourier analysis of the consumed phase current of the AVR at different values of the hysteresis setpoint is shown in fig. 2.70, Fourier analysis of the AVR output voltage shown in fig. 2.71.

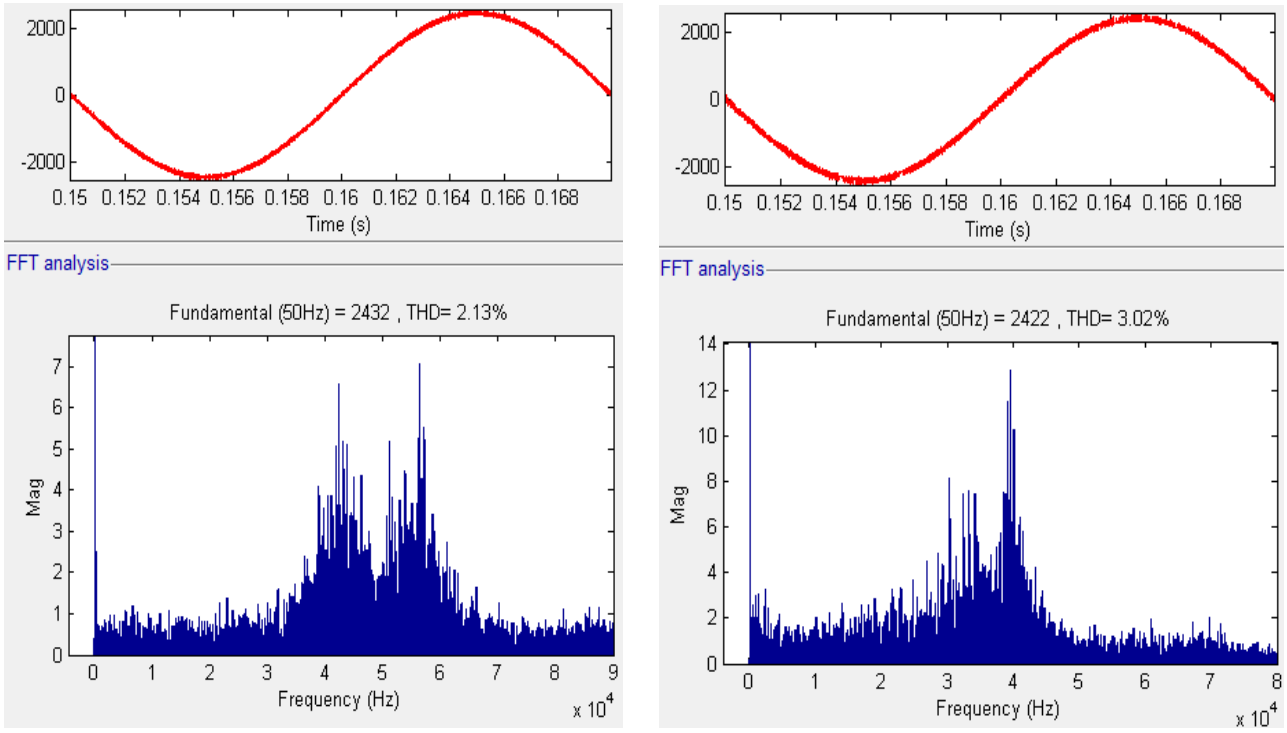

a *b*

Figure 2.70 – Fourier analysis of AVR phase current at hysteresis settings: *a* – 5 A; *b* – 30 A

As follows from the results of Fourier analysis of the input current and output voltage shown in fig. 2.70 and 2.71, with an increase in the hysteresis setpoint value, the main higher harmonic component decreases, but the energy quality under this condition deteriorates due to an increase in the ripple amplitude of the output voltage and an increase in the THD of the input current. The ripple factor of the AVR output voltage with a hysteresis setpoint equal to 5 A is calculated according to the THD of the output voltage shown in fig. 2.71. The ripple factor of the output voltage is calculated as the ratio of the sum of higher harmonics to the constant component:

$$k_{pulse} = \frac{\sum U_{garm}}{U_{DC}}, \tag{2.78}$$

where ΣU_{garm} – the RMS of the sum of the higher harmonics of the output voltage; U_{DC} – the constant component of the output voltage.

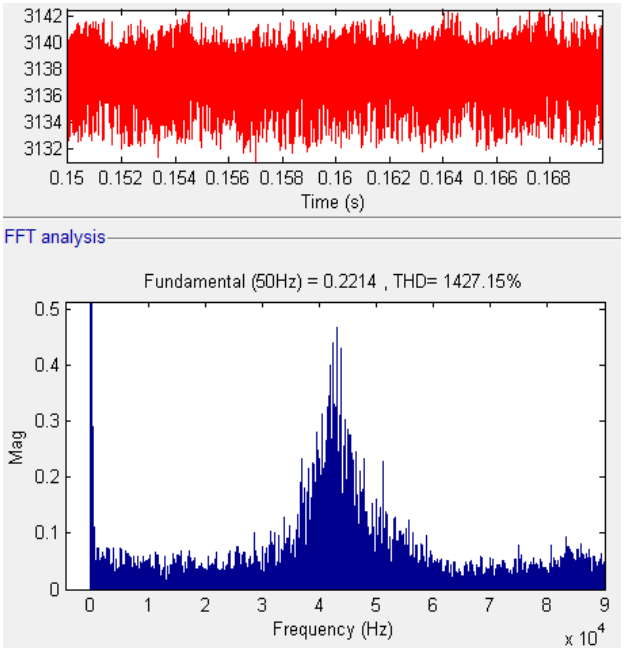

a

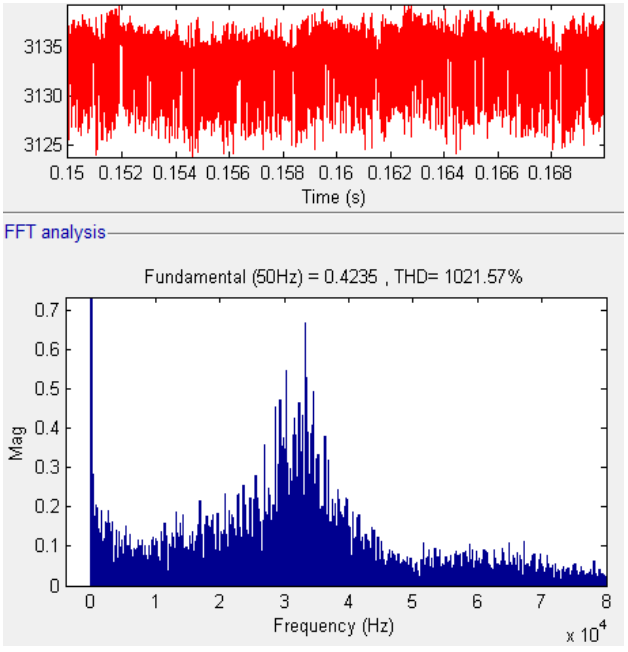

b

Figure 2.71 – Fourier analysis of AVR output voltage at hysteresis settings: *a* – 5 A; *b* – 30 A

The value of the sum of the higher harmonics of the output voltage is calculated according to the THD obtained from Fourier analysis shown in fig. 2.71:

$$THD_{U_{out}} = \frac{\sum U_{garm}}{U_1}; \tag{2.79}$$

$$\sum U_{garm} = THD_{U_{out}} \cdot U_1 = 1427.15 \cdot 0.2214 = 315.97 \text{ В}. \tag{2.80}$$

Thus, the ripple factor of the output voltage of the active rectifier with the hysteresis CS at the hysteresis setpoint of 5 A will be equal to:

$$k_{pulse\_5} = \frac{\sum U_{garm}}{U_{DC}} = \frac{THD_{U_{out}} \cdot U_1}{U_{DC}} = \frac{315.97}{3137} = 0.101\,\%. \tag{2.81}$$

The ripple factor of the output voltage of the AVR with a value of the hysteresis setpoint of 30 A will be equal to:

$$k_{pulse\_30} = \frac{\sum U_{garm}}{U_{DC}} = \frac{THD_{U_{out}} \cdot U_1}{U_{DC}} = \frac{1021.57 \cdot 0.4235}{3137} = \frac{432.63}{3137} = 0.138\,\%. \tag{2.82}$$

The magnitude of the interference voltage is an integral indicator that characterizes the level of higher harmonics in the output voltage of the rectifier, which affect the communication lines, particularly, those in rail circuits. This indicator included both the amplitude and frequency of the interference.

The magnitude of the interference voltage is determined by the expression:

$$U_z = \sqrt{\sum \left(U_k \cdot \alpha_k\right)^2}, \tag{2.83}$$

where U_k – the amplitude of the k-th harmonic; α_k – the psophometric coefficient corresponding to the k-th harmonic.

The dependence of the psophometric coefficient α_k on the frequency of the k-th harmonic is shown in fig. 2.72.

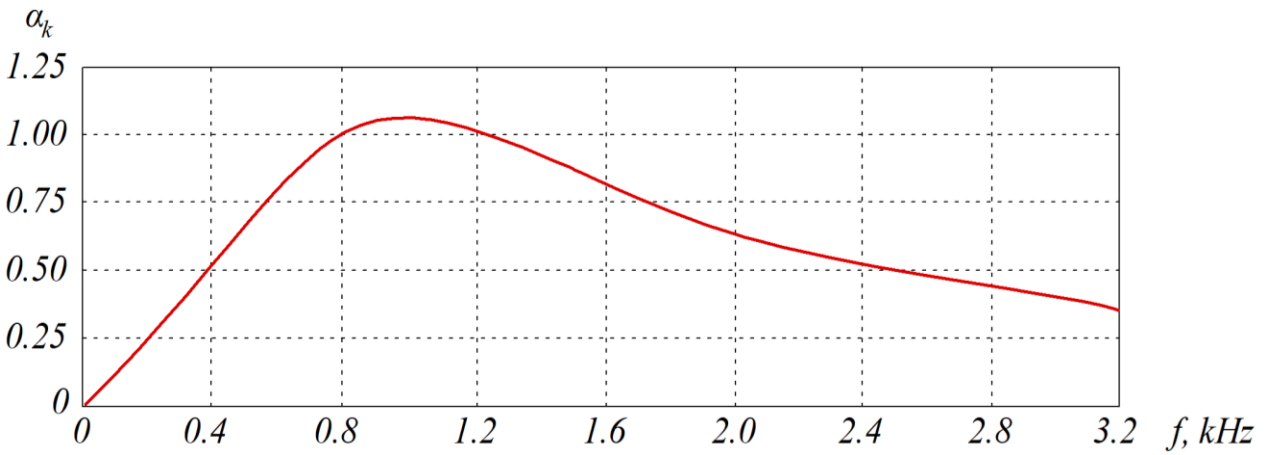

Figure 2.72 – Dependence of psophometric coefficient on harmonic frequency

The psophometric voltage in the AVR with hysteresis modulation is measured in the subsystem shown in fig. 2.73. In the sub-block, the values of the harmonics of the output voltage are calculated, followed by multiplication by the corresponding values of the coefficients α_k.

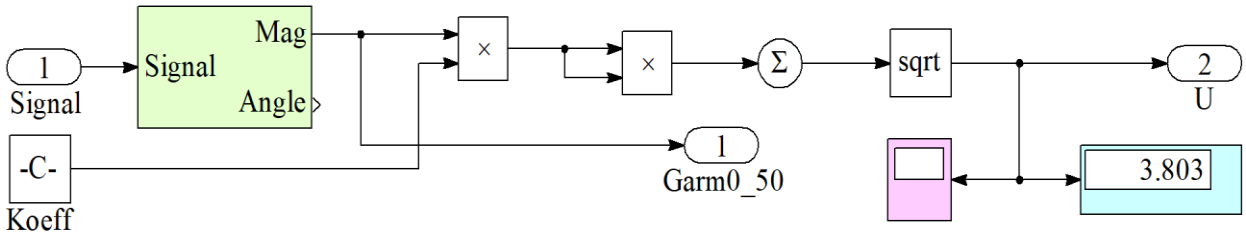

Figure 2.73 – Subsystem for measuring psophometric voltage in AVR

Thus, the AVR with hysteresis modulation provides a significant improvement in the quality of the output voltage and input current.

Fig. 2.74 shows the results of modelling the dynamic mode of the AVR with an integral regulator when its input is affected by a stepped signal.

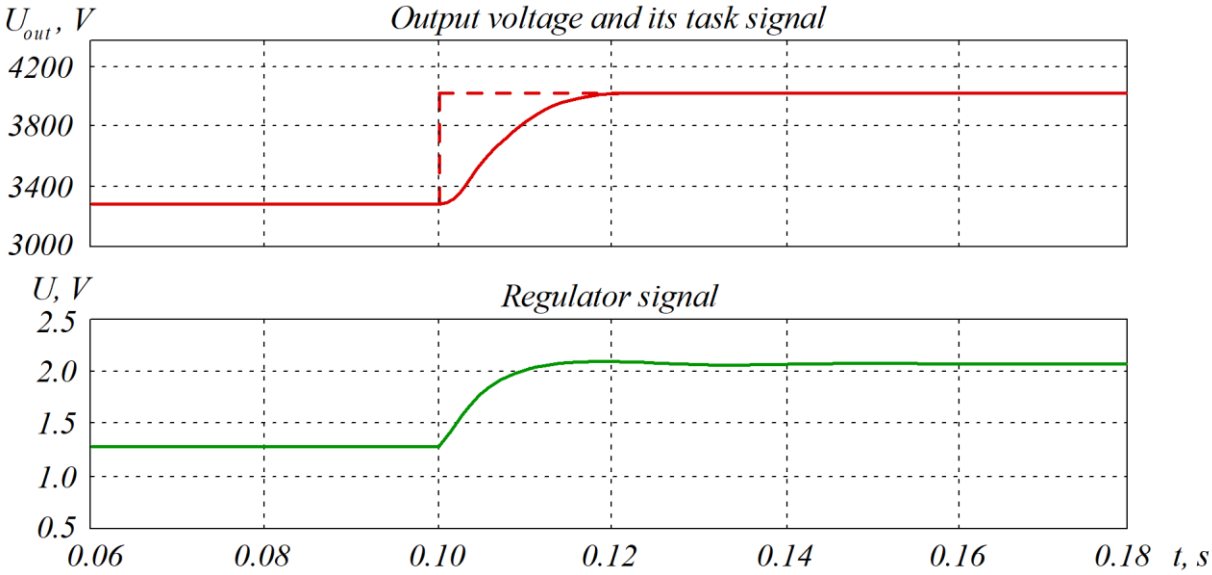

Figure 2.74 – Form of the output voltage of the AVR with an integral regulator

As follows from the oscillograms shown in fig. 2.74, the transient process ends in t_r = 20 ms, which corresponds to a rather small deviation of the results of analytical calculation and simulation. At the same time, it should be noted that the transient process duration is affected by the change in the load resistance. These changes cause deformation of the LAFR of the AVR. An example of deformation of the LAFR shape by changing the load current is shown in fig. 2.75.

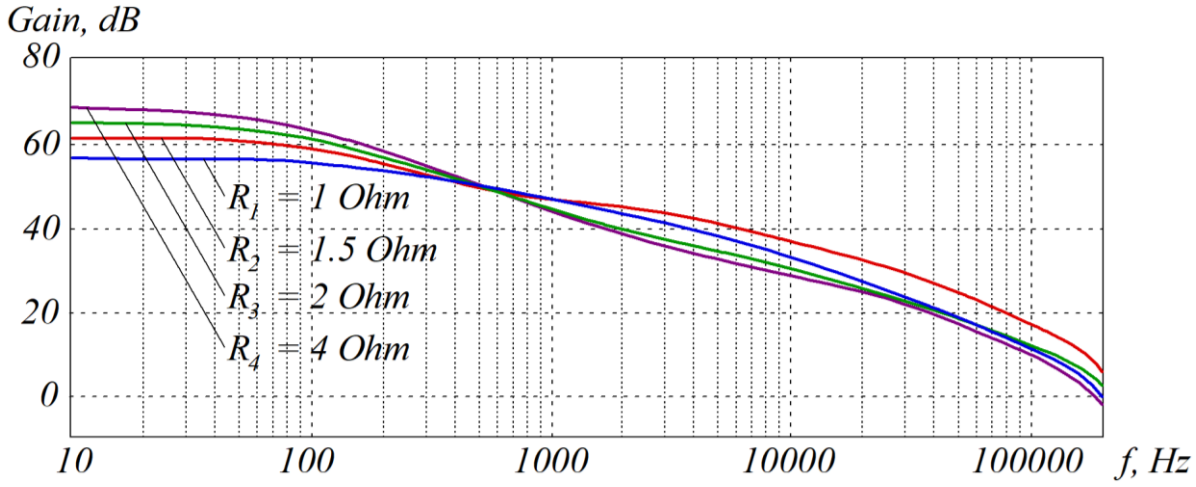

Figure 2.75 – Dependence of LAFR on load resistance

As follows from fig. 2.75, when the load resistance changes, the cut-off frequency of the given LAFR and the transmission coefficient change. The unambiguity of the transient process at a wide range of loads R_l is achieved using an adaptive link that provides correction of the voltage regulator parameters and the coefficient of reduction to a unity current gain ratio, as shown in fig. 2.76.

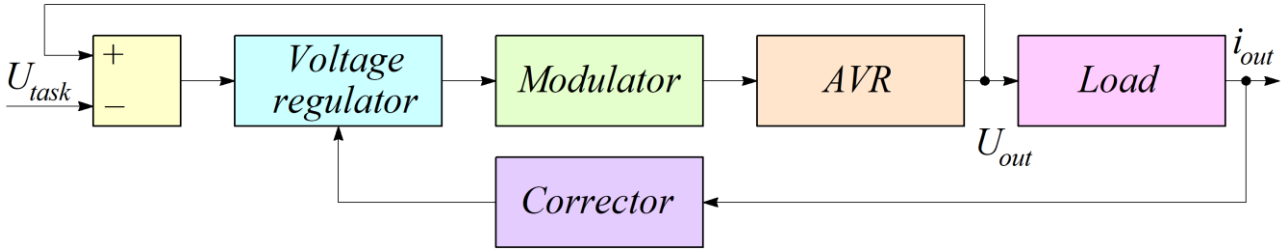

Figure 2.76 – Correction by ARS AVR voltage

The dependence of the AVR transmission coefficient on the load current, arising from equations of the regulatory characteristic (2.56)...(2.59), is as follows:

$$k_n = \frac{U_{out}}{\xi} = \frac{3 \cdot U_{in}^2}{I_{out} \cdot \eta}, \tag{2.84}$$

where k_n – the AVR transmission coefficient; U_{out} – the AVR output voltage; ξ – the adjustment coefficient; I_{out} – the AVR output current; η – the AVR efficiency.

Thus, by means of adding a correction link to the ARS, a system adaptable to the output current change can be obtained.

The results of the EMC of the AVR with the hysteresis CS are given in table 2.16.

Table 2.16 – Electricity quality indicators of AVR with hysteresis CS

Parameter	Value
Power factor, %	0.9974
THD of consumed current, %	2.13
Interference voltage, V	3.803
Output voltage ripple factor, %	0.101
Elementary switching frequency, kHz	≈ 41.32
Transient time, ms	20

Despite the high EMC quality obtained using the AVR with hysteresis modulation, an important disadvantage was identified, namely, a high switching

frequency. This drawback greatly complicates physical implementation causing problems with significant dynamic and efficiency losses.

2.6. Control system for the three-phase active rectifier with power factor compensation with pulse-width modulation

A significant advantage of PWM over hysteresis modulation is the possibility of reducing the switching frequency of AVR switches, which facilitates the physical feasibility of the converter, as well as reduces dynamic losses in the switches and increases the efficiency [83]. The structural diagram of the CS of the AVR with PWM is shown in fig. 2.14.

The structure shown in fig. 2.14 of the CS of the AVR is similar to that shown in fig. 2.13. However, it differs in that the inconsistency signal of the instantaneous values of the phase currents and the task signal through the aperiodic link is supplied to the pulse-width modulator.

The task signal in the CS is formed directly in the *abc*-coordinate system by extracting the first harmonics of phase voltages or by applying the transformations of the *abc*-coordinate systems to other coordinate systems: *αβ0*, *pqr*, *dqo*.

In the CS of the AVR with PWM, the inconsistency signal Δi, obtained between the phase current task signal and the phase voltage of the network, is compared with a sawtooth PWM signal, the frequency of which exceeds the frequency of the network by several orders of magnitude. The sawtooth signal has a constant amplitude and frequency, which leads to the operation of the switches at a fixed switching frequency.

The choice of the value of the inductance of the inlet throttles of the AVR in the PWM mode is described in some detail in [84]. Provided that a lower value of the inductance of the AVR inlet throttles is selected, the rise and drop in the current can occur faster than the rise and drop in the reference PWM signal, which is the reason for false switching. To prevent erroneous triggering, the CS has an aperiodic link acting as a low-pass filter. This link extracts the first harmonic from the inconsistency signal. As a result, an aperiodic link in the CS of the AVR with PWM makes it possible to improve the harmonic composition of the input current and reduce the inductance of the inlet throttles of the converter, which improves its mass and size indicators and cost. The waveforms in the CS with and without an aperiodic link are shown in fig. 2.77.

The CS regulator provides regulation of the output voltage both in the rectification and regeneration mode.

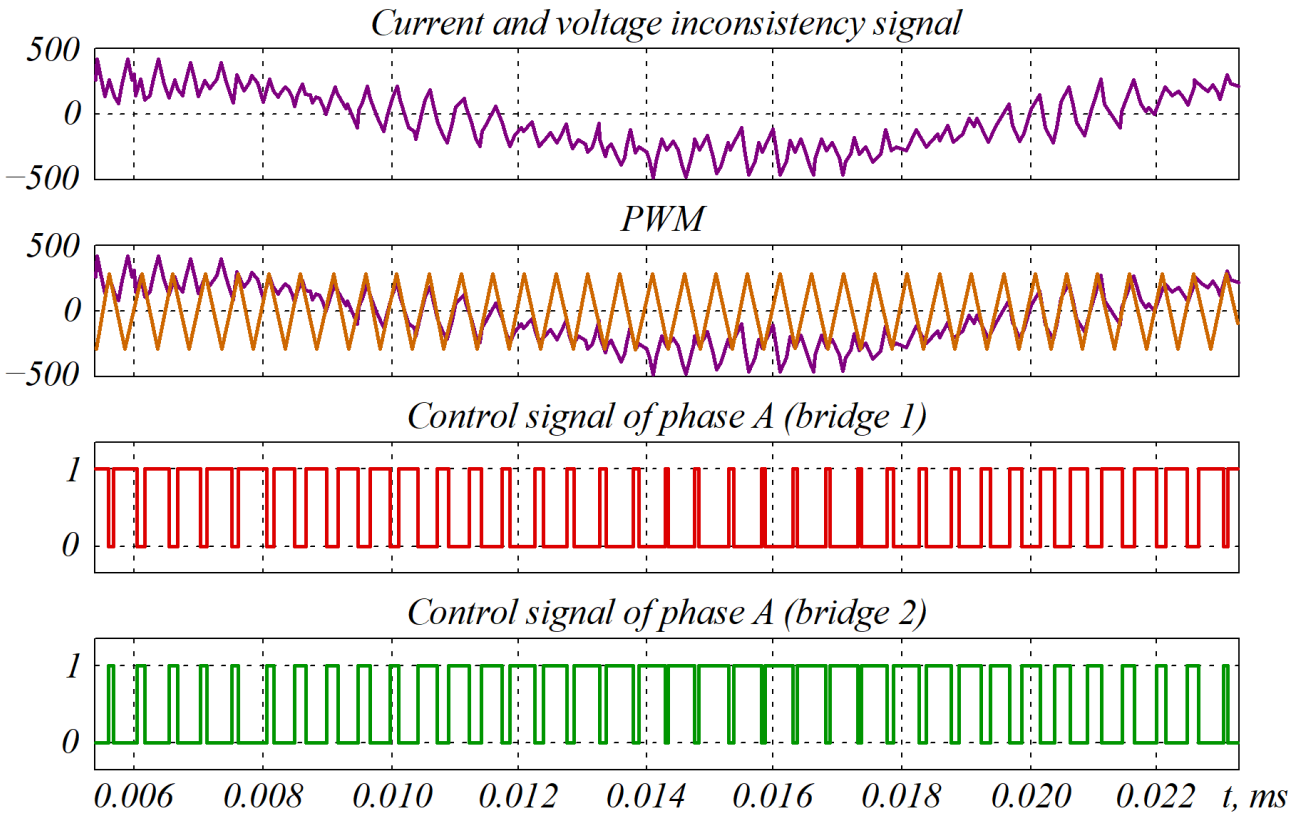

a

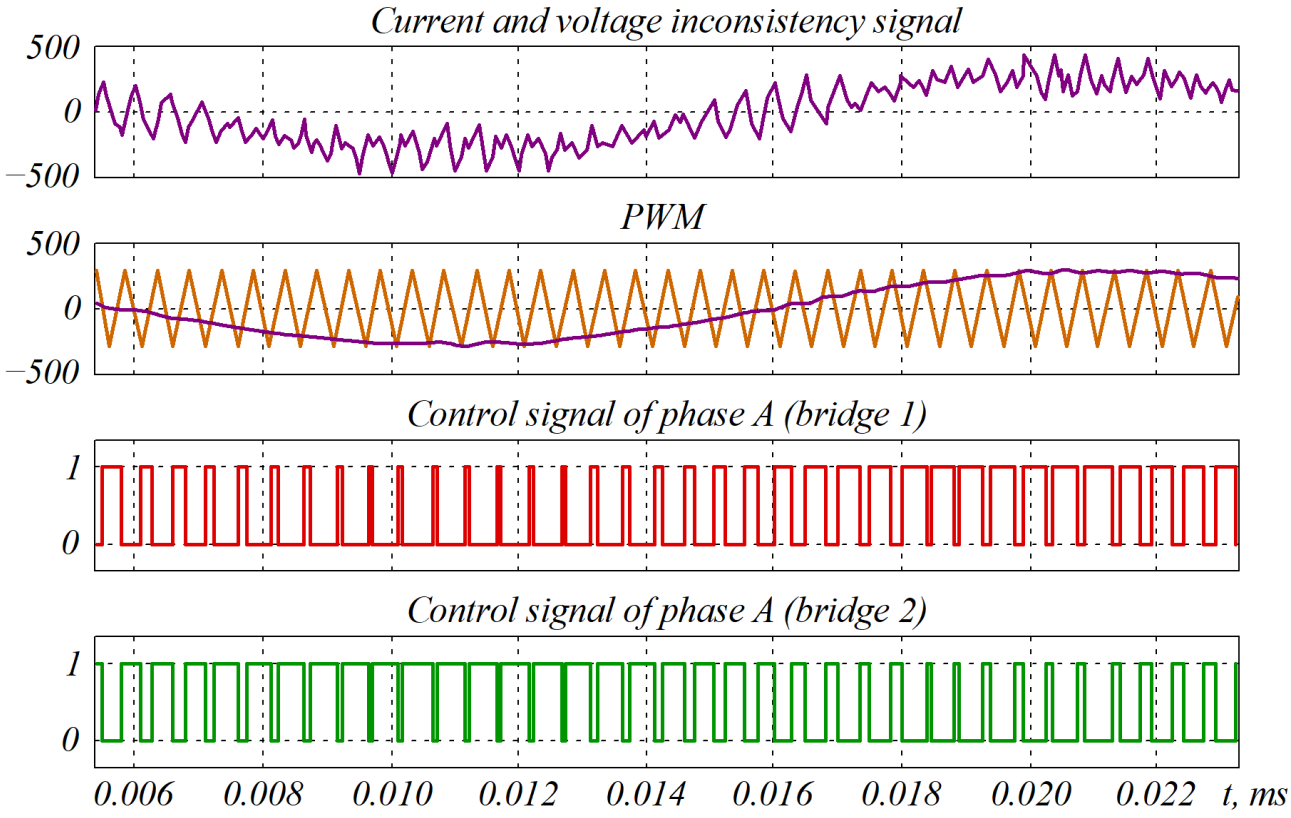

b

Figure 2.77 – Processes in CS of AVR with PWM:
a – without aperiodic link; *b* – with aperiodic link

The regulating characteristic of the PWM AVR, similar to the hysteresis modulated AVR, is constructed on the basis of the equations of energy balance in the converter. The difference in the regulation of the output voltage of the AVR with PWM is the deterioration of the power factor at the control coefficient ξ, close to one, since at $\xi = 1$ the inconsistency signal will decay to zero. Under this condition, the power correction mode will be aborted. The recommended value when regulating the output voltage lies in the range $\xi = 1.3...10$.

One of the most important indicators of the converter is its efficiency. The estimation calculation of the AVR efficiency is performed for the following parameters of the active rectifier: rated output voltage – 3.3 kV; rated load current – 3150 A, three-phase supply voltage – 1200 V.

The following losses are taken into account in the calculation of the efficiency: static losses in IGBT, dynamic losses in IGBT, losses in the active supports of the inlet throttles and converter circles.

The efficiency was calculated by applying the IGBT series CM750HG-130R manufactured by Mitsubishi. The appearance of the IGBT is shown in fig. 2.78. The IGBT specifications are given in table 2.17.

Figure 2.78 – IGBT series CM750HG-130R

Table 2.17 – Main technical specifications of module CM750HG-130R

Parameter	Value
Rated voltage, kV	6.6
Rated switching current, A	750
Maximum pulse switching current, A	1400
Current rise time, μs	0.2
Current drop time, μs	0.42

The form of the current and voltage flowing through the IGBT of the AVR is shown in fig. 2.79.

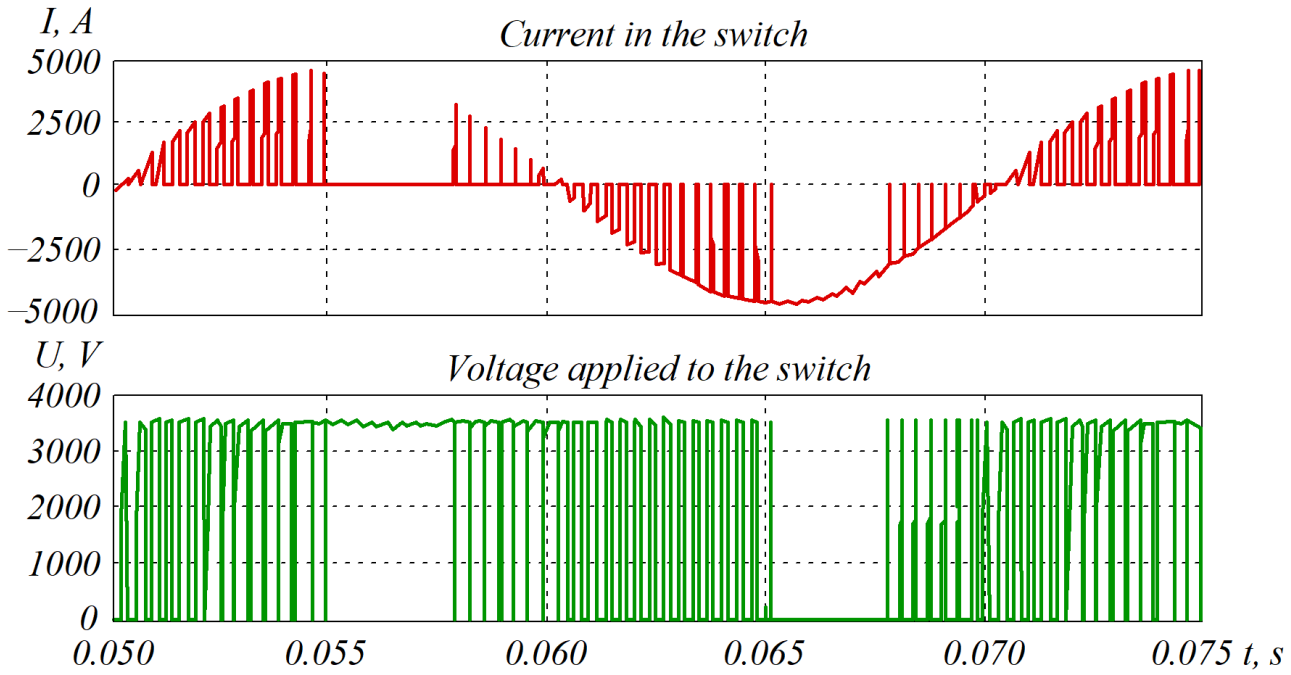

Figure 2.79 – IGBT current and voltage form

For the set values of output voltage, load power and supply voltage amplitude, the value of the consumed current will be:

$$I_{in\_rms} = \frac{U_{out} \cdot I_{out}}{3 \cdot U_{in} \cdot \eta}, \tag{2.85}$$

where η – the efficiency of the AVR with PWM.

$$I_{in\_rms} = \frac{3300 \cdot 3150}{3 \cdot 1250 \cdot 0.95} = 2917.87 \text{ A}.$$

The RMS of the consumed current was 2917 A, it corresponds to an amplitude value of 4171.31 A. Given that the input current amplitude of the AVR exceeds the current limit of the IGBT, a parallel connection of four parallel switches in the converter arms is required.

Thus, twenty-four transistors of the CM750HG-130R series should be used in AVR with a given load current.

The magnitude of the current flowing through one transistor will be:

$$I_{VT\_rms} = \frac{I_{in\_rms}}{4}, \tag{2.86}$$

$$I_{VT\_rms} = \frac{2917.87}{4} = 729.46 \text{ A}.$$

Static losses are due to the power that is dissipated in the switch during the current flow; they depend on the switching current magnitude and the fill ratio and do not depend on the switching frequency. The dependence of the voltage drop between the collector and the emitter in IGBT series CM750HG-130R is shown in fig. 2.80.

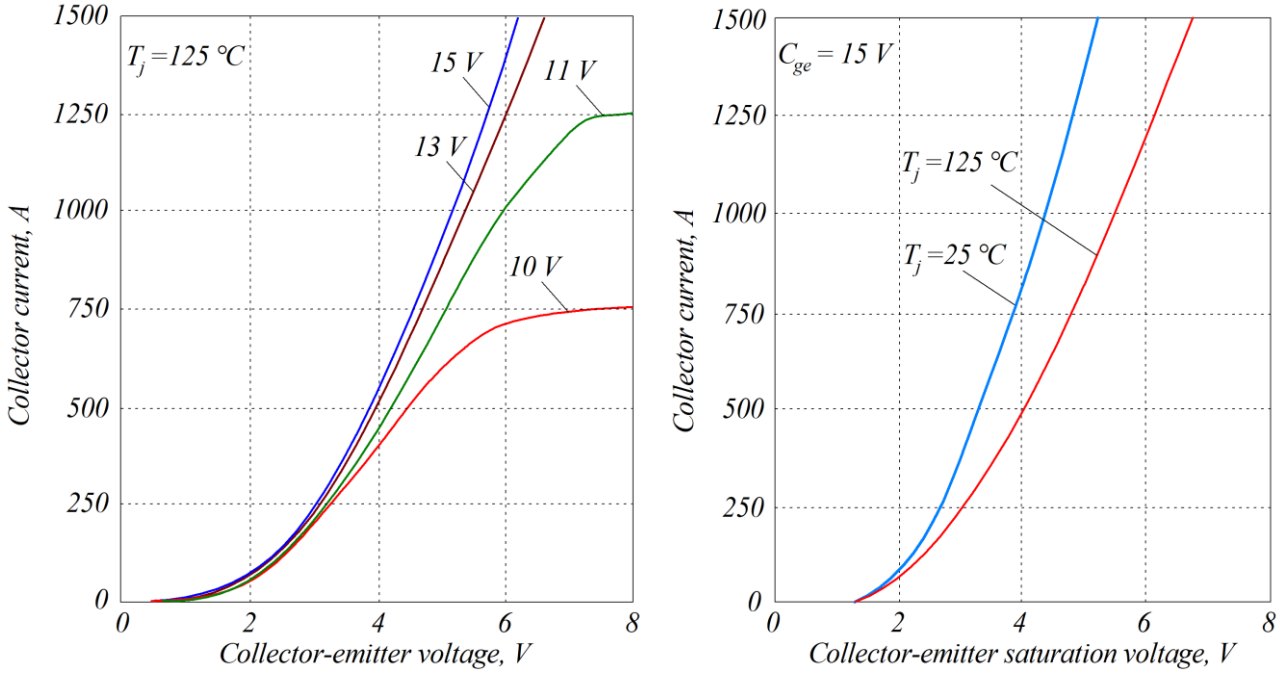

Figure 2.80 – Dependence of voltage drop between collector and emitter of IGBT

Calculation of static losses is given in the equation

$$P_{stat} = V_{ce} \cdot I_{IGBT\_RMS} \cdot n \cdot \gamma, \tag{2.87}$$

where I_{IGBT_RMS} – the RMS of the current flowing through one switch; V_{ce} – the voltage between the collector and the IGBT emitter; n – the number of IGBTs; α – the PWM fill factor.

With sinusoidal modulation, the average relative pulse duration of the PWM is taken as $\gamma = 0.5$. From fig. 2.80, the voltage drop between the collector and the switch emitter for the RMS of the transistor current is determined as 729.46 A. At this conditions the static losses in the AVR will be:

$$P_{stat} = 4.8 \cdot 729.46 \cdot 24 \cdot 0.5 = 42.016 \text{ kW}.$$

Dynamic losses are due to the power dissipated in the switches at the switching intervals. Dynamic losses are determined by the expression:

$$P_{dyn} = \left(E_{on} + E_{off}\right) \cdot f_{sw} \cdot n, \tag{2.88}$$

where E_{on}, E_{off} – the switching-on/off energy; f_{sw} – the switching frequency; n – the number of IGBTs.

The dependence of the switching-on energy E_{on} and switching-off E_{off} of the IGBT series CM750HG-130R on the switched current magnitude is shown in fig. 2.81. From fig. 2.81, the switching-on and off energy for the RMS of the transistor current can be determined.

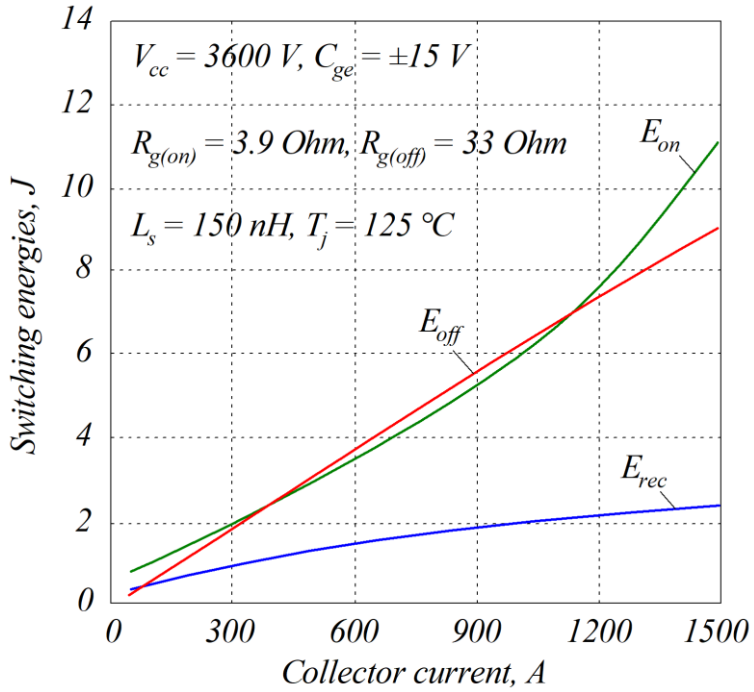

Figure 2.81 – Dependence of switch-on and switch-off energies of IGBT on current

Let us calculate the value of dynamic losses for the studied modulation frequency of the AVR 2 kHz:

$$P_{dyn} = \left(4.5 + 5\right) \cdot 2000 \cdot 24 = 456 \text{ kW}.$$

The losses in an active resistance of the inlet throttles of 0.01 Ohms will be:

$$P_{act} = R_{in} \cdot I_{in}^2 \cdot 3; \tag{2.89}$$

$$P_{act} = 0.05 \cdot 729.46^2 \cdot 3 = 79.935 \text{ kW}.$$

The calculated value of the efficiency of the AVR with a switching frequency of 2 kHz is:

$$\eta = \frac{P_{out}}{P_{in}} = \frac{P_{in} - P_{stat} - P_{dyn} - P_{act}}{P_{in}}; \quad (2.90)$$

$$\eta = \frac{1250 \cdot 2918 \cdot 3 - 42016 - 456000 - 79935}{1250 \cdot 2918 \cdot 3} = 0.947.$$

The dependence of the efficiency on the switching frequency in the AVR is shown in fig. 2.82.

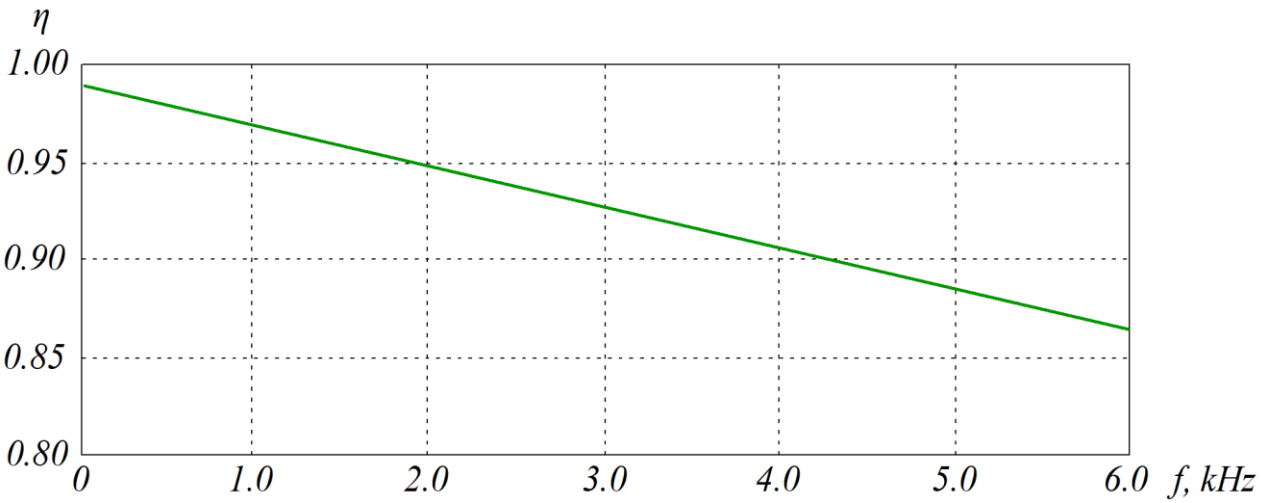

Figure 2.82 – Dependence of efficiency on switching frequency in AVR

From the calculation it follows that the two-level AVR diagram is optimal for use in a PS with a voltage in a DC circle of up to 2000 V and a power of up to 1 MW. These are subways, tram and trolleybus substations.

For the AVR with a voltage in a DC circle of 3.3 kV with a capacity of about 4 MV·A, the two-level circuit requires a parallel connection of switches, which increases the cost of the converter, and also negatively affects the efficiency.

It should be noted that modern transistors with silicon carbide SiC and gallium nitride GaN are becoming more popular [85]. Power switches built on these technologies have a number of advantages: much smaller dynamic and static losses (about several millijoule units) and much higher action rate (the time of the current rise

$t_{on} \approx 40$ nsec and the time of the current drop $t_{off} \approx 80$ nsec in the switch). The use of these switches will significantly reduce losses in the AVR and increase its efficiency to 98 %. The synthesis of the AVR regulator with PWM was performed according to the method for the AVR regulator with the hysteresis CS using the frequency method of the automatic control theory. For this purpose, the AFR of the open AVR system was obtained. The structural diagram of the ARS of the output voltage of the AVR is shown in fig. 2.83.

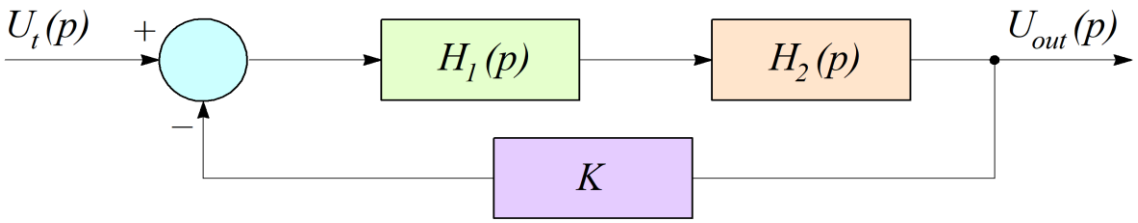

Figure 2.83 – Structural diagram of ARS of AVR output voltage

The following notations are used on the structural diagram: $H_1(p)$ – the transfer function of the regulator; $H_2(p)$ – the transfer function of the AVR; K – the feedback coefficient.

The AFR of the open system is obtained by adding a control signal for the harmonic component and measuring this harmonic in the output voltage. Fig. 2.84 shows the AVR control signal with the addition of a harmonic component of 1 kHz and the form of the output voltage.

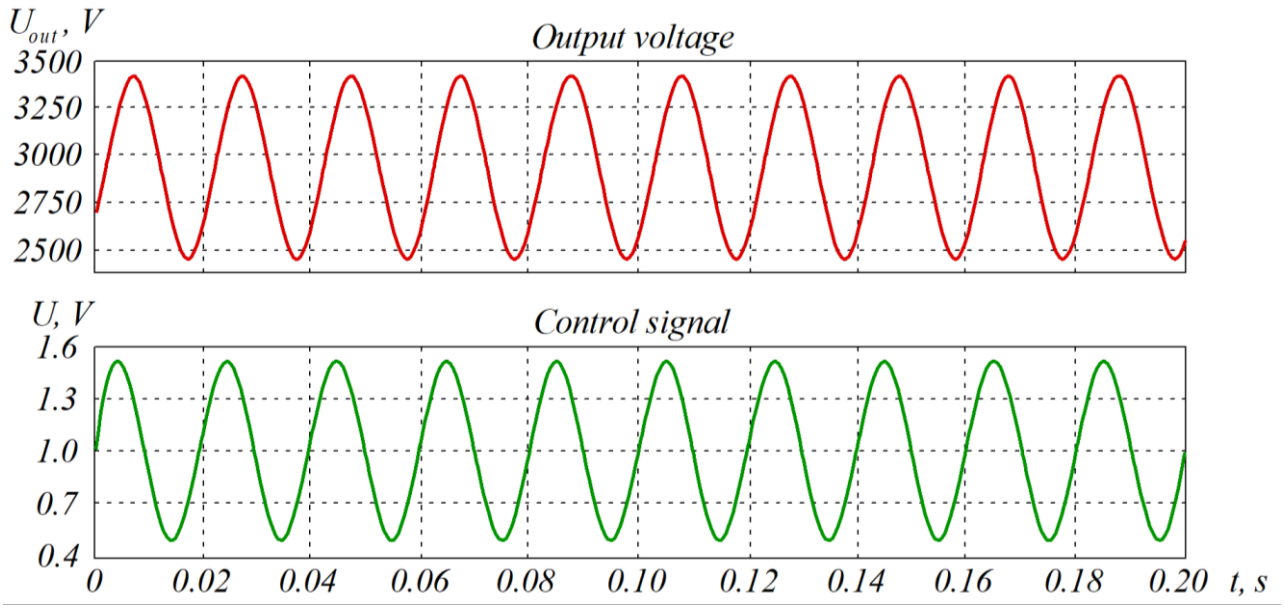

Figure 2.84 – Control signal of AVR and output voltage form

As follows from fig. 2.84, the harmonic component added to the control signal passes into the output voltage.

It should be noted that the form of the output voltage of the AVR with PWM is characterized by its own harmonic composition associated with the PWM frequency. Therefore, harmonics with frequencies not equal to the frequencies of the natural harmonics of the output voltage of the AVR with PWM were added to obtain correct data on the AFR control signal.

The results of the measurement of the AFR are given in table 2.18.

Table 2.18 – AVR response to control signal with frequency components

Frequency of added harmonic component of control signal, kHz	Amplitude of harmonic in output voltage	Gear ratio *K*	Gear ratio *K*, dB
0.1	604.18	428.2553	52.63406
0.4	303.43	215.1064	46.65307
0.75	191.4	135.5106	42.63947
1	139.18	98.24823	39.84649
2	74.9	53.04255	34.49249
3	49.64	35.1773	30.92525
8	18.63	13.17021	22.39186
10	14.91	10.46809	20.39734
20	7.14	4.992908	13.96707
30	4.91	3.439716	10.73045
50	2.89	2.049645	6.233575
80	1.71	1.212766	1.67554
100	1.3	0.921986	–0.70552
200	0.31	0.219858	–13.1571
240	0.06	0.042553	–16.2349

The AFC of the AVR with PWM obtained is shown in fig. 2.85.

By entering the reduction factor in the CS, we obtain a static transmission factor equal to one.

The AVR in the frequency range that determines dynamic processes, according to its AFR, is an aperiodic first-order link.

Asymptotic LAFR systems that are synthesized are shown in fig. 2.86.

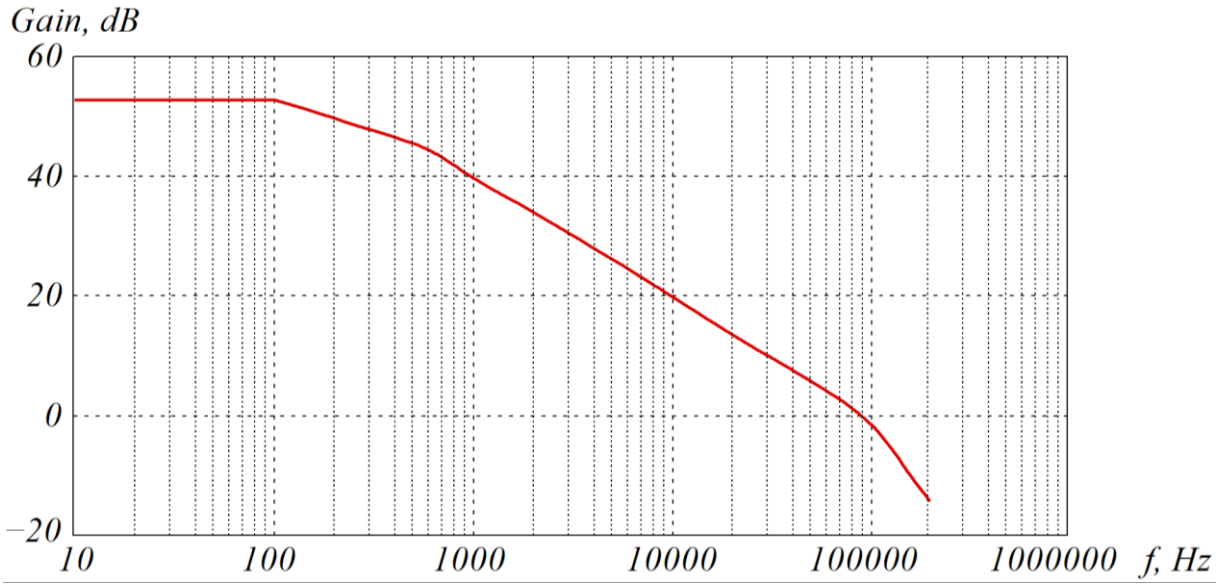

Figure 2.85 – AFR of AVR with PWM

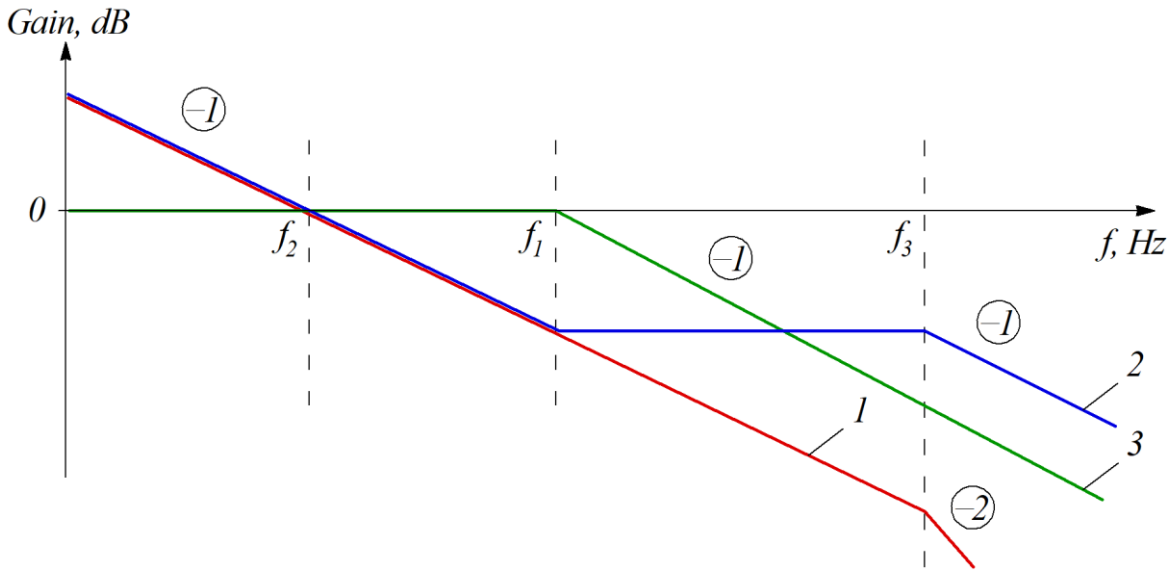

Figure 2.86 – Frequency characteristics of AVR with PWM:
1 – desired LAFR of AVR; *2* – regulator LAFR; *3* – given LAFR

The time constant characterizing the cut-off frequency of the desired LAFR is determined according to the expression:

$$T_2 = \frac{t_r}{\pi \cdot \lambda_\delta}, \tag{2.91}$$

where t_r – the time of output signal setting; λ_δ – the coefficient determined from the set re-adjustment.

The coefficient λ_δ is determined from the permissible re-adjustment δ, %.

The requirements imposed on the ARS of the AVR output voltage, the desired asymptotic LAFR of the open system has a slope of –20 dB/dec. An aperiodic link is installed at the input of the CS of the AVR to increase the immunity.

From the asymptotic LAFRs shown in fig. 2.86, the transfer function of the output voltage regulator of the AVR is obtained:

$$H(p) = \frac{T_1 p + 1}{T_2 p \cdot (T_3 p + 1)}, \tag{2.92}$$

where T_2 – the time factor characterising the cut-off frequency of the desired LAFR; T_3 – the time factor characterising the high frequency range.

From the transfer function of the voltage regulator (2.91) and the LAFR shown in fig. 2.86, it follows that the aperiodic link with the time factor T_3 has little effect on the process in the control system. This is explained by the small values of the transmission coefficient of the frequency range that lie outside its connecting frequency f_3. Properties of the voltage control system in static and dynamic modes are determined by the proportional-integral link. On the basis of the desired LAFR, the transfer function of the closed control system is obtained:

$$W_c = \frac{1}{T_2 p \cdot (T_3 p + 1) + 1} = \frac{1}{T_2 \cdot T_3 p^2 + T_2 p + 1}. \tag{2.93}$$

The transient process of the output voltage during start-up and change of the output voltage task signal with the developed regulator is shown in fig. 2.86. The reaction of AVR in the ARS with PWM to a stepped input action is described by the expression:

$$h(t) = 1 - \frac{e^{-g \cdot \frac{t}{T_0}}}{2 \cdot a} \cdot \left[(a + g) \cdot e^{a \cdot \frac{t}{T_0}} + (a + g) \cdot e^{-a \cdot \frac{t}{T_0}} \right], \tag{2.94}$$

where g – the damping coefficient determined from the expression; T_0 – the time factor.

$$g = \frac{1}{2} \cdot \sqrt{\frac{T_3}{T_4}}; \tag{2.95}$$

$$T_0 = \sqrt{T_3 \cdot T_4}. \qquad (2.96)$$

Fig. 2.87 shows the result of calculating the transient process for the output voltage when changing the task signal and implementing the synthesized regulator by expression (2.93) for the following parameters: $T_4 = 6.4 \cdot 10^{-5}$; $T_3 = 2.4 \cdot 10^{-3}$.

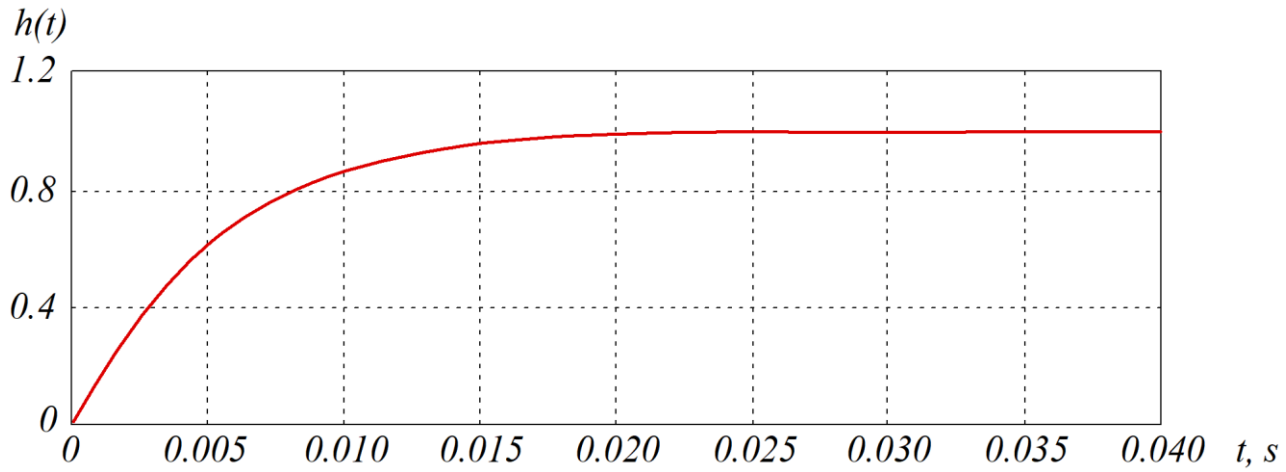

Figure 2.87 – Characteristics of output voltage during transient process

It follows from fig. 2.87 that the CS of the AVR with PWM provides lower speed compared to the AVR with hysteresis modulation.

For studies aimed at confirming the theoretical prerequisites for improving the quality of the input current and output voltage in Matlab, a simulation model of the AVR with PWM was developed [86]. The model consists of the following components: power supply network, power part of the AVR, CS with PWM, output voltage regulator, equivalent *RL*-load with the ERS source, AVR interference voltage meter, and power factor meter.

A previously developed output voltage regulator was applied in the model. The simulation model of the AVR with the CS based on PWM developed in Matlab is shown in fig. 2.88.

In the process of modelling, oscillograms of currents consumed and output voltage were obtained; on the basis of them the analysis of EMC indicators of the AVR with PWM was performed.

The oscillograms of the input phase voltage and currents, as well as the output voltage oscillogram are shown in fig. 2.89.

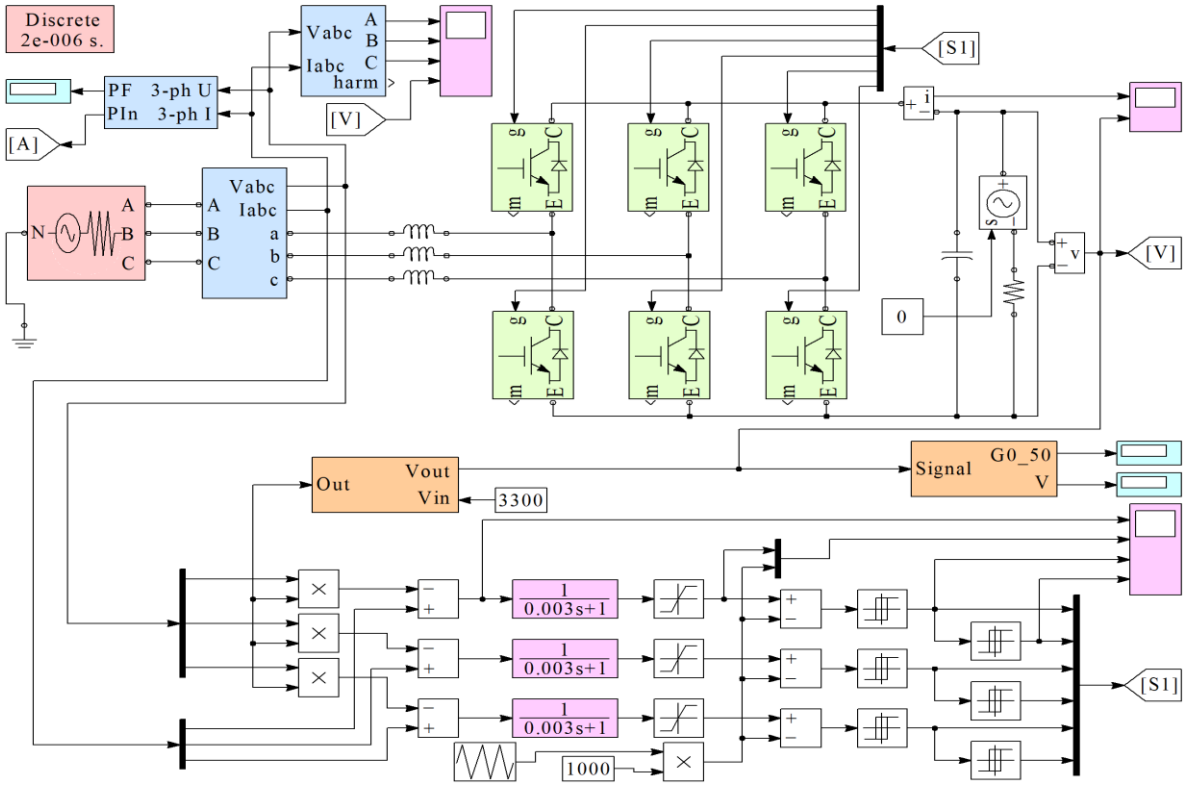

Figure 2.88 – Simulation model of AVR with PWM

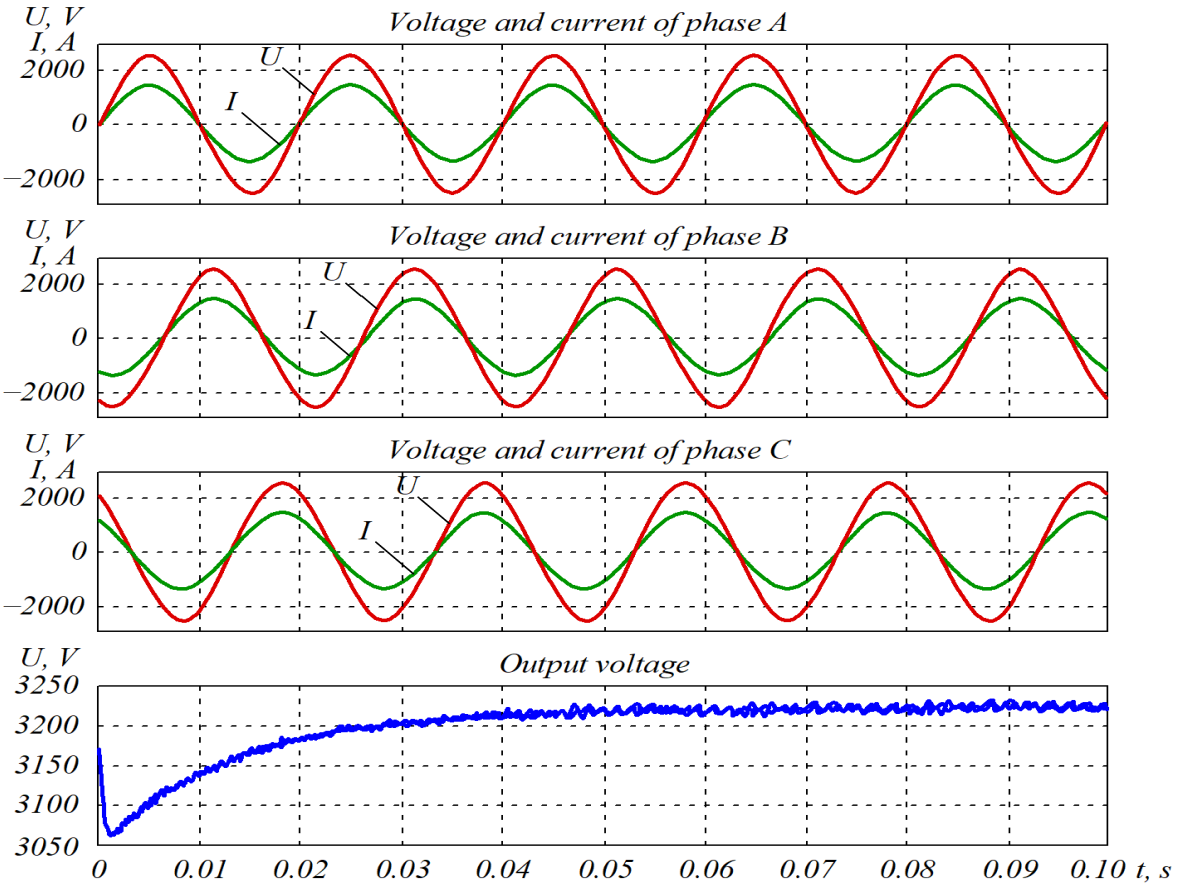

Figure 2.89 – Oscillograms of AVR phase voltages and currents

As follows from fig. 2.89, the input current shape is sinusoidal, and the phase shift of the input current and voltage is close to zero, the amplitude of the ripple in the output voltage does not exceed 30 V.

The results of Fourier analysis of the phase current form of the AVR with PWM at a modulation frequency of 2 kHz are shown in fig. 2.90.

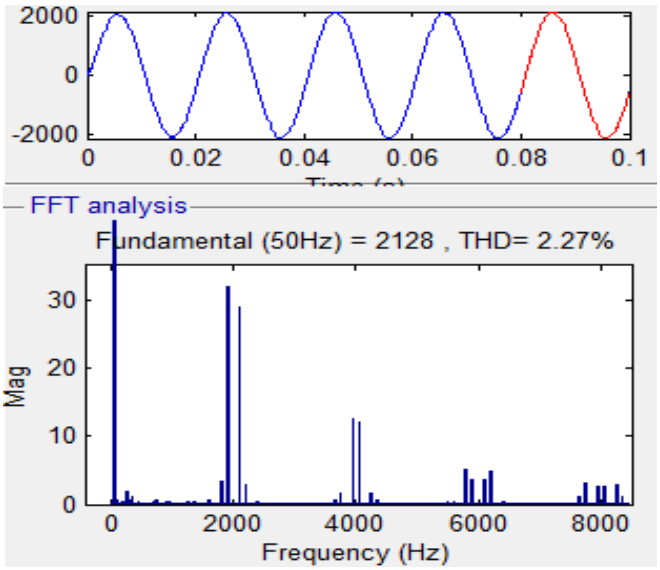

Figure 2.90 – Fourier analysis of phase current

As follows from fig. 2.90, the resulting THD is 2.27 %, which satisfies the specified requirements for the input current quality and confirms the theoretical prerequisites for the possibility of implementing a high quality of the input current and the output voltage of the AVR.

It is found that the spectrum of higher harmonics of the input current and output voltage of the AVR with two-way PWM depends on the network frequency and the modulation frequency. The spectrum of higher harmonics of consumed currents is related to the frequencies of the network and PWM and is subject to the following pattern:

$$f_I = (f_m \mp 2 \cdot f_n) + (f_m \mp 4 \cdot f_n) + (f_m \mp 8 \cdot f_n) + (2 \cdot f_m \mp f_n) + (2 \cdot f_m \mp 5 \cdot f_n) + \\ + (2 \cdot f_m \mp 7 \cdot f_n) + (3 \cdot f_m \mp 2 \cdot f_n) + (3 \cdot f_m \mp 4 \cdot f_n) + (3 \cdot f_m \mp 8 \cdot f_n) + \ldots . \quad (2.97)$$

The output voltage quality is characterized by the interference voltage and the pulse coefficient.

The oscillogram of the output voltage obtained using simulation modelling and its Fourier analysis with a modulation frequency of 2 kHz is shown in fig. 2.91.

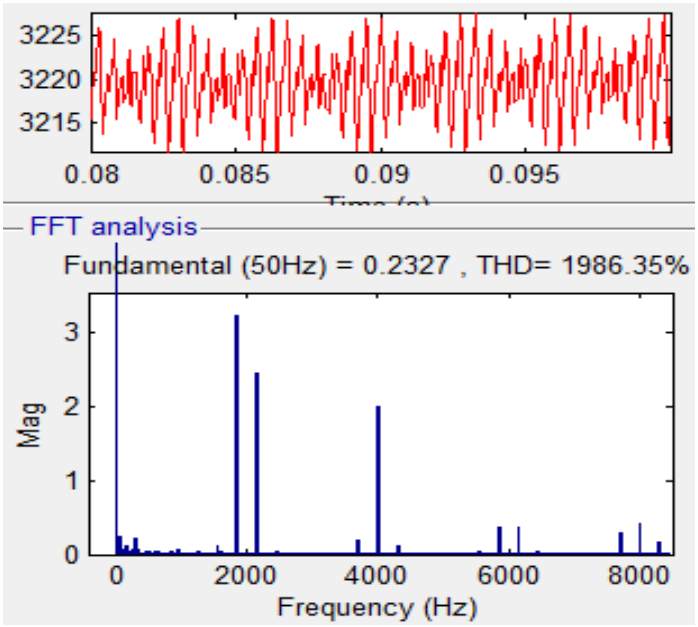

Figure 2.91 – Fourier analysis of AVR output voltage

For two-way PWM, the AVR determines the canonical composition of higher harmonics of the output voltage associated with the switching frequency:

$$f_U = 6\cdot f_n + \left(f_m \mp 3\cdot f_n\right) + \left(f_m \mp 9\cdot f_n\right) + \left(2\cdot f_m\right) + \left(2\cdot f_m \mp 6\cdot f_n\right) + \\ + \left(3\cdot f_m \mp 3\cdot f_n\right) + \left(3\cdot f_m \mp 9\cdot f_n\right) + \left(4\cdot f_m\right) + \left(4\cdot f_m \mp 6\cdot f_n\right) + \ldots. \qquad (2.98)$$

The ripple ratio of the output voltage of the AVR with PWM is determined by the following relation:

$$K_{pulse\_U_{out}} = \frac{\sum U_h}{U_{DC}} = \frac{THD_{U_{out}} \cdot U_1}{U_{DC}}, \qquad (2.99)$$

where THD_{Uout} – the harmonic distortion coefficient of the output voltage obtained from fig. 2.91; U_1 – the first harmonic of the output voltage; U_{DC} – the constant component of the output voltage.

$$K_{pulse\_U_{out}} = \frac{1986\cdot 0.2327}{3220} = \frac{462.2}{3220} = 0.143\,\%.$$

Taking into account the higher harmonics in the phase voltage and current, the power factor is calculated according to the expression:

$$PF = \frac{I_{1RMS}}{I_{RMS}} \cdot \frac{U_{1RMS}}{U_{RMS}} \cdot \cos\varphi. \qquad (2.100)$$

In the simulation model, the meter to measure the factor of power consumed by the AVR with PWM is made in accordance with expression (2.100) and implemented in the subsystem in fig. 2.92.

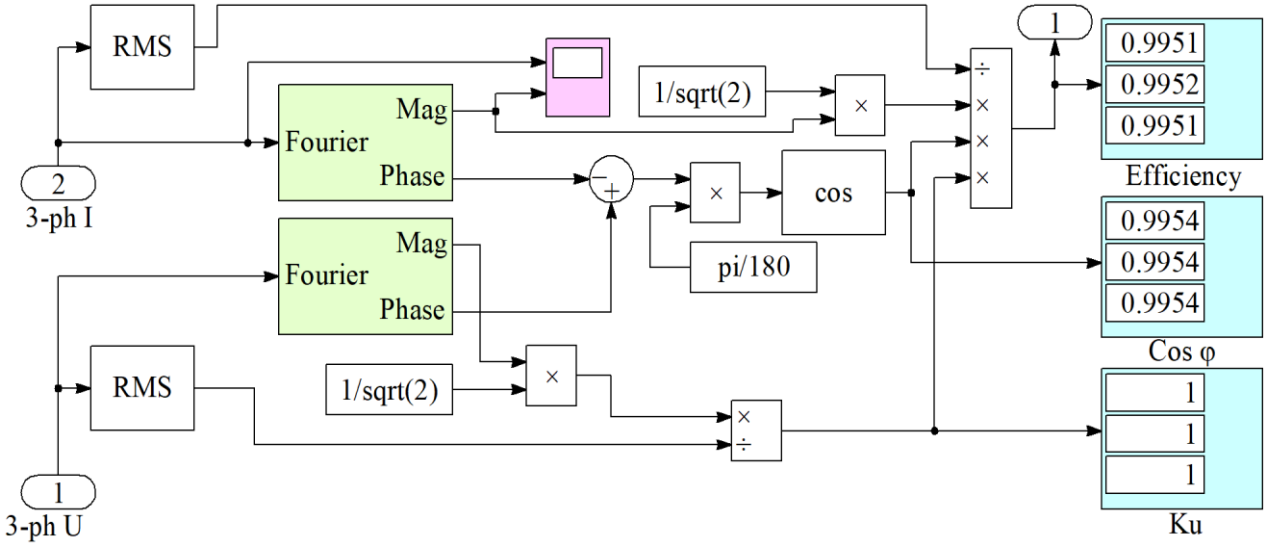

Figure 2.92 – Subsystem for calculating AVR power factor

The measured power factor reaches a value of 99.51 %. The level of interference voltage of the active rectifier with PWM in the overhead network is determined using the subsystem shown in fig. 2.93.

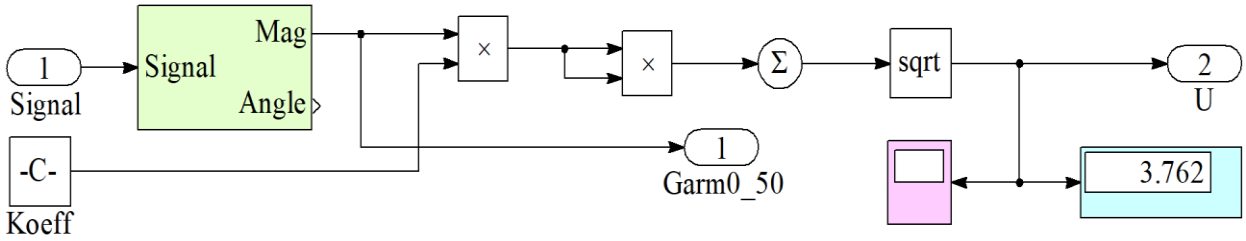

Figure 2.93 – Subsystem for calculating AVR interference voltage

For the form of the AVR output voltage shown in fig. 2.91, the interference voltage is 3.762 V.

The result of the study of dynamic processes of AVR with an output voltage regulator when changing the task signal and implementing the synthesized regulator is shown in fig. 2.94.

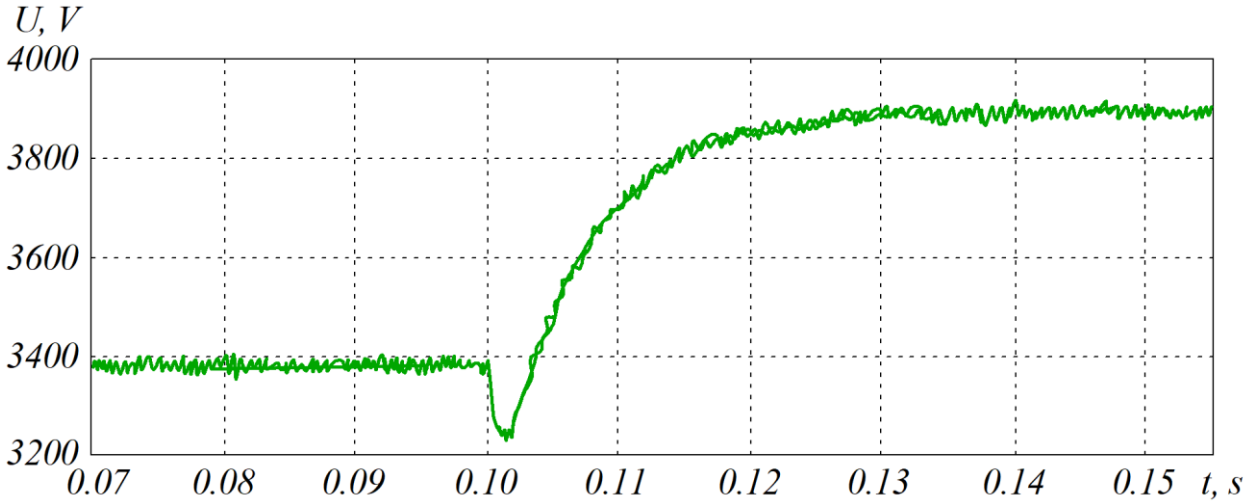

Figure 2.94 – Characteristics of output voltage during transient process

The output voltage oscillograms confirm the adequacy of the transients obtained with the simulation model and calculation.

Table 2.19 shows the indicators of power quality of the AVR with the proposed CS based on PWM.

Table 2.19 – Electricity quality indicators of AVR with CS based on PWM

Parameter	Value
Power factor, %	99.51
THD of consumed current, %	2.27
Interference voltage, V	3.764
Output voltage pulse factor, %	0.143
Elementary switching frequency, kHz	2
Efficiency, %	95.55

The CS of the AVR with two-way PWM meets the specified requirements for the electricity quality when implementing a much lower switching frequency, which makes the CS of the AVR with PWM better.

To theoretically confirm the indicators of EMC of the AVR with the CS with two-way PWM and with power supply network, testing of the AFKU converter unit developed by the R&D Company VERTICAL (Kharkiv) was carried out. The AFKU unit operates in the active rectifier or APF modes. The AFKU converter unit is shown in fig. 2.95.

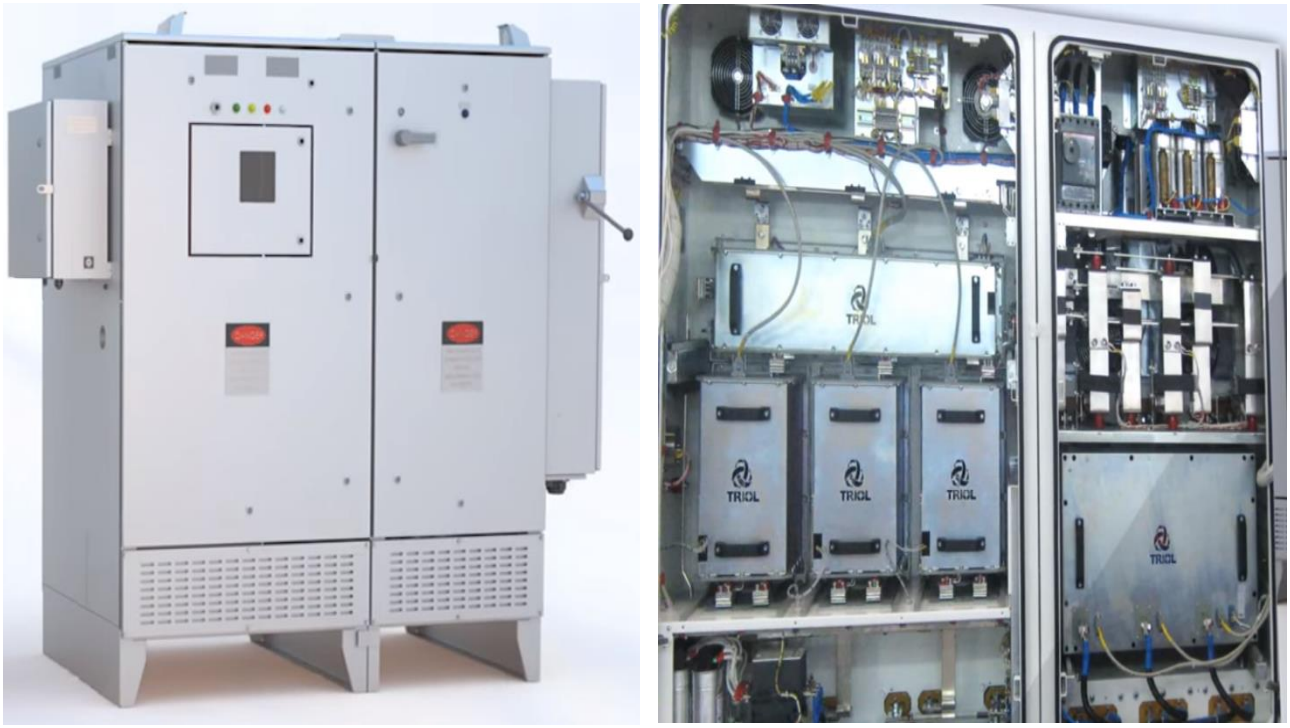

Figure 2.95 – AK06 with AFKU

The AFKU unit was built on the basis of IGBT modules of FF600R17ME4 series manufactured by Infenion.

The computing core of the CS is a specialized processor TMS320F28335 manufactured by Texas Instruments.

The parameters of the power part of the AFKU unit are given in table 2.20.

Table 2.20 – Parameters of power part of AFKU unit

Parameter	Value
Rated power, kW	750
Rated supply voltage, V	3×380
Rated output voltage, V	850
Inductance of inlet throttles, mH	0.12
Capacitance of AFKU capacitor, mF	19
PWM frequency, kHz	5

The oscillogram of the input voltage and currents of AFKU is shown in fig. 2.96.

The spectrum of higher harmonics of the phase current of the AFKU unit is obtained using a Fluke 43 quality analyser. As follows from fig. 2.96, the AFKU unit creates a form of consumed current close to the sinusoid, with a power factor close to one.

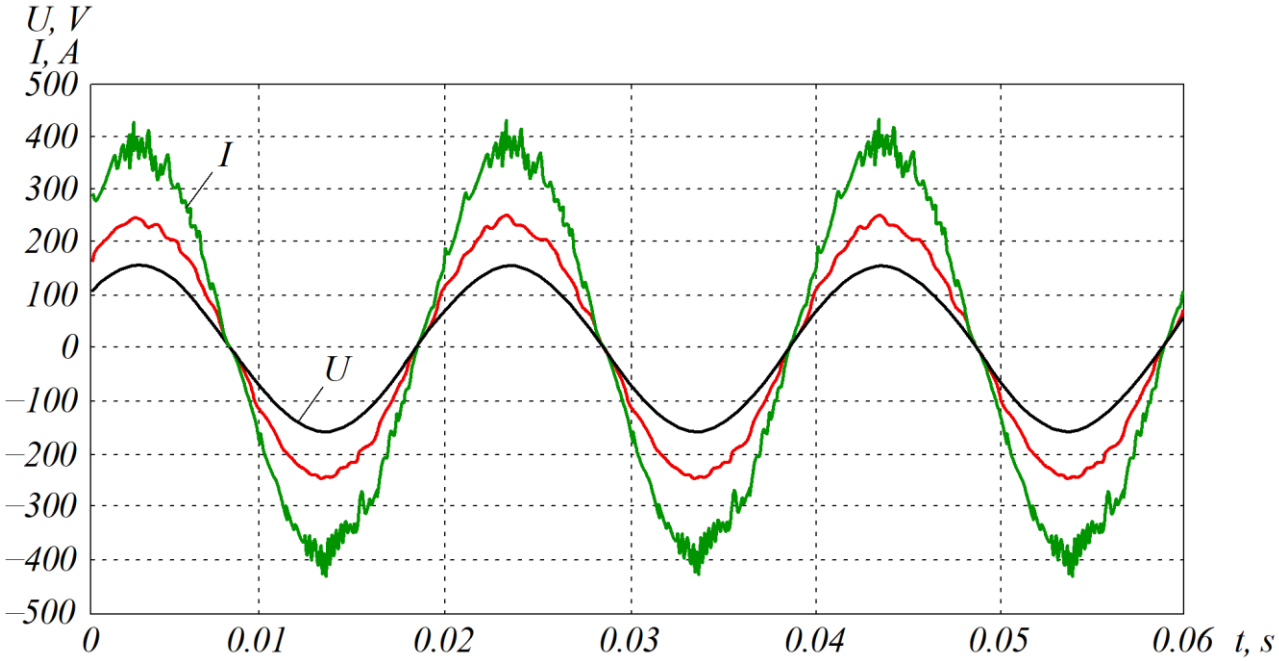

Figure 2.96 – Oscillogram of input voltage and currents of AFKU

The THD of the input current of the AFKU unit, calculated by the Fluke 43 measuring the power quality, is 6.63 %.

2.7. Improvement of the electromagnetic compatibility of frequency converters by the introduction of active rectifiers with power factor compensation

Frequency converters (FC) are powerful sources of higher current harmonics in the network. Due to the strict requirements of national and international standards (GOST 51317.3.12-2006, IEC 61000-3-14, IEC-555, IEEE-519) for the emission of harmonic components of currents consumed by technical means, the issue of reducing the emission of higher current harmonics and increasing the power factor is relevant. The second important issue is the implementation of the FC structure with energy regeneration from the engine into a network with a high quality of energy regeneration. One of the options for solving these problems is the use of active rectifiers with power factor compensation. The peculiarities of the circuits of the active rectifiers are: the possibility of implementing the sinusoidal form of the input phase currents with a power factor close to one and the possibility of implementing regeneration, regulating the output voltage above the phase voltage of the network [87].

The most common is the FC circuit with a three-phase diode rectifier and an AVI. Significant disadvantages of this scheme are: high level of emission of higher

current harmonics, lack of possibility to regulate the voltage level in the DC circuits, and lack of possibility to implement regeneration. The structural diagram of the FC with a diode rectifier is shown in fig. 2.97. The use of thyristor rectifier circuits solves the problem of voltage regulating for the DC circuits, but does not solve the problem of current harmonic emission.

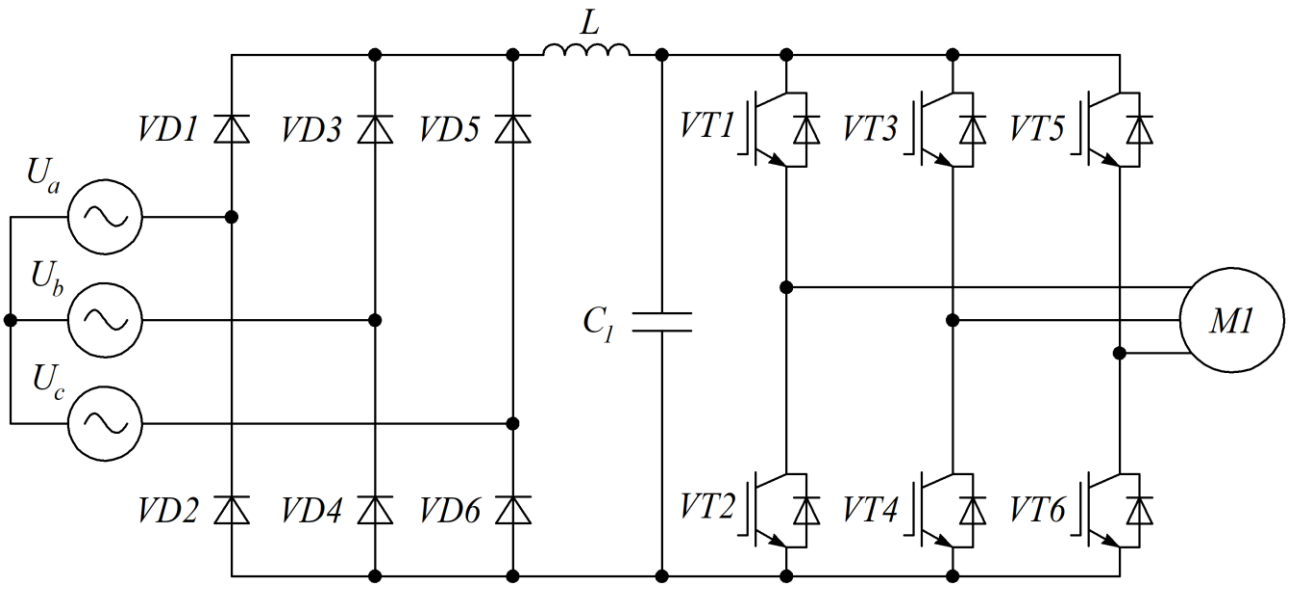

Figure 2.97 – Structural diagram of FC with diode rectifier

The high emission level of higher harmonics in the FC requires additional input filters that increase cost, mass and overall dimensions of the FC.

The FC circuit with the active voltage rectifier and the AVI is assembled on fully lockable valves. The CS of the AVR and the AVI operate under a vector control system. The power circuit of the AVR coincides with the AVI circuit, but it operates in reverse mode. The frequency converter, due to the possibility of operation of the AVR both in the active rectifier mode and in the regeneration mode, provides the implementation of the power factor close to one, the form of the consumed current close to the sinusoid with the coefficient of non-linear current distortions less than 3 %, as well as the implementation of the bi-directional electricity flow between the power supply network and the motor. The structural diagram of the FC based on the two-level AVR–AVI structure is shown in fig. 2.98.

The FC with a two-level AVR–AVI structure needs high loading requirements for switches. The loading requirements for the switches in the scheme can be reduces by implementing a three-level AVR–AVI structure. The use of the three-level AVR–AVI structure not only reduces the power dissipated on the switches, but also reduces the phase current nonlinear distortion coefficient.

The three-level structure of the FC based on the AVR–AVI is shown in fig. 2.99.

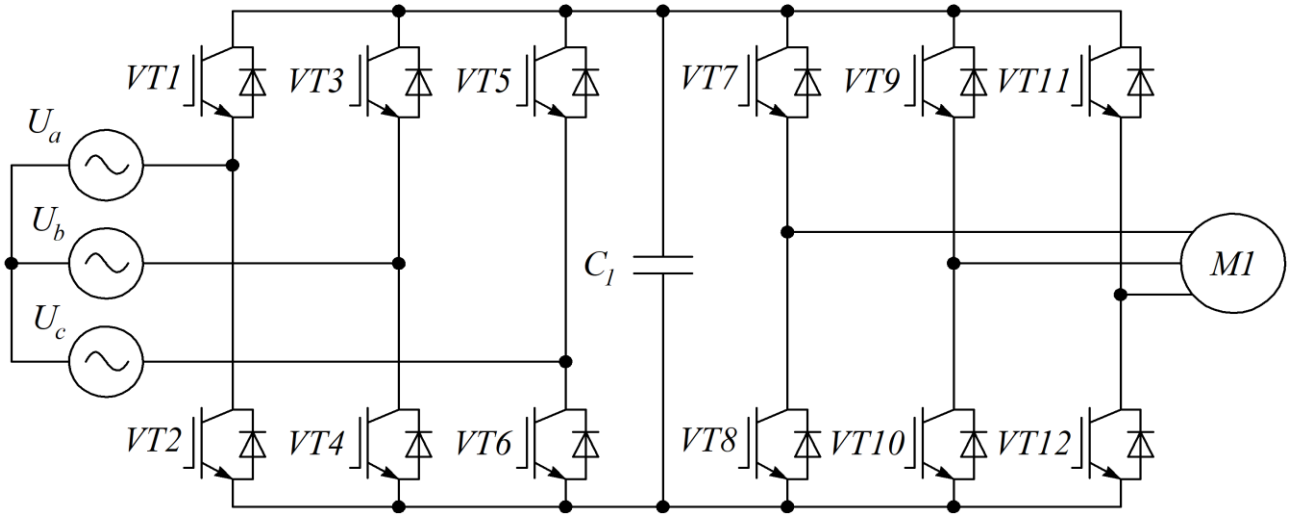

Figure 2.98 – Structural diagram of FC based on two-level AVR–AVI structure

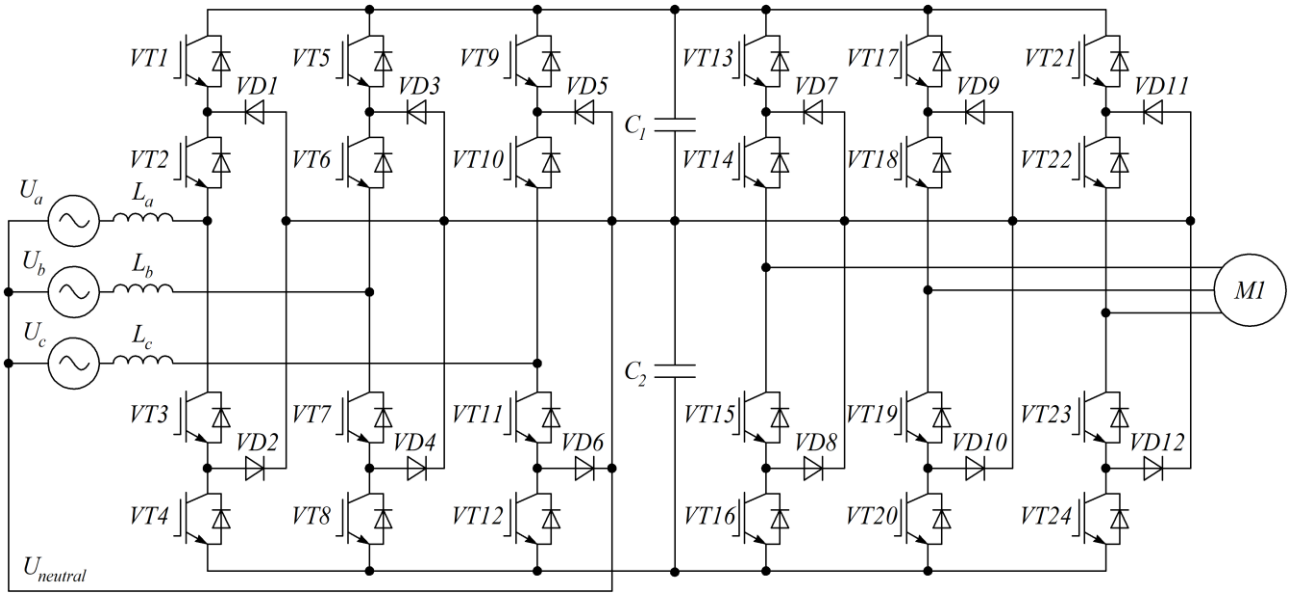

Figure 2.99 – Structural diagram of FC based on three-level AVR–AVI structure

On the basis of the three-level AVR–AVI structure, a FC simulation model was built in Matlab (fig. 2.100) with the following parameters:

– mains phase voltage – 320 V;

– inductance of inlet throttles, 2 mH;

– voltage in DC circuits – 3200 V;

– capacitance in the DC circle – 6 μF;

– load AVI – *RL* = 10 Ohm, *L* = 0.1 Gn;

– PWM frequency – 10 kHz.

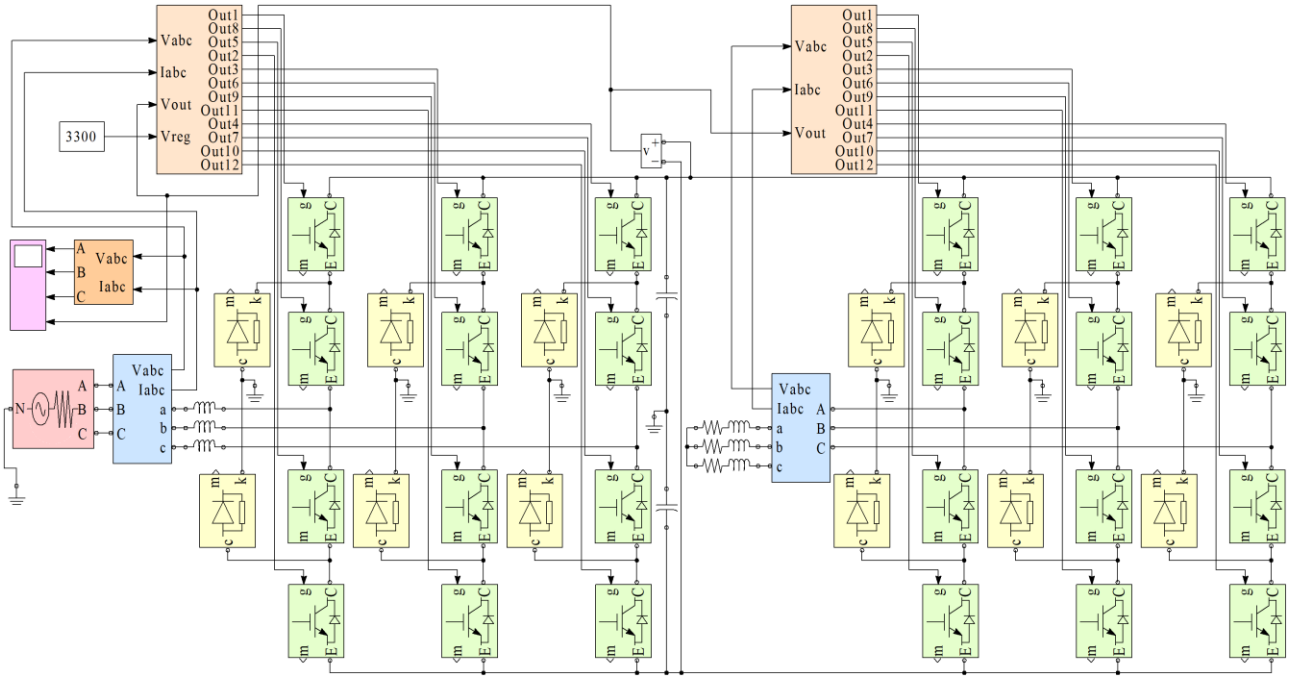

Figure 2.100 – Simulation model of FC based on three-level AVR–AVI structure

The forms of input phase voltages and currents are presented in fig. 2.101. The forms of voltage and current in the DC circuits of the FC are shown in fig. 2.102.

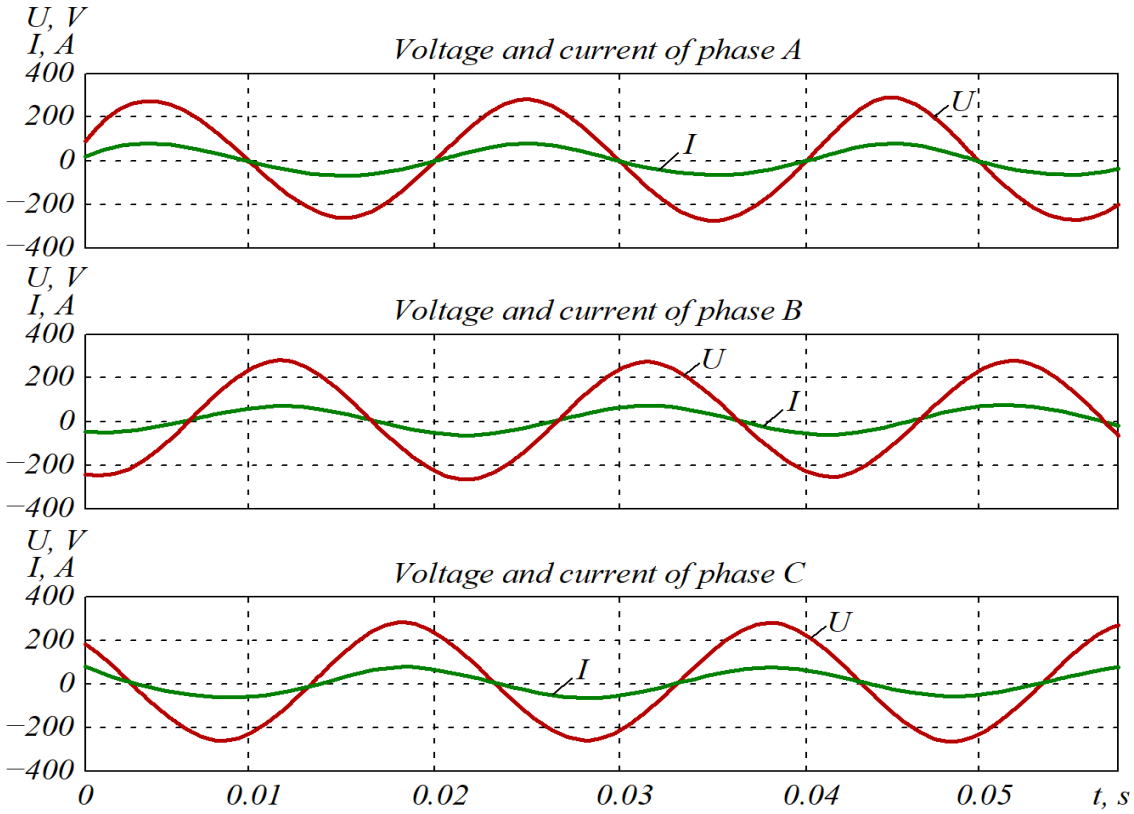

Figure 2.101 – Forms of input phase voltages and currents of AVR

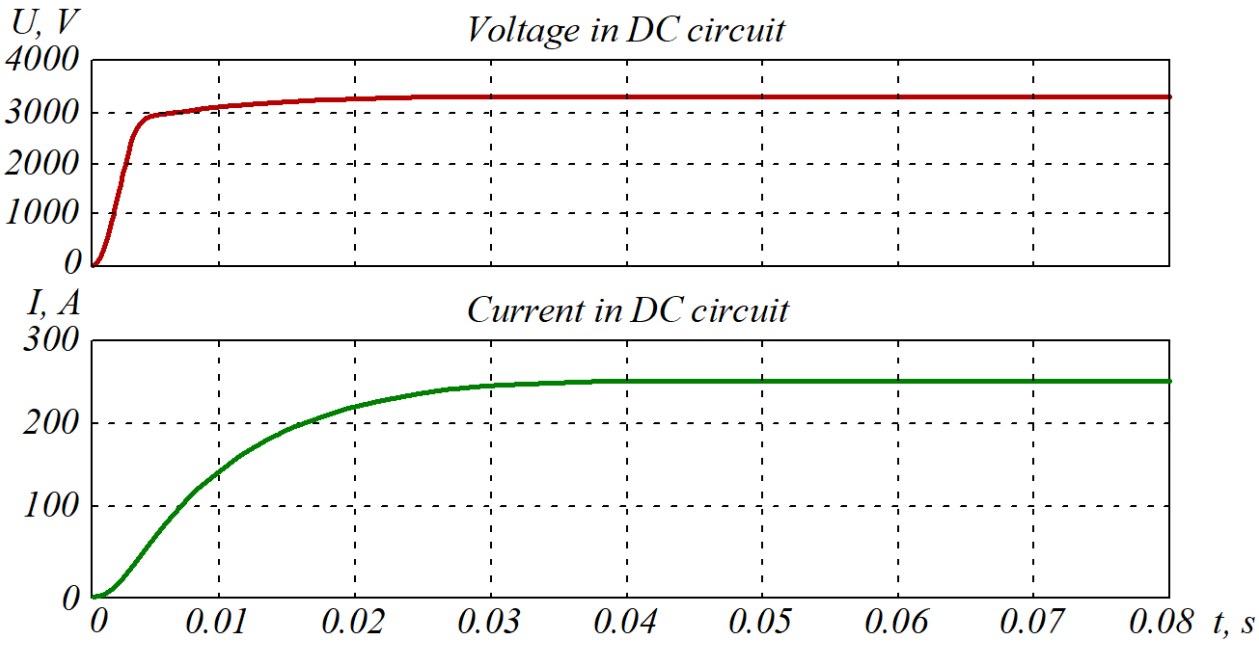

Figure 2.102 – Voltage and current in DC circuit of FC

The results of the analysis of the simulation modelling of the two- and three-level AVR–AVI structures are given in table 2.21.

Table 2.21 – Energy characteristics

Parameter	Bi-level AVR–AVI	Three-level AVR–AVI
Coefficient of power consumed from network, %	98.78	99.34
Coefficient of non-linear distortions of input phase currents, %	1.05	0.61
Coefficient of voltage ripple in DC circle, %	0.43	0.25
Power factor in regeneration mode, %	–98.2	–98.78
Coefficient of nonlinear distortions of the phase current of the AVI in PWM mode, %	4.07	4.07
Power dissipated by one AVR switch, kW·h	0.66	0.33

Three-level active rectifiers have a number of advantages compared to two-level ones: increased power factor consumed from the network, lower emission of higher current harmonics, and lower loading requirements for switches.

CHAPTER 3

INCREASED ENERGY EFFICIENCY OF THE TRACTION ELECTRIC DRIVE FOR ELECTRIC ROLLING STOCK

3.1. Improved energy characteristics of AC rolling stock by using three-level active four-quadrant rectifiers

In order to minimize reactive power and higher current harmonics, as well as to improve EMC of traction power-supply networks and railway automation systems, modern AC ERS uses the active four-quadrant rectifier. The classic topology of this converter is a two-level full-bridge active rectifier, which provides a power factor close to one and regeneration energy to the power supply network. However, the high switching frequency causes high dynamic losses in power transistors and low efficiency. And the use of three-level active four-quadrant rectifiers with power factor correction is promising.

In study [88] the authors propose a CS of a three-level active rectifier with a two-channel equal-shifted sinusoidal PWM. The advantage of the proposed control algorithm, compared to the known ones, is an improvement in the input current quality and a reduction in the switching frequency of the power switches, which leads to lower power losses and improved efficiency of the rectifier. Frequently the input converters of the AC ERS are diode and thyristor rectifiers. These converters cause the consumption of reactive power from the power supply network, as well as a significant emission of higher harmonics of the consumed currents. This causes increased additional losses in power supply systems, as well as a deterioration of EMC of traction power supply networks and railway automation systems.

Recently, two-level active four-quadrant rectifiers, known as 4QS-converters, have been increasingly used for the ERS. The structural diagram of the traction electric drive of an AC electric locomotive with input two-level 4QS-converters is shown in fig. 3.1. Their advantage, compared to classical diode and thyristor rectifiers, is the possibility of implementing the sinusoidal form of the consumed current, providing a power factor close to one (> 99 %), and regeneration energy into the power supply network. In addition, the possibility of smooth start-up adjustment of the ERS makes it possible to reduce the dynamic loads on its mechanical component. However, this topology has a number of drawbacks. At the same time, the need to form a high switching frequency of power switches leads to quite large dynamic losses in power switches with a lower efficiency compared to diode and thyristor rectifiers.

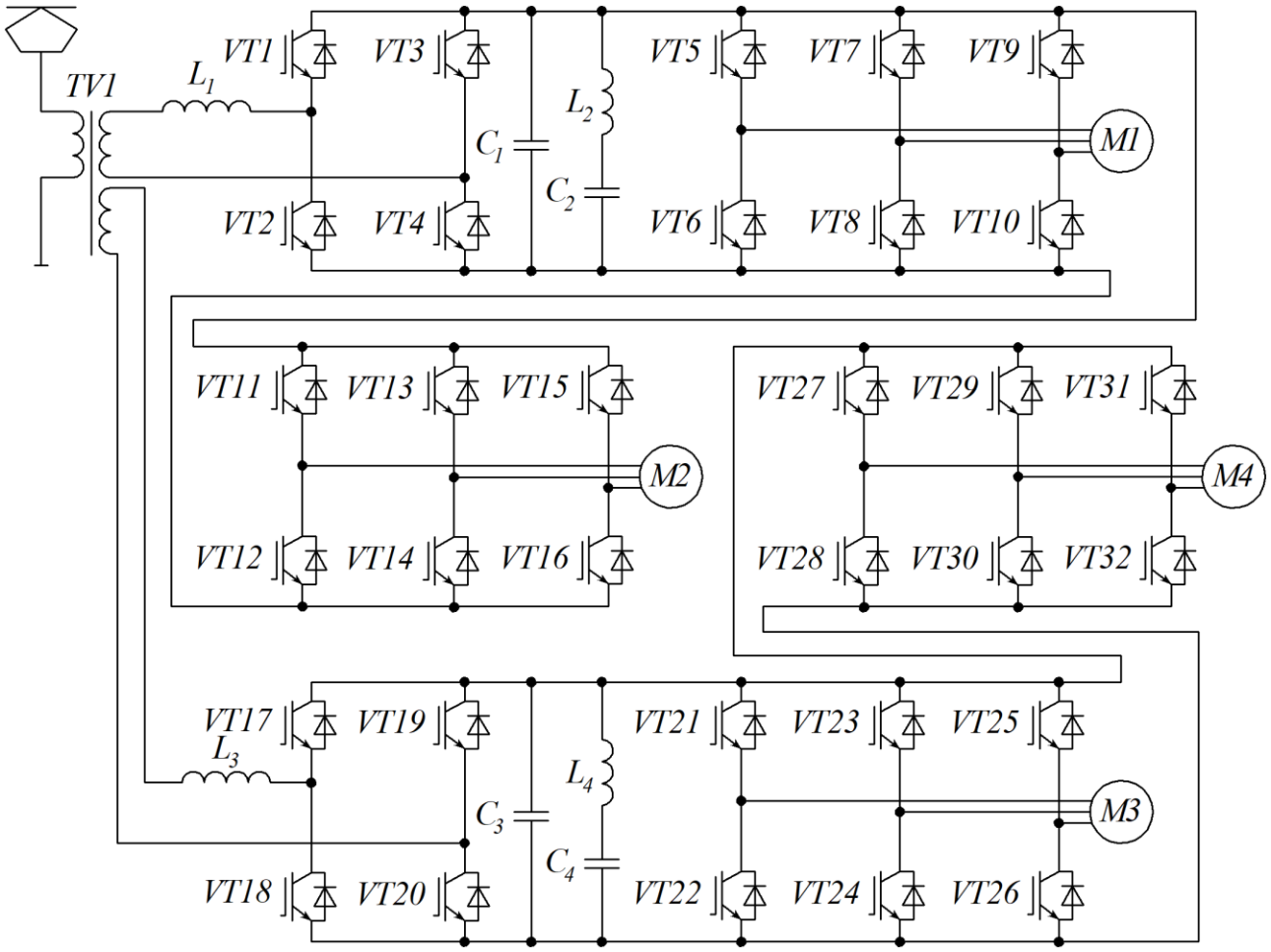

Figure 3.1 – Structural diagram of traction electric drive
with two-level 4QS-converters

Therefore, the task of searching for solutions to increase the efficiency of active four-quadrant rectifiers is urgent. The values of the realized energy characteristics of the active rectifiers largely depend on the selected modulation algorithm and the power circuit.

Study [89] presents the results of the research into two-level active rectifiers, the CS of which is based on hysteresis modulation. The disadvantage of the CS of active rectifiers with a hysteresis switching algorithm is a changing and quite high switching frequency of power transistors (over several tens of kilohertz). High switching frequency causes, on the one hand, high electric power quality, but, on the other hand, high dynamic losses in power transistors and low efficiency.

Study [90] presents the results of the research into of a two-level active rectifier with the CS built on PWM. The PWM in the CS makes it possible to provide a lower and constant switching frequency of power switches (≈1 kHz), which leads to lower dynamic losses and higher efficiency. However, with a decrease in the switching frequency of power switches, the quality of electricity decreases as well.

In study [91] the authors research into increased sinusoidality of the input current in active double-level rectifiers with PWM, obtained in implementation of the data interleaving algorithm. Interleaving is a mode of mutual compensation of higher harmonics in input currents in two or more converters powered from one power supply network. However, interleaving algorithms can only be used in systems where several active rectifiers powered from the same network are used.

Publication [92] presents a study of comparative indicators of losses in power IGBT switches of different classes. For the ERS, in the diagram of a two-level active switch rectifier, it is necessary to use higher-class switches (6.5 or 4.5 kV) at nominal voltage, which have higher values of static and dynamic losses if compared with lower-class switches. This results in excess power losses in the converter. A promising way to increase the energy efficiency of AC ERS is to use the topology of a three-level active rectifier (fig. 3.2). Fig. 3.2 shows current collector, input step-down transformer, three-level active rectifier, capacitive filter and equivalent *RL*-load. Compared to the two-level active rectifier, the three-level active rectifier circuit contains twice as many IGBTs and four additional power diodes. However, the three-level circuit makes it possible to use switches with a rated voltage two times lower.

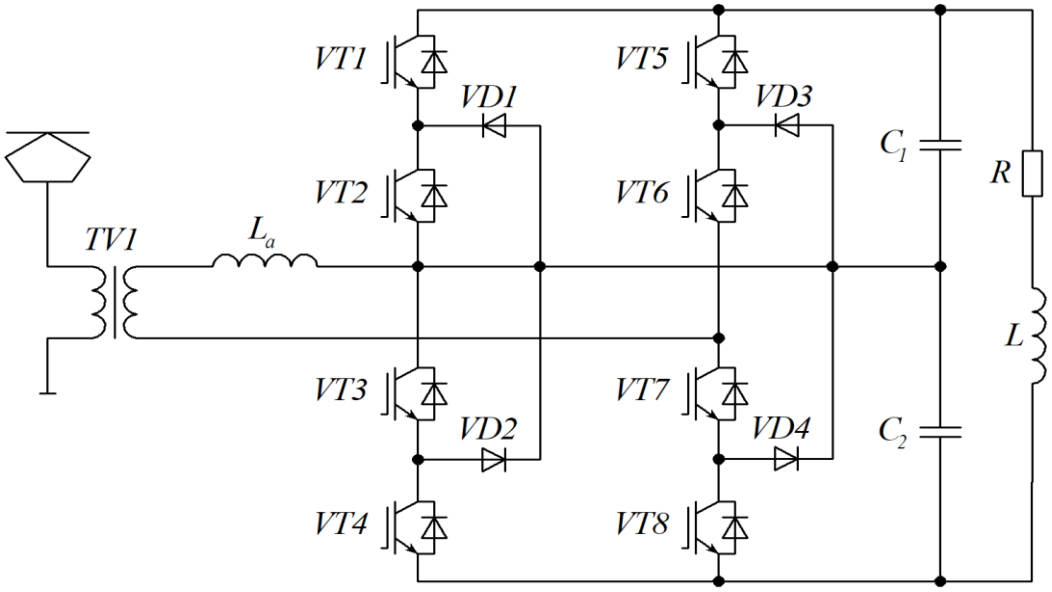

Figure 3.2 – Diagram of traction electric drive with three-level rectifiers

The application of a three-level topology of the active rectifier makes it possible to use lower-class switches to implement the same voltage in the DC circle. At the same time, the characteristic feature of lower-class switches is a lower drop between the collector and the emitter, as well as a lower switching energy. The characteristics of IGBTs of different classes designed for one current are given in table 3.1.

Table 3.1 – Characteristics of IGBTs of different classes

Type	Current, A	Voltage, V	V_{ce}, V	E_{on}, J/imp	E_{off}, J/imp
CM750HG-130R	750	6600	3.8 (at 25 ℃) 4.8 (at 125 ℃)	3.5 (at 25 ℃) 4.4 (at 125 ℃)	3.4 (at 25 ℃) 4.9 (at 125 ℃)
CM800HC-90R	800	4500	3.5 (at 25 ℃) 4.5 (at 125 ℃)	3.1 (at 25 ℃) 3.8 (at 125 ℃)	2.15 (at 25 ℃) 2.85 (at 125 ℃)
CM800HC-66H	800	3300	3.3 (at 25 ℃) 3.6 (at 125 ℃)	1.4 (at 25 ℃) 1.7 (at 125 ℃)	2.15 (at 25 ℃) 2.85 (at 125 ℃)
CM800HB-50H	800	2500	2.8 (at 25 ℃) 3.15 (at 125 ℃)	0.65 (at 25 ℃) 0.80 (at 125 ℃)	0.75 (at 25 ℃) 0.96 (at 125 ℃)
CM800HA-34H	800	1700	2.75 (at 25 ℃) 3.15 (at 125 ℃)	0.3 (at 25 ℃) 0.37 (at 125 ℃)	0.3 (at 25 ℃) 0.39 (at 125 ℃)
CM800DX-24T1	800	1200	1.9 (at 25 ℃) 2.15 (at 125 ℃)	0.08 (at 25 ℃) 0.1 (at 125 ℃)	0.084 (at 25 ℃) 0.11 (at 125 ℃)

The current voltage characteristics of transistors $V_{ce}(I_c)$, as well as the dependence of switching energy on switched current $E_{on}(I_c)$ and $E_{off}(I_c)$ for the IGBTs described in table 3.1 are shown in fig. 3.3.

As can be seen from the dependencies shown in fig. 3.3, at the same switching frequency and load current, the half-lower-class switches have significantly lower switching losses.

Numerical calculation of power losses in high-voltage IGBTs included in two-level and three-level AVIs was carried out in a specialized program MelcoSim 5.4 designed by Mitsubishi (fig. 3.4). The advantage of this program is taking into account real characteristics of the transistors as they declared.

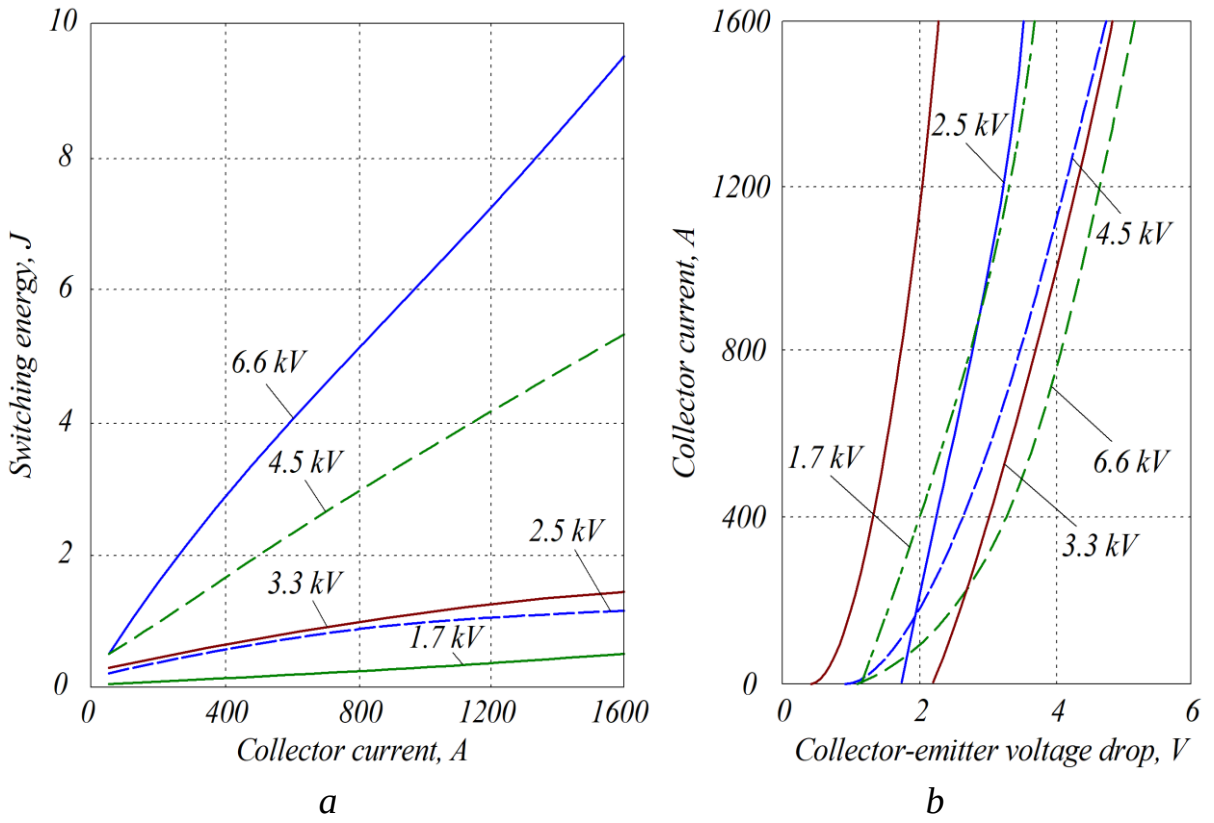

Figure 3.3 – IGBT characteristics:
a – dependence of switching energy of IGBTs of different classes on current;
b – dependency of voltage drop in collector-emitter on current

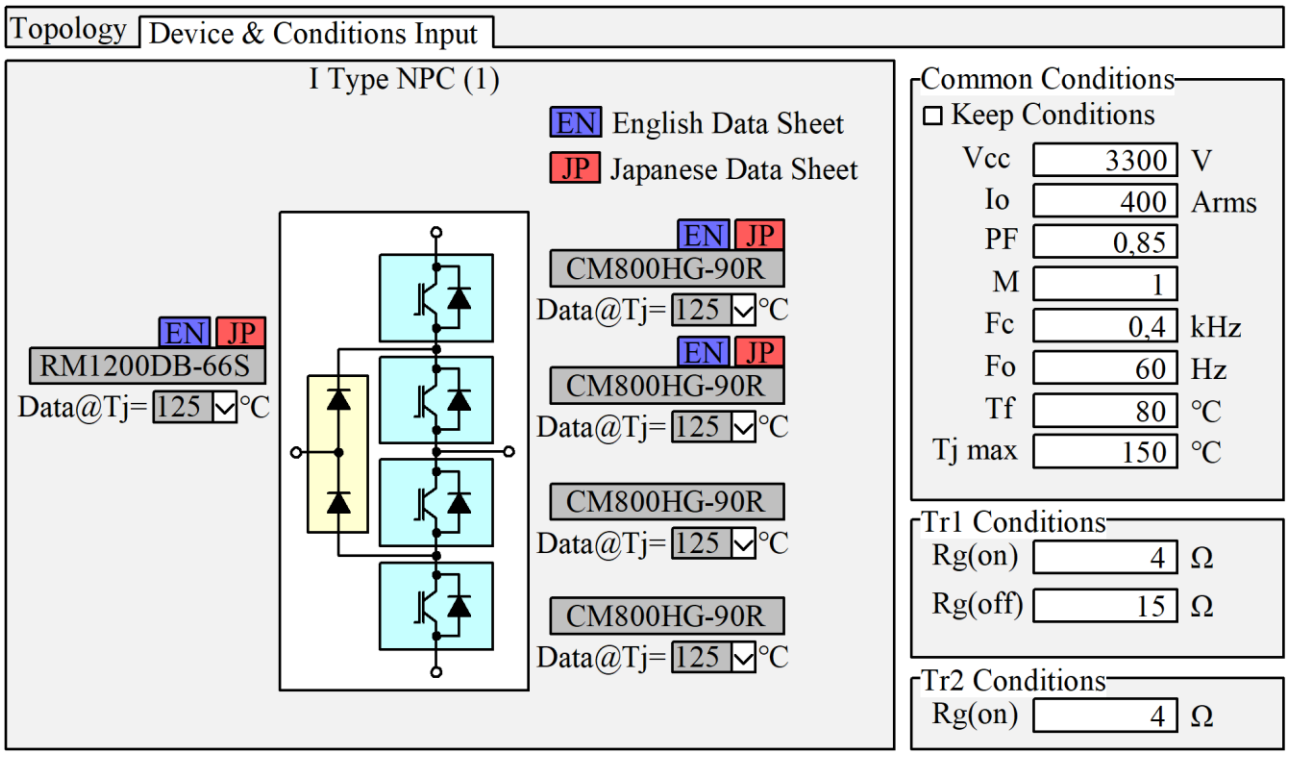

Figure 3.4 – Interface of MelcoSim 5.4 for calculation of losses

The calculation of power losses for the three-level active rectifier was carried out for an IGBT of the 33rd class of series CM800HG-90R and diodes of series RM1200DB-66S.

For a two-level active rectifier, the loss calculation was performed for transistors of the 65th class of series CM750HG-130R. The calculation was carried out with the following output data: voltage in the DC circle – 3.3 kV, phase current – 400 A, modulation type – sinusoidal PWM.

The results of calculating the power losses in the specified IGBT modules for a two-level active rectifier and a three-level active rectifier are shown in fig. 3.5.

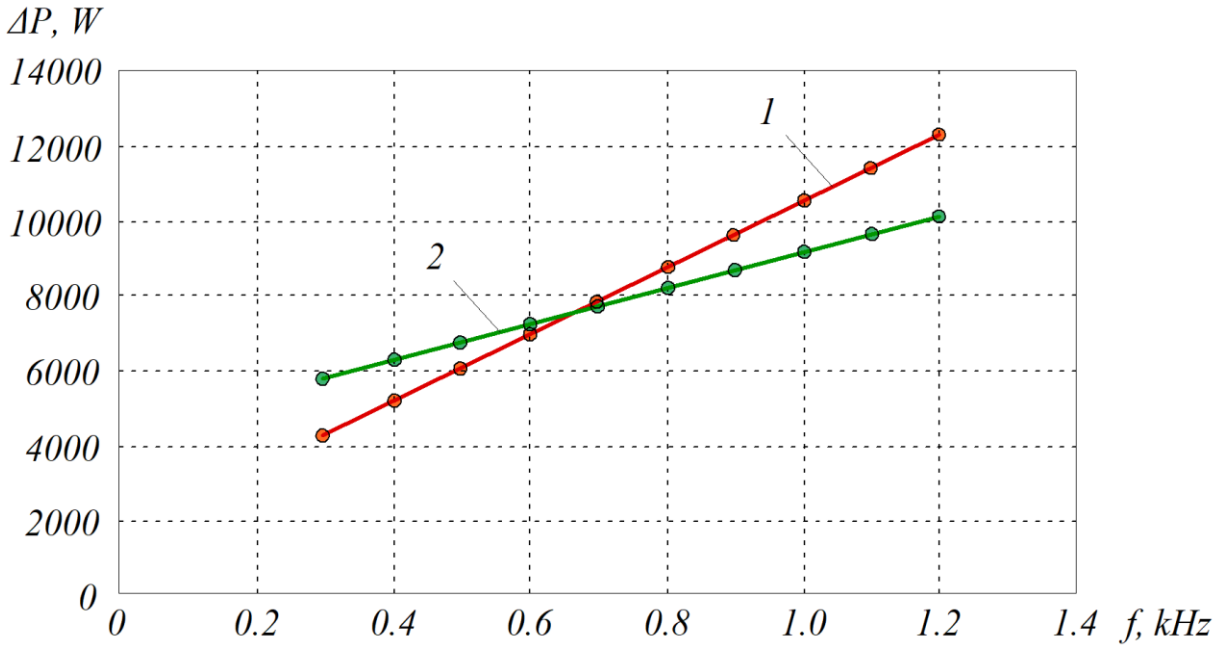

Figure 3.5 – Dependence of power losses on frequency:
1 – in two-level rectifier; *2* – in three-level rectifier

The dependence of the efficiency of a two-level active rectifier and a three-level active rectifier (without losses in the active resistance of the conductors) on the switching frequency is shown in fig. 3.6.

As can be seen from fig. 3.6, starting from a frequency of 700 Hz, the losses in the three-level topology become lower compared to the losses in the two-level topology, and the efficiency becomes higher, which indicates the feasibility of applying this topology at given frequencies.

In single-phase three-level active rectifiers, by analogy with three-level AVIs, a single-channel equal-shift PWM is used (fig. 3.7). The special feature of such a modulation algorithm is that the input current of the single-phase three-level active rectifier is switched with the frequency of the reference signal.

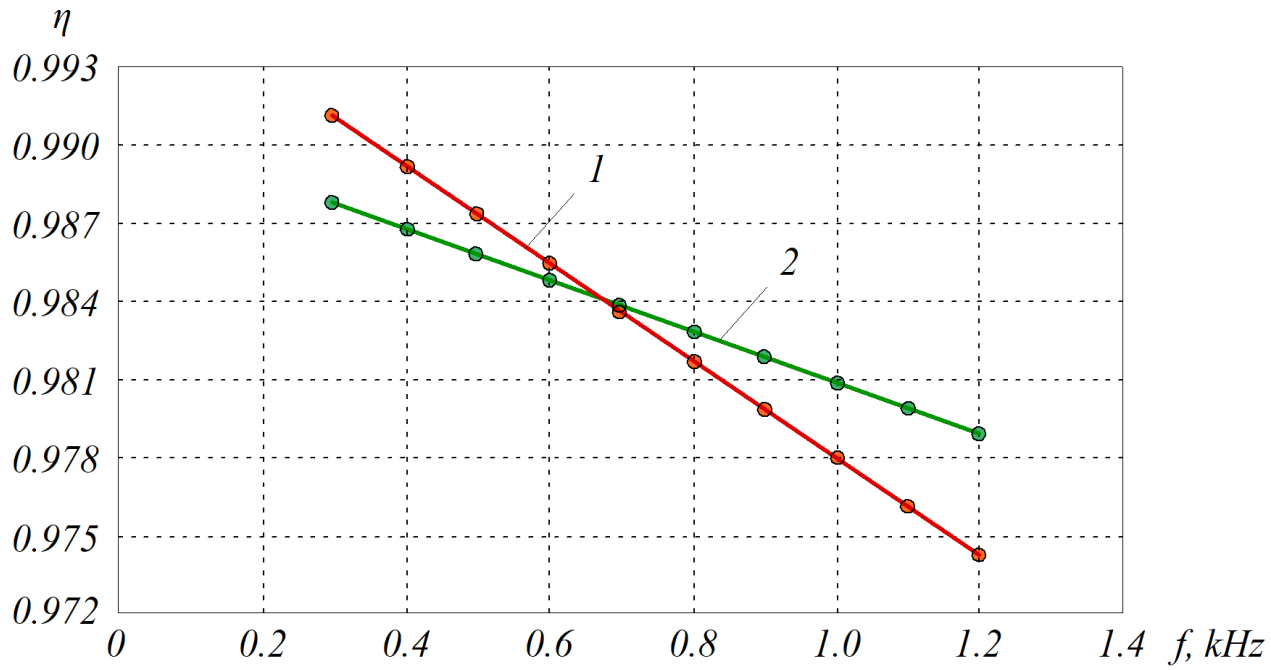

Figure 3.6 – Dependence of efficiency on switching frequency:
1 – in two-level rectifier; *2* – in three-level rectifier

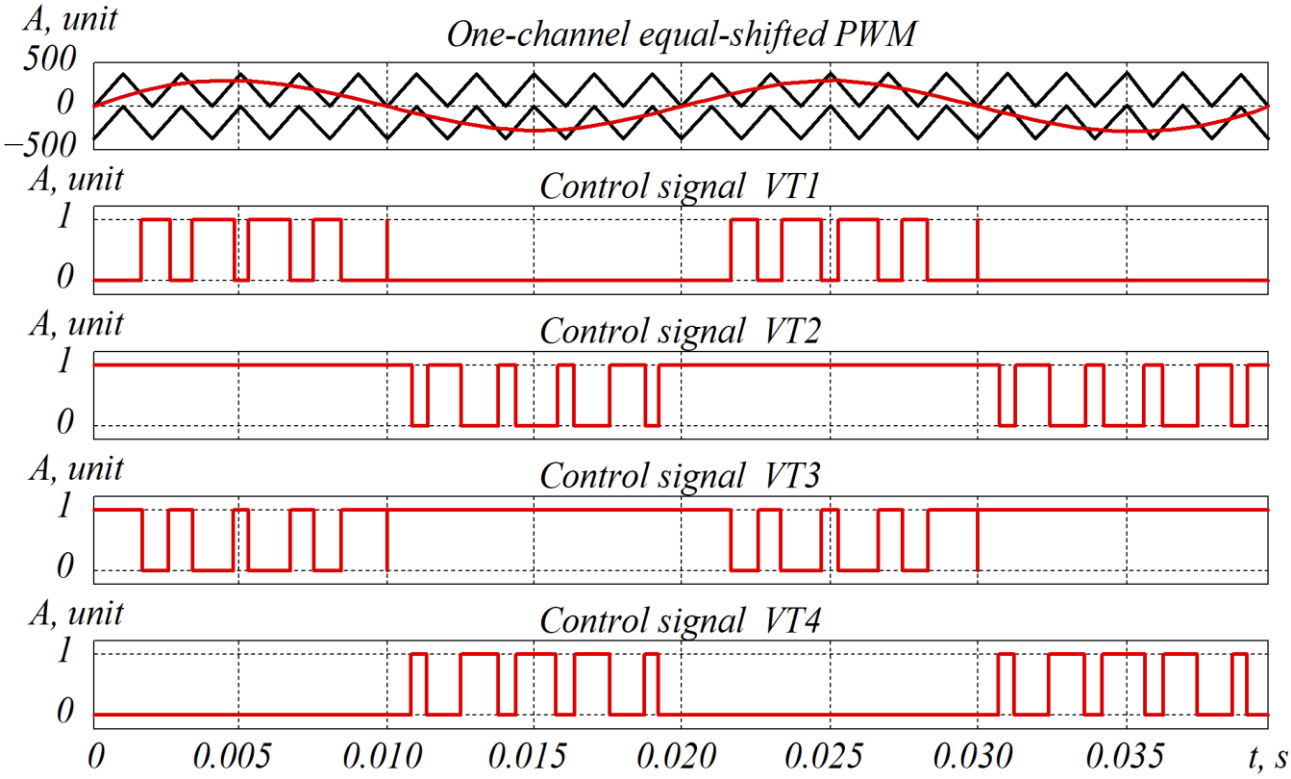

Figure 3.7 – One-channel sinusoidal equal-shifted PWM

The use of the two-channel equal-shifted PWM (DCUS PWM) is proposed (fig. 3.8).

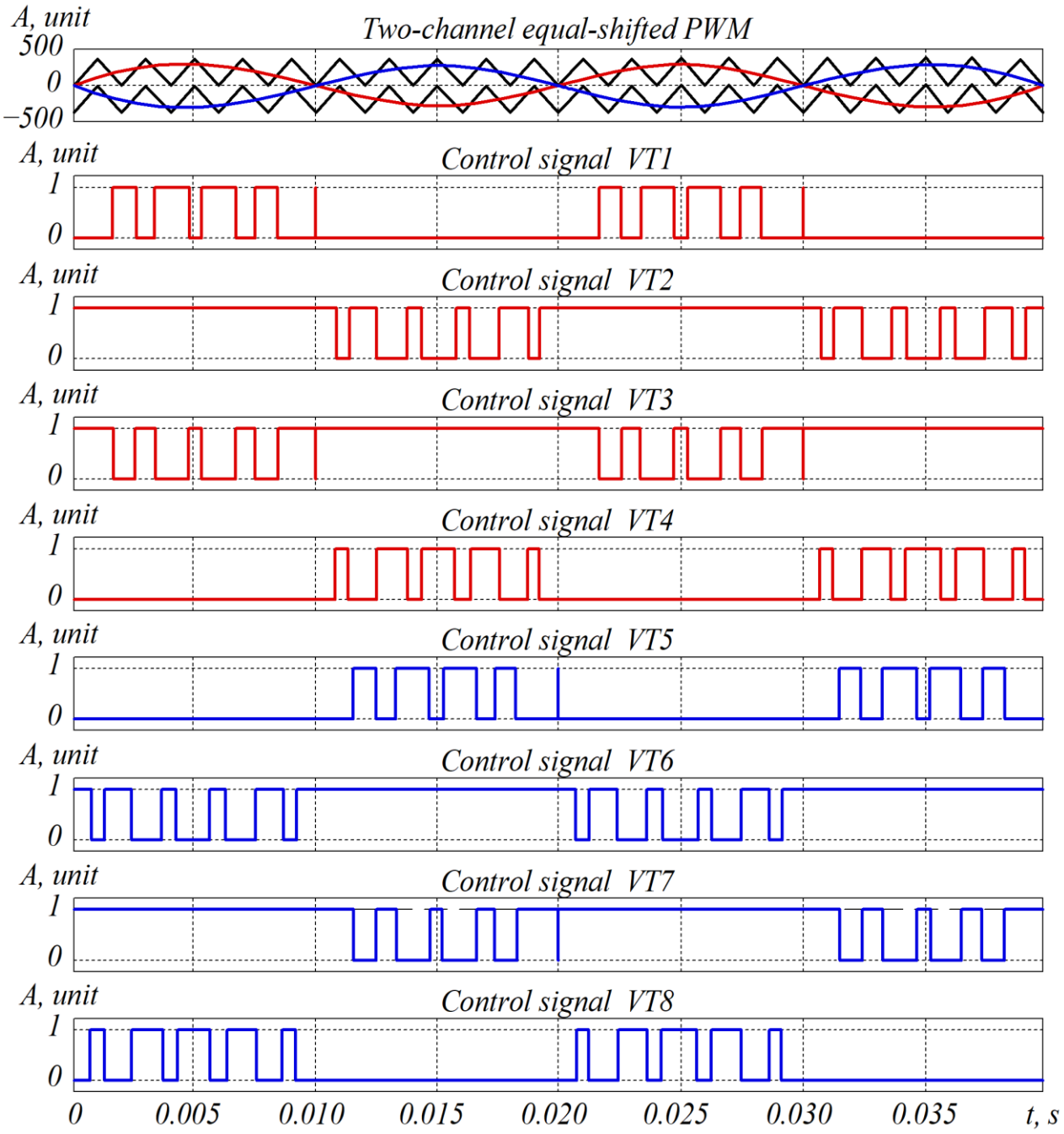

Figure 3.8 – Two-channel sinusoidal equal-shifted PWM

The proposed two-channel PWM is used to add an additional inverse sinusoidal task signal to the modulation algorithm. This achieves the following: at the same switching frequency of the power switches, the phase current switching frequency is doubled. This leads to increased sinusoidality of the consumed current from the power supply network. The increased current sinusoidality causes a decrease in the emission of higher current harmonics. Appropriate simulation models were developed to study and compare the qualitative EMC indicators of two-level and three-level active rectifiers with the supply network in Matlab 2017b (fig. 3.9).

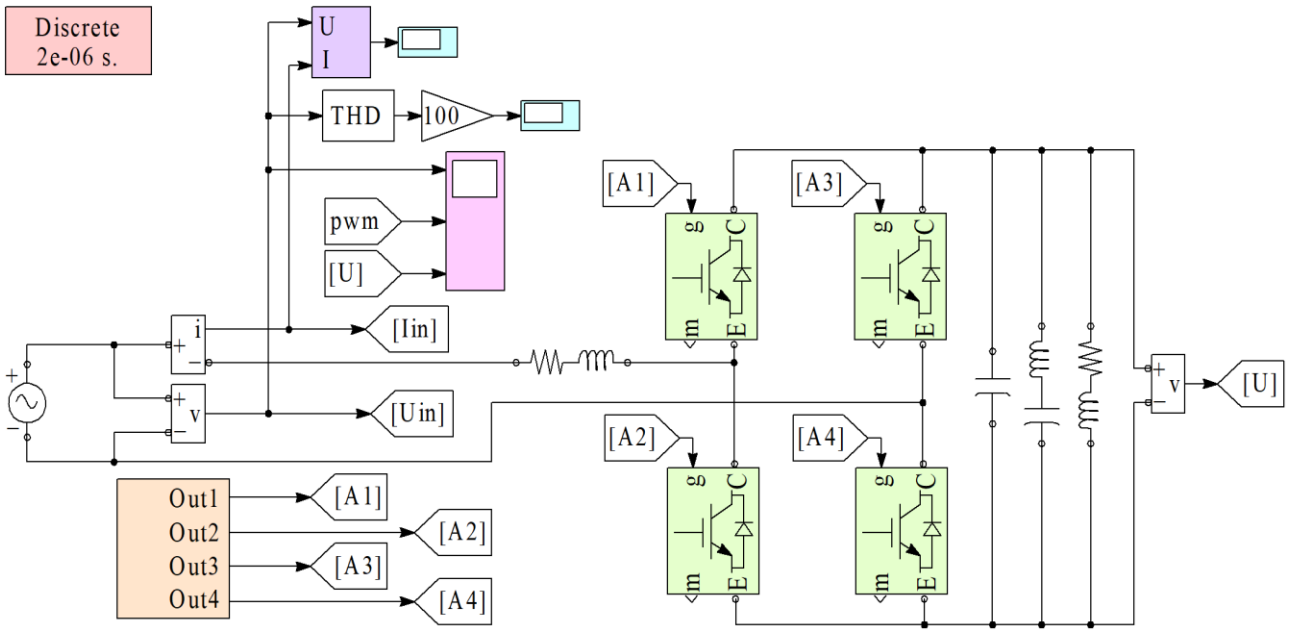

a

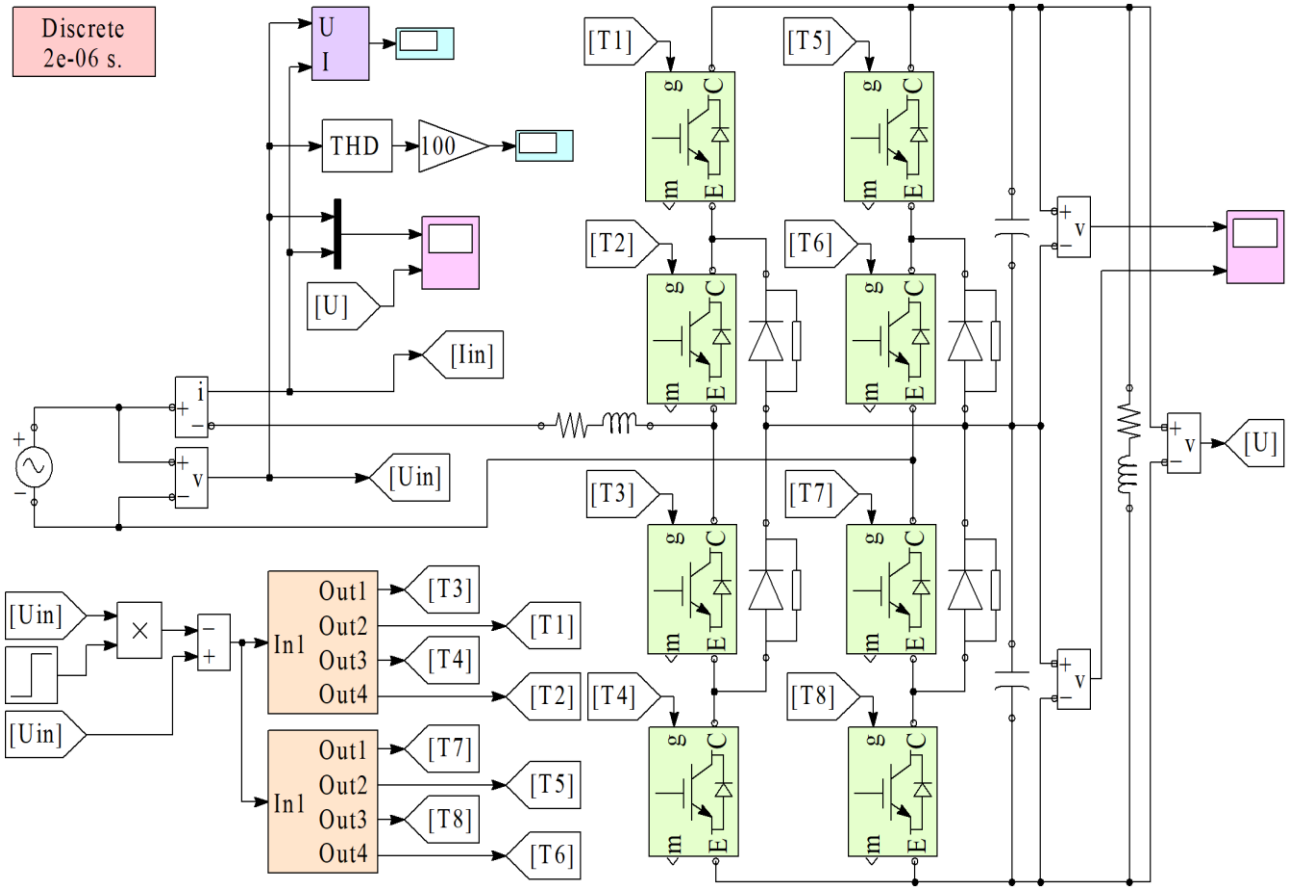

b

Figure 3.9 – Simulation models of active rectifiers:
a – two-level; *b* – three-level

Parameters of the simulation model: input voltage amplitude 600 V; input reactor inductance 0.5 mH, output capacitor capacity 24 mF, output voltage 800 V, output

power 320 kW. The modelling was carried out when solving differential equations describing the models with the ode23tb operator; this operator uses the implicit Runge-Kutta method at the beginning, and then the method, which uses the expressions of reverse differentiation of the 2nd order. The allowable relative error of calculation is 0.01 %.

An important characteristic of active rectifiers is the possibility of energy regeneration to the power supply network.

The transition of the active three-level rectifier from the rectification mode to the regeneration mode is shown in fig. 3.10.

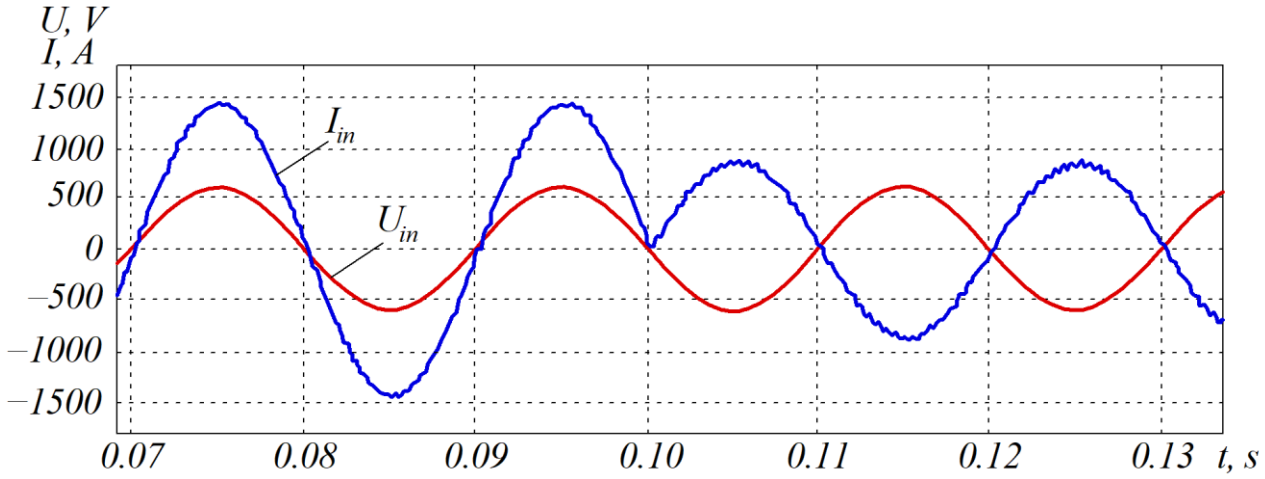

Figure 3.10 – Transient current and voltage processes in three-level rectifier

As can be seen from fig. 3.10, the transition from the rectification mode to the regeneration mode is advisable at the moment of transition of the instantaneous value of the input voltage in the zero region.

The results of the harmonic analysis of the input current shape of two-level and three-level active rectifiers in the traction mode at an IGBT switching frequency of 1 kHz are shown in fig. 3.11.

The quality of active rectifiers was evaluated by comparing the power factor value ξ and the THD of harmonics in the input current. The THD of the input current is calculated according to the expression:

$$THD = \frac{I_k}{I_1}, \tag{3.1}$$

where I_k – the RMS of the sum of the higher current harmonics; I_1 – the RMS of the first current harmonic.

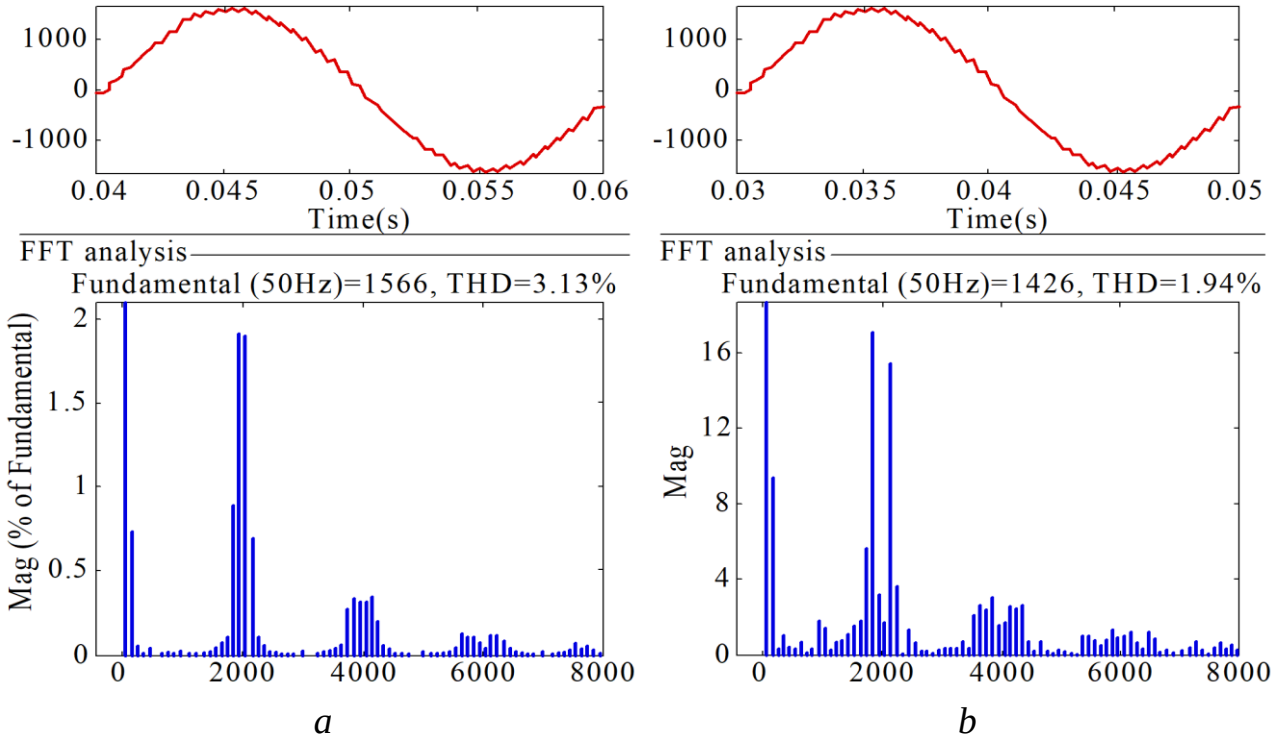

Figure 3.11 – Fourier analysis of input current:
1 – in two-level rectifier; *2* – in three-level rectifier

The value I_{k_RMS} is determined according to the expression:

$$I_{k\_RMS} = \sqrt{\sum_{n=2}^{n=m} I_n^2}, \tag{3.2}$$

where m – the number of higher harmonics; I_n – the n-th higher current harmonic.

Accordingly, the lower the THD is, the lower the content of higher harmonics in the current and the lower additional losses in the network will be.

The power factor ξ was calculated according to the expression:

$$\xi = \frac{P_1}{S} = \frac{U_1 \cdot I_1 \cdot \cos(\alpha)}{U \cdot I}, \tag{3.3}$$

where P_1 – the RMS of first harmonic power; U_1 – the RMS of the first voltage; S – the total power.

During the modelling, the dependencies of the values of the THD in the input current of the two-level active rectifier and of the three-level active rectifier with a two-channel equal-shifted sinusoidal PWM on the switching frequency of the IGBT were obtained; they are shown in fig. 3.12.

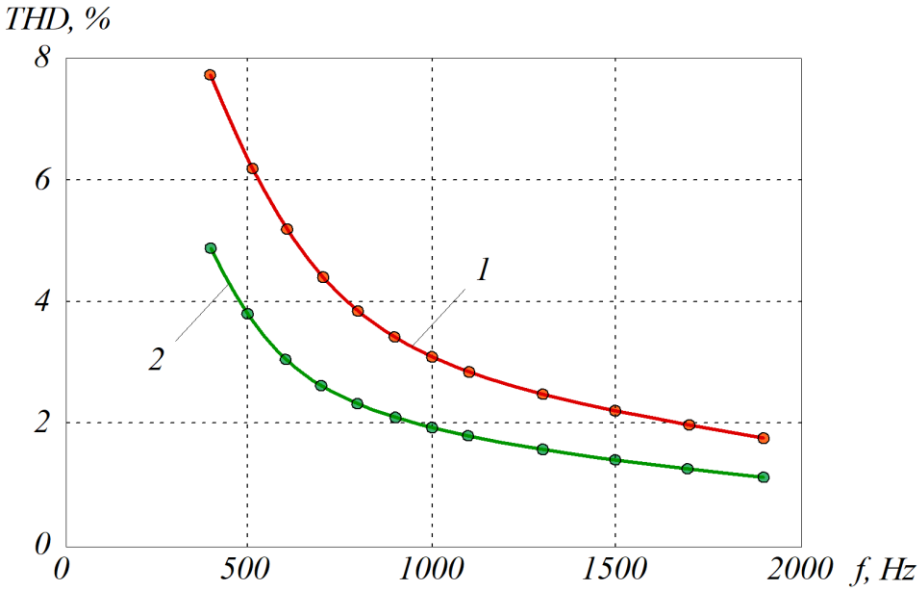

Figure 3.12 – Dependence of THD on IGBT switching frequency:
1 – in two-level rectifier; *2* – in three-level rectifier

From the dependencies in fig. 3.12, it can be seen that in the full range of switching frequencies of power transistors, the three-level active rectifier has improved sinusoidality of the input current and causes a lower emission of higher current harmonics. The energy characteristics of the two-level and three-level active rectifier at an IGBT switching frequency of 1 kHz are given in table 3.2.

Table 3.2 – Comparative analysis of performance indicators of two-level and three-level active rectifiers

Parameter	Two-level active rectifier with two-channel PWM	Three-level active rectifier with one-channel PWM	Three-level active rectifier with two-channel PWM
IGBT switching frequency, Hz	1000	1000	1000
THD of the input current, %	3.13	3.83	1.94
Power factor, %	99.63	99.72	99.77
THD of the output voltage, %	3.6	5.26	7.2
Efficiency, %	97.8	98.1	98.55

The choice of the real topology of the active rectifier depends on many components, such as: cost, efficiency and qualitative performance indicators, namely, power factor and THD. Under this condition, the three-level topology is better in all of the above-mentioned indicators, which testifies the feasibility of its use.

The research conducted confirms the expediency of using the three-level active rectifier with the CS based on DCUS PWM for the AC ERS. The three-level active rectifier circuit, if compared to the two-level circuit, has a higher efficiency value, lower cost of power transistors and can produce a lower emission of higher harmonics, which is confirmed by calculation and simulation.

The results obtained are explained by the fact that the three-level active rectifier circuit makes it possible to use half-the-nominal-voltage IGBT switches with static and dynamic losses.

The peculiarity of the proposed CS with DCUS PWM is its potential to double the switching frequency of the input current relative to the clock PWM frequency. This makes it possible to obtain improved quality indicators of the input current at the same power losses in the converter.

The limitations of this study are due to the fact that the proposed CS DCUS PWM can work with the modulation coefficient in the range from 0 to 1 and cannot work in the re-modulation mode. The disadvantages of this study is that it does not include the impact of the impulse load of the three-level active rectifier during the simulation. However, this will be done in the following studies.

Regarding the study of the three-level active rectifier with DCUS PWM it is advisable to create mathematical models of electromagnetic processes, synthesis of the ARS of the output voltage and study the mode of energy regeneration to the feeder network. Once the theoretical part has been completed, it is necessary to create an experimental layout sample of the conductor.

3.2. Improved energy efficiency of AC rolling stock by compensating for higher harmonics in input four-quadrant converters with phase-shifted pulse-width modulation

Modern ERS is a complex electromechanical system, which includes several power converters that operate in parallel from the contact network [93, 94]. Thus, there can be up to eight power converters operating in parallel in electric locomotives and electric trains. The power scheme of a two-section electric locomotive is shown in fig. 3.13. Most modern CSs of semiconductor converters, in particular AVIs and 4QS-converters on the ERS, are based on digital or analogue PWM. In the course of the studies given in the previous chapters, it was found that not only the order of higher harmonics depends on the PWM frequency, but also the phases of higher harmonics depend on the reference PWM signal phase [95, 96].

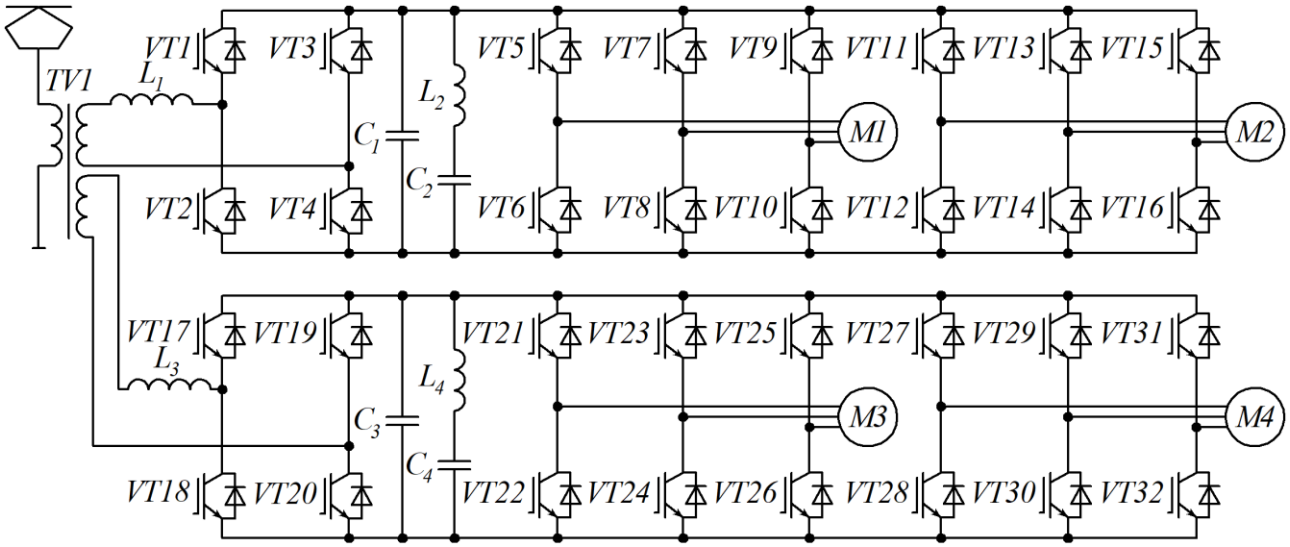

Figure 3.13 – Structural diagram of traction electric drive with input 4QS-converters

Given that the total current consumed by the ERS is the sum of the currents consumed by the parallel converters, the phase shift of the higher harmonics in the parallel bridges relative to each other by the required electric angle makes it possible to obtain the effect of mutual compensation of the higher harmonics of the consumed current.

Application of the principle of phase compensation of higher harmonics in the total consumed current by synchronizing control channels of converters operating in parallel, will allow obtaining improved indicators of the quality of electric energy in the modes of traction and regeneration, and to reduce the switching frequency of power valves, which will lead to a decrease in dynamic losses in the converters and an overall increase in the ERS efficiency.

At the same time, it should be noted that for mutual higher harmonic compensation it is necessary to fulfil the condition of equality of the input inductances in the bridges of the compensation 4QS-converter.

Schematically, to compensate for higher harmonics, the serial or parallel connection of converters is needed. The circuit of the compensation 4QS-converter with the series connection of bridges is shown in fig. 3.14.

An additional advantage of serial connection of converters to obtain a common DC circle is the possibility of applying a lower-class IGBT with lower rated currents. A prerequisite for the circuit implementation of successive compensation active rectifiers is galvanic isolated power supply of each converter bridge, which is implemented by power supply from various taps of the traction transformer.

The compensation 4QS-converter circuit with the series connection of bridges is shown in fig. 3.15.

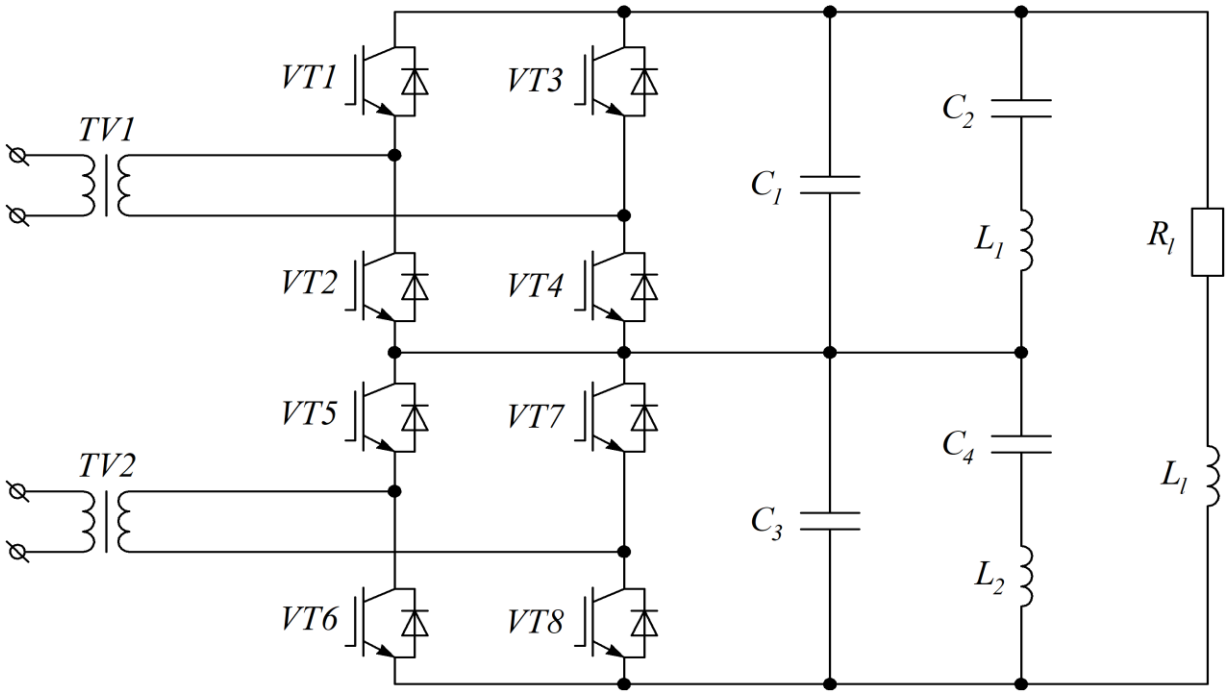

Figure 3.14 – Compensation 4QS-converter with serial load supply

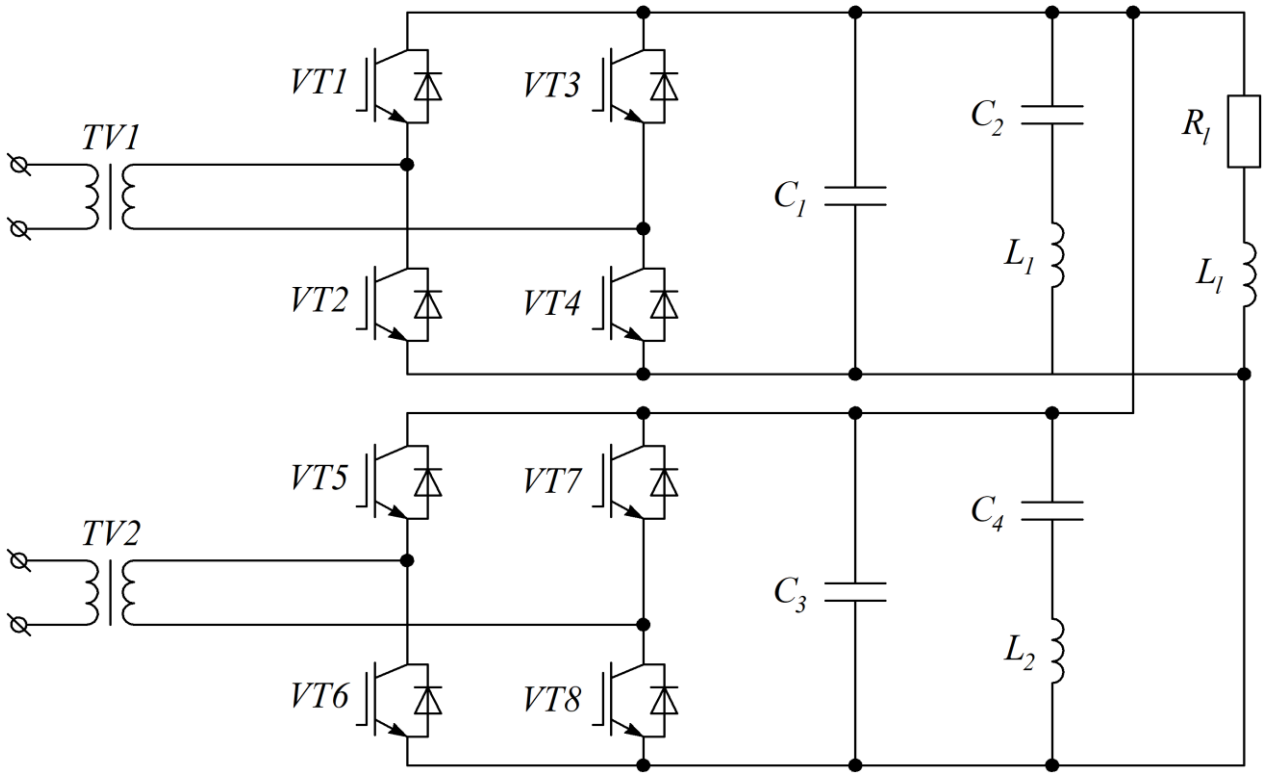

Figure 3.15 – Compensation 4QS-converter with parallel load supply

In compensation 4QS-converters, the number of bridges operating in parallel or in series may be different, which determines the value of the required angle between the reference PWM signals in the control channels of each bridge of the compensation

converter. In addition, the output voltage regulators for the series and parallel connection of the bridges will be different.

The schematic implementation of compensation 4QS-converters with parallel and serial load connections makes it possible to obtain an improved harmonic composition of the consumed input currents and output voltage. This is achieved by synchronizing the CS with individual bridges and shifting the reference PWM signals in the control channels of each bridge relative to each other, which can mutually compensate for higher harmonics of input currents and the output voltage.

The number of input power rectifiers in the ERS may vary. At the same time, the shift angle φ of the reference signal in order to achieve the compensation effect must be appropriate to the number of bridges connected in parallel. The optimal shift angle of the reference PWM signals depends on the number of bridges of the compensation 4QS-converter and is determined by the expression:

$$\varphi = \frac{360}{2 \cdot n}, \tag{3.4}$$

where n – the number of bridges in the compensation 4QS-converter.

The CS of the compensation 4QS-converter with two parallel bridges consists of two control channels for each bridge with the use of phase-shifted two-channel PWM. The CS of a compensation 4QS-converter, which includes two parallel bridges and two control channels, is shown in fig. 3.16.

Fig. 3.16 presents the CS system of the compensation 4QS-converter consisting of two channels, each of which repeats the two-channel CS of a 4QS-converter.

The application of the above-mentioned principle of controlling the compensation 4QS-converter makes it possible to implement improved indicators of emission of higher harmonics of the input current and the output voltage. For this reason simulation models of a traction electric drive with a compensation 4QS-converter, an AVI and an asynchronous traction motor were developed.

Fig. 3.17 shows a simulation model of a traction electric drive with two bridges of a compensation 4QS-converter with parallel bridge connection. The block diagram of the traction electric drive consists of a contact network sub-model, two parallel bridges of the compensation active rectifier, which are powered from one network. A smoothing filter with a resonance link tuned to a frequency of 100 Hz is installed at the output of the 4QS-converter. The load of the 4QS-converter is the AVI, which feeds the traction asynchronous motor. The CSs of the 4QS-converters are marked with sub-blocks Control System1 and Control System2.

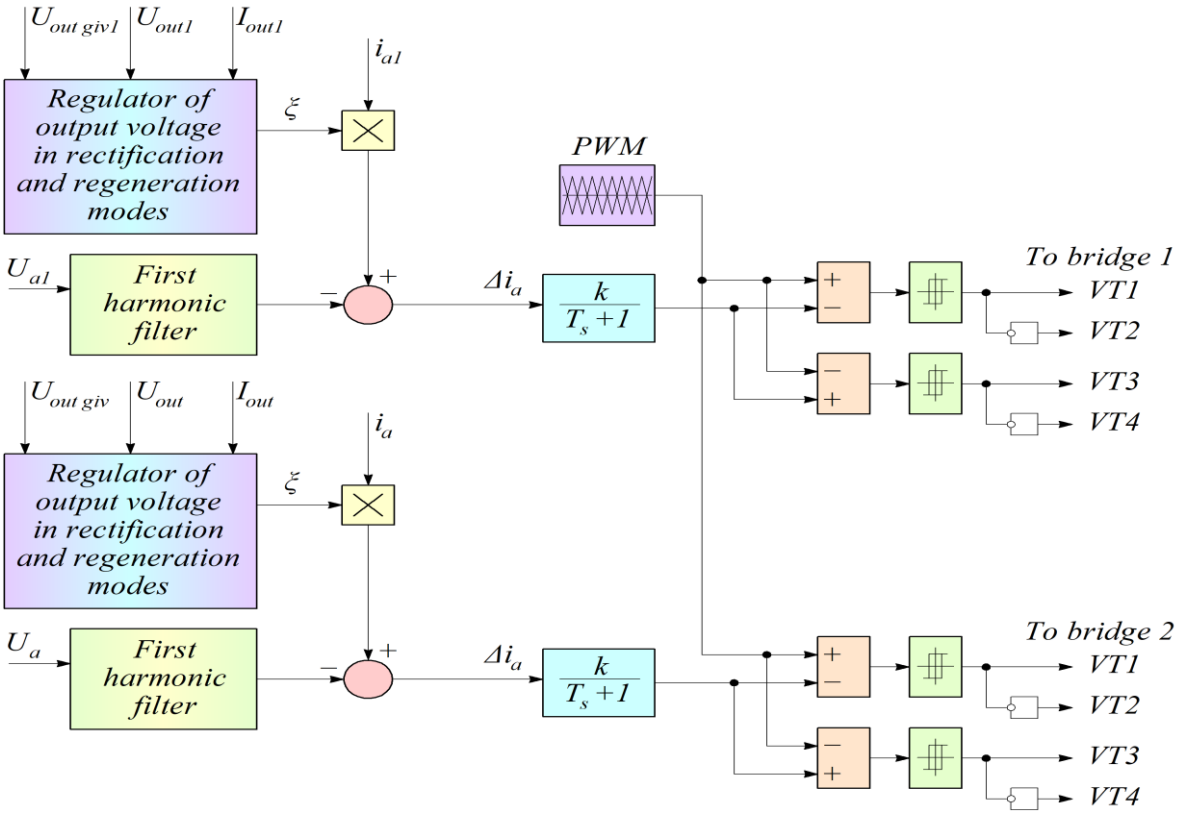

Figure 3.16 – CS with compensation 4QS-converter

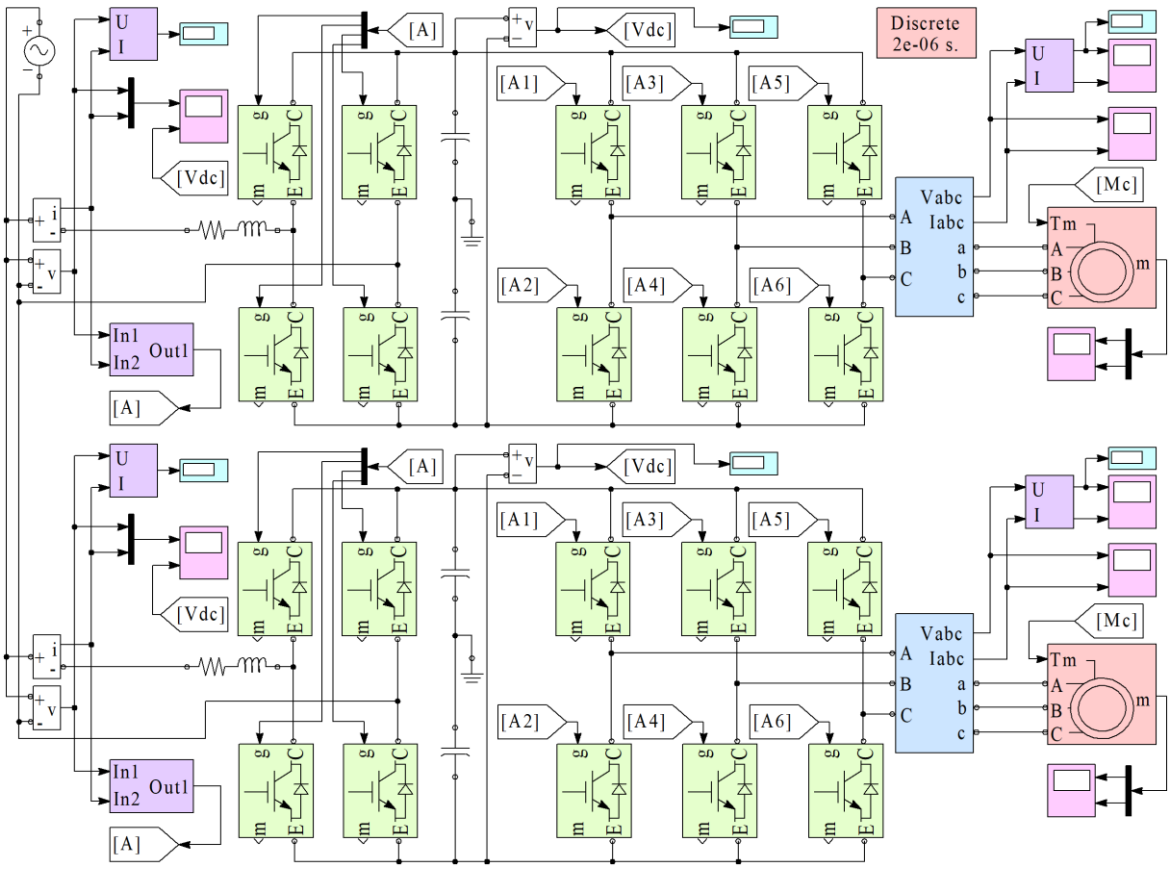

Figure 3.17 – Simulation model with two bridges of compensation 4QS-converter

Parameters of the simulation model are given in table 3.3.

Table 3.3 – Parameters of simulation model of compensation active rectifier

Simulation model parameter	Value
Input voltage, V	800
Active resistance of mains, Ohm	0.2
Inductive network resistance, mH	0.1
Inductance of input filters, mH	0.8
Capacitance of output capacitor, mF	2
Active load resistance, Ohm	1…12
Inductive load resistance, mH	1
Load voltage, V	1400

The shape of the phase voltage and current consumed by one bridge of the 4QS-converter is shown in fig. 3.18.

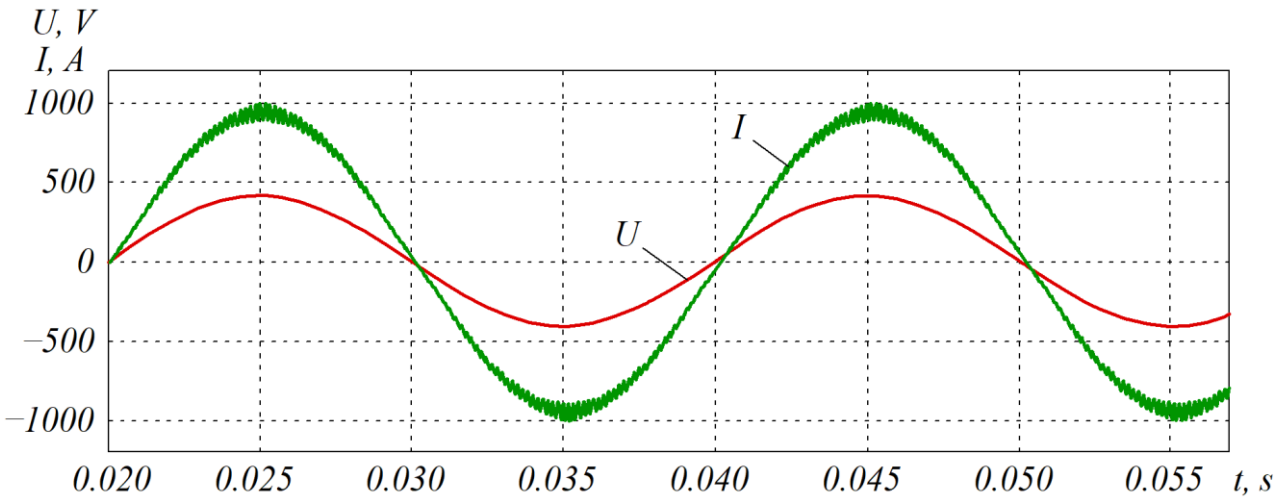

Figure 3.18 – Transient processes of phase voltage and current of one bridge of 4QS-converter

The total current consumption of the 4QS-converter bridges is shown in fig. 3.19.

The ripple frequency of the output voltage of the compensation 4QS-converter, caused by higher harmonics, has doubled compared to the two-pulse rectifier.

The oscillograms of the charge current of the output capacitor formed by the bridges of the 1st and 2nd compensation 4QS-converters, and the output voltage without the output resonance filter are shown in fig. 3.20. Voltage oscillograms at the input and the output of the resonance filter are shown in fig. 3.21.

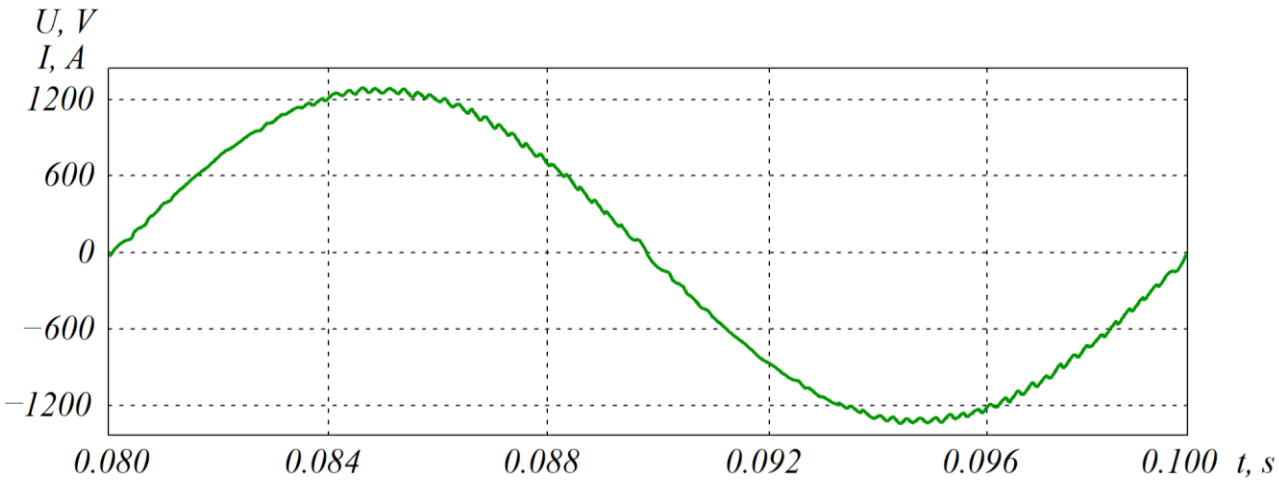

Figure 3.19 – Total consumed current of 4QS-converter bridges

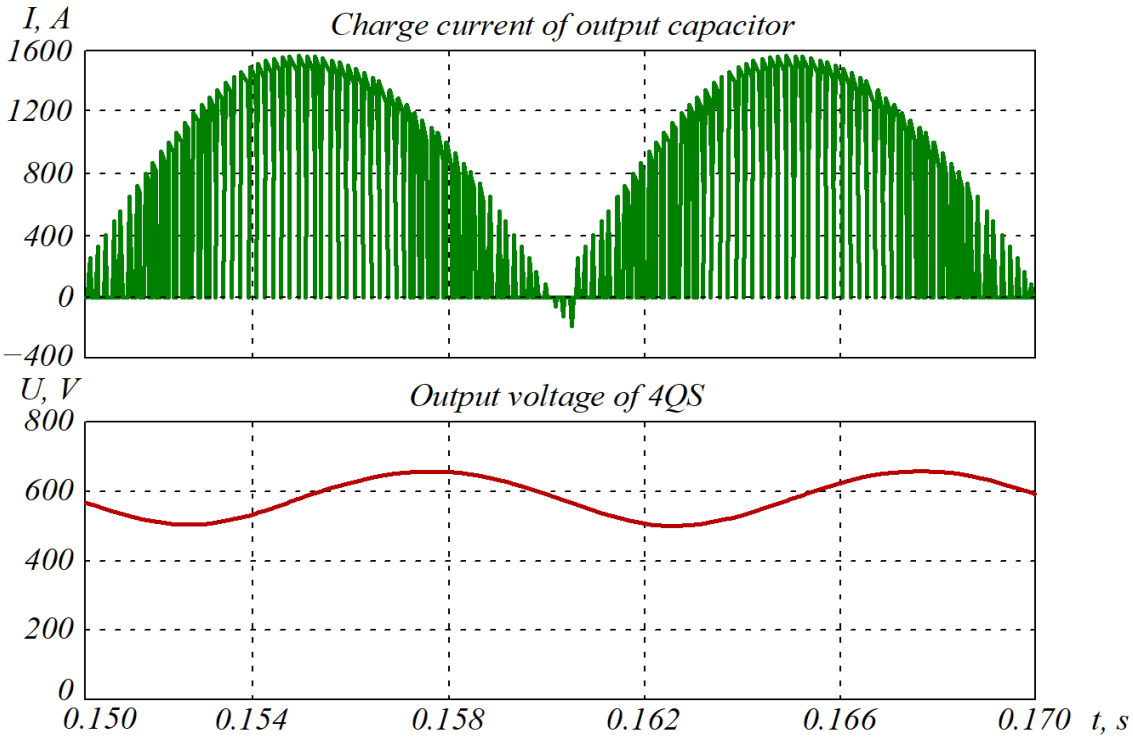

Figure 3.20 – Oscillograms of output capacitor charge current and output voltage without output resonance filter

As follows from fig. 3.21, the proposed CS implements the phase currents form close to sinusoidal, cosφ, close to one, as well as a small amplitude of ripple output voltage. On the simulation model of the compensation 4QS-converter with PWM developed in Matlab, the following EMC parameters were studied: power factor, THD of phase current, ripple factor of output voltage, and interference voltage magnitude.

Fourier analysis of the output voltage form of the compensation 4QS-converter is shown in fig. 3.22.

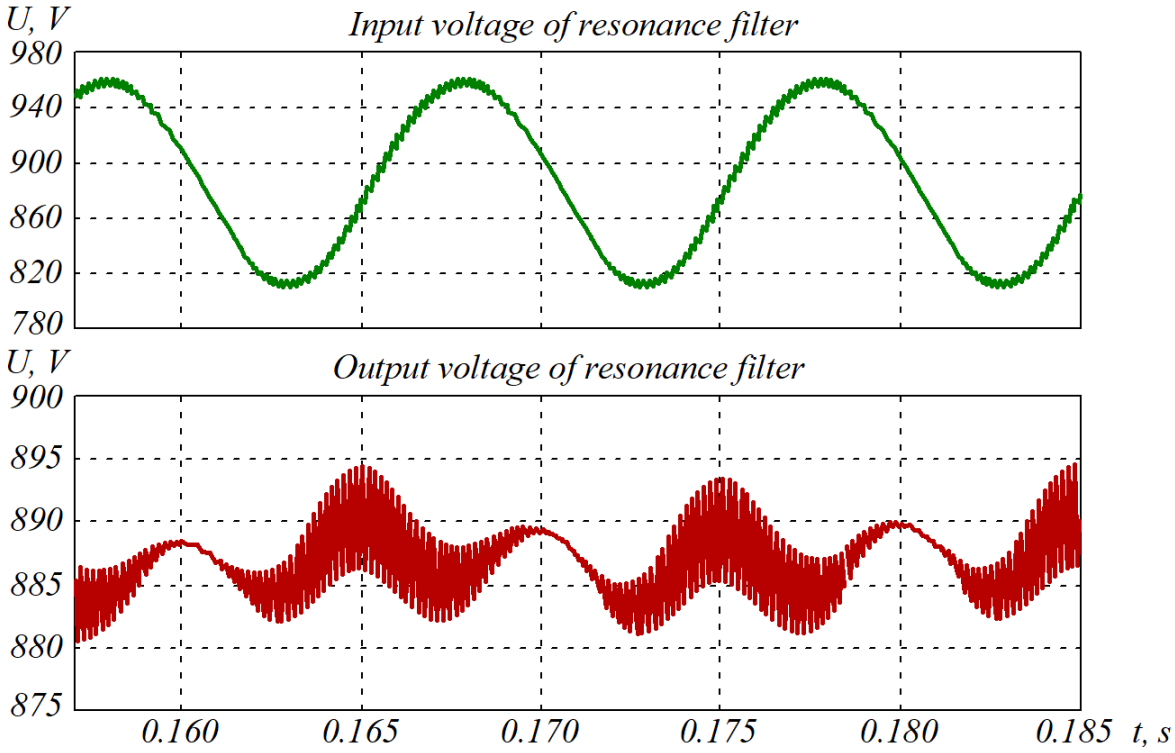

Figure 3.21 – Oscillograms of voltage at input and output of resonance filter

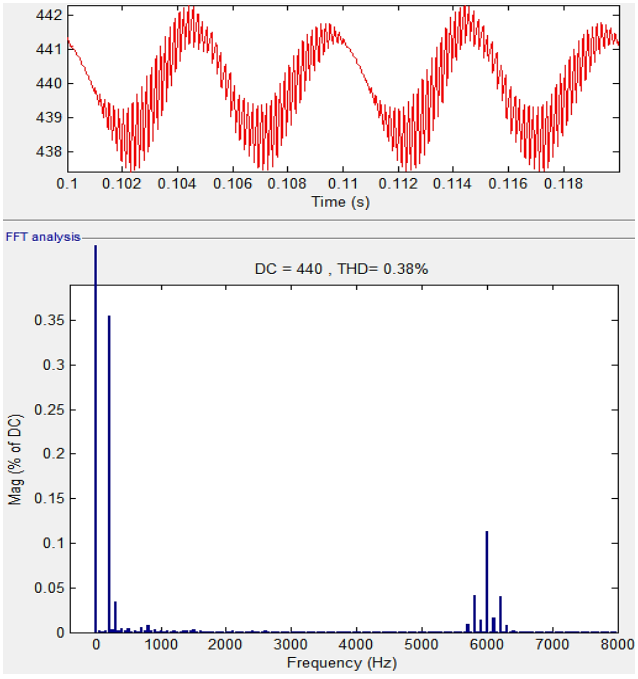

Figure 3.22 – Fourier analysis of output voltage of compensation 4QS-converter

In the simulation model, the calculation of the power factor was performed using the subsystem shown in fig. 3.23. Similar studies were made for the traction electric drive model used four parallel converters. A simulation model of the structure of the traction electric drive with four parallel 4QS-converters is shown in fig. 3.24.

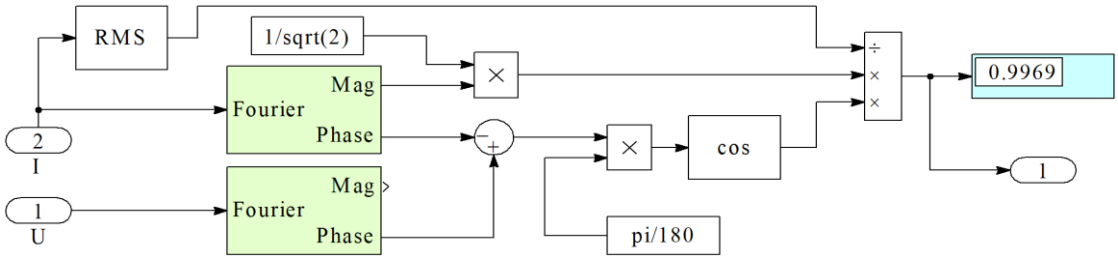

Figure 3.23 – Subsystem for calculating power factor

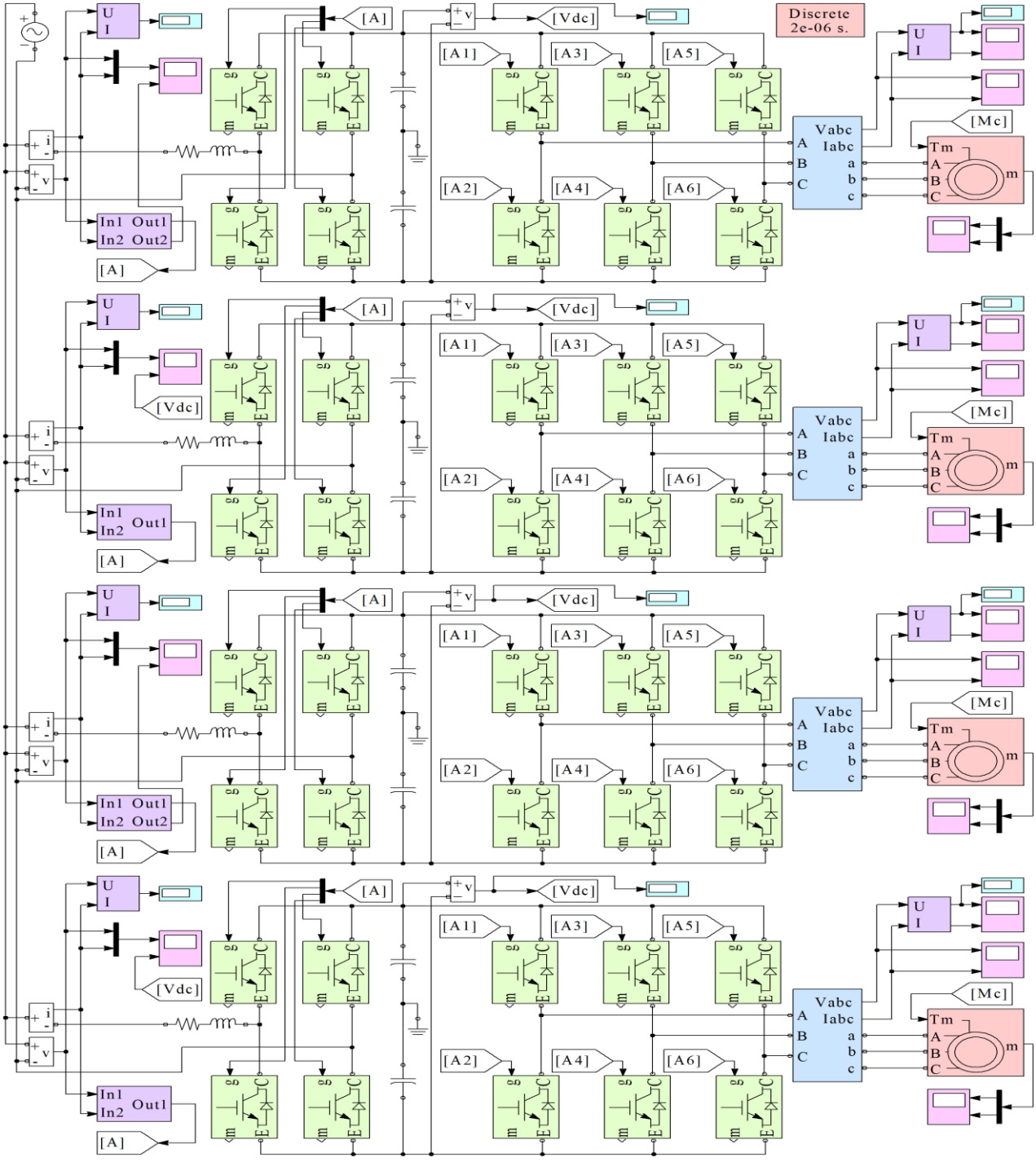

Figure 3.24 – Simulation model with four 4QS-converters

The results of the simulation modelling of the compensation converter with four parallel 4QS-converters in an AC electric locomotive at an input inductance of 0.8 mH are given in table 3.4.

Table 3.4 – Energy parameters of traction electric drive

Switching frequency of power switches, Hz	THD of current of one bridge	THD of total consumed current	Efficiency, %
500	11.14	1.27	98.75
1000	7.84	0.98	97.91
2000	4.84	0.69	96.26
4000	1.12	0.32	94.6

From the results given in table 3.4, it follows that already at a switching frequency of 500 Hz, the required quality of the input current and the highest value of efficiency are achieved.

Comparison of the results of energy efficiency for the active rectifier structures studies is given in table 3.5.

Table 3.5 – Comparative analysis of electricity quality indicators of input converters

Parameter	Four-zone rectifier	Classic hysteresis modulation	Improved hysteresis modulation	One-channel PWM	Two-channel PWM	Compensation PWM (2 bridges)	Compensation PWM (4 bridges)
1	2	3	4	5	6	7	8
Efficiency (at input power 1200 kW), %	98.5	82.2	88.74	96.26	96.26	97.9	98.75
Dynamic losses in IGBT CM1200HP-90R (at load current of one switch 1000 A), W	Applies thyristor modules	26760	18049	5606.04	5606.04	3117.29	1872.91
Switching frequency, Hz	50	10500	7000	2000	2000	1000	500

Continuation of table 3.5

1	2	3	4	5	6	7	8
Spectrum of input current harmonics relative to PWM frequency	–	Wide and variable input current spectrum	Wide and variable input current spectrum	(1, 2, 3, 4)·f_{PWM}	(2, 4, 6, 8, 10)·f_{PWM}	(4, 8, 12, 16)·f_{PWM}	(8, 16, 24, 32)·f_{PWM}
Power factor λ in rectification mode, %	84	99.98	99.99	99.63	99.87	99.86	99.92
Power factor λ in regeneration mode, %	65	99.97	99.89	99.23	99.74	99.74	99.89
THD of input current in rectification mode, %	24.3	1.89	1.68	5.57	2.07	7.11→1.82	11.14→1.27
THD of input current in regeneration mode, %	31.5	2.43	2.32	26.79	7.25	17.5→3.57	12.4→2.71
Output voltage ripple factor, %	12.2	6.84	6.45	8.16	7.19	7.21	7.36

From the results given in table 3.5, it follows that a traction electric drive with a compensation 4QS-converter based on a two-link CS with phase-shifted PWM with four parallel control channels has the best energy indicators.

3.3. Investigation of intrinsic power losses in parallel power active filters and their impact on the energy efficiency and the power quality

A fairly large number of studies are devoted to the analysis of the negative impact of higher harmonics of current and reactive power on electrical networks, as well as on methods of their elimination [97]. The source of higher current harmonics in electrical systems is most often semiconductor converters, such as thyristor rectifiers and

frequency converters. At the same time, the harmonic frequencies are quite different and depend on the type and modulation frequency in the converters, which complicates their compensation by filters [98].

Study [99] provides a universal methodology for proving the feasibility of using the APF provided that the value of the energy-saving effect in the network is higher than the power loss in the APF.

One of the most promising methods of reducing higher current harmonics in electrical networks is the use of parallel APFs (fig. 3.25) [100, 101]. Parallel APFs make it possible to almost completely compensate for the reactive component, as well as higher harmonics of the load current. The principle of operation of parallel APFs is that the filter consumes from the network the current form similar to the form of higher harmonics and the reactive component of the load current with the opposite sign (in the opposite phase), which provides compensation for higher current harmonics at the point of connection of APFs.

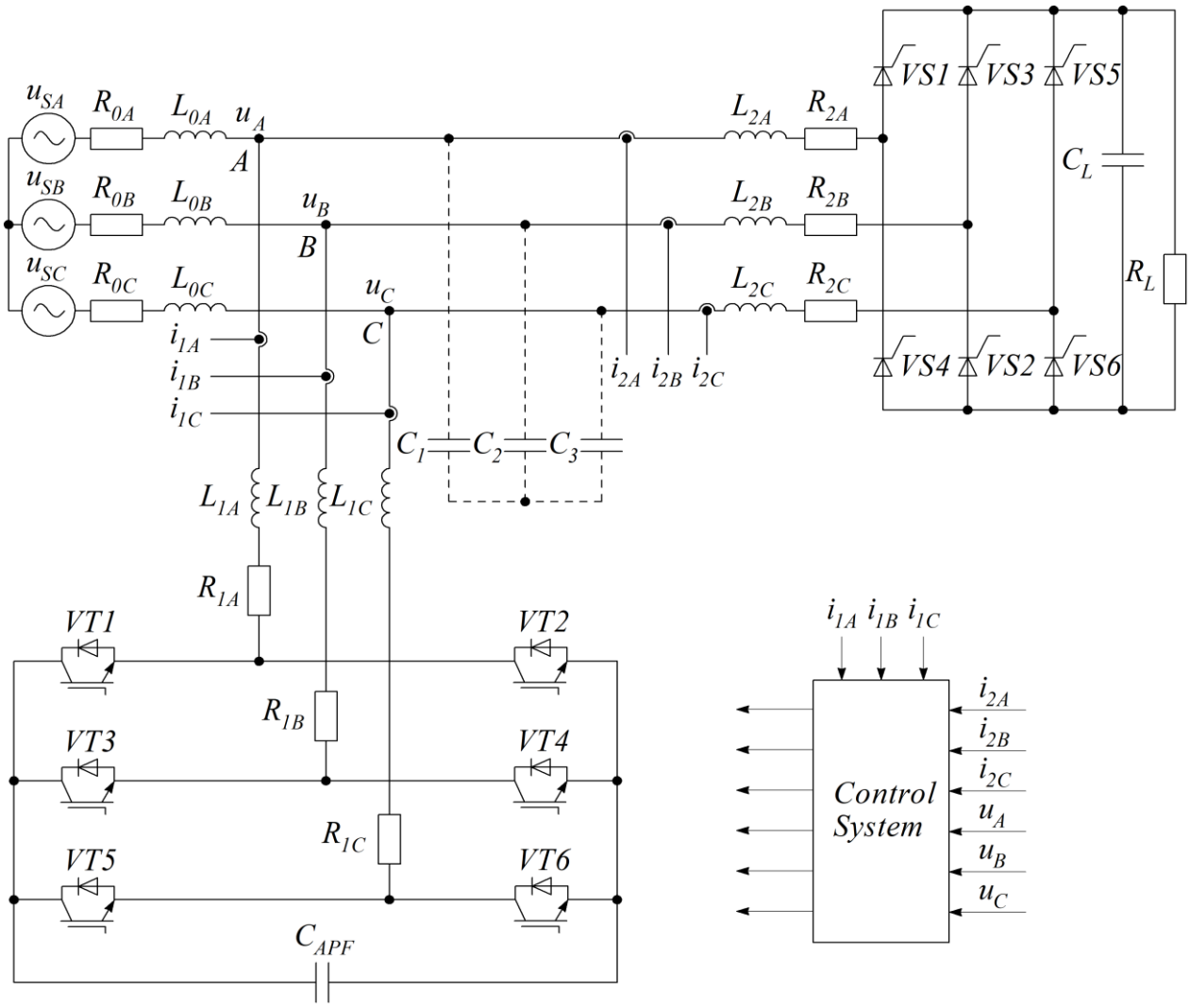

Figure 3.25 – Diagram of power supply system with thyristor rectifier and APF

Graphically, the principle of compensation (filtration) of higher harmonics of the parallel APF is shown in fig. 3.26.

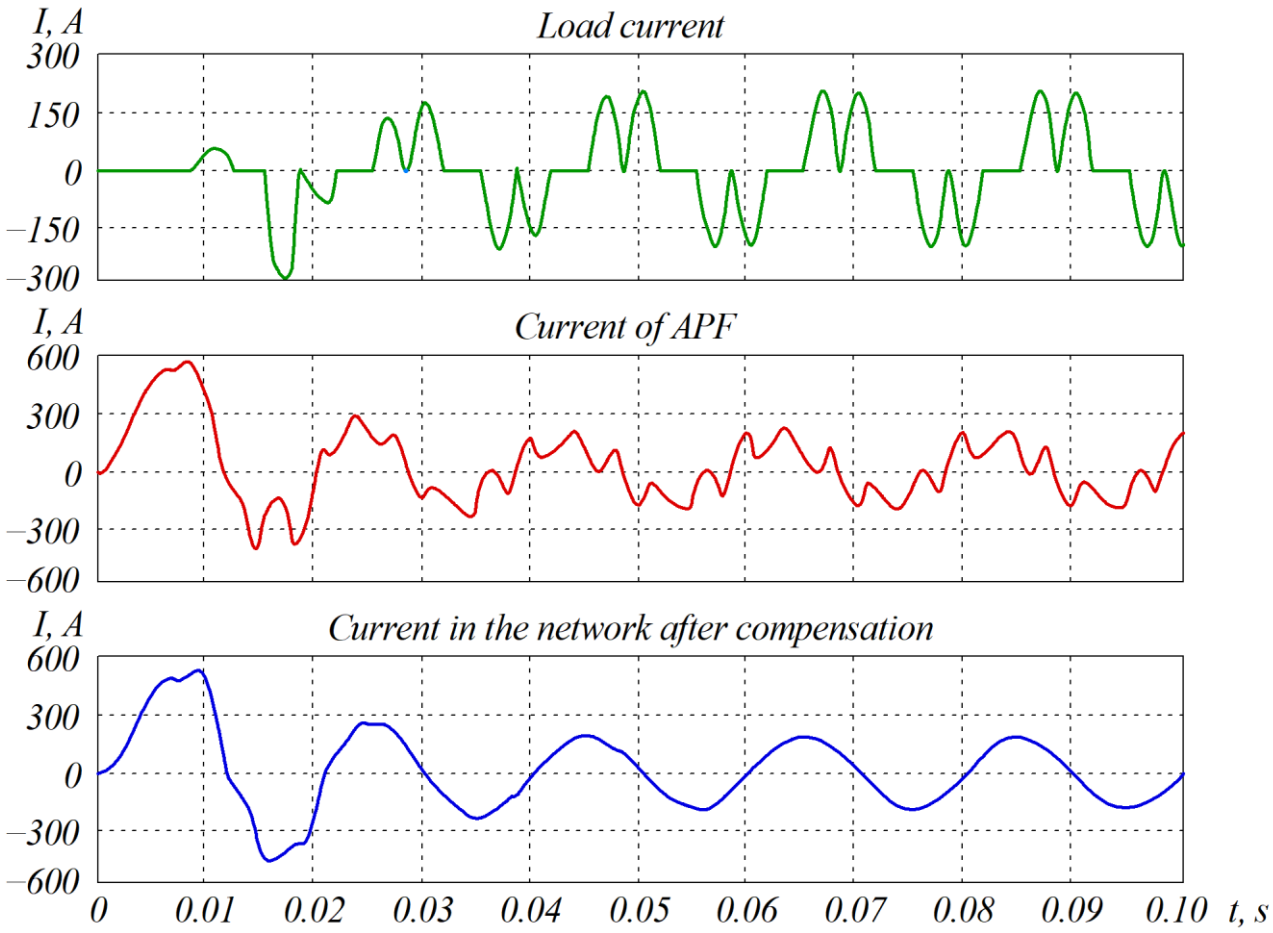

Figure 3.26 – Transients in APF

A large number of publications are devoted to qualitative improvements of the harmonic current composition when using the APF in different electrical networks with different CSs [102, 103].

However, a significant disadvantage of these publications is that the energy-saving effect was not studies, taking into account the power losses in the APF including the active losses in the inlet throttles, as well as the static and dynamic power losses in the power MOSFETs.

Publication [104] provides a study of a parallel APF with an automatic control system based on a double-circuit ARS with PWM. The results of a physical experiment in which the power losses in the APF are 6...8 % of the load power, which is a rather high level of losses, are provided. In addition, the disadvantage of this work is the lack of comparison of power losses in the APF and analysis of the energy-saving effect in the network, which complicates the analysis of the feasibility of using the APF.

Study [105] presents the dependencies of power quality parameters on the switching frequency and the dependence of power losses in the APF on the switching frequency.

The disadvantages of the study are that the APF with the proposed operation algorithm in the process of work increases the RMS load current, which increases power losses in the electrical network, besides it does not provide a comparison of power losses in the APF, power load of the APF and energy-saving effect of compensating for higher harmonics, which makes it difficult to determine the feasibility of using the APF.

Publication [106] provides a study of the dependence between the efficiency of a three-phase power supply system and the load power factor when working with a parallel APF.

The approximate process of current and voltage switching in MOSFET and the graphical distribution of static and dynamic losses are shown in fig. 3.27.

Power losses in the MOSFET and the by-pass diode are determined by the expressions:

$$E_{loss.IGBT} = E_{loss.VT} + E_{loss.VD}; \tag{3.5}$$

$$E_{lossVT} = E_{VT.DC} + E_{VT.SW}; \tag{3.6}$$

$$E_{lossVD} = E_{VD.DC} + E_{VD.SW}, \tag{3.7}$$

where $E_{VT.DC}$ – the static loss energy in the MOSFET; $E_{VT.SW}$ – the dynamic loss energy in the MOSFET; $E_{VD.DC}$ – the static loss energy in parallel diodes; $E_{VD.SW}$ – the dynamic loss energy in parallel diodes.

Static losses in the MOSFET are determined from the expression:

$$E_{VT.DC} = \int_{t_i}^{t_{i+1}} \left(i_c \cdot u_{ce}\right) \cdot dt, \tag{3.8}$$

where i_c – the collector current; $u_{ce}(i_c)$ – the voltage between the collector and the emitter, which depends on the value of the collector current.

Dynamic losses in the IGBT are determined from the expression:

$$E_{VT.SW} = \int_{t_1}^{t_2} P_{on}\left(I_c\right) \cdot dt + \int_{t_3}^{t_4} P_{off}\left(I_c\right) \cdot dt, \tag{3.9}$$

where $P_{on}(I_c)$ – the power losses in the transistor when it is turned on, depending on the value of the collector current; $P_{off}(I_c)$ – the power losses in the transistor when it is turned off, depending on the value of the collector current.

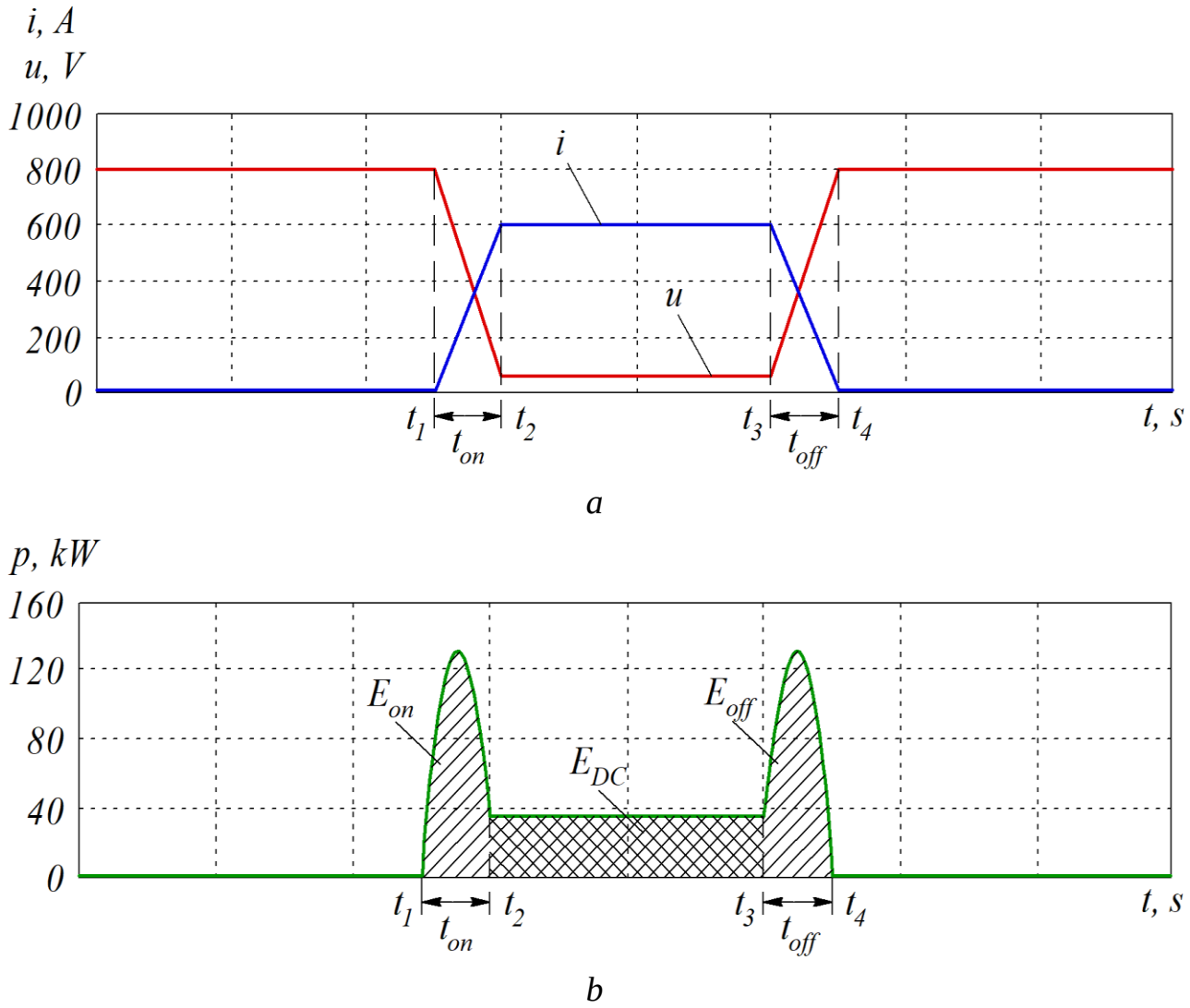

Figure 3.27 – Switching process in MOSFET:
a – current and voltage transients; *b* – power transients

Static losses in by-pass diodes are determined from the expression:

$$E_{VD.DC} = \int_{t_i}^{t_{i+1}} \left(u_{fwd} \cdot i_{vd} \right) \cdot dt, \qquad (3.10)$$

where u_{fwd} – the voltage drop across the by-pass diode; i_{vd} – the by-pass diode current.

Dynamic losses in by-pass diodes are determined from the expression:

$$E_{VD.SW} = \int_{t_i}^{t_{i+1}} P_{rec}\left(i_{vd}\right) \cdot dt, \tag{3.11}$$

where P_{rec} – the recovery energy of the by-pass diode.

For further calculations, the data $P_{on}(i_c)$, $P_{off}(i_c)$, $P_{rec}(i_c)$, $u_{ce}(i_c)$, $u_{fwd}(i_{vd})$ were used from the specification for the FMF800DX-24A module.

The energy characteristics of the MOSFET series FMF800DX-24A are shown in fig. 3.28.

When determining the MOSFET power losses, the following dependencies are basic:

– dependence of the collector current on the voltage between the collector and the emitter (current voltage characteristic of the transistor) (fig. 3.28, *a*);

– current voltage characteristic of the by-pass diode (fig. 3.28, *b*); and

– dependence of the energy of switch-on and off of the transistor, as well as the recovery energy of the by-pass diode from the current emitter of the transistor (fig. 3.28, *c*).

It is worth noting that the energy characteristics of the transistor at temperatures of 25 and 125 °C vary considerably and with increasing temperature the losses in the transistor increase.

There are different types of approximation: linear, partial linear, static, exponential and polynomial [107].

In addition, there are various mathematical methods that make it possible to perform approximation. The purpose of approximation is to determine the mathematical functions that most accurately describe the obtained dependencies $U_{se}(I)$, $U_{VD}(I)$, $E_{rec}(I)$, $E_{on}(I)$, $E_{off}(I)$.

Polynomial approximation makes it possible to describe quite accurately the energy dependencies of power transistors in a given range, but outside this range the function will behave incorrectly, which imposes restrictions on the application of this method, namely – the losses are calculated correctly only in a given current limitation range.

Consideration in the simulation of static and dynamic power losses of MOSFETs when using the obtained characteristics in Matlab is given in more detail in [108].

To carry out an automated calculation of power losses in power MOSFETs, the current voltage characteristics of the transistor and the energy dependence of the switch-on and switch-off energy on the load current were approximated by the least squares method. The mathematical approximation was performed in Wolfram Mathematica.

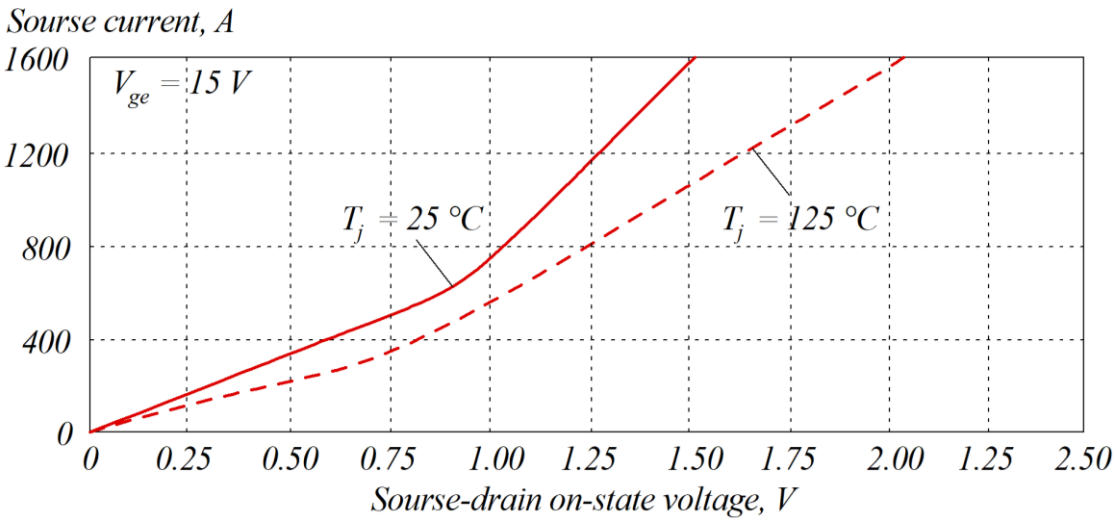

a

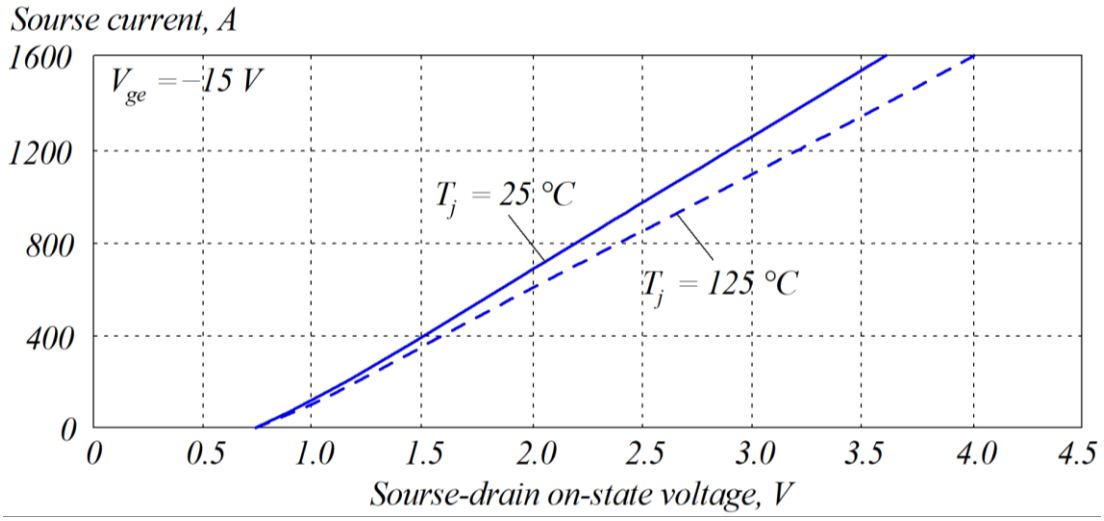

b

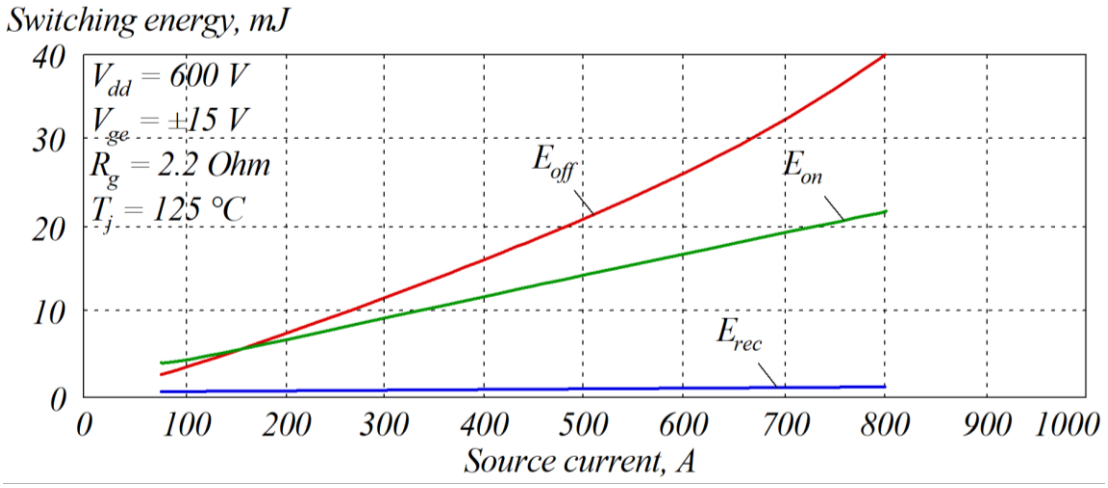

c

Figure 3.28 – Energy characteristics of MOSFET:
a – CVC of transistor; *b* – CVC of by-pass diode; *c* – dependence of switch-on energy E_{on}, switch-off energy E_{off} and regeneration energy of by-pass diode E_{rec} on current

The results of approximation of the energy characteristics of the power MOSFET are presented by the expressions:

$$U_{ce}(I) = 5.8 \cdot 10^{-10} \cdot I^3 - 1.8 \cdot 10^{-6} \cdot I^2 + 2.65 \cdot 10^{-3} \cdot I + 4; \quad (3.12)$$

$$U_{VD}(I) = 0.0018 \cdot I + 0.8039; \quad (3.13)$$

$$E_{rec}(I) = \frac{(0.0007 \cdot I + 0.5035)}{1000}; \quad (3.14)$$

$$E_{on}(I) = \frac{(0.0221 \cdot I + 3.954)}{1000}; \quad (3.15)$$

$$E_{off}(I) = \frac{\left(2.36 \cdot 10^{-5} \cdot I^2 + 0.0265 \cdot I + 3.27\right)}{1000}. \quad (3.16)$$

For convenience, the coefficients in approximated functions of dependence on the current are described in kiloamperes. A simulation model of a three-phase APF that filters the higher harmonics and the reactive component of the thyristor rectifier load current in Matlab / Simulink is shown in fig. 3.29.

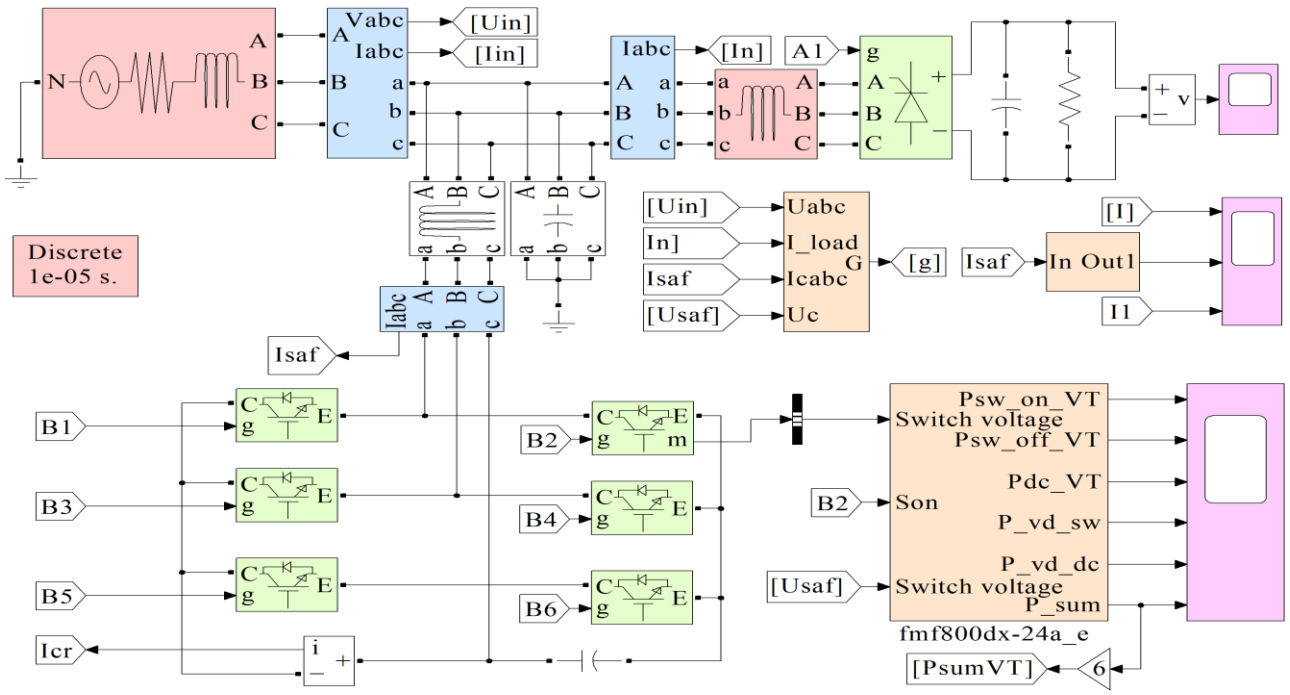

Figure 3.29 – Simulation model of APF with thyristor rectifier

Main parameters of the simulation model are given in table 3.6.

Table 3.6 – Parameters of simulation model

Model Component	Parameter	Value
Power supply	Phase voltage U_{RMS}, V	380
	Resistance R_0, mΩ	10
	Inductance L_0, mH	0.614
Active power filter	Phase inductance L_1, mH	0.2
	PWM frequency f_1, kHz	10
	Output filter capacity C_f, mF	50
Controlled rectifier	Input rectifier inductance L_2, mH	0.4
	Load capacitance C_L, mF	8
	Load resistance R_L, Ohm	3
	Passive C-filter capacitance C_1, μF	50

The peculiarity of the thyristor rectifier is that the THD of its input current depends significantly on the opening angle of the thyristors [109]. The dependence of the THD input current of the thyristor rectifier on the opening angle of the thyristors at different values of the input inductances is shown in fig. 3.30.

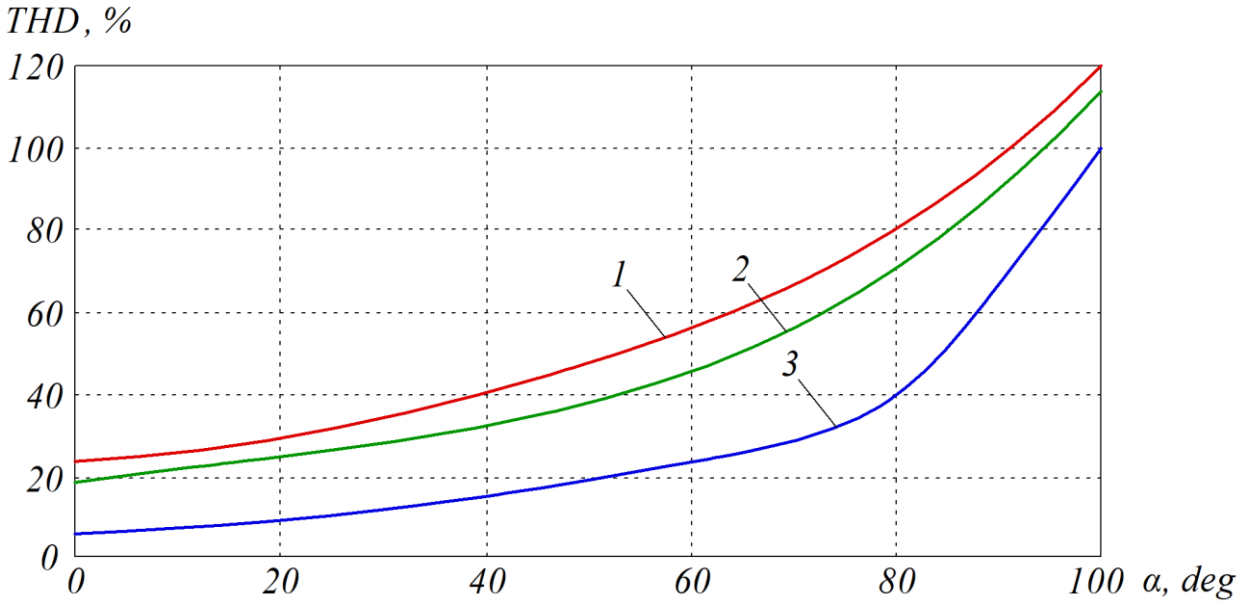

Figure 3.30 – Dependence of THD on thyristor opening angle at inductance:
1 – 0.04 mH; *2* – 0.4 mH; *3* – 4 mH

The results of the research conducted are given in table 3.7.

Table 3.7 – Electricity quality parameters

Electrical angle α		0	20	40	60	80	100
Rectifier input current I_{2RMS}, A		131.1	131.5	122.6	103.3	70.1	29.6
First harmonic of input current I_{21RMS}, A		125.9	125.1	111.4	87.1	53.4	18.7
THD of rectifier input current, %		30	34.22	47.79	67.09	86.45	125
APF current I_{RMS}, A		61.2	69.8	96.1	101	84.6	49.5
First harmonic of APF current I_{1RMS}, A		49.1	56.86	82	85	71.7	42.9
Total APF losses, W	no filter	602.6	645	841.5	919.1	839	613.4
	with C-filter	656.5	706.4	881.2	970.9	875.3	687.6
THD of current source with APF, %	no filter	2.14	2.36	3.76	4.6	7.69	9.05
	with C-filter	4.48	4.63	4.76	7.13	12.2	15.5
THD of voltage at general connection point, %	no filter	77.22	83.29	96.9	107.3	111.1	102.3
	with C-filter	9.75	9.79	9.15	10	13.3	9.9

As can be seen from table 3.7, the APF is quite good at compensating for the higher harmonics of the load current, but there are significant distortions in the supply voltage at the connection point.

The form of voltage and current in the electrical network at the connection point in the presence and absence of an additional capacitive filter is shown in fig. 3.31.

It can also be seen from the data in table 3.7 that with a significant change in the current value of the thyristor rectifier, the power losses in the APF do not change significantly.

Switching-on the APF will cause power losses in power transistors, so it is necessary to clearly understand what will be the losses in the network from higher harmonics. A method for determining additional thermal losses in the active resistance of the AC power network from higher harmonics is proposed in view of the resulting THD value of the source current.

As known, the THD of the alternating current is defined as:

$$THD_I = \frac{\sqrt{\sum_{m=2}^{m=\infty} I_m^2}}{I_1}, \qquad (3.17)$$

where I_m – the RMS of the m-th harmonic.

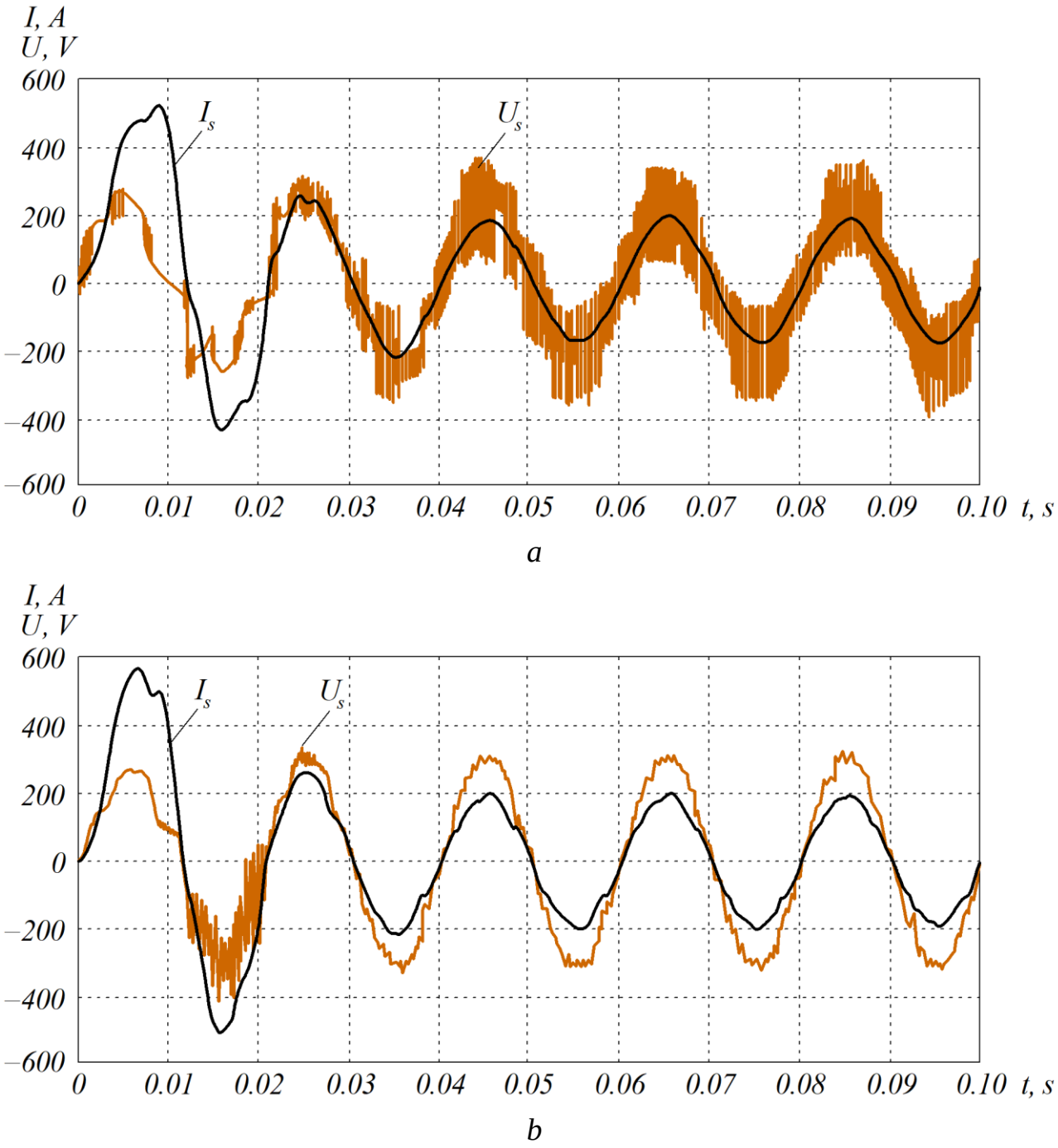

Figure 3.31 – Transient process when switching-on APF:
a – with capacitive filter; *b* – without capacitive filter

As is known, the effective value (i.e., RMS) of alternating (or direct pulsating) current is equal to the value of such direct current, which, for a time equal to one period of alternating current, will perform the same work (thermal or electrodynamic effect) as the considered alternating current:

$$I_{RMS} = \sqrt{\frac{1}{T} \cdot \int_0^T i^2(t)\,dt}. \tag{3.18}$$

The RMS of the AC can also be expressed through the spectrum of higher harmonics:

$$I_{RMS} = \sqrt{I_1^2 + \sum_{m=2}^{m=\infty} I_m^2}. \tag{3.19}$$

From expression (3.17) it is possible to determine the sum of the squares of higher harmonics:

$$\sum_{m=2}^{m=\infty} I_m^2 = \left(THD_I \cdot I_1\right)^2. \tag{3.20}$$

Then RMS of the current can be presented as follows:

$$I_{RMS} = \sqrt{I_1^2 + \left(THD_I \cdot I_1\right)^2} = \sqrt{I_1^2 \cdot \left(1 + THD_I^2\right)}; \tag{3.21}$$

$$I_{RMS} = I_1 \cdot \sqrt{\left(1 + THD_I^2\right)}. \tag{3.22}$$

The dependence of the RMS of the current on the THD_I value is shown in fig. 3.32, in which the RMS value of the first current harmonic is taken as 100 %.

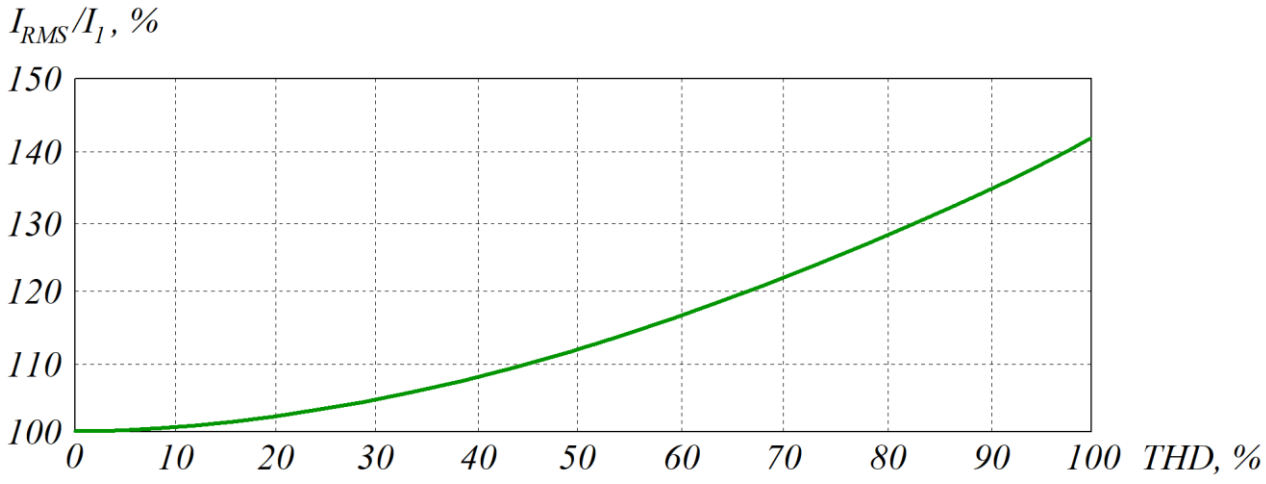

Figure 3.32 – Dependence of RMS on THD_I

The relative increase in the power losses in the active resistance of the network R_s, caused by higher harmonics, can be expressed as:

$$\Delta P = \frac{I_{RMS}^2 \cdot R_s}{I_1^2 \cdot R_s} = \frac{I_1^2 \cdot R_s \cdot \left(1 + THD_I^2\right)}{I_1^2 \cdot R_s} = 1 + THD_I^2, \tag{3.23}$$

where R_s – the resistance of the system.

Thus, an unambiguous relationship has been established between the THD of the consumed current and the percentage of additional power losses.

The dependence of the relative value of additional power losses in the active resistance of the electrical network on the THD value is shown in fig. 3.33, in which the losses caused by the fundamental harmonic are taken as 100 %.

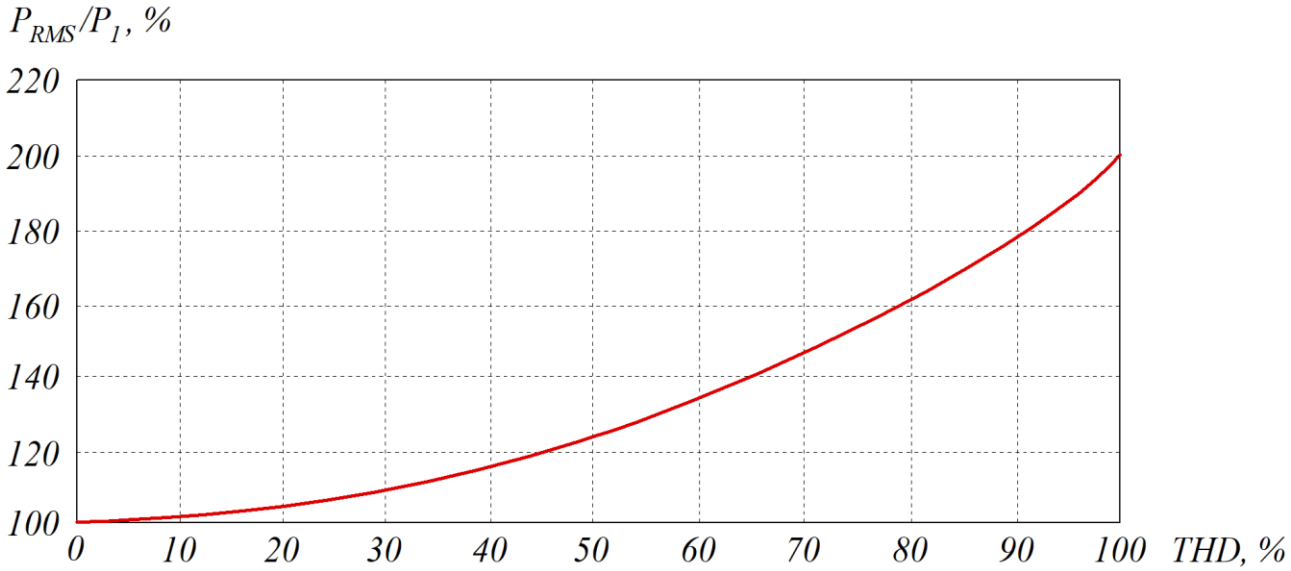

Figure 3.33 – Dependence of additional power losses on THD_I

The ratios shown in fig. 3.32 make it possible to determine additional losses in the power supply system on the value of the load current harmonic distortion factor THD_I.

It can be seen from fig. 3.33 that the distortions of the mains current from THD = 50 % causes an increase in power losses in the electrical network by about 25 %.

The effect of energy saving E_e in the power network with the APF is defined as:

$$E_e = \left(\Delta P_{gr1} - \Delta P_{gr2}\right) - \Delta P_f, \tag{3.24}$$

where ΔP_{gr1} – the power losses in the electric power network without the APF; ΔP_{gr2} – the power losses in the electric power network with the APF; ΔP_f – the total dynamic and static power in the MOSFET with the APF.

The planes of losses in the APF and the energy-saving effect in the network are shown in fig. 3.34.

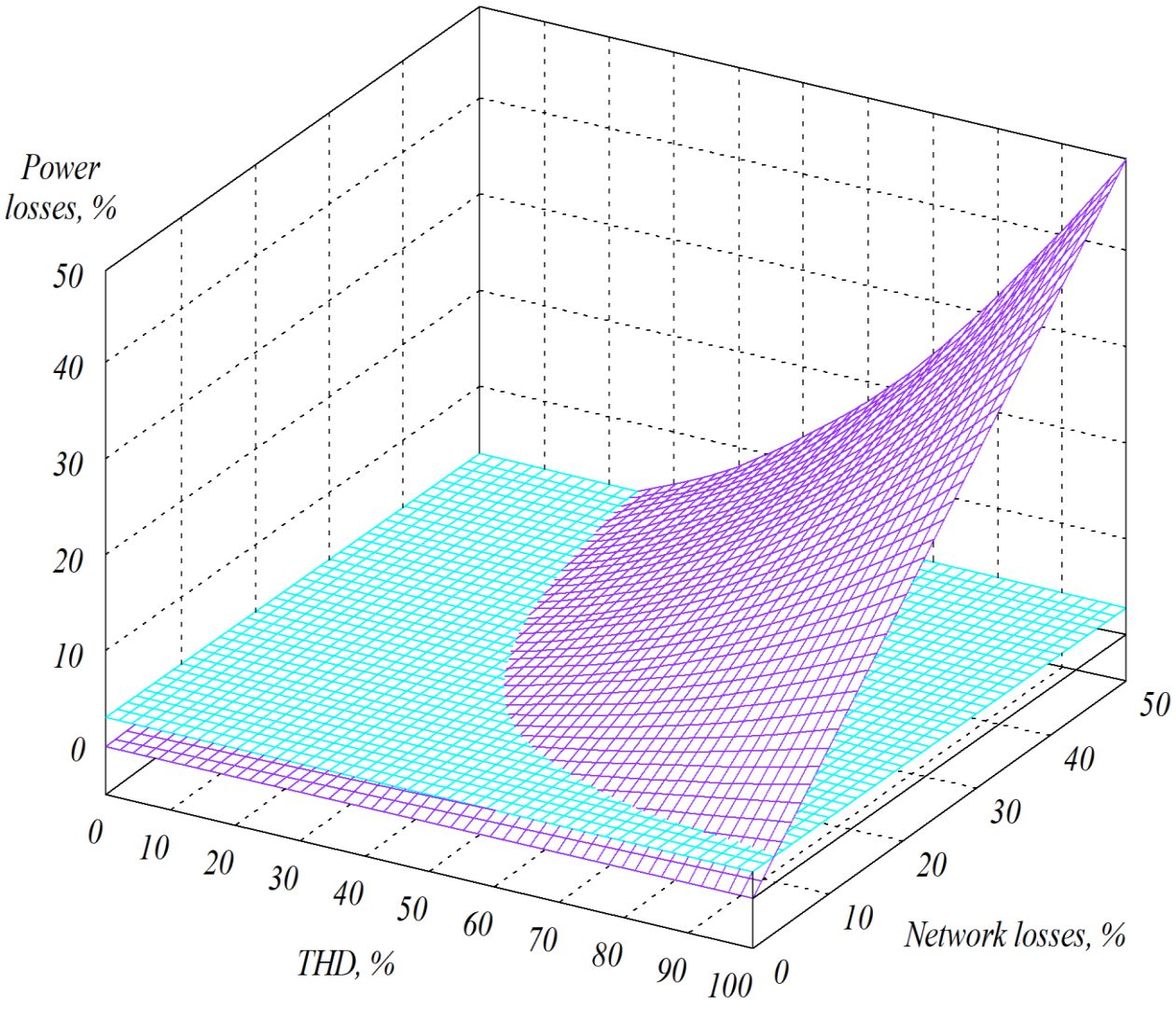

Figure 3.34 – Losses in APF (*1*) and energy-saving effect in network (*2*)

In fig. 3.34, the violet plane (the energy-saving effect of compensating for higher harmonics) above the blue plane is the level of power losses in the APF (up to 3 % of the network load power), at the same time, the zone corresponds to the mode when the use of the APF is justified and in general (integrally) has an energy-saving effect.

Table 3.8 provides an analysis of the intrinsic power losses in the APF and the energy-saving effect in the network from the compensation of higher harmonics at different values of the network resistance.

Table 3.8 – Energy-saving effect in the network from compensation of higher harmonics

Electrical angle α		0	20	40	60	80	100
Rectifier input current I_{2RMS}, A		131.1	131.5	122.6	103.3	70.1	29.6
First harmonic of input current I_{21RMS}, A		125.9	125.1	111.4	87.1	53.4	18.7
Total APF losses, W		656.5	706.4	881.2	970.9	875.3	687.6
Losses without APF, W	R_s = 10 mOhm	171.9	172.9	150.3	106.7	49.1	8.8
	R_s = 100 mOhm	1718	1729	1503	1067	491.4	87.6
	R_s = 1 Ohm	17187	17292	15030	10670	4914	876.2
Losses with APF, W	R_s = 10 mOhm	158.6	156.6	124.3	76	28.7	3.5
	R_s = 100 mOhm	1586	1566	1243	760.2	286.8	35.3
	R_s = 1 Ohm	15858	15658	12427	7602	2868	352.6
Energy saving effect, W	R_s = 10 mOhm	13.3	16.3	26	30.7	20.5	5.2
	R_s = 100 mOhm	132.9	163.4	260.3	306.8	204.6	52.4
	R_s = 1 Ohm	1329	1634	2603	3068	2046	524

It can be seen from table 3.8 that with different configurations of the electric network resistance, the own power losses in the APF can be more or less than the energy-saving effect in the network from the use of the APF. This also indicates the feasibility of future studies to optimize the operation frequency of the APF according to the criterion of frequencies of “suppressed” harmonics and to reduce its own power losses.

REFERENCES

1. Sevostyanov, A., Vagin, G. (2020). The impact of electrical power quality indicators on the accuracy of industrial power supply system management. *E3S Web of Conferences*, 216, 01068. DOI: 10.1051/e3sconf/202021601068.

2. Naumov, A. (2020). The required quality of electrical energy provision. *Power engineering: research, equipment, technology*, 22, 85–92. DOI: 10.30724/1998-9903-2020-22-1-85-92.

3. Lettl, J., Bauer, J. (2010). Compatibility of different types of frequency converters with supply network. *Piers Online*, 6, 537–541. DOI: 10.2529/PIERS100120073114.

4. Nerubatskyi, V., Plakhtii, O., Hordiienko, D., Khoruzhevskyi, H. (2020). Study of energy parameters in alternative power source microgrid systems with multi-level inverters. *International scientific journal «Industry 4.0»*, 5, 118–121.

5. Hanzelka, Z., Szpyra, W., Cziker, A., Piatek, K. (2012). Reactive power compensation. *Electrical Energy Efficiency: Technologies and Applications*, 1, 371–398. DOI: 10.1002/9781119990048.ch13.

6. Khomenko, I., Piskurev, M., Stasiuk, I. (2018). On the issue of reactive power compensation in electrical systems. *Bulletin of NTU KhPI Series Problems of Electrical Machines and Apparatus Perfection The Theory and Practice*, 32 (1308), 71–76. DOI: 10.20998/2079-3944.2018.32.13.

7. Khomenko, I. V., Fedoseenko, O. M., Stasiuk, I. V. (2017). Improving the reliability of power transformers oltc devices. *Collected scientific works of Ukrainian State University of Railway Transport*, 170, 60–71. DOI: 10.18664/1994-7852.170.2017.111280.

8. Lezhniuk, P. D., Kulyk, V. V., Burykin, O. B., Malogulko, Yu. V. (2018). Distributed energy sources in the local electrical systems: monograph. Riga: LAP LAMBERT Academic Publishing, 148.

9. Plakhtii, O., Nerubatskyi, V., Khomenko, I., Tsybulnyk, V., Syniavskyi, A. (2020). Comprehensive study of cascade multilevel inverters with three level cells. *2020 IEEE 7th International Conference on Energy Smart Systems (ESS)*, 277–282. DOI: 10.1109/ESS50319.2020.9160258.

10. Sahli, Z., Abdellatif, H., Bekrar, A., Trentesaux, D. (2018). Reactive power dispatch optimization with voltage profile improvement using an efficient hybrid algorithm. *Energies*, 11, 8, 2134. DOI: 10.3390/en11082134.

11. Ouyang, S. (2010). An improved catastrophic genetic algorithm and its application in reactive power optimization. *Energy and Power Engineering,* 2, 306–312. DOI: 10.4236/epe.2010.24043.

12. Plakhtii, O., Nerubatskyi, V., Mashura, A., Hordiienko, D. (2020). The analysis of mathematical models of charge-discharge characteristics in lithium-ion batteries. *2020 IEEE 40th International Conference on Electronics and Nanotechnology (ELNANO),* 635–640. DOI: 10.1109/ELNANO50318.2020.9088827.

13. Scherbak, Ya., Plakhtii, O., Nerubatskyi, V., Hordiienko, D., Shelest, D., Semenenko, Yu. (2021). Analysis of exact and approximating dependences of the active resistance of conductor on the frequency of current under the action of skin effect. *IEEE EUROCON 2021 – 19th International Conference on Smart Technologies,* 438–442. DOI: 10.1109/EUROCON52738.2021.9535581.

14. Plakhtii, O. A., Nerubatskyi, V. P., Shelest, D. A., Tsybulnyk, V. R. (2021). Investigation of the influence of the skin effect on power losses in DC traction power supply systems. *Information and Control Systems at Railway Transport,* 4, 3–14. DOI: 10.18664/ikszt.v26i4.247224.

15. Vamanan, N., John, V. (2018). Dual-comparison one-cycle control for single-phase bidirectional power converters. *IEEE Transactions on Industry Applications,* 54, 5, 4621–4631. DOI: 10.1109/TIA.2018.2836359.

16. Venkatramanan, D., Bharadwaj, P., Adapa, A. K., John, V. (2019). Power conversion technologies for high-performance AC micro-grid. *INAE Lett,* 4, 1, 27–35. DOI: 10.1007/s41403-018-00062-6.

17. Torre, J. L., Barros, L. A. M., Afonso, J. L., Pinto, J. G. (2019). Development of a proposed single-phase series active power filter without external power sources. *2019 International Conference on Smart Energy Systems and Technologies (SEST).* DOI: 10.1109/sest.2019.8849010.

18. Asiminoaei, L., Rodriguez, P., Blaabjerg, F., Malinowski, M. (2008). Reduction of switching losses in active power filters with a new generalized discontinuous-PWM strategy. *IEEE Transactions on Industrial Electronics,* 55 (1), 467–471. DOI: 10.1109/tie.2007.896554.

19. Artemenko, M. Y., Batrak, L. M., Polishchuk, S. Y., Mykhalskyi, V. M., Shapoval, I. A. (2016). The effect of load power factor on the efficiency of three-phase four-wire power system with shunt active filter. *2016 IEEE 36th International Conference on Electronics and Nanotechnology (ELNANO).* DOI: 10.1109/elnano.2016.7493067.

20. Marcu, M., Popescu, F.-G., Niculescu, T., Pana, L., Handra, A. D. (2014). Simulation of power active filter using instantaneous reactive power theory. *2014 16th*

International Conference on Harmonics and Quality of Power (ICHQP), 581–585. DOI: 10.1109/ichqp.2014.6842783.

21. Plakhtii, O., Nerubatskyi, V., Sushko, D., Hordiienko, D., Khoruzhevskyi, H. (2020). Improving the harmonic composition of output voltage in multilevel inverters under an optimum mode of amplitude modulation. *Eastern-European Journal of Enterprise Technologies*, 2, 8 (104), 17–24. DOI: 10.15587/1729-4061.2020.200021.

22. Shruti, K. K., Valsalan, T., Poorani, S. (2017). Single phase active front end rectifier system employed in three phase variable frequency drive. *International Journal of Innovative Research in Electrical, Electronics, Instrumentation and Control Engineering*, 5, 1, 121–129. DOI: 10.17148/IJIREEICE.

23. Plakhtii, O., Tsybulnyk, V., Nerubatskyi, V., Mittsel, N. (2019). The analysis of modulation algorithms and electromagnetic processes in a five-level voltage source inverter with clamping diodes. *2019 IEEE International Conference on Modern Electrical and Energy Systems (MEES)*, 294–297. DOI: 10.1109/MEES.2019.8896567.

24. Nerubatskyi, V. P., Plakhtiy, O. A., Gladka, A. V. (2018). Pokrashchennia elektromahnitnoyi sumisnosti tyahovoho elektropryvoda zminnoho strumu shlyakhom zastosuvannia 4QS-vypryamliachiv. *Collected scientific works of Ukrainian State University of Railway Transport*, 178, 21–28. DOI: 10.18664/1994-7852.178.2018.138906.

25. Plakhtiy, O. A., Nerubatskyi, V. P., Silantiev, A. S. (2017). Energoefficiency analisys of active rectifier with improved hysteretic control system. *Information and Management Systems of Railway Transport*, 3, 10–16.

26. Plakhtii, O., Nerubatskyi, V., Ryshchenko, I., Zinchenko, O., Tykhonravov, S., Hordiienko, D. (2019). Determining additional power losses in the electricity supply systems due to current's higher harmonics. *Eastern-European Journal of Enterprise Technologies*, 1, 8 (97), 6–13. DOI: 10.15587/1729-4061.2019.155672.

27. Plakhtii, O. A., Nerubatskyi, V. P., Kavun, A. M., Mashura, A. V. (2018). Compensation of input current harmonics in parallel multiple voltage sourse inverters. *Electrotechnic and computer systems*, 27 (103), 65–74. DOI: 10.15276/eltecs.27.103.2018.07.

28. Arcega, F. J., Pardina, A. (2014). Study of harmonics thermal effect in conductors produced by skin effect. *IEEE latin america transactions*, 12, 8, 1488–1495. DOI: 10.1109/TLA.2014.7014518.

29. Tsuchiya, A., Onodera, H. (2011). Effect of anomalous skin effect on transmission-line loss. *Leice Technical Report Microwaves,* 111, 351, 77–81.

30. Zagirnyak, M., Maliakova, M., Kalinov, A. (2015). Analysis of operation of power components compensation systems at harmonic distortions of mains supply voltage. *Joint International Conference – ACEMP 2015*: *Aegean Conference on Electrical Machines and Power Electronics, OPTIM 2015: Optimization of Electrical and Electronic Equipment and ELECTROMOTION 2015: International Symposium on Advanced Electromechanical Motion Systems,* 355–362. DOI: 10.1109/OPTIM.2015.7426958.

31. Akimzhanov, T. B., Kharlov, N. N., Borovikov, V. S., Ushakov, V. Ya. (2014). Development of calculation methods for additional electrical power losses during transportation. *2014 9th International Forum on Strategic Technology – IFOST,* 351–354. DOI: 10.1109/IFOST.2014.6991138.

32. Al-Mashakbeh, A. S., Zagirnyak, M., Maliakova, M., Kalinov, A. (2017). Improvement of compensation method for non-active current components at mains supply voltage unbalance. *EasternEuropean Journal of Enterprise Technologies*, 1, 8 (85), 41–49. DOI: 10.15587/1729-4061.2017.87316.

33. Ben, C. J. (2012). The practical issues involved in designing, specifying and installing skin effect current tracing systems. *IEEE Petroleum and Chemical Industry Conference Europe Conference Proceedings (PCIC EUROPE).*

34. Zaikin, D. (2015). Round and tubular wire skin effect modeling and usage SPICE as Maxwell's equations solver. *2015 23rd Telecommunications Forum Telfor (TELFOR),* 650–653. DOI: 10.1109/TELFOR.2015.7377551.

35. Blahnik, V., Talla, J. (2016). Single-phase synchronization for traction active rectifier. *International Conference on Applied Electronics (AE)*, 23–26. DOI: 10.1109/ae.2016.7577233.

36. Plakhtii, O. A., Nerubatskyi, V. P., Hordiienko, D. A., Khoruzhevskyi, H. A. (2020). Calculation of static and dynamic losses in power IGBT-transistors by polynomial approximation of basic energy characteristics. *Naukovyi Visnyk Natsionalnoho Hirnychoho Universytetu*, 2 (176), 82–88. DOI: 10.33271/nvngu/2020-2/082.

37. Nerubatskyi, V., Plakhtii, O., Kotlyarov, V. (2019). Analysis of topologies of active four-quadrant rectifiers for implementing the INDUSTRY 4.0 principles in traffic power supply systems. *International scientific journal «INDUSTRY 4.0»,* 4, 3, 106–109.

38. Bouzida, A., Abdelli, R., Ouadah, M. (2016). Calculation of IGBT power losses and junction temperature in inverter drive. *2016 8th International Conference*

on Modelling, Identification and Control (ICMIC), 768–773. DOI: 10.1109/icmic.2016.7804216.

39. Gervasio, F., Mastromauro, R., Liserre, M. (2015). Power losses analysis of two-levels and three-levels PWM inverters handling reactive power. *IEEE International Conference on Industrial Technology (ICIT)*, 1123–1128. DOI: 10.1109/icit.2015.7125248.

40. Shobini, M. M., Kamala, J., Rathna, R. (2017). Analysis and simulation of flying capacitor multilevel inverter using PDPWM strategy. *2017 International Conference on Innovative Mechanisms for Industry Applications (ICIMIA)*, 91–95. DOI: 10.1109/icimia.2017.7975578.

41. Shcherbak, Ya. V., Plakhtii, O. A., Nerubatskiy, V. P. (2017). Regulatory characteristics of the active quadrature converter in regimens and recuperation modes. *Technical electrodynamics*, 6, 26–31. DOI: 10.15407/techned2017.06.026.

42. Ahmadzadeh, T., Sabahi, M., Babaei, E. (2017). Modified PWM control method for neutral point clamped multilevel inverters. *2017 14th International Conference on Electrical Engineering/Electronics, Computer, Telecommunications and Information Technology (ECTI-CON)*, 765–768. DOI: 10.1109/ECTICon.2017.8096351.

43. Plakhtii, O. A., Nerubatskyi, V. P. (2018). Analyses of energy efficiency of interleaving in active voltage-source rectifier. *2018 IEEE 3rd International Conference on Intelligent Energy and Power Systems (IEPS)*, 253–258. DOI: 10.1109/IEPS.2018.8559514.

44. Zhao, G. I., Wang, L., Li, Q., Chen, G. (2014) Analyze and compare the efficiency of two-level and three-level inverter in SVPWM. *9th IEEE Conference on Industrial Electronics and Applications*, 1954–1958. DOI: 10.1109/iciea.2014.6931488.

45. Vasil'ev, B. Yu. (2015). Providing overmodulation mode and increasing energy conversion efficiency in autonomous power inverters of electric drives. *Electricity*, 6, 47–55.

46. Rodder, S., Biswas, M., Khan, Z. (2016). A modified PWM technique to improve total harmonic distirtion of multilevel inverter. *9th International Conference on Electrical and Computer Engineering (ICECE)*, 46–54. DOI: 10.1109/ICECE.2016.7853970.

47. Ferdowsi, F., Yazdankhah, A., Rohani, H. (2014). A combinative method to control output power fluctuations of large gridconnected photovoltaic systems. *2014 14th International Conference on Environment and Electrical Engineering (EEEIC)*, 260–264. DOI: 10.1109/EEEIC.2014.6835875.

48. Ferdowsi, F., Edrington, C. S., El-mezyani, T. (2015). Real-time stability assessment utilizing non-linear time series analysis. *North American Power Symposium (NAPS)*. DOI: 10.1109/NAPS.2015.7335189.

49. Nerubatskyi, V., Plakhtii, O., Hordiienko, D., Mykhalkiv, S., Ravlyuk, V. (2021). A method for calculating the parameters of the sine filter of the frequency converter, taking into account the criterion of starting current limitation and pulse-width modulation frequency. *Eastern-European Journal of Enterprise Technologies*, 1, 8 (109), 6–16. DOI: 10.15587/1729-4061.2021.225327.

50. Nerubatskyi, V. P., Plakhtii, O. A., Tugay, D. V., Hordiienko, D. A. (2021). Method for optimization of switching frequency in frequency converters. *Scientific bulletin of National mining university*, 1 (181), 103–110. DOI: 10.33271/nvngu/2021-1/103.

51. Gupta, K. K., Ranjan, A., Bhatnagar, P., Sahu, L. K., Jain, S. (2016). Multilevel inverter topologies with reduced device count: A review. *IEEE Transactions on Power Electronics*, 31 (1), 135–151. DOI: 10.1109/tpel.2015.2405012.

52. Ahmed, B., Aganah, K. A., Ndoye, M., Arif, M. A., Luciano, C., Murphy, G. V. (2017). Single-phase cascaded multilevel inverter topology for distributed DC sources. *2017 IEEE 8th Annual Ubiquitous Computing, Electronics and Mobile Communication Conference (UEMCON)*, 514–519. DOI: 10.1109/uemcon.2017.8248980.

53. Mykhal′s′kyi, V. M. (2013). Zasoby pidvyshchennia yakosti elektroenerhiyi na vkhodi i vykhodi peretvoryuvachiv chastot iz shyrotno-impul′snoyu moduliatsiyeyu. Kyiv: Instytut elektrodynamiky NAN Ukrayiny, 340.

54. Kirichenko, M. V., Drozdov, A. N., Zaitsev, R. V., Khrypunov, G. S., Drozdova, A. A., Zaitseva, L. V. (2020). Design of electronic devices stress testing system with charging line based impulse generator. *2020 IEEE KhPI Week on Advanced Technology*, 38–42. DOI: 10.1109/KhPIWeek51551.2020.9250146.

55. Hou, C.-C. (2013). A multicarrier PWM for parallel three-phase active front-end converters. *IEEE Trans Power Election*, 28 (6), 2753–2759. DOI: 10.1109/TPEL.2012.2220860.

56. Plakhtii, O., Nerubatskyi, V., Mashura, A., Hordiienko, D., Khoruzhevskyi, H. (2020). Improving energy indicators of the charging station for electric vehicles based on a three-level active rectifier. *Eastern-European Journal of Enterprise Technologies*, 3, 8 (105), 46–55. DOI: 10.15587/1729-4061.2020.204068.

57. Rajesh, B., Manjesh. (2016). Comparison of harmonics and THD suppression with three and 5 level multilevel inverter-cascaded H-bridge. *2016*

International Conference on Circuit, Power and Computing Technologies (ICCPCT). DOI: 10.1109/ICCPCT.2016.7530116.

58. Plakhtii, O. A., Nerubatskyi, V. P., Hordiienko, D. A., Tsybulnyk, V. R. (2019). Analysis of the energy efficiency of a two-level voltage source inverter in the overmodulation mode. *Scientific bulletin of National mining university*, 4 (172), 68–72. DOI: 10.29202/nvngu/2019-4/9.

59. Vasilchenko, S., Cherny, S., Khrulkov, V. (2020). Improving dynamic and energy characteristics of electromechanical systems with single-phase rectifiers. *2020 International Conference on Industrial Engineering, Applications and Manufacturing (ICIEAM).* DOI: 10.1109/ICIEAM48468.2020.9111902.

60. Plakhtii, O., Nerubatskyi, V., Karpenko, N., Ananieva, O., Khoruzhevskyi, H., Kavun, V. (2019). Studying a voltage stabilization algorithm in the cells of a modular six-level inverter. *Eastern-European Journal of Enterprise Technologies*, 6, 8 (102), 19–27. DOI: 10.15587/1729-4061.2019.185404.

61. Chen, L., Wang, Y., Martin, D. (2010). Design of parallel inverters for smooth mode transfer microgrid applications. *IEEE Transactions on Power Electronics*, 25, 1, 6–15. DOI: 10.1109/TPEL.2009.2025864.

62. Zhihong, Y., Boroyevich, D., Jae-Young, C., Lee, F. C. (2002). Control of circulating current in two parallel three-phase boost rectifiers. *IEEE Transactions on Power Electronics*, 17, 5, 609–615. DOI: 10.1109/TPEL.2002.802170.

63. Pan, C.-T., Liao, Y.-H. (2008). Modeling and control of circulating currents for parallel three-phase boost rectifiers with different load sharing. *IEEE Transactions on Industrial Electronics*, 55, 7, 2776–2785. DOI: 10.1109/TIE.2008.925647.

64. Hou, C.-C., Cheng, P.-T. (2011). A multi-carrier pulse width modulator for the auxiliary converter and the diode rectifier. *IEEE Transactions on Power Electronics*, 26, 4, 1119–1126. DOI: 10.1109/TPEL.2010.2098050.

65. Bohra, A., Sajeesh, D., Patel, C., Saldanha, M. (2016). Modulation techniques in single phase PWM rectifier. *IJCA Proceedings on International Conference on Advances in Science and Technology*, 5–7.

66. Plakhtii, O. A., Nerubatskyi, V. P., Kavun, V. Ye., Hordiienko, D. A. (2019). Active single-phase four-quadrant rectifier with improved hysteresis modulation algorithm. *Scientific bulletin of National mining university*, 5 (173), 93–98. DOI: 10.29202/nvngu/2019-5/16.

67. Plakhtiy, O. A., Nerubatskiy, V. P., Sushko, D. L., Kavun, V. E. (2018). Reduction of dynamic losses in the active one-phase four-quadrant converter with the improved algorithm of hysteresis modulation. *Works of the Institute of electrodynamics*

of the National academy of sciences of Ukraine, 51, 88–94. DOI: 10.15407/publishing2018.51.088.

68. Kiran, Y., Parthiban, B., Jena, P., Prakash, P. (2016). Design and implementation of sliding mode voltage controller for DC to DC buck converter by using hysteresis modulation and pulse width modulation. *2016 Biennial International Conference on Power and Energy Systems: Towards Sustainable Energy (PESTSE)*. DOI: 10.1109/pestse.2016.7516439.

69. Sondur, V. V., Sondur, V. B., Rao, D. H., Latte, M. V., Ayachit, N. H. (2007). Issues in the design of equiripple FIR higher order digital differentiators using weighted least squares technique. *2007 IEEE International Conference on Signal Processing and Communications*. DOI: 10.1109/icspc.2007.4728287.

70. Popoli, A., Sandrolini, L., Cristofolini, A. (2021). Reduction in the electromagnetic interference generated by AC overhead power lines on buried metallic pipelines with screening conductors. *Electricity*, 2, 316–329. DOI: 10.3390/electricity2030019.

71. Colak, K., Asa, E., Czarkowski, D. (2016). A novel phase control of single switch active rectifier for inductive power transfer applications. *2016 IEEE Applied Power Electronics Conference and Exposition (APEC)*, 1767–1772. DOI: 10.1109/apec.2016.7468107.

72. Wei, Y, Jankovic, L., Patel, Z, Hu, J. (2016). Single phase precharge control method for active front end rectifier. *2016 IEEE Energy Conversion Congress and Exposition (ECCE)*. DOI: 10.1109/ecce.2016.7855436.

73. Swamy, M., Guddanti, C. (2014). An improved single-phase active front end rectifier system for use with three-phase variable frequency drives. *2014 IEEE Applied Power Electronics Conference and Exposition – APEC 2014*, 1558–1564. DOI: 10.1109/apec.2014.6803514.

74. Suhara, E. M., Nandakumar, M. (2015). Analysis of hysteresis current controlled three phase PWM rectifier with reduced switching loss. *IJCTA*, 8 (3), 877–887.

75. Plakhtii, O., Nerubatskyi, V., Karpenko, N., Hordiienko, D., Butova, O., Khoruzhevskyi, H. (2019). Research into energy characteristics of single-phase active four-quadrant rectifiers with the improved hysteresis modulation. *Eastern-European Journal of Enterprise Technologies*, 5, 8 (101), 36–44. DOI: 10.15587/1729-4061.2019.179205.

76. Plakhtii, A. A. (2015). Dinamicheskaya model' aktivnogo trekhfaznogo vypryamitelya s korrektsiei koeffitsienta moshchnosti. *Sbornik nauchnykh trudov NUK*, 7, 33–39.

77. Shcherbak, Ya. V. (1999). Shirotno-impul'snyi preobrazovatel' s shirotno-impul'snoi modulyatsiei vtorogo roda v usloviyakh nesimmetrii. *Tekhnicheskaya elektrodinamika*, 1, 31–35.

78. Kazachkovskii, N. N., Yakupov, D. V. (2008). Upravlenie aktivnym vypryamitelem s releino-vektornym konturom toka dlya sistem chastotno-reguliruemogo elektroprivoda. *Vestnik Priazov. goss. tekhn. un-ta: sb. nauch. trud.*, 18, 2, 40–43.

79. Yakupov, D. V., Kazachkovskii, N. N. (2010). Upravlenie aktivnym vypryamitelem s shirotno-impul'snoi modulyatsiei pri vozmushcheniyakh so storony nagruzki. *Visnyk Kremenchuts'koho derzhavnoho universytetu im. M. Ostrohrads'koho*, 4 (63), 1, 16–19.

80. Plakhtii, A. A. (2013). Gisterezisnaya sistema upravleniya aktivnogo trekhfaznogo vypryamitelya s korrektsiei koeffitsienta moshchnosti. *Sbornik nauchnykh trudov NUK*, 4, 82–88.

81. Plakhtii, A. A., Shcherbak, Ya. V. (2014). Issledovanie rezhima rekuperatsii aktivnogo trekhfaznogo vypryamitelya s korrektsiei koeffitsienta moshchnosti. *Zbirnyk naukovykh prats' Ukrayins'koyi derzhavnoyi akademiyi zaliznychnoho transportu*, 143, 188–194.

82. Rashid, M. H. (2007). Power electronics handbook: devices, circuits, and applications. *Third Edition. Elsevier*, 250–251.

83. Plakhtii, A. A. (2015). Analiz energeticheskikh kharakteristik trekhfaznogo aktivnogo vypryamitelya s korrektsiei koeffitsienta moshchnosti pri rabote s postoyannoi chastotoi modulyatsii. *Vestnik NTU "KhPI"*, 12, 430–434.

84. Zhemerov, G. G., Koval'chuk, O. I., Tugai, D. V. (2011). Vybor induktivnosti reaktorov aktivnogo vypryamitelya – istochnika napryazheniya, rabotayushchego s postoyannoi chastotoi ShIM. *Elektrotekhnika i elektromekhanika*, 6, 32–37.

85. Wurfl, J., Hilt, O., Bahat, E., Zhytnytska, R., Klein, K., Kotara, P., Brunner, F., Knauer, A., Kruger, O., Weyers, M., Trankle, G. (2013). Technological approaches towards high voltage, fast switching GaN power transistors. *ECS Transactions*, 52, 1, 979–989.

86. Shcherbak, Ya. V., Tsekhovskoi, M. V. Plakhtii, A. A. (2014). Uluchshenie elektromagnitnoi sovmestimosti preobrazovatelei chastoty putem primeneniya aktivnykh vypryamitelei s korrektsiei koeffitsienta moshchnosti. *Elektricheskie i komp'yuternye sistemy*, 95, 344–347.

87. Nerubatskyi, V. P., Plakhtii, O. A., Hordiienko, D. A., Karpenko, N. P. (2021). Simulation of power losses in the frequency converter. *Modern engineering*

and innovative technologies, 16, 1, 44–57. DOI: 10.30890/2567-5273.2021-16-01-035.

88. Plakhtii, O., Nerubatskyi, V., Sushko, D., Ryshchenko, I., Tsybulnyk, V., Hordiienko, D. (2019). Improving energy characteristics of AC electric rolling stock by using the three-level active four-quadrant rectifiers. *Eastern-European Journal of Enterprise Technologies,* 4, 8 (100), 6–14. DOI: 10.15587/1729-4061.2019.174112.

89. Bashir, S. B., Memon, Z. A. (2018). An improved voltage balancing method for grid connected PV system based on MMC under different irradiance conditions. *2018 IEEE 61st International Midwest Symposium on Circuits and Systems (MWSCAS),* 865–868. DOI: 10.1109/MWSCAS.2018.8623947.

90. Adapa, A. K., John, V. (2019). An auxiliary-capacitor-based active phase converter with reduced device current stress. *IEEE Transactions on Industrial Electronics,* 66, 9, 6925–6935. DOI: 10.1109/TIE.2018.2877087.

91. Wu, R., Wen, J., Wu, J., Chen, Z., Peng, C., Wang, Y. (2012). Analysis of power losses in voltage source converter with new generation IGBTs. *2012 IEEE International Conference on Computer Science and Automation Engineering (CSAE),* 674–678. DOI: 10.1109/csae.2012.6272683.

92. Dai, P., Guoand, G., Gong, Z. (2016). A selection precharge method for modular multilevel converter. *International Journal of Control and Automation,* 9, 4, 161–170. DOI: 10.14257/ijca.2016.9.4.16.

93. Maurya, S., Mishra, D., Singh, K., Mishra, A., Pandey, Y. (2019). An efficient technique to reduce total harmonics distortion in cascaded h-bridge multilevel inverter. *2019 IEEE International Conference on Electrical, Computer and Communication Technologies (ICECCT).* DOI: 10.1109/icecct.2019.8869424.

94. Saeedian, M., Adabi, J., Hosseini, S. M. (2017). Cascaded multilevel inverter based on symmetric–asymmetric DC sources with reduced number of components. *IET Power Electronics,* 10 (12), 1468–1478. DOI: 10.1049/iet-pel.2017.0039.

95. Singh, D., Bansal, P. (2018). A power effective asymmetric topology for 7-level multilevel inverter with different PWM techniques. *International Journal of Science, Engineering and Technology Research (IJSETR),* 7, 6, 413–417.

96. Mohamad, A. S., Radzi, M. A., Mailah, N. F., Othman, M. L. (2019). The effects of number of conducting switches in a cascaded multilevel inverter output. *2019 IEEE 10th Control and System Graduate Research Colloquium (ICSGRC),* 26–31. DOI: 10.1109/ icsgrc.2019.8837065.

97. Nerubatskyi, V. P., Plakhtii, O. A., Hordiienko, D. A., Khoruzhevskyi, H. A., Philipjeva, M. V. (2021). Analysis of exact and approximating

dependences of active resistance of a conductor on the current frequency based on the influence of skin effect. *Collected scientific works of Ukrainian State University of Railway Transport,* 197, 99–112. DOI: 10.18664/1994-7852.197.2021.248216.

98. Habibolahzadeh, M., Roudsari, H. M., Jalilian, A., Jamali, S. (2021). Using C-type filter with partial compensation method for capacity reduction of hybrid power quality conditioner in co-phase traction power system. *IET Power Electron*, 14, 2350–2373. DOI: 10.1049/pel2.12185.

99. Shcherbak, Y., Semenenko, Y., Semenenko, O., Karpenko, N., Suprun, O., Plakhtii, O., Nerubatskyi, V. (2021). Synthesis of the transfer function of the voltage controller in an active filter-stabilizer converter. *Eastern-European Journal of Enterprise Technologies,* 2, 2 (110), 71–77. DOI: 10.15587/1729-4061.2021.229827.

100. Deng, F., Chen, Z. (2015). Voltage-balancing method for modular multilevel converters switched at grid frequency. *IEEE Transactions on Industrial Electronics,* 62 (5), 2835–2847. DOI: 10.1109/tie.2014.2362881.

101. Martinez-Rodrigo, F., Ramirez, D., Rey-Boue, A., de Pablo, S., Herrero-de Lucas L. (2017). Modular multilevel converters: control and applications. *Energies,* 10 (11), 1709. DOI: 10.3390/en10111709.

102. Nerubatskyi, V. P., Plakhtii, O. A., Karpenko, N. P., Hordiienko, D. A., Tsybulnyk, V. R. (2019). Analysis of energy processes in a seven-level autonomous voltage inverter at various modulation algorithms. *Information and Control Systems at Railway Transport,* 5, 8–18. DOI: 10.18664/ikszt.v24i5.181286.

103. Mali, S. M., Patil, Dr. B. (2018). THD minimization in multilevel inverter using optimization approach. *International Journal of Engineering Research & Technology (IJERT),* 7, 6, 97–100. DOI: 10.17577/IJERTV7IS060048.

104. Sonia, K., Seshadri, G. (2015). Analysis and modelling of a multilevel inverter in distribution system with FACTS capability. *International Journal of Innovative Research in Science, Engineering and Technology,* 4, 5, 3015–3021. DOI: 10.15680/IJIRSET.2015.0405072.

105. Kurwale, M. V., Sharma, P. G., Bacher, G. (2014). Performance analysis of modular multilevel converter (MMC) with continuous and discontinuous pulse width modulation (PWM). *International Journal of Advanced Research in Electrical, Electronics and Instrumentation Engineering,* 3, 2, 7463–7474.

106. Yang, H., Saeedifard, M. (2017). A capacitor voltage balancing strategy with minimized AC circulating current for the DC–DC modular multilevel converter. *IEEE Transactions on Industrial Electronics,* 64, 2, 956–965. DOI: 10.1109/tie.2016.2613059.

107. Du, V., Dekka, A., Wu, B., Zargari, N. (2018). Modular multilevel converters: analysis, control and applications. *Wiley-IEEE Press,* 368. DOI: 10.1002/9781119367291.

108. Bashir, S. B., Beig, A. R. (2018). An improved voltage balancing algorithm for grid connected MMC for medium voltage energy conversion. *International Journal of Electrical Power & Energy Systems*, 95, 550–560. DOI: 10.1016/j.ijepes.2017.09.002.

109. Zhemerov, G. G., Krylov, D. S. (2018). Concept of construction of power circuits of a multilevel modular converter and its transistor modules. *Electrical Engineering & Electromechanics,* 6, 26–32. DOI: 10.20998/2074-272X.2018.6.03.

Scientific publication

NERUBATSKYI Volodymyr Pavlovych
PLAKHTII Oleksandr Andriiovych
HORDIIENKO Denys Anatoliiovych

SCIENTIFIC FOUNDATIONS OF HIGHER ENERGY EFFICIENCY AND ELECTROMAGNETIC COMPATIBILITY OF SEMICONDUCTOR ELECTRIC ENERGY CONVERTERS

Monograph

Responsible for release Nerubatskyi V. P.

Author's edition

Sent to the printer 15.09.2022. Format 60×84/16.
Type Times New Roman. Offset paper.
Printer's sheet 15.18. 50 printed copies. Order № 121515. Agreed price.

Publisher Machulin L.
61057, Kharkiv, Rymars′ka str., 17/14
tel. +38(068)886-52-57; editor2016@ukr.net
Certificate of state registration XK #125 of 24.11.2004

Manufacturer Individual person-entrepreneur
LLC "VOSKHOD-PRINT"
61057, Kharkiv, Rymars′ka str., 3/5